An Isotopic and Petrologic Study of an Exposure of the

Deep Sierra Nevada Batholith, Tehachapi Mountains, California

Thesis by

David Alan Pickett

In Partial Fulfillment of the Requirements

for the Degree of

Doctor of Philosophy

California Institute of Technology

Pasadena, California

1991

(submitted April 23, 1991)

DEDICATION

This thesis is lovingly dedicated to my parents, John and Dana Pickett, who nurtured in me a curiosity about and respect for nature that has sustained me through all my studies. I cannot adequately express the true importance to me of their love and support.

Acknowledgements

The major part of the work in this thesis was performed under the guidance of Professor Jason Saleeby, whom I gratefully acknowledge. Aside from introducing me to the fascinating geology of the Tehachapi Mountains, Jason provided a regional geologic and tectonic context for my results at those times when I would begin to lose sight of the importance of my work. He nudged me into the world of isotope geology, and offered me a great deal of responsibility and freedom in his laboratory. Most of all, I will remember Jason's unwavering support, friendship, and enthusiasm.

Professor Jerry Wasserburg opened his laboratory to me and provided a thorough grounding in isotope geochemistry which made possible much of my work with Jason. He challenged me to broaden not only my knowledge, but also my perspective. A tangible result of this challenge was the research in New Zealand reported in Appendix 1.

Professor Lee Silver was generous with both his time and his vast geologic knowledge; discussions and courses with him were invaluable in forcing me to shape ideas. Dr. Dimitri Papanastassiou shared some of his considerable knowledge of isotopic analysis and unselfishly gave advice, spikes, and standards in support of my efforts in Jason's lab. Professor Ed Stolper was the first to put me to work in a geochemistry laboratory, and courses by him and Professor Hugh Taylor gave me a firm foundation in chemical approaches to geologic problems. Professor Jim Westphal generously provided computer facilities and office space during the completion of this thesis.

In the Lunatic Asylum, I benefitted from Dr. Henry Ngo's patient training, advice from Drs. Dominique Weis and Jim Chen, and aid from Paul Knust-Graichen, Lindsey Hedges, and Chris Price. In Professor Saleeby's lab, Mahmood Chaudhry helped keep things running smoothly, and Vic Nenow's trouble-shooting was invaluable. Dr. Paul Carpenter offered tireless training in and advice on microprobe analysis and things Mac. Drs. Sally Newman and Yigal Erel trained me in DCP procedures. Professor Lawford

iv

Abstract

The Tehachapi Mountains, southernmost Sierra Nevada, California, are composed of variably deformed Cretaceous batholithic intrusive rocks and their high-grade framework. The purpose of this study is to 1) establish stronger constraints on the apparently great depths of exposure, and 2) characterize isotopically and chemically the petrogenesis of the intrusive rocks.

The Al contents of hornblendes imply igneous pressures from 3.2 kbar in the extreme north of the study area to around 8 kbar in the south. The southern values are the highest yet determined for the entire Sierra Nevada. The rocks commonly show subsolidus recrystallization and metamorphism producing local, fluid-related, garnet-bearing assemblages. Pressures based on garnet-hornblende-plagioclase-quartz and garnet-biotite-plagioclase-quartz equilibria in these metaigneous rocks and framework rocks (7-8 kbar at 670-760°C) confirm the igneous results. There is also recorded in one area a lower-pressure event (4 kbar, 600°C) which apparently occurred after uplift which quickly followed initial crystallization of the magmas. The recognition of deformed quartz-bearing rocks at such great depths implies that the young, warm, deep batholith may represent a site favorable for major delamination of the crust.

Initial $^{87}Sr/^{86}Sr$ of the igneous rocks of the main study area generally ranges from 0.7041 to 0.7054, with ϵ_{Nd} = +2.9 to -0.9. Lower ϵ_{Nd} and higher $^{87}Sr/^{86}Sr$ values are found in the tonalite of Bear Valley Springs to the north. Combined with Pb and published O results, the isotopic data are most consistent with a model of mixing between mantle-derived magmas and metasedimentary rocks of chiefly continental provenance. (Two granites from the older suite deviate from this pattern, probably due to fluid interaction.) However, isotopic ratios do not show coherent variation trends consistent with this model when combined with chemical data. The chemical data suggest that lithologic variation

among the intrusive rocks results from fractional crystallization acting on mafic to intermediate parent magmas which obtained their diverse isotopic characteristics at a deeper level (>25-30 km). This study reveals the deep Sierra Nevada batholith to be more heterogeneous and somewhat more mafic than analogous portions of the higher batholith, and suggests that isotopic hybridization of batholith magmas takes place in its deepest levels.

Table of Contents

CHAPTER 1

Introduction

Over time, geologists have discovered the features of the crust of the continents that distinguish it readily from that of the ocean floor. Among these are its thickness, composition, density, age, geologic diversity, and physiographic patterns. The great magmatic arcs which are major constituents of continental orogenic belts both past and present reflect important processes in the evolution of the continents -- adding to and recycling of the stuff of the continents.

For these reasons the granitoid batholiths are deemed worthy of special attention, and much effort has been addressed to the problem of the origin of their magmas. Variations in the petrochemical and isotopic characteristics of these rocks are generally attributed to the effects of one or both of two classes of petrogenetic processes: 1) tapping of distinct and variable deep crustal and/or upper mantle sources, and 2) modification of less variable, mantle-derived primary materials by interaction with pre-existing crustal materials. The assignation of the relative importance of these two effects is a subject which varies by researcher and, indeed, may vary in truth from batholith to batholith.

This thesis is concerned with addressing these issues by way of two different approaches at two different locales -- California and New Zealand -- which share the following basic features: a Phanerozoic granitoid-composition batholith is intruded into a complex assemblage of metamorphic rocks reflecting long-lived continental-margin geologic processes. In New Zealand (Appendix 1), the approach is one of large scale, selective sampling in order to assess batholith genesis and crustal history and character as reflected in the isotopic and trace-element character of the rocks. In contrast, the

California study, which constitutes the bulk of this thesis, is smaller scale, more based in considerations of regional tectonic setting and metamorphic history, and can be viewed in the context of extensive work carried out elsewhere in the batholith. Both studies point to the importance of the interaction between crustal and mantle sources and to the difficulties in seeing through subsequent petrogenetic processes in an attempt to identify ultimate sources and components.

The Sierra Nevada Batholith

As a well-known and accessible example of the genre, the Mesozoic Sierra Nevada batholith of California has received its fair share of attention. Early workers recognized the overall compositional character of the belt, and subsequent research has revealed details of the metamorphic framework, compositional patterns, structural features, and age characteristics of the various plutons making up the batholith. While many observations and interpretations have proven indisputable, consensus has been elusive on many questions regarding the belt, not least of which are two addressed here: How do the physical and chemical characteristics of the batholith vary with depth? What are the petrogenetic processes responsible for generation of the voluminous magmas exposed in the batholith?

The southern half of the Sierra Nevada range appears roughly to represent an oblique cross section through the Cretaceous batholith, affording us the opportunity to observe products and effects of the active batholith in the third dimension. The present study area in the Tehachapi Mountains represents the culmination of this southward deepening, and thus offers the deepest available view of the intrusive and metamorphic products of batholith construction. This view may allow us to say something about the loci of batholith igneous processes, allowing us to ask such fundamental questions as "If crustal assimilation is an important process, does it take place at higher or lower levels?" Furthermore, it is of interest to consider the subsequent tectonic history that has been

responsible for the present exposure of such deep levels.

New Zealand Granitoids

Although the Paleozoic and Mesozoic New Zealand batholithic rocks apparently shared a tectonic environment roughly analogous to that in the Sierra Nevada, the New Zealand crustal block today is in a rather unique, isolated setting. Since drifting from its Gondwanaland homeland in more recent times, the New Zealand block has been cut by complex faulting episodes, invaded by hot-spot magmas, and apparently thinned. The purpose of the study in Appendix 1 is to explore possible petrogenetic pathways for production of the granitoids, to examine the implications of granitoid isotope characteristics for earlier crustal history, and to speculate on how these and later magmatic events may have altered the gross characteristics of the block.

Note: This thesis is written in the form of a series of published or publishable papers, each of which is intended to eventually stand alone. This accounts for some of the overlap in the material presented in Chapters 2-4. A modified version of Appendix 1 was published as the following:

Pickett, D.A., and G.J. Wasserburg, Nd and Sr isotopic characteristics of New Zealand granitoids and related rocks, *Contrib. Mineral. Petrol., 103*, pp. 131-142, 1989.

CHAPTER 2

Thermobarometric constraints on the depth of exposure and conditions of plutonism and metamorphism at deep levels of the Sierra Nevada batholith, Tehachapi Mountains, California

2.1. Introduction

The Sierra Nevada batholith is a well-studied example of the Phanerozoic plutonic belts common to continental margins. Until recently, however, information about the properties of the belt in the depth dimension was available only indirectly through regional geologic [Hamilton and Myers, 1967] and geophysical [Bateman and Eaton, 1967; Pakiser and Brune, 1980; Saleeby et al., 1986] considerations. Newer studies are beginning to show that the southern exposures of the batholith provide us with a window into its deeper structure. In this study, we determine estimated physical conditions attendant on intrusion and metamorphism in the southernmost portion of the batholith (Tehachapi Mountains) in an attempt to characterize the processes that may operate deep in an active magmatic arc. The rocks studied prove to be the deepest yet known from the Cretaceous batholith, and their compositional, mineralogical, and structural features have implications for the description of the geophysical and petrologic nature of deep batholithic crust.

The Tehachapi Mountains lie at the southern end of the Sierra Nevada range in central California (Figures 2.1 and 2.2). South and west of the Cretaceous tonalite of Bear Valley Springs, the crystalline basement of the range is composed of gneisses representing Cretaceous calcalkaline intrusive rocks and their metamorphic country rocks [Sharry,

1981; Ross, 1985, 1989; Saleeby et al., 1987; Sams and Saleeby, 1988]. Previous studies [Sharry, 1981; Sams and Saleeby, 1988] have presented data suggestive of high-pressure conditions during the thermal maximum, and Saleeby [1990] has incorporated these observations into a model of the southern half of the Sierra Nevada batholith as an oblique section through the Cretaceous magmatic arc (a model supported by the regional-scale igneous barometric data of Ague and Brimhall, [1988]). The crystalline rocks of the Tehachapi Mountains represent the culmination of this southward deepening; in fact, Ross [1985] has referred to the Tehachapi basement as a "batholithic root." Here we present new field, petrographic, and thermobarometric data that not only lend more substantial support to the high pressure model for the Tehachapi crystalline rocks, but also reveal a complex metamorphic and tectonic history. This scenario may help shed light on the larger-scale tectonic history of the Sierra Nevada and southern California, particularly with respect to those mechanisms responsible for the uplift of such deep rocks. Preliminary results of this study have appeared in abstract form [Pickett and Saleeby, 1989, 1990].

2.2. Geologic Setting

The Tehachapi Mountains are underlain by variably foliated gabbroic to granitic rocks which have intruded chiefly psammitic and calcareous metasedimentary assemblages (Figure 2.2). These basement rocks are overlain by Tertiary sedimentary and volcanic strata, the lowest belonging to the Eocene Tejon Formation [Nilsen, 1987]. These strata have been affected by relatively recent folds and high-angle faults [Goodman et al., 1989; Malin et al., in review], and the range in the study area has apparently undergone ~60° of clockwise rotation since Cretaceous time [Kanter and McWilliams, 1982; McWilliams and Li, 1985], with at least 30° of that occurring during Miocene time [Plescia and Calderone, 1986]. The crystalline rocks of the Tehachapi range, as considered in this study, are bounded on the southeast by the Pastoria thrust and the north branch of the

Figure 2.1 - Basement geologic map of the southern Sierra Nevada with sample localities

in the northern study area. Modified after Ross [1989], Sams [1986], and Sharry [1981].

Sample localities are from Sams [1986].
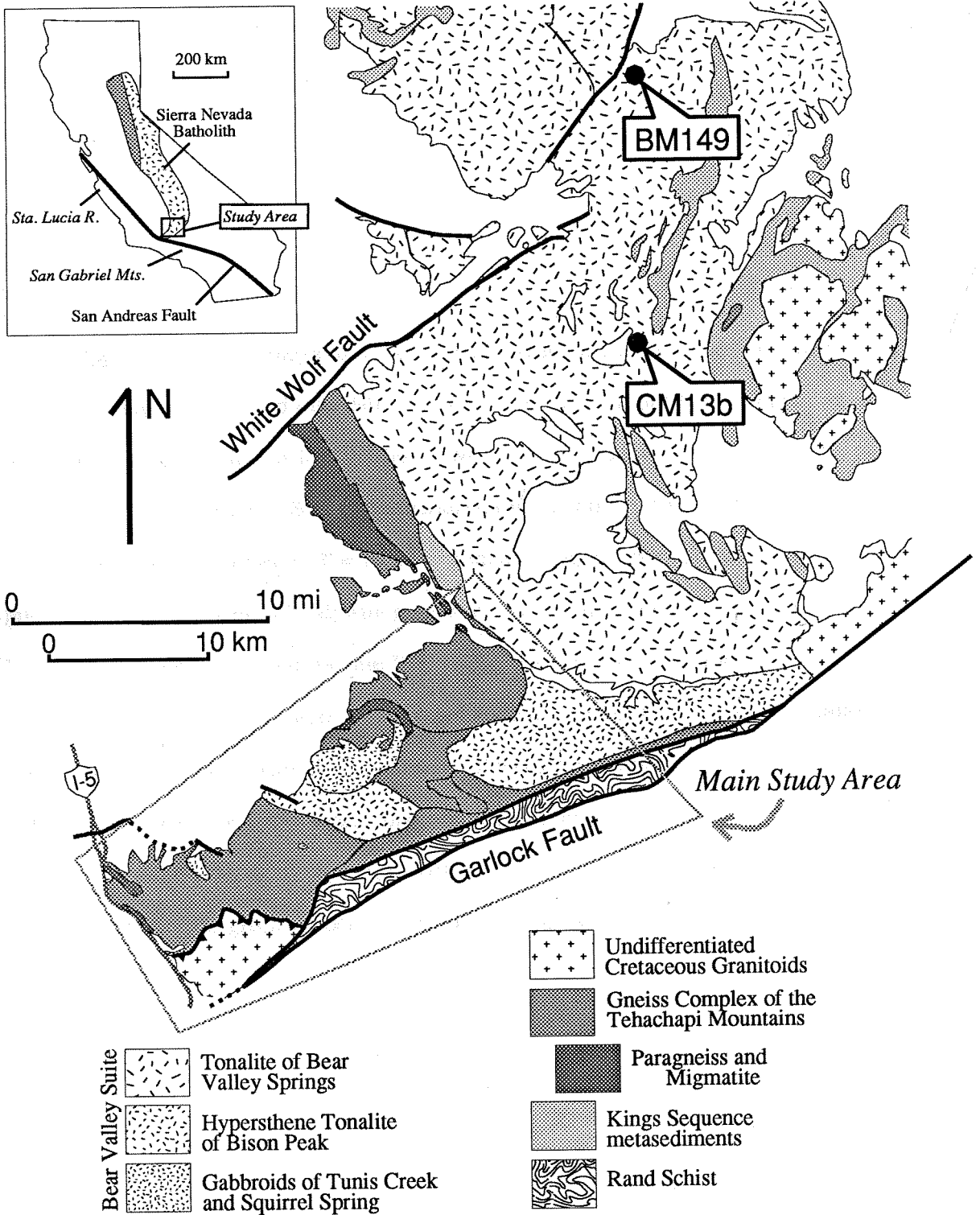
Fig. 2.1

Figure 2.2 - Basement geologic map of the main study area, Tehachapi Mountains, with

sample localities. Modified after Sharry [1981] and Sams [1986], supplemented by new

mapping. Sample localities for CM650b, CM657, and WR27a from Sams [1986], and for

80-301 and "CORE" from J. Sharry (personal communication). Units of the gneiss complex

of the Tehachapi Mountains: T = tonalite gneiss of Tejon Creek, P = quartzofeldspathic

gneiss of Pastoria Creek, W = diorite gneiss of White Oak, CP = paragneiss of Comanche

Point, GP = migmatite of Grapevine Peak, GC = paragneiss of Grapevine Canyon. G =

garnet-biotite tonalite of Grapevine (of the intrusive suite of Bear Valley). Smaller, sub-

map-scale paragneiss bodies are not shown. Filled foliation symbols = magmatic or high-

temperature metamorphic fabrics; open foliation symbols = lower-temperature ductile

deformation fabrics. For clarity, map patterns are omitted for the Kings Sequence body

in the north and the granitic rocks south of the Pastoria thrust (Figure 2.1).

Bear Valley Suite

- Tonalite of Bear Valley Springs
- Hypersthene Tonalite of Bison Peak
- Gabbroids of Tunis Creek and Squirrel Spring

- Gneiss Complex of the Tehachapi Mountains
- Paragneiss and Migmatite
- Rand Schist
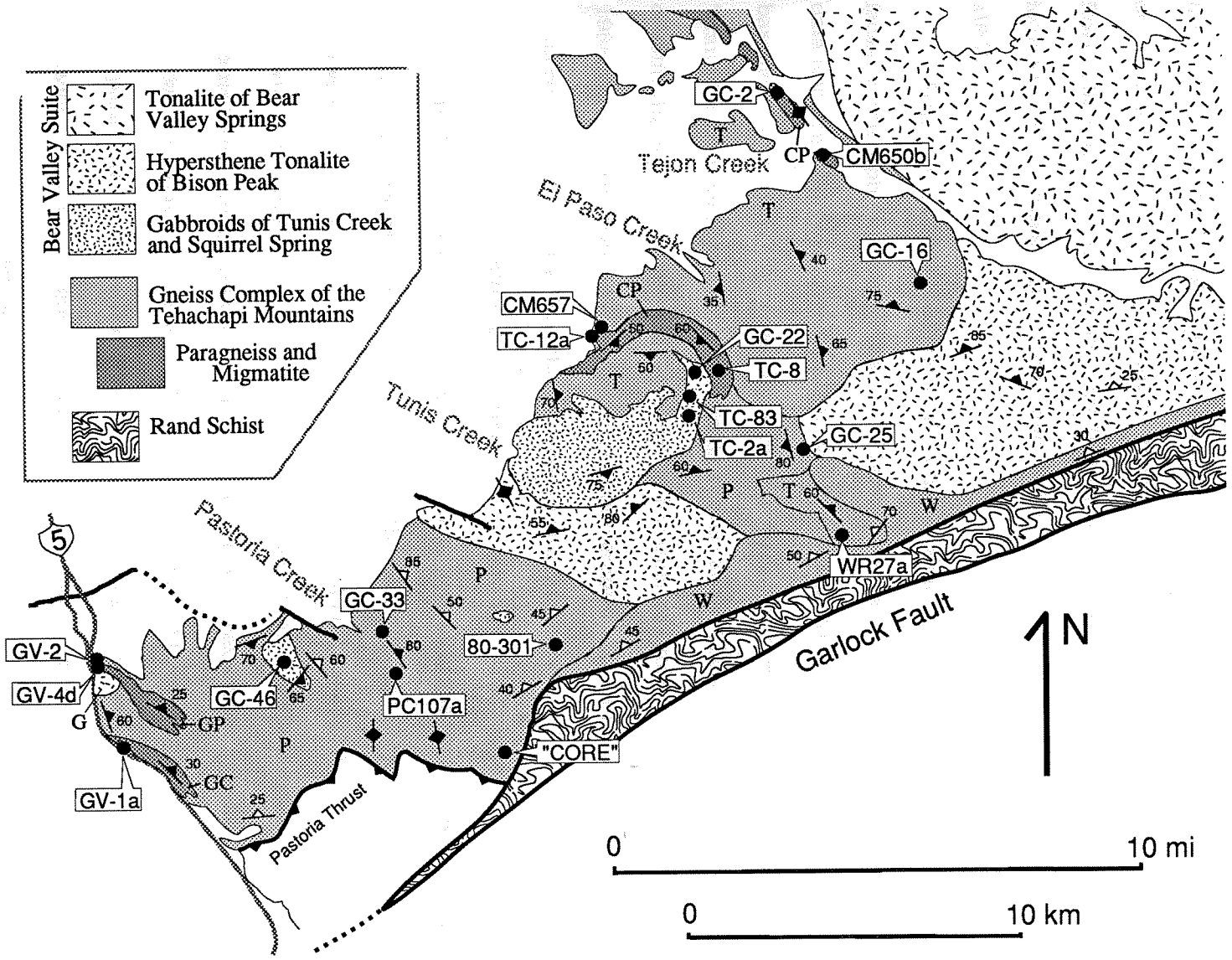
Fig. 2.2

Garlock fault, which separate them from a sliver of Rand Schist as well as other Cretaceous igneous and high-temperature metamorphic rocks [Ross, 1989 and references therein]. Models for initial uplift of the range are few [May, 1989], but some constraints on the timing of uplift are provided by mineral K-Ar ages of 80-87 Ma (summarized in Ross, 1989) and by the Eocene (~50 Ma) surface exposure of the basement rocks as indicated by the oldest ages at the base of the unconformably overlying strata [Nilsen, 1987].

Whereas Sharry [1981] referred to the basement rocks as products of granulite facies metamorphism, Saleeby et al. [1987] and Sams and Saleeby [1988] used U-Pb zircon data and regional geologic mapping to demonstrate a Cretaceous intrusive age for the basement, and they argued for an igneous origin for most of the pyroxene-bearing "granulitic" assemblages. It is misleading to refer to the Tehachapi crystalline rocks as constituting a granulite terrane since, with a few isolated exceptions [Sams and Saleeby, 1988; Ross, 1989], they do not possess prograde granulite facies assemblages. It is also not accurate to refer to the Tehachapi basement as a "mafic gneissic complex" [Ross, 1985] since the predominant lithology is tonalite.

The Tehachapi crystalline rocks are weakly to strongly gneissic, showing effects of both high- and low-temperature deformation. They were divided by Saleeby et al. [1987] into two suites: the gneiss complex of the Tehachapi Mountains and the intrusive suite of Bear Valley (Figures 2.1 and 2.2). The lithologically diverse Tehachapi gneiss complex contains three orthogneiss units -- the ~115 Ma Tejon Creek tonalite gneiss, the ~115 Ma Pastoria Creek quartzofeldspathic gneiss, and the White Oak diorite gneiss -- as well as three paragneiss units -- the Comanche Point paragneiss and the newly recognized Grapevine Canyon paragneiss and Grapevine Peak migmatite (see below). The orthogneisses of the Tehachapi gneiss complex consist mainly of biotite and/or hornblende tonalites grading to biotite granites, with small-scale lithologic heterogeneities, including

common dioritic layers. The igneous rocks of the generally less-deformed intrusive suite of Bear Valley (~100 Ma) are assigned to four units. The biotite- and/or hornblende-bearing tonalite of Bear Valley Springs constitutes a major batholith-scale pluton (Figure 2.1) which extends from the northern part of the main study area more than 60 km to the vicinity of Lake Isabella. It grades on the south into the Bison Peak hypersthene tonalite. Also included in the Bear Valley suite are the gabbroids of Tunis Creek and Squirrel Spring (norite to hornblende gabbro, commonly recrystallized and/or metamorphosed) and the newly recognized garnet-biotite tonalite of Grapevine. Separate reports (Chapters 3 and 4) will discuss the igneous petrology and isotopic characteristics of these suites.

The metasedimentary framework rocks consist of high-grade equivalents of quartz-rich clastic and calcareous, continental margin-type sedimentary assemblages with subordinate metavolcanic rocks. To the north (Figure 2.1) these are termed Kings Sequence, after Saleeby et al. [1978], and are correlated with similar metasedimentary pendants exposed throughout the southern Sierra Nevada. Ross [1989] refers to these rocks as "the metasedimentary rocks of Keene." The higher-grade, more gneissic metasedimentary rocks of the main part of the study area (the Comanche Point and Grapevine Canyon paragneisses) are not termed Kings Sequence, but they are compositionally similar. These rocks occur at many scales, from mappable, km-scale bodies to outcrop-size enclaves. They are always structurally concordant with the intrusive rocks, show no discernible metamorphic gradient near intrusive contacts, and the quartzofeldspathic varieties are commonly migmatitic. The migmatite of Grapevine Peak is a major, mappable belt of migmatitic paragneiss showing apparent effects of both partial melting and injection. The metasedimentary rocks of this report are restricted to the paragneisses of Comanche Point and Grapevine Canyon and the migmatite of Grapevine Peak, within the Tehachapi gneiss complex suite; the Kings sequence rocks of the more coherent pendants to the north are not discussed.

Deformation fabrics are pervasive in the study area (see also Sharry, [1981]; Sams, [1986]; Saleeby et al., [1987]; Sams and Saleeby, [1988]). These range from high-temperature, synplutonic (including igneous flow and cumulate layering) and synmetamorphic foliations to protomylonitic fabrics (e.g., augen gneiss) to solid-state mylonite in discrete domains (Figure 2.3). The mylonitic fabrics are best developed in quartz-rich varieties, and formed at intermediate temperatures (usually above chlorite stability) except near the north branch of the Garlock fault. Although local variations in structural pattern are common (notably around the Tunis Creek gabbroid, Figure 2.2), the regional structural pattern is as follows: the higher temperature fabrics (metamorphic and protoclastic) tend to strike from north to west with moderate to steep dips to the northeast, while protomylonitic to mylonitic fabrics near the north branch of the Garlock fault strike northeast with shallow to moderate dips to the northwest. Transitional zones between the two patterns are evident, such as along the Aqueduct Access Road east of Pastoria Creek. Mylonitic fabrics are also locally well-developed to the north in the Bear Valley Springs tonalite [Sams, 1986; Ross, 1989].

2.3. Metamorphic assemblages

a. Quartzofeldspathic metasedimentary rocks

These rocks are generally quartz-rich with subordinate pelitic component. Ross [1989] and Sams and Saleeby [1988] report sillimanite in a sliver of Kings sequence north of Tejon Creek as well as in exposures to the north, but south of this location there is but one recognized occurrence of an Al_2SiO_5 phase (discussed below). The most common assemblage is quartz + plagioclase + alkali feldspar + biotite + graphite, with the common addition of garnet. Muscovite is a common retrograde phase, although some occurrences of larger, subhedral grains may belong to the peak assemblage. Sams [1986] and Ross [1989] report a few examples of hypersthene-bearing gneisses which appear to have a

Figure 2.3 - Contrasting deformation textures. a) Photomicrograph (9 mm across) of typical high-grade granoblastic fabric in paragneiss TC-8, consisting of quartz, plagioclase, alkali feldspar (stained), biotite, garnet, and graphite. b) Field photograph of augen gneiss, with highly strained quartz and augen of alkali feldspar.
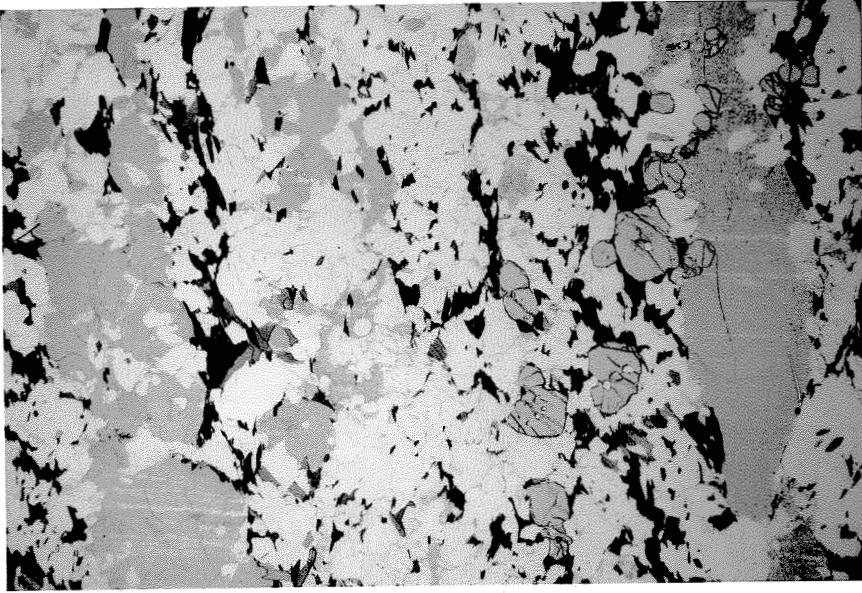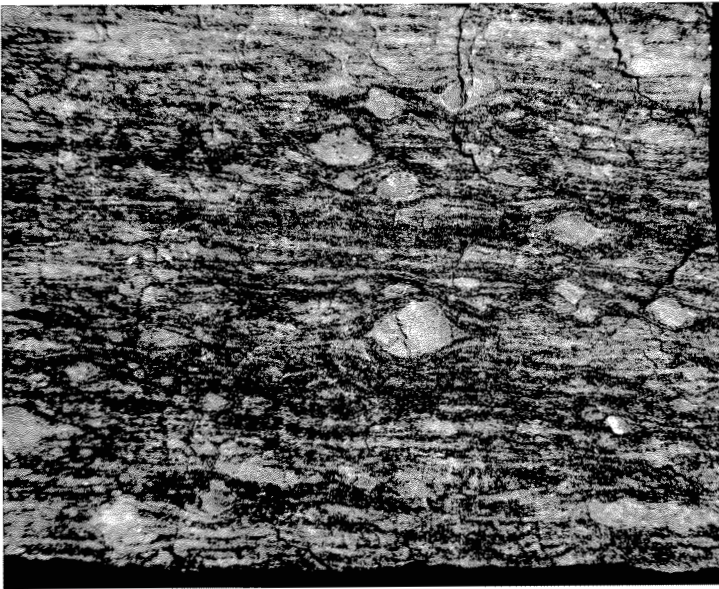
Fig. 2.3

Fig. 2.3

sedimentary protolith based on, for example, high $^{18}O/^{16}O$ ratios. Metasedimentary textures are gneissic with well-developed migmatitic layers (Figure 2.4a) defined by irregular-width quartz-feldspar leucosomes and biotite-rich melanosomes, suggestive of the production of an incompletely mobilized partial melt. This texture is most profoundly expressed in the migmatite of Grapevine Peak (Figure 2.2), where in biotite ± muscovite melanosomes are lath-shaped aggregates of white-mica which presumably are retrograde pseudomorphs after an Al_2SiO_5 phase (Figure 2.4b). Microscopic examination revealed no evidence for the identity of the original phase, but an X-ray diffraction pattern of a powder of the aggregate, though dominated by quartz and muscovite spectra, suggests that it was most likely kyanite. This is based on the following observations: a computer match search of the spectral peaks gave the highest figure-of-merit to kyanite, all expected kyanite peaks are present (at values of 2θ not in the muscovite or quartz spectra), and many prominent sillimanite and andalusite peaks were not observed. In summary, paragneiss assemblages are amphibolite facies with rare occurrences of granulite assemblages. Peak temperatures evidently reached the granite solidus, producing partial melts.

b. Calc-silicate rocks

Calcareous metasedimentary rocks in the Comanche Point paragneiss range from almost pure marble (calcite-graphite) to more siliceous compositions. Calc-silicate gneisses have the assemblages quartz + plagioclase + diopside + sphene plus either alkali feldspar + hornblende or garnet + scapolite. An exception is a sample from an enclave on the north slope of Winters Ridge (GC-25 on Figure 2.2), which contains quartz + diopside + scapolite + wollastonite + calcite + sphene, with late-stage symplectic intergrowths of garnet ± quartz mantling scapolite. Such relations have been reported by Warren et al. [1987] for similar rocks in the granulite terrane of the Arunta Block of central Australia. They attribute the symplectic reaction texture to a lowering of CO_2 activity by a local influx

of H_2O-rich fluids. The Winters Ridge calc-silicate crops out within 100 m of a well-developed mylonite zone, which may have served as a fluid conduit. It is notable that an adjacent small enclave of amphibolite (hornblende + plagioclase + quartz + epidote) also shows evidence for retrograde hydration, with actinolite and chlorite replacing hornblende.

c. Metaigneous rocks

The most distinctive characteristic of subsolidus crystallization in the Cretaceous intrusive rocks of the Tehachapi Mountains is the growth of red garnet porphyroblasts (see Ross [1989] for observed localities). Its occurrence is widespread but not pervasive; it is most commonly distributed in discrete zones, particularly near contact zones with metasedimentary enclaves or other intrusive bodies. In the hornblende ± hypersthene gabbros of Tunis Creek and Squirrel Spring (Figure 2.2), the garnet is present as a subsolidus, typically inclusion-filled (plagioclase, quartz, ilmenite) phase in three mesoscopic settings (Figure 2.5a): 1) in coarse, felsic layers, 2) in discordant veins, and 3) dispersed randomly (less common). In all cases, the garnets are rarely in contact with, and appear to have grown at the expense of, hornblende, resulting in felsic haloes (Figure 2.5b) typically containing quartz which otherwise is absent in the primary assemblage. Garnet was never found in apparent textural equilibrium with hypersthene. Zones of garnet growth in the Tunis Creek unit are concentrated in a tongue of well-foliated, commonly recrystallized gabbro in the northeast sector of the unit, bounded on either side by Tejon Creek tonalite gneiss and Comanche Point paragneiss. Another general garnet occurrence in mafic rocks is in diorites along contacts with more felsic intrusive rocks in heterogeneous zones of the Tehachapi gneiss complex suite.

Garnet is also common in tonalite bodies, particularly in biotite tonalites of the gneiss complex of the Tehachapi Mountains. Textural evidence is ambiguous as to whether the garnet is magmatic or subsolidus, an ambiguity compounded by the common

Figure 2.4 - a) Field photograph of typical migmatized paragneiss. Leucosomes composed

chiefly of quartz, plagioclase, and alkali feldspar; melanosomes composed of these phases

plus graphite and abundant biotite. Hammer head is 10 cm long. b) Field photograph of

migmatite of Grapevine Peak (sample locality GV-4) with biotite ± garnet melanosomes,

quartz + two-feldspar leucosomes, and injection veins of biotite tonalite. Note white,

rectangular pseudomorphs (best expressed at the top of the photo), after kyanite (?),

composed chiefly of muscovite. Hammer head is 12.5 cm long.

a
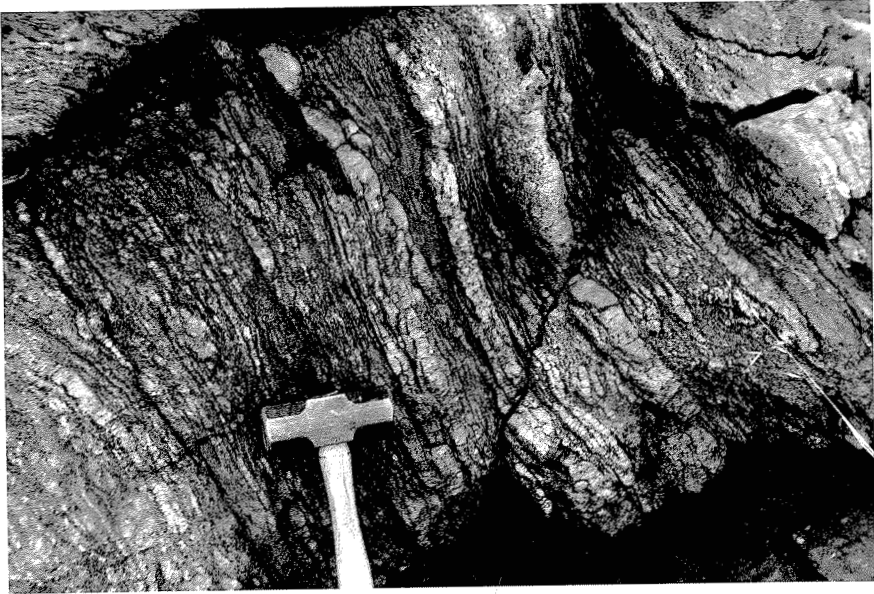
b

Fig. 2.4

Figure 2.5 - a) Field photograph of garnet paragenesis in metagabbro. Matrix rock is hornblende + plagioclase + ilmenite ± hypersthene. Note two garnet textural settings: as coarse porphyroblasts with felsic haloes in coarser, leucocratic gabbro layers; and as smaller grains along brittle fracture cutting earlier fabric across the center of the photo. There are no significant mineral compositional contrasts between the two settings. Pen is 14 cm long. b) Photomicrograph (24 mm across) of metagabbro TC-83, showing halo of plagioclase and quartz around the inclusion-riddled garnet. Mafic minerals are hornblende (with some patchy cummingtonite exsolution) and ilmenite.

a

b
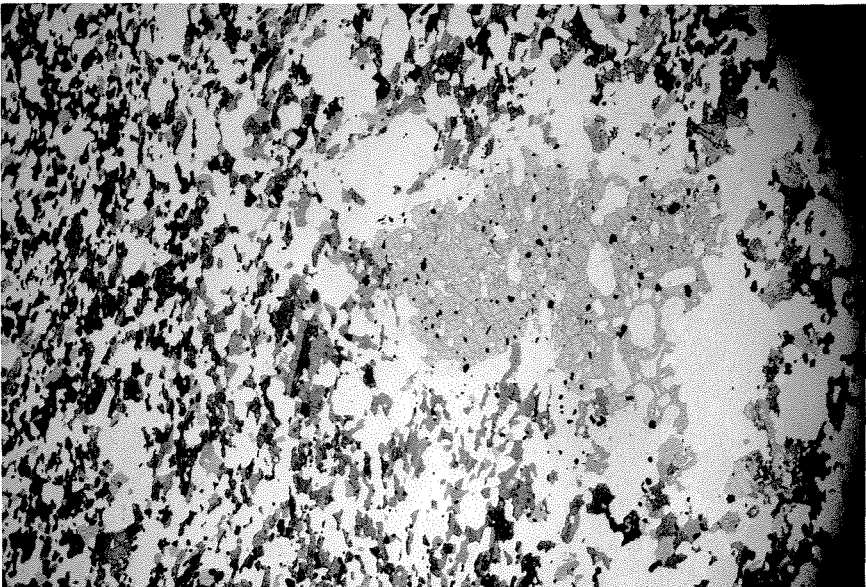
Fig. 2.5

deformation of igneous fabrics. Nevertheless, the garnet shows apparent equilibrium textures with all the primary tonalite phases (biotite, quartz, plagioclase, hornblende), with no segregations or haloes as in the gabbros. In some tonalites, such as the garnet-biotite tonalite of Grapevine (sample GV-2), the garnet is distributed evenly throughout the rock, suggesting a possible magmatic origin. In others (e.g., PC-107a), the garnet is more localized and defines crude veins, consistent with a subsolidus origin. Rarely in the Pastoria Creek unit, large garnet porphyroblasts occur with felsic haloes in hornblende-rich tonalites.

Cummingtonite is common in gabbroic rocks, after hypersthene and in reaction relation with hornblende. In some gabbros, hypersthene is replaced by rims of cummingtonite, which are in turn rimmed by hornblende. Cummingtonite also occurs as patchy exsolution zones in hornblende. Another interesting subsolidus assemblage occurs in troctolite of a gabbroic plug in the Pastoria Creek quartzofeldspathic gneiss. Here primary calcic plagioclase and olivine have reacted to produce coronas consisting of orthopyroxene and symplectic hornblende and green spinel. The latter is sometimes missing, and the pyroxene and spinel also form a few larger grains. Other minor phases present include chromite-rich spinel (picotite), Fe-rich amphibole, and corundum.

Epidote is a common subsolidus phase in the tonalites and granites, found intergrown with biotite in elongate, biotite-rich aggregates. The epidote is commonly large and subhedral, with euhedral crystal faces against biotite. However, it cannot be clearly demonstrated in thin section that epidote and biotite were in equilibrium with a melt phase (counter to arguments in Sams [1986]). Lower-temperature, post-deformational alteration has produced white mica and chlorite throughout the study area.

2.4. Analytical procedures

Mineral compositions in garnet-bearing assemblages (Tables 2.1 to 2.5) were

measured because of their potential for providing pressure and temperature information. Also measured were hornblende in tonalites and granodiorites for pressure determination (see below). Sample localities are depicted on Figures 2.1 and 2.2. Samples BM149, WR27a, CM13b, CM657, and CM650b were culled from David Sams' thesis collection at Caltech, and sample "CORE" was obtained from John Sharry.

Polished rock thin sections were carbon-coated and analyzed on a JEOL 733 electron microprobe fitted with five wavelength spectrometers. The accelerating voltage was 15 keV, the probe current was 25 nA (measured on brass), count time was 60 seconds, and the probe diameter was 10 μm. Element standards were well-characterized silicates and oxides, and the data were corrected using the "CITZAF" correction program [Armstrong, 1988]. In order to ensure the measurement of equilibrium compositions in coexisting phases, rim analyses were emphasized. From each of three different sites on a section where the requisite phases were in mutual contact, at least three rim spots were analyzed for each phase. Compositions were averaged for each site, and the site means were averaged for the entire thin section to yield the results reported in Tables 2.1 to 2.5. Core spots were also measured for most samples, with the means usually involving 2-3 spots from 2-3 different grains. A few grain traverses were performed, with the results discussed below.

Hornblende data were corrected for unknown Fe^{3+} using the method of Spear and Kimball [1984], with the choice of particular correction dependent on the application (see below). For garnet and biotite, all Fe was assumed to be Fe^{2+}, except for garnet in CM650b. Considering the evidence for relatively reducing conditions in the area, including the presence of phases such as graphite and ilmenite and the paucity of magnetite, this assumption likely results in negligible error.

2.5. Mineral compositions

a. Garnet

Garnets in all occurrences (with the exception of the calc-silicate rock CM650b) are almandine-rich and rather uniform in composition, with $X(al) = 0.58 - 0.73$ (Table 2.1). Garnets from metagabbros tend to higher pyrope contents, characterized by $X(py) = 0.17 - 0.25$, than those in metatonalites and paragneisses (mostly 0.06 - 0.18). Spessartine component is generally highest in the paragneisses. Paragneiss grossular components are generally lower than in both metaigneous types, while the calc-silicate rock (CM650b) has garnet that is 84% grossular. $Fe/(Fe+Mg)$ ratios are lower in metagabbros (0.71 - 0.79) than in metatonalites (0.81 - 0.90), with the paragneisses spanning a large range. Five previously published [Schürmann, 1938; Ross, 1989] and four unpublished (C. Gallup, pers. comm.) garnet analyses from metaigneous rocks in the area fall within these compositional limits.

Zoning is apparent in most garnets in the form of rapid change in $Fe/(Fe+Mg)$ near the rims with fairly uniform interiors, which we interpret to be the result of re-equilibration ("type c" zoning of Selverstone and Chamberlain, [1990]). The difference in $Fe/(Fe+Mg)$ values between rims and cores (Figure 2.6) is variable (between 0.013 and 0.068), whereas the garnet in the metagabbro from Grapevine Canyon (GV-1a) shows no zoning. Grossular component is typically not significantly zoned, with three exceptions: "CORE", a metatonalite from the Pastoria Creek unit near the north branch of the Garlock fault, and paragneisses GC-2 and GV-4d. In these cases, the increase in $X(gr)$ from core to rim usually corresponds to a decrease in both $X(al)$ and $X(py)$ and an increase in $X(sp)$.

b. Hornblende

Hornblende compositions (Table 2.2) are recalculated [Spear and Kimball, 1984] by different criteria depending on how the data are to be used. For those in textural

Table 2.1 - Garnet Compositions

	Metatonalites								Metagabbros			
	PC107a (h)		PC107a (b)		"CORE"		GV-2		GC-46		TC-2a	
	rim	core	rim	core	rim	core	rim	core	rim	core	rim	core
SiO_2	38.36	38.10	37.92	38.31	37.24	37.79	37.76	37.85	38.37	38.28	38.87	38.21
Al_2O_3	21.80	21.26	21.66	21.26	21.03	21.38	22.05	22.15	22.18	22.31	22.04	21.80
MgO	2.51	3.30	2.85	3.15	1.62	2.82	3.59	4.06	6.15	6.56	5.10	5.67
FeO	31.23	31.36	32.46	31.60	26.61	30.42	31.97	31.82	28.80	28.78	30.44	29.79
MnO	2.27	1.72	1.37	1.37	4.72	2.57	2.43	2.39	1.96	1.90	1.05	1.42
CaO	5.36	5.32	5.32	5.28	8.77	6.43	3.69	3.50	3.65	3.63	4.44	4.30
Total	101.53	101.06	101.58	100.97	99.99	101.41	101.49	101.77	101.11	101.46	101.94	101.19
Si	3.013	3.006	2.985	3.020	2.983	2.981	2.967	2.961	2.974	2.956	3.001	2.973
Al	2.018	1.977	2.009	1.975	1.986	1.988	2.042	2.042	2.027	2.030	2.006	2.000
Mg	0.293	0.387	0.335	0.370	0.194	0.332	0.421	0.474	0.711	0.756	0.587	0.658
Fe	2.052	2.069	2.137	2.083	1.782	2.007	2.101	2.082	1.867	1.858	1.965	1.939
Mn	0.151	0.115	0.092	0.091	0.320	0.172	0.162	0.159	0.129	0.124	0.068	0.093
Ca	0.452	0.450	0.449	0.446	0.754	0.543	0.311	0.293	0.303	0.300	0.368	0.359
X_{py}	0.099	0.128	0.111	0.124	0.064	0.109	0.141	0.158	0.236	0.249	0.196	0.216
X_{al}	0.696	0.685	0.709	0.697	0.584	0.657	0.702	0.692	0.620	0.612	0.658	0.636
X_{sp}	0.051	0.038	0.030	0.030	0.105	0.056	0.054	0.053	0.043	0.041	0.023	0.031
X_{gr}	0.153	0.149	0.149	0.149	0.247	0.178	0.104	0.097	0.101	0.099	0.123	0.118

Table 2.1 (cont.)

	Metagabbros (cont.)				Paragneisses						calc-sil.
	GV-1a		TC-83	GC-22	TC-8		GC-2		GV-4d		CM650b *
	rim	core	rim	rim	rim	core	rim	core	rim	core	rim
SiO_2	39.54	38.73	38.77	39.29	38.07	38.36	37.51	37.30	37.41	37.73	39.17
Al_2O_3	22.31	22.02	22.05	21.98	22.26	22.49	21.64	21.57	22.04	22.17	19.37
MgO	5.46	5.15	4.64	4.51	4.71	5.93	1.43	2.21	2.53	4.35	0.16
FeO	29.54	28.71	30.57	31.03	31.44	30.28	26.80	29.16	32.87	33.28	5.79
MnO	1.16	1.91	1.56	1.49	4.17	3.79	10.69	9.36	4.35	3.02	0.38
CaO	4.78	5.28	4.64	4.56	1.29	1.27	3.92	2.55	2.60	1.47	35.33
Total	102.79	101.80	102.23	102.86	101.94	102.12	101.99	102.15	101.80	102.02	100.50
Si	3.012	2.988	2.995	3.017	2.971	2.965	2.979	2.962	2.962	2.957	2.971
Al	2.003	2.003	2.008	1.989	2.048	2.050	2.026	2.019	2.056	2.048	1.732
Mg	0.620	0.592	0.534	0.517	0.549	0.683	0.169	0.261	0.299	0.509	0.018
Fe	1.882	1.853	1.975	1.992	2.052	1.957	1.780	1.937	2.177	2.181	0.221
Mn	0.075	0.125	0.102	0.097	0.276	0.248	0.719	0.630	0.292	0.201	0.025
Ca	0.390	0.436	0.384	0.375	0.108	0.105	0.334	0.217	0.221	0.123	2.871
X_{py}	0.209	0.197	0.178	0.173	0.184	0.228	0.056	0.086	0.100	0.169	0.005
X_{al}	0.634	0.616	0.659	0.668	0.687	0.654	0.593	0.636	0.728	0.724	0.064
X_{sp}	0.025	0.042	0.034	0.033	0.092	0.083	0.240	0.207	0.098	0.067	0.007
X_{gr}	0.131	0.145	0.128	0.126	0.036	0.035	0.111	0.071	0.074	0.041	0.836

For PC107a, (h) = touching hornblende and (b) = touching biotite.

Cations corrected to 12 oxygens, with all Fe as Fe^{2+} (except CM650b, corrected to 8 cations).

* For CM650b, $Fe^{3+}=0.146$ and $X_{andr}=0.087$.

Figure 2.6 - Core vs. rim values of Fe/(Fe+Mg) in garnets. Rim increase is due to

retrograde re-equilibration with biotite or hornblende.
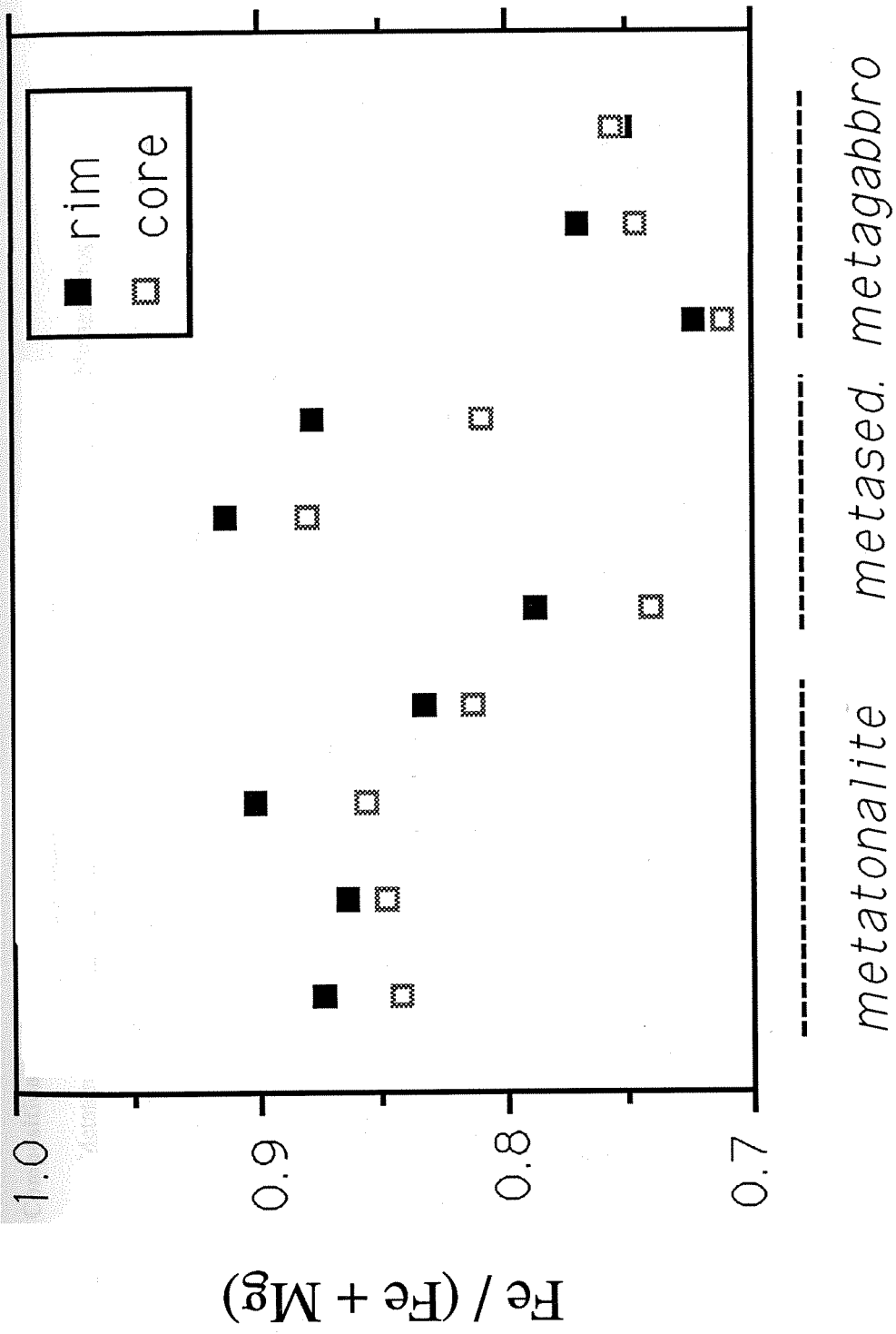
Fig. 2.6

Table 2.2 - Hornblende Compositions

	Metatonalites							Metagabbros						
	PC107a		PC107a (p)	"CORE"		"CORE" (p)		GC-46		GC-46 (p)		TC-2a		TC-2a (p)
	rim	core	rim	rim	core	rim	core	rim	core	rim	core	rim	core	rim
SiO_2	40.42	40.69	41.01	40.60	40.44	40.32	39.99	41.91	43.50	41.69	43.63	44.73	43.98	43.51
Al_2O_3	16.63	15.45	15.59	15.47	14.71	15.74	15.21	16.76	14.21	15.71	14.28	11.99	12.30	14.66
TiO_2	0.13	0.24	0.66	0.75	0.96	0.66	0.87	0.19	0.78	0.53	0.79	1.28	1.03	0.92
MgO	4.84	5.72	6.01	5.41	5.47	5.39	5.56	7.36	10.53	9.38	10.42	11.01	10.39	8.89
FeO^*	21.20	21.46	20.84	21.37	22.19	21.71	22.17	17.27	15.12	16.00	16.03	16.40	18.31	18.24
MnO	0.24	0.26	0.19	0.32	0.31	0.32	0.30	0.26	0.25	0.25	0.25	0.10	0.18	0.16
CaO	11.24	11.21	11.62	11.42	11.41	11.41	11.50	11.45	10.60	10.67	10.17	10.59	9.85	10.09
Na_2O	1.37	1.83	1.57	1.59	1.59	1.62	1.55	1.53	1.81	2.04	1.82	1.72	1.57	1.91
K_2O	0.90	0.77	0.88	0.98	1.12	1.03	1.24	0.29	0.23	0.22	0.23	0.40	0.27	0.52
Total	96.98	97.64	98.36	97.90	98.20	98.20	98.39	97.02	97.02	96.49	97.62	98.22	97.89	98.90
Si	6.216	6.238	6.194	6.214	6.209	6.136	6.096	6.287	6.451	6.205	6.366	6.592	6.547	6.346
Al^{iv}	1.784	1.762	1.806	1.786	1.791	1.864	1.904	1.713	1.550	1.795	1.634	1.408	1.453	1.654
Al^{vi}	1.231	1.030	0.969	1.004	0.872	0.961	0.829	1.251	0.934	0.961	0.823	0.675	0.706	0.866
Ti	0.016	0.028	0.075	0.086	0.111	0.075	0.100	0.022	0.087	0.059	0.087	0.142	0.116	0.101
Mg	1.110	1.307	1.354	1.233	1.250	1.222	1.263	1.646	2.326	2.079	2.266	2.418	2.305	1.932
Fe^{3+}			0.192		0.005	0.224	0.307			0.435	0.575		0.011	0.509
Fe^{2+}	2.726	2.751	2.440	2.736	2.844	2.540	2.519	2.166	1.875	1.557	1.381	2.021	2.269	1.716
Mn	0.032	0.034	0.024	0.042	0.040	0.041	0.039	0.033	0.031	0.031	0.031	0.012	0.023	0.020
Ca	1.853	1.841	1.880	1.872	1.877	1.861	1.878	1.841	1.686	1.702	1.590	1.672	1.571	1.577
Na^{M4}	0.032	0.009	0.066	0.026	0.000	0.076	0.065	0.041	0.061	0.175	0.247	0.059	0.000	0.279
Na^A	0.377	0.534	0.393	0.445	0.472	0.403	0.393	0.403	0.460	0.413	0.267	0.433	0.453	0.261
K	0.177	0.151	0.169	0.191	0.219	0.200	0.241	0.056	0.044	0.043	0.043	0.075	0.052	0.097
$Fe^{2+}/(Fe^{2+}+Mg)$	0.711	0.678	0.643	0.689	0.695	0.675	0.666	0.568	0.447	0.428	0.379	0.455	0.496	0.470

Table 2.2 (cont.)

	Metagabbros (cont.)					Non-metamorphosed Tonalites & Granodiorites							
	GV-1a		TC-83	TC-83 (p)	GC-22	BM149	CM13b	WR27a	TC-12a	GC-16	CM657	GC-33	GC-33 (p)
	rim	core	rim	rim	rim	rim	rim	rim	rim	rim	rim	rim	rim
SiO_2	43.02	44.88	44.44	44.09	44.30	47.13	42.56	42.74	42.14	40.93	39.74	39.69	39.26
Al_2O_3	17.71	14.30	12.34	13.38	12.64	8.05	11.48	12.80	12.31	12.63	13.06	13.74	14.40
TiO_2	0.36	0.74	1.47	0.98	1.29	0.73	0.70	1.38	0.88	0.43	1.13	1.41	0.91
MgO	8.34	10.64	10.73	8.79	10.13	10.89	5.45	8.96	7.26	6.06	5.10	5.70	5.41
FeO^*	15.58	14.64	16.52	19.44	17.05	17.31	24.07	17.33	19.71	21.89	23.18	22.42	22.89
MnO	0.13	0.12	0.14	0.30	0.12	0.41	0.56	0.43	0.43	0.91	0.61	0.54	0.56
CaO	11.48	11.16	10.93	10.01	10.97	12.05	11.48	11.78	11.58	10.96	11.26	11.42	11.45
Na_2O	1.55	1.55	1.74	1.81	1.47	0.89	1.43	1.42	1.53	1.75	1.63	1.38	1.32
K_2O	0.41	0.26	0.50	0.44	0.58	0.74	1.48	1.60	1.44	1.58	1.83	1.93	1.98
Total	98.58	98.27	98.81	99.24	98.55	98.20	99.21	98.44	97.28	97.14	97.54	98.23	98.17
Si	6.281	6.534	6.529	6.432	6.536	6.967	6.508	6.394	6.457	6.351	6.211	6.119	6.057
Al^{iv}	1.719	1.466	1.471	1.568	1.464	1.033	1.492	1.606	1.543	1.649	1.789	1.881	1.943
Al^{vi}	1.329	0.988	0.666	0.734	0.734	0.370	0.577	0.651	0.681	0.661	0.618	0.616	0.676
Ti	0.040	0.080	0.162	0.108	0.143	0.081	0.080	0.155	0.101	0.050	0.133	0.164	0.105
Mg	1.815	2.308	2.349	1.911	2.227	2.399	1.242	1.998	1.658	1.401	1.188	1.311	1.243
Fe^{3+}				0.572		0.203	0.178	0.096	0.077	0.258	0.175	0.266	0.388
Fe^{2+}	1.902	1.782	2.030	1.800	2.104	1.937	2.900	2.072	2.449	2.583	2.855	2.625	2.564
Mn	0.016	0.014	0.017	0.037	0.015	0.051	0.073	0.054	0.056	0.120	0.081	0.070	0.073
Ca	1.796	1.741	1.721	1.565	1.734	1.909	1.881	1.888	1.901	1.822	1.886	1.887	1.893
Na^{M4}	0.102	0.086	0.055	0.274	0.043	0.049	0.069	0.085	0.077	0.105	0.065	0.061	0.057
Na^A	0.337	0.353	0.441	0.238	0.378	0.206	0.355	0.327	0.378	0.422	0.429	0.353	0.336
K	0.076	0.049	0.094	0.082	0.109	0.140	0.289	0.305	0.282	0.313	0.365	0.379	0.389
$Fe^{2+}/(Fe^{2+}+Mg)$	0.512	0.436	0.464	0.485	0.486	0.447	0.700	0.509	0.596	0.648	0.706	0.667	0.674

(p) = measured touching plagioclase only. Otherwise, measured touching garnet, plagioclase, and quartz in metamorphosed rocks, and touching quartz in non-metamorphosed rocks. See text for correction procedures.

equilibrium with garnet, plagioclase, and quartz, and which, therefore, will be used in P-T calculations by the method of Kohn and Spear [1990], the option giving minimum Fe^{3+} (usually "all Fe^{2+}") is used. For other applications, the "average Fe^{3+}" option is used.

Hornblendes in the metaigneous rocks are all quite aluminous, with Al(total) = 2.08 - 3.36, a characteristic shared with those in unmetamorphosed intrusive rocks (data below and unpublished SEM-EDS data). In the two metatonalites for which they were measured, the hornblendes range in classification [Leake, 1978] from ferro-alumino-tschermakite to ferroan pargasite, with most qualifying as the latter. The ratio $Fe^{2+}/(Fe^{2+}+Mg)$ ranges from 0.64 - 0.71, with the cores either the same or somewhat lower. Al(total) is always lower in the cores than in the rims.

Hornblendes in metagabbros are more silicic than those in the metatonalites, lying compositionally near the boundaries between tschermakitic, magnesio-, and edenitic hornblendes. $Fe^{2+}/(Fe^{2+}+Mg)$ ratios and K contents are lower than in the metatonalite hornblendes, reflective of primary igneous compositional differences. $Fe^{2+}/(Fe^{2+}+Mg)$ ratios are similar to those measured on two unmetamorphosed gabbros from the Tunis Creek unit (unpublished SEM-EDS data), except for GC-46 (Liveoak Canyon) , which has more ferrous hornblendes. With one exception (TC-2a), both $Fe^{2+}/(Fe^{2+}+Mg)$ and Al(total) are lower in the cores than in the rims. Among both metaigneous types, substantial differences in hornblende compositions within one slide were observed, dependent on the adjacent phases (e.g., garnet-plagioclase-quartz versus plagioclase alone); however, these variations are largely nonsystematic. One notable contrast is in $Fe^{2+}/(Fe^{2+}+Mg)$ of hornblende adjacent to and away from garnets: this ratio is lower away from garnets in three samples (PC107a, "CORE", and GC-46) but higher in two (TC-2a and TC-83 from the Tunis Creek metagabbro). These differences are likely preserved because of the lack of mesoscale equilibrium during the metamorphic garnet-forming event; igneous hornblende compositions are probably retained away from the garnets.

Hornblende compositions were also measured in unmetamorphosed tonalites and granodiorites which contained assemblages appropriate for Al-in-hornblende igneous barometry (see below). These compositions range from magnesio-hornblende in sample BM149 in the north (Figure 2.1) to ferroan pargasite in the main study area (Figure 2.2). These hornblendes are generally high in Al(total), although they do not reach values as high as those in the metaigneous rocks.

c. Biotite

The biotites have a fairly wide range of compositions (Table 2.3). $Fe/(Fe+Mg)$ ranges from 0.43 to 0.69, while Ti contents vary between 0.14 and 0.39 atoms per 22 oxygens. There is considerable overlap in compositional parameters between metatonalites and metasediments, so that gross lithologic differences do not alone account for the biotite variability. An extreme case is the biotite from sample GC-2 of the Comanche Point paragneiss, with the highest Si, Al^{vi}, and Mn, and lowest Ti, among all samples.

Zoning is quite limited in the biotites. For instance, for the $Fe/(Fe+Mg)$ ratio the largest rim-core contrast is the 3% change measured in metatonalite PC107a. Cores are usually somewhat higher in Ti and lower in Si and Al^{vi} than rims; these same relationships are noted in paragneiss TC-8 between matrix biotites (i.e., those not touching garnet) and biotite rims in contact with garnet. Sample PC107a is an exception to these zoning characteristics in that its cores show the opposite trends. Biotites in the migmatite of Grapevine Peak (GV-4d) are completely homogenized, and those in GC-2 are nearly so.

d. Plagioclase

In the paragneisses and metatonalites, plagioclase anorthite contents (Table 2.4) are relatively low, in the range An_{22-38}, while in the metagabbros, they span An_{33-74}. The easternmost metagabbros -- GC-46 (Liveoak Canyon) and GV-1a (Grapevine Canyon) --

Table 2.3 - Biotite Compositions

	Metatonalites						Paragneisses						
	PC107a		"CORE" (no g)	GV-2			TC-8		TC-8 (no g)	GC-2		GV-4d	
	rim	core	rim	rim	core		rim	core	rim	rim	core	rim	core
SiO_2	34.69	35.14	36.03	36.05	35.87		36.55	36.33	36.28	36.71	36.65	35.74	35.72
Al_2O_3	17.32	17.83	17.51	19.82	19.29		19.44	19.39	19.56	18.58	18.58	19.14	19.25
TiO_2	2.79	2.46	2.56	1.91	2.29		2.80	2.92	3.53	1.11	1.21	1.90	1.88
MgO	6.55	6.08	7.49	9.59	9.93		11.66	11.68	11.08	6.71	6.69	9.81	9.81
FeO	23.81	24.32	22.44	18.71	18.74		15.42	15.80	15.73	21.78	22.09	19.65	19.60
MnO	0.12	0.14	0.16	0.15	0.10		0.08	0.07	0.11	0.44	0.40	0.12	0.10
CaO	0.09	0.03	0.02	0.03	0.00		0.12	0.01	0.01	0.07	0.06	0.00	0.00
Na_2O	0.07	0.14	0.10	0.12	0.21		0.10	0.09	0.08	0.05	0.04	0.21	0.25
K_2O	8.83	9.05	9.39	9.30	9.38		9.08	9.55	9.67	8.64	8.32	9.22	9.19
Total	94.27	95.21	95.7	95.68	95.81		95.25	95.84	96.05	94.09	94.04	95.79	95.80
Si	5.460	5.484	5.541	5.427	5.404		5.430	5.390	5.373	5.682	5.672	5.405	5.398
Al^{iv}	2.540	2.516	2.459	2.573	2.596		2.570	2.610	2.627	2.318	2.328	2.595	2.602
Al^{vi}	0.673	0.763	0.715	0.942	0.830		0.835	0.781	0.788	1.070	1.060	0.817	0.828
Ti	0.330	0.288	0.296	0.215	0.259		0.313	0.326	0.393	0.129	0.141	0.215	0.215
Mg	1.537	1.414	1.717	2.152	2.229		2.581	2.584	2.447	1.548	1.542	2.211	2.210
Fe	3.135	3.177	2.886	2.356	2.361		1.917	1.960	1.948	2.818	2.859	2.485	2.478
Mn	0.016	0.018	0.021	0.018	0.013		0.010	0.008	0.014	0.058	0.052	0.016	0.013
Ca	0.016	0.005	0.004	0.005	0.000		0.018	0.002	0.002	0.012	0.010	0.000	0.000
Na	0.021	0.041	0.030	0.034	0.060		0.028	0.027	0.023	0.015	0.013	0.062	0.072
K	1.772	1.801	1.843	1.787	1.802		1.722	1.808	1.828	1.706	1.642	1.779	1.771
Fe/(Fe+Mg)	0.671	0.692	0.627	0.523	0.514		0.426	0.431	0.443	0.645	0.650	0.529	0.529

(no g) = not touching garnet.
Cations corrected to 22 oxygens with all Fe as Fe^{2+}.

Table 2.4 - Plagioclase Compositions

	Metatonalites											
	PC107a (h)		PC107a (b)	PC107a (no g)	"CORE" (h)		"CORE" (no g)		"CORE" (no g, h)		GV-2	
	rim	core	rim	rim	rim	core	rim	core	rim	core	rim	core
SiO$_2$	59.91	59.23	60.23	59.92	61.99	61.50	61.21	59.55	59.35	59.15	58.45	59.97
Al$_2$O$_3$	25.22	25.84	25.71	25.22	23.52	24.06	24.83	25.70	25.56	25.70	27.01	26.11
FeO	0.10	0.02	0.11	0.18	0.20	0.10	0.21	0.05	0.00	0.02	0.34	0.05
CaO	6.67	7.43	6.99	6.74	4.84	5.39	6.00	7.19	7.01	7.29	8.37	7.37
Na$_2$O	8.00	7.63	8.35	7.91	9.28	8.94	8.66	7.94	8.07	7.90	7.52	8.28
K$_2$O	0.07	0.10	0.08	0.20	0.08	0.08	0.08	0.14	0.08	0.10	0.14	0.07
Total	99.97	100.25	101.47	100.17	99.91	100.07	100.99	100.57	100.07	100.16	101.83	101.85
Si	2.670	2.638	2.652	2.669	2.748	2.731	2.700	2.645	2.648	2.639	2.579	2.634
Al	1.326	1.357	1.334	1.324	1.229	1.260	1.291	1.346	1.344	1.351	1.401	1.352
Fe	0.004	0.001	0.004	0.007	0.007	0.004	0.008	0.002	0.000	0.001	0.013	0.002
Ca	0.319	0.354	0.330	0.322	0.230	0.257	0.283	0.342	0.335	0.348	0.395	0.347
Na	0.692	0.659	0.713	0.683	0.798	0.769	0.740	0.683	0.698	0.683	0.643	0.705
K	0.004	0.006	0.005	0.011	0.005	0.004	0.004	0.008	0.004	0.006	0.008	0.004
X(an)	0.314	0.347	0.315	0.317	0.223	0.250	0.276	0.331	0.323	0.336	0.378	0.329
X(ab)	0.682	0.647	0.680	0.672	0.773	0.747	0.721	0.661	0.673	0.659	0.615	0.668

Table 2.4 (cont.)

	Metagabbros											
	GC-46		GC-46 (no g)		GC-46 (no g, h)		TC-2a		TC-2a (no g)	GV-1a		TC-83
	rim	core	rim	core	rim	core	rim	core	rim	rim	core	rim
SiO_2	58.71	55.02	56.51	54.72	54.25	54.57	51.53	49.54	51.77	59.93	57.36	49.58
Al_2O_3	25.25	28.27	27.16	28.67	28.49	28.34	31.64	32.24	31.45	26.51	27.47	32.90
FeO	0.20	0.11	0.11	0.03	0.08	0.01	0.23	0.08	0.11	0.26	0.01	0.25
CaO	7.10	10.37	9.06	10.61	10.46	10.08	13.91	15.05	13.71	7.99	9.14	15.31
Na_2O	7.87	5.99	6.83	5.84	5.93	6.05	4.35	3.20	4.46	7.38	6.83	3.32
K_2O	0.09	0.05	0.06	0.05	0.08	0.10	0.05	0.04	0.06	0.06	0.07	0.04
Total	99.22	99.81	99.73	99.92	99.29	99.15	101.71	100.15	101.56	102.13	100.88	101.40
Si	2.641	2.486	2.547	2.470	2.466	2.480	2.311	2.259	2.323	2.624	2.552	2.238
Al	1.339	1.505	1.442	1.525	1.526	1.518	1.673	1.733	1.663	1.368	1.441	1.751
Fe	0.007	0.004	0.004	0.001	0.003	0.000	0.009	0.003	0.004	0.010	0.000	0.009
Ca	0.342	0.502	0.438	0.513	0.510	0.491	0.669	0.736	0.659	0.375	0.436	0.741
Na	0.687	0.525	0.597	0.511	0.523	0.533	0.379	0.283	0.387	0.626	0.590	0.290
K	0.005	0.003	0.004	0.003	0.005	0.006	0.003	0.003	0.003	0.004	0.004	0.002
X(an)	0.331	0.487	0.422	0.500	0.491	0.477	0.637	0.720	0.628	0.373	0.423	0.717
X(ab)	0.664	0.510	0.575	0.498	0.504	0.517	0.361	0.277	0.369	0.623	0.573	0.281

Table 2.4 (cont.)

	Metagabbros (cont.)		Paragneisses						Tonalite
	TC-83 (no g) rim	GC-22 rim	TC-8 rim	core	TC-8 (no g, b) rim	GC-2 rim	core	CM650b *calc-sil.* rim	GC-33 (h) rim
SiO$_2$	52.86	50.57	60.67	60.66	59.75	62.40	62.23	45.06	60.52
Al$_2$O$_3$	30.95	32.63	25.74	25.59	25.95	24.54	24.48	35.21	25.08
FeO	0.19	0.17	0.20	0.01	0.01	0.26	0.06	0.00	0.11
CaO	13.07	15.27	6.79	6.79	7.31	5.47	5.54	18.43	6.52
Na$_2$O	4.94	2.99	8.42	8.38	7.50	9.24	9.18	1.07	7.94
K$_2$O	0.06	0.04	0.22	0.32	0.32	0.22	0.29	0.04	0.37
Total	102.07	101.67	102.04	101.75	100.84	102.13	101.78	99.81	100.54
Si	2.357	2.269	2.657	2.664	2.645	2.721	2.723	2.080	2.684
Al	1.627	1.725	1.329	1.325	1.354	1.262	1.262	1.916	1.311
Fe	0.007	0.008	0.007	0.000	0.001	0.010	0.002	0.000	0.004
Ca	0.624	0.734	0.319	0.319	0.347	0.256	0.260	0.912	0.310
Na	0.427	0.260	0.715	0.714	0.644	0.781	0.779	0.096	0.682
K	0.003	0.002	0.012	0.018	0.018	0.012	0.016	0.002	0.021
X(an)	0.592	0.737	0.305	0.304	0.344	0.244	0.246	0.903	0.306
X(ab)	0.405	0.261	0.684	0.679	0.638	0.745	0.738	0.095	0.673

(h) = touching hornblende and garnet, except GC-33 with no garnet; (b) = touching biotite and garnet; (no g) = not touching garnet; (no g,h), (no g,b) = not touching garnet or hornblende or biotite.
Cations corrected to 8 oxygens.

have An contents that are markedly lower than those from the Tunis Creek metagabbro. Not surprisingly, the plagioclase from the calc-silicate sample (CM650b) is An_{90}.

Interesting contrasts may be seen among plagioclase of differing textural settings in the same thin section. Of the six samples in which plagioclase not touching garnet was also measured, three ("CORE", TC-8, and GC-46) had higher Ca contents in such plagioclases as compared to those in equilibrium with garnet, while two (TC-83 and TC-2a from the Tunis Creek metagabbro) had lower Ca away from garnet. (Unpublished SEM and probe data by C. Gallup on a few Tunis Creek samples substantiate the latter observation.) These variations probably reflect differing Ca partitioning between plagioclase and garnet during garnet growth. In two samples ("CORE" and GC-46), plagioclases not contacting hornblende were more calcic than those contacting hornblende but not garnet. Assuming this plagioclase represents primary igneous compositions, this relationship is suggestive of subsolidus exchange with hornblende as well as garnet.

Zoning is preserved in plagioclase from the metaigneous rocks, but not in the paragneisses (Figure 2.7). In samples for which cores were measured, all but two (GV-2 and contacting quartz in GC-46) have cores more calcic than rims, with the contrast being more marked among the metagabbros. By far the largest core-rim contrast is in plagioclase touching garnet in metagabbro GC-46 (An_{49} vs. An_{33}).

e. Others

In the calc-silicate CM650b (with the assemblage quartz + plagioclase + diopside + scapolite + grossular + sphene), a scapolite grain in textural contact with plagioclase, diopside, quartz, and grossular has the composition $X_{Ca} = 0.74$ (Table 2.5). Sphenes from this rock are quite aluminous, with $Al^{vi} = 0.63$ per formula unit, while the clinopyroxene is salite with Mg/(Mg+Fe) = 0.66. Alkali feldspar in paragneiss TC-8 was measured in order to help constrain fluid compositions (see below), yielding Or_{88} (Table 2.5). Opaque

Figure 2.7 - Core vs. rim values of anorthite content (mole %) in plagioclases. Note the

large core-rim contrasts in the metagabbros.
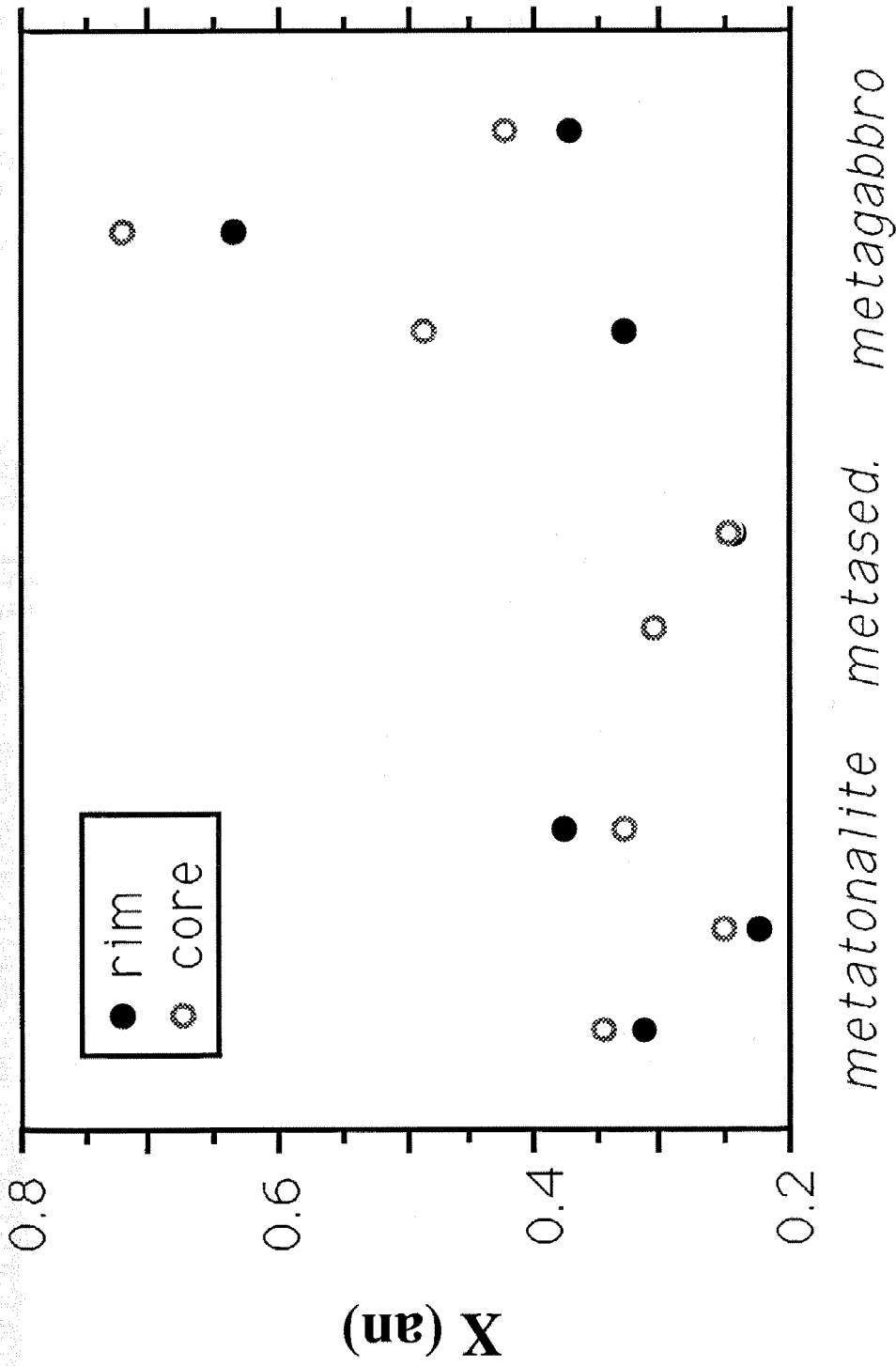
Fig. 2.7

Table 2.5 - Scapolite and Alkali Feldspar Compositions

CM650b scapolite			TC-8 alkali feldspar	
SiO_2	46.20		SiO_2	63.25
Al_2O_3	27.71		Al_2O_3	18.96
CaO	17.96		CaO	0.04
Na_2O	3.26		Na_2O	1.28
K_2O	0.37		K_2O	14.60
Total	95.50		Total	98.13
Si	7.030		Si	2.966
Al	4.970		Al	1.048
Ca	2.927		Ca	0.002
Na	0.962		Na	0.117
K	0.072		K	0.873
X(Ca)	0.739		X(an)	0.002
X(Na)	0.243		X(ab)	0.118
			X(or)	0.880

Other oxide percentages were negligible.
Scapolite cations corrected to 12 (Si,Al). Feldspar cations corrected to 8 oxygens.

oxide compositions were determined for a limited number of samples; ilmenite was ubiquitous in metamorphosed and unmetamorphosed gabbros to tonalites. Magnetite was present in only a few tonalites, subordinate to ilmenite. On this basis, the intrusive rocks would be classified as "ilmenite series."

2.6. Pressures, temperatures, and fluid conditions of intrusion and metamorphism

a. Temperature

Obviously, the majority of rocks in the study area have experienced magmatic temperatures (~675°C and above). The intent of our thermobarometric work here is not to determine such "peak" temperatures, but rather to determine depths of emplacement and metamorphism, as well as post-intrusive thermal histories. Because of the evidence for prolonged, slow cooling, it is not clear that even the framework metamorphic rocks will record peak conditions. For these reasons, and heeding the reservations of Selverstone and Chamberlain [1990] concerning the validity of core-matrix pressure-temperature determinations as estimates of peak conditions, we here emphasize rim mineral compositions in apparent equilibrium settings.

Garnet-hornblende and plagioclase-hornblende -- Temperatures based on Fe-Mg exchange between garnet and hornblende [Graham and Powell, 1984] were applied to five metagabbros and two garnet-bearing tonalites (Table 2.6). The three gabbros from one part of the Tunis Creek metagabbro gave very similar temperatures of 580-590°C, while the other two, GC-46 from Liveoak Canyon (760°C) and GV-1a from Grapevine Canyon (700°C), record significantly higher temperatures. This difference is substantiated by the aforementioned observation that $Fe^{2+}/(Fe^{2+}+Mg)$ in hornblende is lower adjacent to garnet as compared to those in the matrix of the Tunis Creek samples, but not elsewhere. That is, Tunis Creek hornblendes have exchanged more extensively with garnet because they equilibrated at lower temperatures. Garnet core-matrix hornblende pairs imply a

minimum peak temperature of 700°C for one Tunis Creek sample (TC-2a), but for the Liveoak Canyon sample (GC-46) yield a temperature of 680°C, which is 80°C lower than that obtained for rim compositions. This latter result suggests a lack of equilibrium between garnet and nonadjacent hornblende early in the crystallization history of the garnet and may reflect the localized, vein-related nature of garnet growth in the gabbros.

Two tonalites (PC107a and "CORE") from the Pastoria Creek quartzofeldspathic gneiss unit give garnet-hornblende temperatures (690-700°C) similar to those in non-Tunis Creek metagabbros. These are lower than tonalite solidus temperatures and suggest a mechanism for garnet growth similar to that in the gabbros. Core-matrix temperatures are the same in PC107a (from Pastoria Creek) but 50°C higher in "CORE" (near the north branch of the Garlock fault).

Blundy and Holland [1990] have recently proposed a geothermometer based on Na and Al exchange between coexisting amphibole and plagioclase, and derived temperatures are also shown in Table 2.6. When determined for hornblende-plagioclase pairs adjacent to garnet, these temperatures are always higher than the garnet-hornblende temperatures by up to 280°C. The difference is even higher for hornblende-plagioclase pairs away from garnet. In fact, the hornblende-plagioclase temperatures are sufficiently high to reflect primary igneous conditions. However, this difference is lowest in those rocks giving higher garnet-hornblende temperatures. Figure 2.8 shows this convergence of the two temperatures, and suggests that the discrepancy is due to kinetic effects; i.e., re-equilibration of the hornblende-plagioclase pair with decreasing temperature may be more sluggish in those rocks which experienced garnet growth at lower temperatures. However, it is surprising that such a large difference would persist and that garnet growth would not affect more strongly the plagioclase-hornblende exchange in immediately adjacent grains; surely the hornblende participates in the garnet-forming reaction. We must leave this issue unresolved pending further usage and testing of the hornblende-plagioclase

thermometer. We regard the garnet-hornblende thermometer as the more reliable indicator of metamorphic conditions, particularly in the light of the aforementioned observations implying continued subsolidus exchange among the three phases (see sections on hornblende and plagioclase compositions).

Garnet-biotite -- The difficulty of obtaining reliable garnet-biotite Fe-Mg exchange temperatures in high-grade terranes is well-established [e.g., Indares and Martignole, 1985; Chipera and Perkins, 1988]. The obstacles to success are not only kinetic, but are also attributable to the increase with temperature of the discrepancies among the various calibrations. This problem is exemplified by the results in Table 2.7, showing temperatures calculated from the calibrations of Ferry and Spear [1978] (with modifications of Hodges and Spear [1982]) and those of Perchuk and Lavrent'eva [1983]. (The version of Indares and Martignole [1985] which accounts for the effects of Ti and Al in the biotite, was not used because Ti contents here were not nearly as high as those used in their calibration.) Also included are recalculations of data on two samples in Sharry [1981]. Although a part of the discrepancies between the two calibrations, which range from 10 to 280°C, can be attributed to the different pressures used in each case (see below), the major part of the differences lies in calibration. In a comparative study of various garnet-biotite geothermometers in the temperature range 600-725°C, Chipera and Perkins [1988] found that the Ferry and Spear [1978] version gave unreasonably high temperatures. This seems to be the case for some samples in the present study as well, as evidenced by results such as 960°C in a metatonalite. Chipera and Perkins [1988] concluded that the calibration of Perchuk and Lavrent'eva [1983] gave the most consistent temperatures in their study area and was thus the preferred version, and we tend to agree for the purposes of the present study.

Using the Perchuk and Lavrent'eva [1983] calibration, garnet-biotite rim temperatures range from 550-680°C, with no apparent geographic pattern. The

Table 2.6 - Garnet-hornblende temperatures[1], garnet-hornblende-plagioclase-quartz pressures[2], and hornblende-plagioclase temperatures[3]

	T, °C rims	P, kbar rims	T core-matrix	P core-matrix	T hb-pl (rims)
TC-83	578	3.8			863
GC-22	586	3.6			863
TC-2a	588	4.2	697	4.6	850
GV-1a	676	7.5			800
GC-46	757	7.3	678	6.1	785
"CORE"	686	10.8	743	9.8	711
PC107a	701	8.2	707	8.3	779

[1] Graham and Powell [1984].
[2] Kohn and Spear [1990], calculated at gt-hb temperature; average of results from Fe and Mg end-member reactions.
[3] Blundy and Holland [1990], calculated at gt-hb-pl-qz pressure.

Figure 2.8 - Garnet-hornblende temperature [Graham and Powell, 1984] and hornblende-plagioclase temperature [Blundy and Holland, 1990] for garnet-hornblende-plagioclase-quartz samples. The two estimates converge at higher garnet-hornblende temperatures, but hornblende-plagioclase temperatures are unreasonably high in other samples.
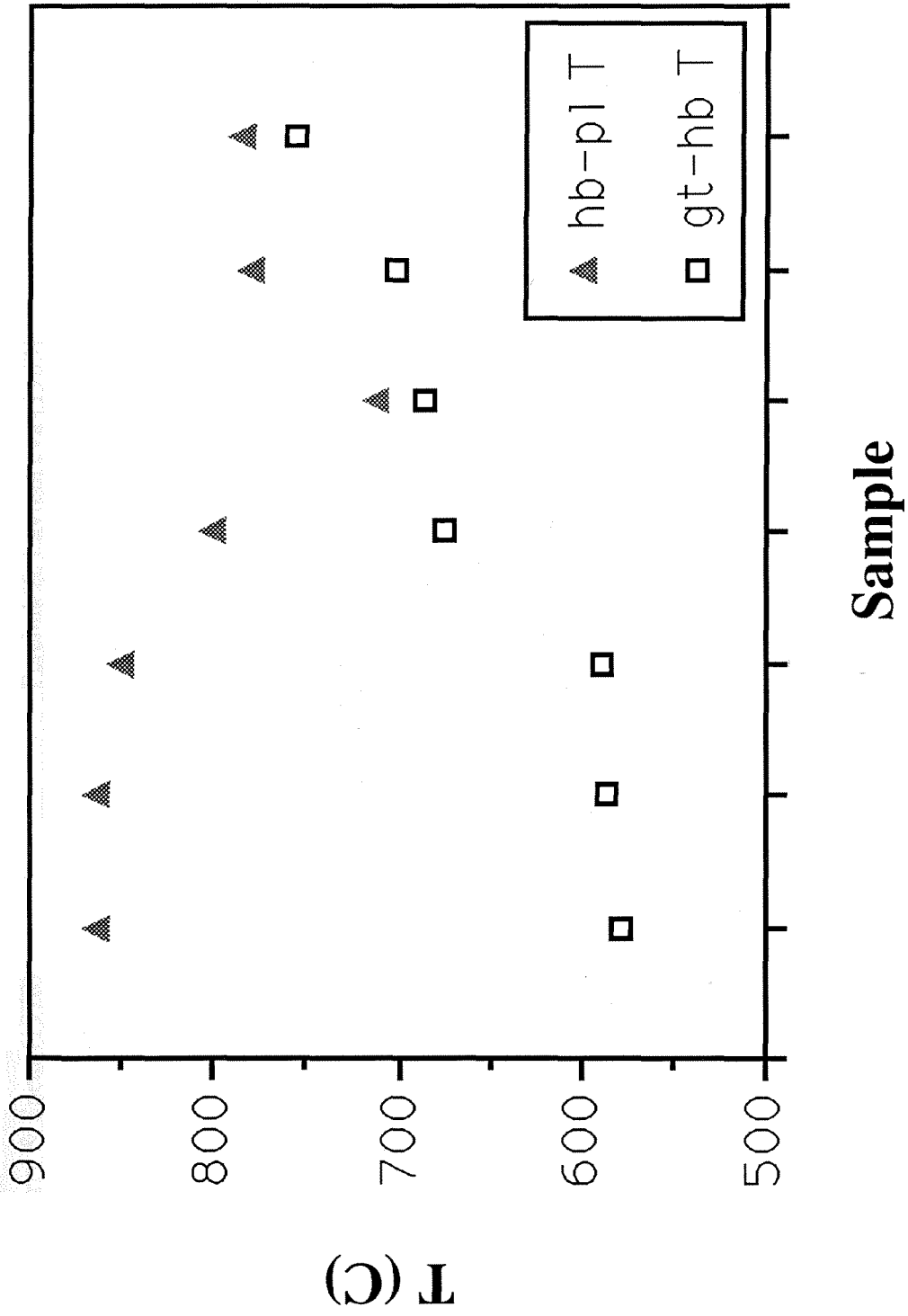
Fig. 2.8

Table 2.7 - Garnet-biotite temperatures[1] and garnet-biotite-plagioclase-quartz pressures[2]

| | Ferry & Spear (1978) | | Perchuk & Lavrent'eva [1983] | | | | |
	T, °C (rims)	P, kbar (rims)	T (rims)	P (rims)	T (c-m)	P (c-m)	T (c-c)
"CORE"*	735	12.6	588	9.5	641	11.5	
PC107a	957	17.4	674	11.3			723
GV-2	716	9.4	617	7.5			633
80-301§	788	7.1	682	5.6			
TC-8	630	4.3	619	4.1	686	4.9	673
GC-2	626	8.7	571	7.5			646
GV-4d	574		551				654

[1] Using Ferry and Spear [1978] (Hodges and Spear [1982]) or Perchuk and Lavrent'eva [1983] calibration.
[2] Average of reactions R1 and R2 of Hoisch [1990], calculated simultaneously with the indicated thermometer.
(c-m) = core garnet and matrix biotite and plagioclase.
(c-c) = core garnet and core biotite.
* Rim calculations are based on data in Sharry [1981], while core-matrix calculations are based on new data.
§ Calculations are based on data in Sharry [1981]. Sample is a metatonalite.

recalculations of Sharry's [1981] data for 80-301/A and "CORE" resulted in temperatures 100 and 50°C lower, respectively, than he calculated. In two samples (PC107a and "CORE") for which garnet-hornblende temperatures were also determined, the garnet-biotite temperatures are 30 and 100°C lower, respectively. (It should be noted that we were unable to locate suitable garnet-biotite pairs in our section of "CORE", restricting our measurements to garnet-hornblende-plagioclase and matrix biotite.) In two samples, TC-8 and "CORE", core garnet-matrix biotite pairs are 70°C and 50°C higher than rims. In other samples, cores of adjacent garnet and biotites, which may indicate minimum peak temperatures (particularly in "normal" prograde metasedimentary rocks such as GC-2 and GV-4), yield temperatures 20 to 100°C higher than rims, as high as 720°C in PC107a. In summary, garnet-biotite pairs record a range of temperatures (550-720°C) overlapping those recorded by garnet and hornblende but tending to be lower, and lacking the geographic dichotomy of the latter.

Plagioclase-scapolite -- In the calc-silicate sample CM650b (from the Comanche Point paragneiss), the temperature was calculated using compositions of coexisting plagioclase and scapolite based on the calibration of Goldsmith and Newton [1977]. The thermometer is based on Na-Ca exchange between the two phases and yields 780°C. Although this result is quite high and the reliability of the method is open to question, it is not completely inconsistent with some of the other estimates of metamorphic temperature. The sample comes from a relatively thin septum of paragneiss surrounded by tonalite (Figure 2.2). It would not be surprising for a refractory calc-silicate rock to have recorded such a temperature in such a setting.

b. Pressure

Sams and Saleeby [1988] summarized the arguments suggestive of high pressure for the plutonic and metamorphic rocks of the Tehachapi Mountains. We would add one

caveat to the portion of that discussion concerning magmatic epidote: the lithologies showing possible magmatic epidote do not usually contain all the phases required to constrain pressure to >6 kbar [Zen, 1989]. Furthermore, the two pressure determinations of Sharry [1981] are based on an assemblage in which the state of equilibrium is suspect (see below). In light of the uncertainties inherent in these previous arguments, we here present an attempt to gain a more quantitative basis for high pressure claims.

We noted above the probable presence of kyanite in a partially melted paragneiss (sample GV-4 of the Grapevine Peak migmatite; Figures 2.2 and 2.4b). Using the intersection of the fluid-present metapelite-metagraywacke liquidus and the sillimanite-kyanite curve as presented in Vielzeuf and Holloway [1988], these relations indicate a minimum temperature of 690°C at a minimum pressure of 7.1 kbar. Thus, it is clear that metamorphism, probably accompanying intrusion at the thermal maximum, was at both high temperature and pressure. We have combined quantitative geobarometers with the above geothermometers to better place metamorphism in pressure-temperature space.

Garnet-hornblende-plagioclase-quartz -- Kohn and Spear [1990] have recently proposed an empirically-calibrated geobarometer for garnet amphibolites based on the reaction 6 anorthite + 3 tremolite = 2 grossular + 1 pyrope + 3 tschermakite + 6 quartz and its Fe end-member equivalent. This reaction has quite a low slope in P-T space (<~7 bar/degree in the range of this study) and Kohn and Spear [1990] suggest a precision of less than 1 kbar. This barometer is combined with the garnet-hornblende geothermometer [Graham and Powell, 1984] discussed above. The results (Table 2.6, Figure 2.9) place the samples into the same two groupings as did the temperatures. The three samples of the Tunis Creek metagabbro (in the center of the study area), which gave the lower garnet-hornblende temperatures, yield pressures of 3.6 - 4.2 kbar. The other samples, from the western part of the study area, evidently equilibrated at much higher pressures: 8.2, 7.3, and 7.5 kbar from Pastoria Creek, Liveoak Canyon, and Grapevine

Figure 2.9 - Map of main study area showing calculated pressures by the gt-hb-pl-qz [Kohn and Spear, 1990] and gt-bt-pl-qz [Hoisch, 1990] methods. Note proximity of high igneous pressures (Figure 2.10) to the 4 kbar metamorphic zone. For "CORE" and PC107a, only the gt-hb-pl-qz results, which are preferred, are shown. Units are the same as in Figure 2.2.
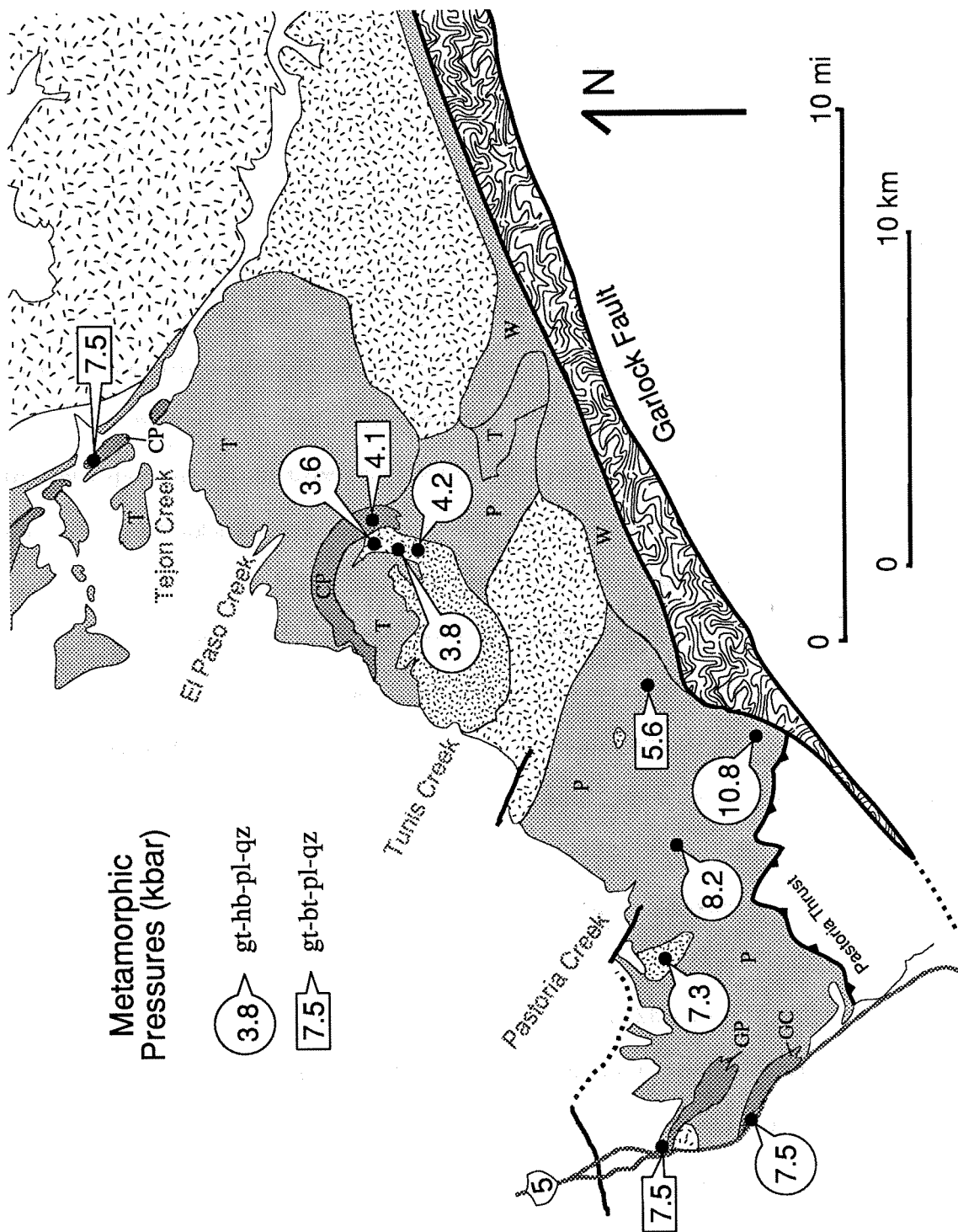
Fig. 2.9

Canyon, respectively, and 10.8 kbar from "CORE" from near the convergence of the Pastoria thrust and the north branch of the Garlock fault. It should be mentioned that the garnet and hornblende $Fe^{2+}/(Fe^{2+}+Mg)$ ratios in tonalites PC107a and "CORE" are higher than the recommended range of Kohn and Spear [1990], meaning that the pressures may be somewhat overestimated; this qualification does not, however, apply to the metagabbros.

Such a large pressure difference within the study area, among units with no discernible major tectonic boundaries, is somewhat surprising. The major variable affecting the barometric calculation is the partitioning of Ca between plagioclase and garnet, i.e., relative activities of anorthite and grossular. It was noted above that only in the lower-pressure Tunis Creek samples was plagioclase not touching garnet less calcic than that touching garnet. This suggests that the garnet-plagioclase equilibrium initiated by the garnet-forming reaction produced significantly increased Ca contents in adjacent plagioclase, a relationship expected at lower pressures. In the other cases, higher pressures resulted in partitioning of Ca out of plagioclase into garnet, leaving plagioclase more Ab-rich than those that did not exchange with garnet. (Since hornblende was consumed by the garnet-forming reaction in both cases, these observed shifts in plagioclase composition imply open-system behavior of Na.) Another test is the degree to which intergrain transfer has affected core-rim zoning in plagioclase. As noted above, metagabbro GC-46 (7.3 kbar) shows a much more pronounced core-to-rim drop in An content than the Tunis Creek metagabbros (3.6 - 4.2 kbar), consistent with higher-pressure equilibrium with garnet. For these reasons, we have confidence in the results.

We have mentioned our suspicion that garnet cores were not necessarily ever in equilibrium with matrix phases in the metaigneous rocks (see also Selverstone and Chamberlain, [1990]); matrix compositions of plagioclase and hornblende may rather reflect primary igneous conditions. Calculated garnet core-matrix plagioclase and

hornblende pressures are shown in Table 2.6, and they show no particular pattern: they are within ±1 kbar of rim results. Robust information about the earlier pressure history of these particular rocks is lacking.

Garnet-biotite-(muscovite)-plagioclase-quartz -- A Mg end-member reaction based on this assemblage was used by Sharry [1981] on samples "CORE" and 80-301 for P-T determinations using an unpublished calibration by K. Hodges. Sharry reports values of 640°C, 8.5 kbar for "CORE," and 779°C, 8.1 kbar for 80-301. A new check of these calculations gives 8.9 and 7.0 kbar, respectively. Using Sharry's data with the calibration of Ghent and Stout [1981], we calculate 635°C, 7.6 kbar ("CORE") and 763°C, 4.5 kbar (80-301). Outside of the uncertainties due to the use of different calibrations, there is some doubt that the muscovite in this assemblage is an equilibrium phase [Sharry, 1981]. In the present study, as well as in that of Sams [1986], there are no observed samples with strong textural evidence for equilibrium among all these phases. However, Hoisch [1990] has proposed six empirically calibrated geobarometers utilizing such assemblages with or without muscovite. We have applied the two muscovite-free reactions (R1 and R2 of Hoisch [1990]) to our samples and the two Sharry [1981] samples, combining the calculations with the garnet-biotite geothermometers of Ferry and Spear [1978] and Perchuk and Lavrent'eva [1983] (Table 2.7).

For two samples, PC107a and "CORE", we can compare the garnet-biotite-plagioclase-quartz results to those based on the garnet-hornblende-plagioclase-quartz geobarometer. In line with our preference for the garnet-biotite geothermometer of Perchuk and Lavrent'eva [1983] (see above), pressures calculated using those temperatures (11.3 kbar for PC107a, 9.5 kbar for "CORE") are closer to the garnet-hornblende-plagioclase-quartz pressures (8.2 and 10.8 kbar, respectively) than those using temperatures obtained with the Ferry and Spear [1978] calibration (17.4 and 12.6 kbar). We consider the pressures derived using the Perchuk and Lavrent'eva [1983] calibration

for temperature to be the most reliable. There is still a large discrepancy for PC107a -- it is notable that for this sample and for "CORE", biotite composition and one of the equilibrium constants are outside of Hoisch's [1990] recommended range, casting some doubt on the result. Whatever the source of the discrepancy, the garnet-hornblende-plagioclase-quartz pressures for both PC107a and "CORE" are more in line with the other results in this study than are the garnet-biotite-plagioclase-quartz pressures, and the former are plotted on the map in Figure 2.9.

Pressures for the other samples (Figure 2.9) range from 4.1 to 7.5 kbar, and an interesting areal variation pattern is evident. One of the samples of Comanche Point paragneiss (TC-8) yields the same low pressure (4.1 kbar) as the nearby Tunis Creek metagabbros. The Grapevine tonalite (GV-2) yields the same pressure (7.5 kbar) as the nearby metagabbro GV-1a, and the new calculation for Sharry's [1981] sample 80-301 gives an intermediate value of 5.6 kbar. The one sample from north of the low-pressure zone near Tunis Creek, Comanche Point paragneiss GC-2, yields a high pressure of 7.5 kbar. Thus there is again a dichotomy, with high-pressure rocks lying on either side of the low-pressure Tunis Creek area. Sample 80-301 seems to have the only intermediate pressure.

P-T calculations using core garnets and matrix biotite and plagioclase were performed for two samples (TC-8 and "CORE") with characteristics that would lend more credibility to the results [Selverstone and Chamberlain, 1990]. These samples have smaller garnet grains dispersed through the sample rather than concentrated in veins or layers as in the metagabbros. In paragneiss TC-8, core-matrix estimates (Table 2.7) are 70°C and 0.8 kbar higher than for rims, and in the metatonalite from near the north branch of the Garlock fault ("CORE"), they are 50°C and 2.0 kbar higher.

Al-in-hornblende igneous geobarometer -- An effort was made to locate granitoids with the proper assemblage for estimating pressure from the Al contents of hornblendes

[Hammarstrom and Zen, 1986; calibration of Hollister et al., 1987]. Only a few such rocks were found that also lacked extensive deformation and alteration features, and their calculated pressures are shown in Table 2.8 and Figure 2.10. Sample BM149, from 45 km north of the center of the main study area and 2 km south of Walker Basin, has the lowest hornblende pressure of 3.2 kbar. Tonalite CM13b, from near Keene on Tehachapi Creek, yields 6.9 kbar. In their batholith-wide survey of the Sierra Nevada, Ague and Brimhall [1988] report pressures consistent with these on four nearby samples (Figure 2.10), some of which, however, lack sphene.

Five samples from the main study area, from the Tejon Creek and Pastoria Creek gneiss units, give higher pressures of 7.8 - 9.3 kbar (the calibration of Hammarstrom and Zen, 1986, gives pressures 0.5 - 0.7 kbar lower). These are similar to the higher metamorphic pressures, but these high igneous pressures are found even where the lower metamorphic pressures were determined, i.e., near the Tunis Creek metagabbro. Johnson and Rutherford [1989] have experimentally calibrated the hornblende geobarometer (but at temperatures higher than the solidus), and the derived pressures are 1.7 - 2.2 kbar lower than those using the Hollister et al. [1987] calibration. We favor the Hollister et al. [1987] calibration, not only because it gives pressures more in line with our metamorphic results, but also because it is based on natural assemblages in geologic settings similar to those in this study.

Blundy and Holland [1990] have recently questioned the validity of this geobarometer, asserting that the Al^{iv} content of hornblende is a better function of temperature than of pressure. However, the necessary assumption for the geobarometer, that the hornblende rims crystallized at roughly the same temperature, appears valid. Had all the samples (excluding BM149) crystallized at 5 kbar, for example, assuming plagioclase is An_{30}, temperatures calculated by the Blundy and Holland method would span the range 760-840°C. This is not only a large range for such similar rocks, but it is

also high [Hammarstrom and Zen, 1986; Hollister, et al., 1987]; this supports the notion that the pressure differences are real. Since the Blundy and Holland geothermometer has a negative dP/dT slope, in order for the temperatures to be more realistic, pressures must have been higher than 5 kbar. For GC-33, we measured adjacent plagioclase and hornblende and calculated a temperature of 790°C at its calculated hornblende pressure of 9.3 kbar; this is unreasonably high. Furthermore, a plot of Al^{iv} vs. Al^T (Figure 2.11) shows a monotonic correlation (as in Hammarstrom and Zen [1986]) that would not be expected were the variations in Al^{iv} due solely to temperature variation in the substitution scheme of Blundy and Holland [1990]. Finally, had the hornblende rim compositions been altered by subsolidus reactions, Al concentrations would have been lowered, resulting in *under*estimates of pressure in the igneous geobarometer. For all these reasons, we believe that the Al-in-hornblende pressures are correct to ±2 kbar at the worst.

In spite of the uncertainties, two important conclusions may be drawn without reservation from the Al-in-hornblende study. First, the igneous rocks of the main study area crystallized at higher pressures (~8 kbar) than any others in the entire Sierra Nevada batholith (see Ague and Brimhall [1988] for comparison), and these pressures correspond to crustal levels at least 25-30 km deep. Second, crystallization took place at the same deep level throughout the main study area, in contrast to the variety of metamorphic, subsolidus pressures.

c. Summary of P-T results

Preferred pressures are shown on the maps of Figures 2.9 and 2.10, the pressures and temperatures are plotted in Figure 2.12, and all results are summarized in Table 2.8. The available data show that the igneous rocks of the Tehachapi Mountains crystallized at pressures of ~8 kbar. Metamorphism of framework metasedimentary rocks, as well as subsolidus crystallization and equilibration in the igneous rocks, occurred at 7-8 kbar in

Figure 2.10 - Map showing distribution of aluminum-in-hornblende igneous pressures (calibration of Hollister et al. [1987]). Included are pressures from Ague and Brimhall [1988], some of which are from rocks lacking sphene. Units as in Figure 2.1.

Aluminum-in-Hornblende Pressures (kbar)

3.2 This study

5.7 Ague and Brimhall (1988)
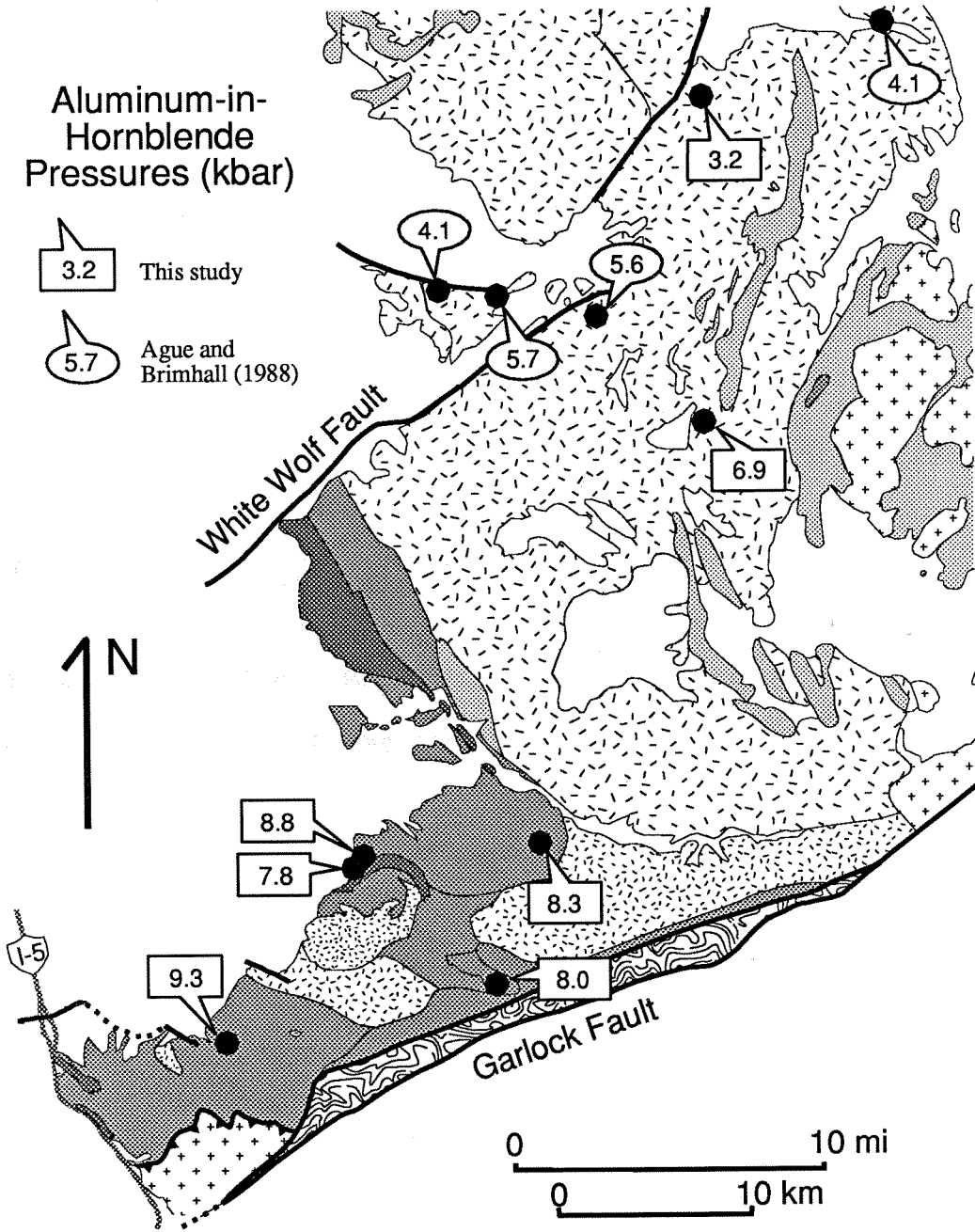
Fig. 2.10

Figure 2.11 - Plot of Al^{iv} vs. Al^T for igneous hornblendes from which pressures were calculated. The samples show a monotonic covariation and plot near the empirical line of Hammarstrom and Zen [1986] relating Al^{iv} and Al^T concentrations, demonstrating consistency with their substitution scheme.
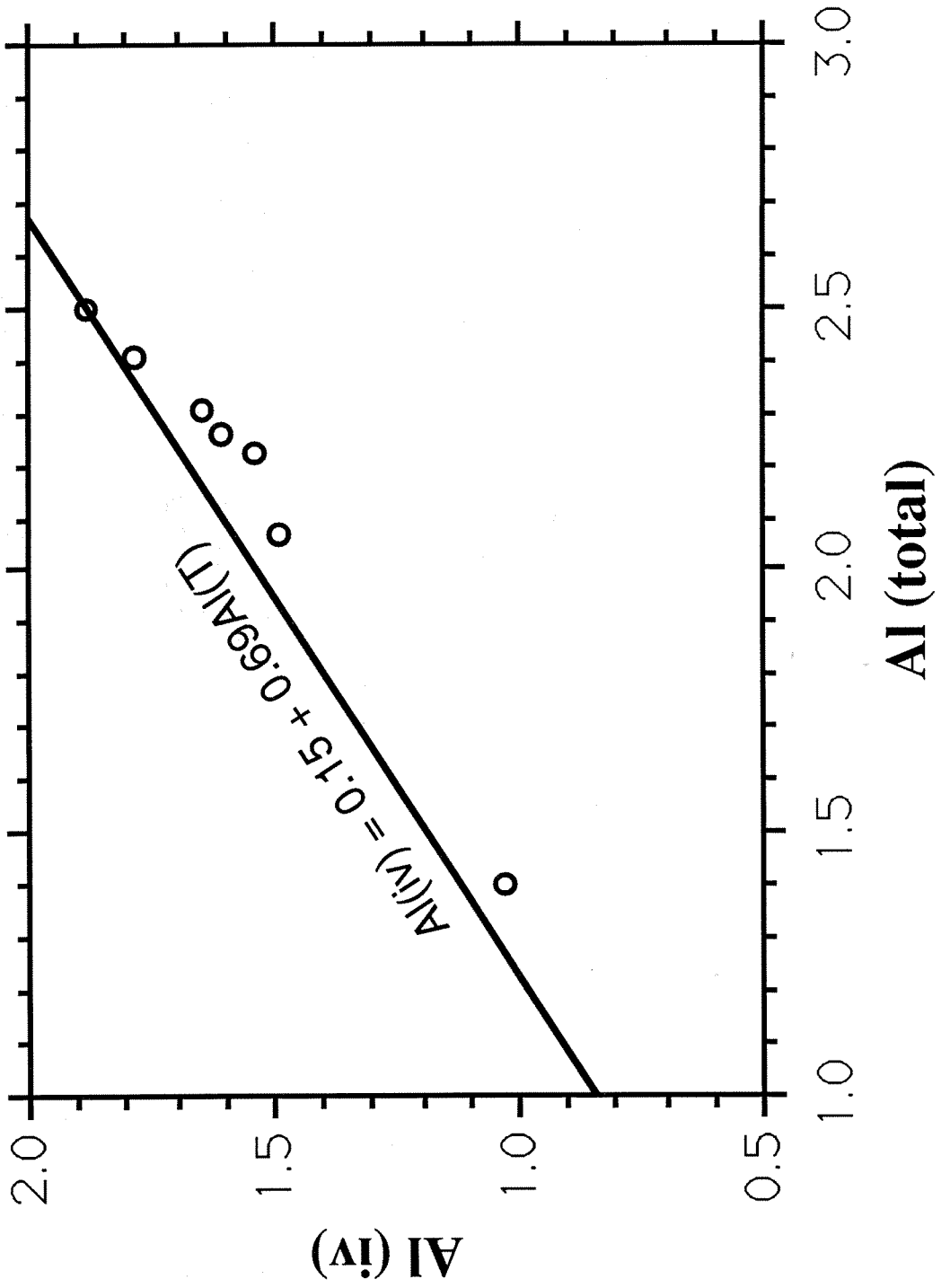
Fig 2.11

Table 2.8 - **Summary of preferred temperatures, pressures, and fluid compositions**

	lithology	T (°C)	P (kbar)	X_{H_2O}
TC-83	metagabbro	580	3.8	0.01
GC-22	metagabbro	590	3.6	0.02
TC-2a	metagabbro	590	4.2	0.02
GV-1a	metagabbro	680	7.5	0.05
GC-46	metagabbro	760	7.3	0.05
CORE	metatonalite	690	10.8	0.6
PC107a	metatonalite	700	8.2	0.1
GV-2	metatonalite	620	7.5	
80-301	metatonalite	680	5.6	
TC-8	paragneiss	620	4.1	0.2
GC-2	paragneiss	570	7.5	
GV-4d	paragneiss	550		
CM650b	calc-silicate			0.7
BM149	tonalite		3.2	
CM13b	granite		6.9	
WR27a	tonalite		8.0	
TC-12a	tonalite		7.8	
GC-16	granite		8.3	
CM657	tonalite		8.8	
GC-33	granodiorite		9.3	

Figure 2.12 - Summary plot of pressure and temperature information using calculations based on rim compositions. Igneous pressures are plotted at 700°C for convenience; this temperature was not calculated. Squares = gt-hb-pl-qz [Kohn and Spear, 1990], triangles = gt-bt-pl-qz [Hoisch, 1990], circles = Al-in-hornblende [Hollister et al., 1987].

Fig. 2.12

most parts of the study area, but at considerably lower pressures (~4 kbar) between Tunis and El Paso Creeks. Higher pressure (9-10 kbar) is sugge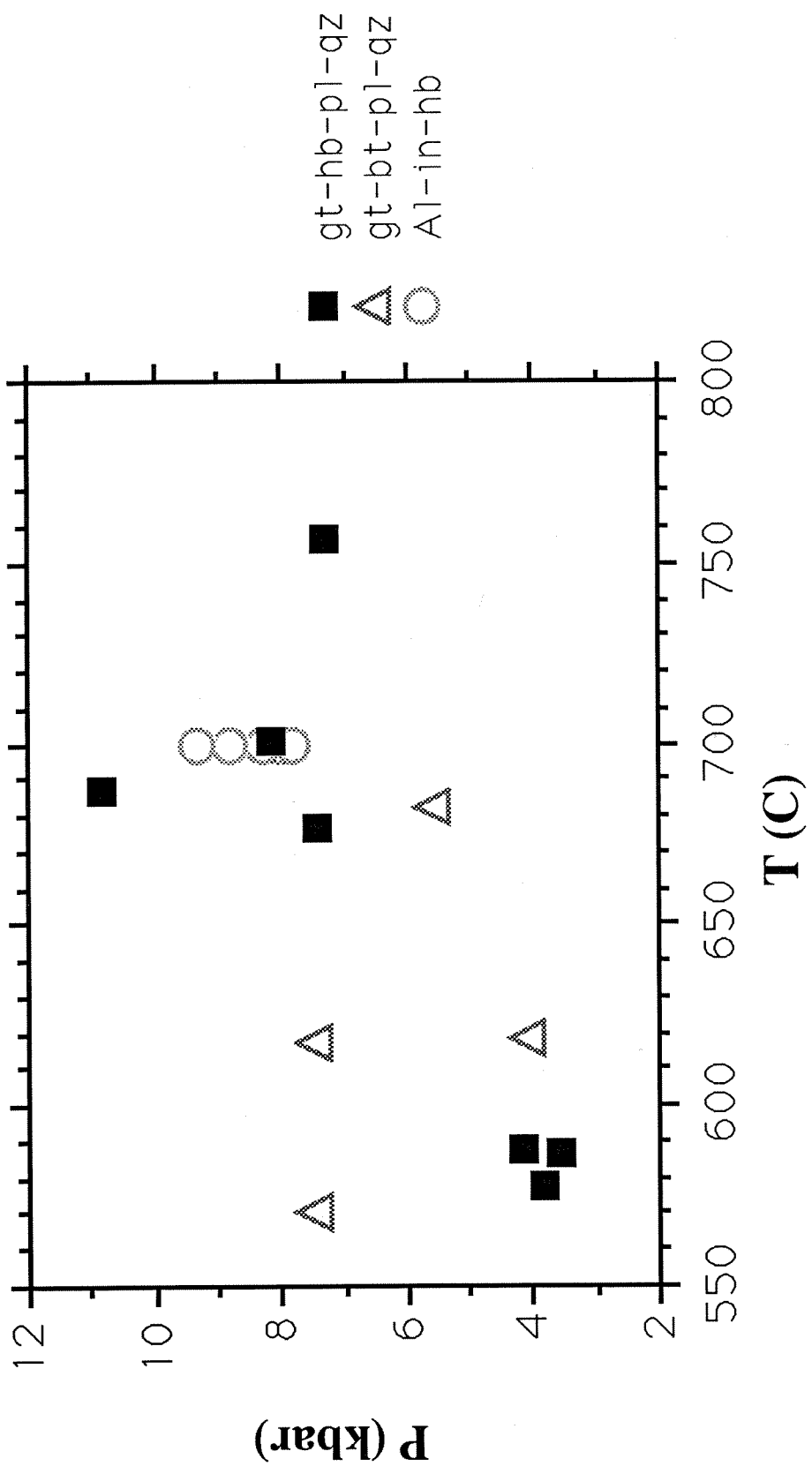sted for a sample from near the convergence of the Pastoria thrust and the north branch of the Garlock fault, and an intermediate result (5.6 kbar) comes from south of the low-pressure zone. Evidence for earlier higher pressures from core-matrix measurements is usually lacking or equivocal; paragneiss TC-8 may give a reliable core-matrix pressure (4.9 kbar) that is 0.8 kbar higher than the rim result.

Temperatures do not follow systematic areal patterns, except for garnet-hornblende results, which are 680-760°C in the higher-pressure rocks and ~580°C in the lower. Garnet-biotite temperatures are 550-680°C for rim pairs, the large range probably due to re-equilibration on cooling. The samples show evidence for minimum "peak" garnet-biotite temperatures of 630-720°C.

Pressures of intrusion are lower for more northern samples of the Bear Valley Springs tonalite, implying that the more gneissic rocks of the main study area may constitute the plutonic substrate of the large Bear Valley Springs batholith.

d. Fluid compositions

For many assemblages containing hydrous or carbonate phases, volatile-present reactions can be written that will define curves in $P-X_{H_2O}$, $T-X_{H_2O}$, $P-X_{CO_2}$, or $T-X_{CO_2}$ space, allowing estimation of fluid compositions attendant on equilibrium if independent estimates of pressure and temperature are available. Such reactions have been constructed for the rocks whose mineral compositions were measured for the pressure and temperature estimates discussed above, and calculated fluid compositions are shown in Table 2.8. The reactions were calculated using the program PTX-SYSTEM of Perkins et al. [1986] with the thermodynamic data base of Berman et al. [1985]. Any fluid phase is assumed to consist only of the components H_2O and CO_2, with nonideal mixing as modeled

by the equations of Kerrick and Jacobs [1981]. The activity models used are: Newton et al. [1980] for plagioclase, Hodges and Spear [1982] for garnet, Fuhrman and Lindsley [1988] for alkali feldspar, Oterdoom and Gunter [1983] for scapolite, Ghent [1988] for tremolite in hornblende, and ideal mixing for biotite ($a_{phl} = X_{Mg}^3$).

    <u>6 tremolite + 21 anorthite = 11 grossular + 10 pyrope + 27 quartz + 6 H$_2$O</u> -- Ghent [1988] proposed this equilibrium for use in H$_2$O activity determinations. In the present study, it was applied to all samples for which garnet-hornblende-plagioclase-quartz pressures and temperatures were determined. Ghent [1988] utilized two tremolite activity models -- coupled substitution and ionic -- and found no advantage of one over the other. We report results using the coupled substitution model because it always results in higher X_{H_2O}, meaning our estimates of X_{H_2O} are maximum values. For the three low-pressure Tunis Creek metagabbros, X_{H_2O} is very low (~0.02); taking into account the ~1 kbar error on the pressure, X_{H_2O} is constrained to be <0.07. (The effect of the temperature uncertainty is much less significant.) The other two metagabbros also give a low X_{H_2O} of 0.05, constrained to <0.2 within uncertainty. Tonalites "CORE" and PC107a give higher values, but because of the rapid steepening of the reaction curves in X_{H_2O}-P space at higher pressures, the errors are much larger. Thus the calculated X_{H_2O} for PC107a is 0.12, but the range of uncertainty is 0.05 - 0.4; "CORE" gives X_{H_2O} = 0.6, but the pressure uncertainty range of 9.8 - 11.8 kbar results in an error range in X_{H_2O} of 0.1 - 1.0. In general, though, this reaction defines low to near-zero H$_2$O activities in the garnet-hornblende assemblages, particularly in the metagabbros. This is not too surprising since, in the metagabbros, garnet appears to grow at the expense of hornblende (Figure 2.5), resulting in a net dehydration. While it is possible that the low H$_2$O activities could result from the absence of fluids during metamorphism, the appearance of garnet in veins and specific textural zones and the scattered, nonubiquitous occurrence suggest that fluids were present, and that they in fact provided a kinetic impetus to the garnet-forming

reaction. We therefore conclude that the appearance of garnet, at least in these particular rocks, resulted from a subsolidus, channelized, nonpervasive influx of CO_2-rich fluids.
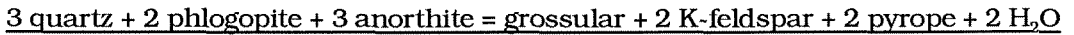
<u>3 quartz + 2 phlogopite + 3 anorthite = grossular + 2 K-feldspar + 2 pyrope + 2 H_2O</u>
-- Application of this equilibrium to sample TC-8 from the Comanche Point paragneiss (619°C, 4.1 kbar) yields X_{H_2O} = 0.24. Applying a temperature error of ±25°C and a pressure error of ±1 kbar gives an uncertainty range of 0.13 - 0.47, meaning that the fluid in equilibrium with this assemblage was not H_2O-rich. If we assume again that the fluid is primarily a CO_2-H_2O mixture, we may then calculate CO_2 fugacity; since this rock also contains graphite, we may then use the equilibrium C + O_2 = CO_2 to calculate f_{O2} [e.g., Edwards and Essene, 1988]. Activity and fugacity coefficients used for CO_2 are from Kerrick and Jacobs [1981], CO_2 free energy and graphite volume data are from Robie et al. [1979], and graphite thermal expansion and compressibility are from Clark [1966]. This method estimates quite a low $\log f_{O_2}$ of -19.2, with the uncertainty in X_{H_2O} translating to an error of ~ 0.8 log units. This evidence for quite reducing conditions is consistent with the qualitative evidence for widespread low f_{O_2} mentioned above.

<u>2 meionite + quartz = grossular + 5 anorthite + 2 CO_2</u> -- Moecher and Essene [1985] proposed this equilibrium for calculating CO_2 activities in scapolite-bearing calc-silicate rocks. This equilibrium was applied to data from sample CM650b (Comanche Point paragneiss), for which a poorly constrained temperature of 780°C was determined above. The pressure of equilibration of this assemblage is unknown, but the sample does lie only 2.3 km along strike from paragneiss GC-2, for which 7.5 kbar was estimated. At 780°C and 7.5 kbar, calculated X_{CO_2} is 0.34; for lower temperatures, X_{CO_2} would be even lower. Had CM650b equilibrated at lower pressures, say 4 kbar, X_{CO_2} must still have been <0.6, meaning that this rock experienced fluids more aqueous than did the previously discussed samples. Earlier in this paper, we described another calc-silicate sample which bore evidence for retrograde hydration by aqueous fluids.

In summary, fluid compositions during metamorphism appear to have been variable and were not controlled by a pervasive influx. While garnet-bearing metagabbros show clear evidence for the action of H_2O-poor fluids, somewhat more aqueous fluids are allowed in the case of the paragneiss TC-8, and H_2O-rich (but still CO_2-bearing) fluids are indicated for the calc-silicate rocks.

2.7. Discussion

a. Physical and chemical conditions

Thermobarometric estimates indicate that the 115-100 Ma intrusive rocks of the Tehachapi Mountains, which comprise calcalkaline components of the Cretaceous Sierra Nevada batholith, were emplaced at pressures of ~8 kbar. Assuming a granodioritic crustal density of 2.7 g/cm^3, this corresponds to depths of ~30 km, making them the deepest-formed exposed rocks of the batholith. Subsolidus, retrograde metamorphism of these igneous rocks and metamorphism of framework metasedimentary rocks, some of which was related to channelized influx of CO_2-rich fluids, occurred at these same depths and at temperatures of higher than 620°C; exceptions are a higher-pressure rock (~10 kbar) adjacent to the north branch of the Garlock fault and a group of lower-pressure rocks (~4 kbar) between Tunis and El Paso Creeks. The 10 kbar sample ("CORE") is from an area with a complex and poorly-defined structural setting near the conjunction of the Pastoria thrust and the north and south branches of the Garlock fault (see Ross, 1989, for discussion), so its significance cannot be fully evaluated. Garnet-biotite temperatures in the higher-pressure rocks (550-680°C) most likely do not reflect peak conditions; the abundant migmatization and the lack of metamorphic gradients adjacent to intrusive rocks suggest that rocks throughout the crystalline complex reached temperatures in excess of 700°C. Subsequent essentially isobaric cooling from magmatic conditions was responsible for lower-temperature re-equilibration along grain rims.

Igneous pressures decrease to the north in the tonalite of Bear Valley Springs, through 7 kbar to 5.6 kbar [Ague and Brimhall, 1988] to 3.2 kbar in the far north. These are supportive of the general view [Sams and Saleeby, 1988] of the more gneissic rocks south of Tejon Creek as a substrate to the large, 100 Ma Bear Valley Springs pluton.

The 4 kbar garnet-forming event is superimposed on an area that bears evidence for intrusion at 8 kbar, and high-pressure intrusion and metamorphism is found both to the north and southwest of this zone (Figures 2.9 and 2.10). There is no field evidence for major structural breaks bounding this zone or separating the low-pressure rocks from the nearby intrusive rocks yielding high Al-in-hornblende pressures. We therefore conclude that the metamorphism recorded in this zone occurred after the entire crystalline complex had been uplifted from ~30 km depth to ~15 km, and its localized character and vein paragenesis in the metagabbros are attributed to a channelized influx of CO_2-rich fluids. Such fluids are considered to be a fairly common, though not ubiquitous, feature of the lower crust [e.g., Newton, 1989]. That temperatures of ~600°C were attained in this event can be attributed to: (1) a local, intrusion-related thermal anomaly, (2) advection of heat by the invading fluids, or (3) rapid uplift before the rocks had cooled below 600°C. The first alternative is unlikely in the absence of evidence for a lower-pressure intrusive event. We cannot assess the relative merits of the latter two alternatives; both may have been factors. However, the ambient temperature must have been relatively high for such high-temperature fluids to have been present, suggesting that uplift was most likely rapid (see below). The one low-pressure paragneiss (TC-8) does not have veins suggestive of fluid flux, and garnet zoning implies earlier higher pressures (Table 2.7). The fact that lower pressures were not recorded elsewhere points to the importance of the local fluid influx.

Calculated fluid compositions are variable, arguing against any large-scale, pervasive fluid influx. Results from garnet-bearing metaigneous rocks point to the localization of CO_2-rich fluids along veins and specific textural zones for both the low and

high pressure rocks. Without further work, we can but speculate on the sources of these fluids. Enclaves of metacarbonate rocks, which would release CO_2 during prograde metamorphism, are present throughout the area, but a systematic spatial relationship between these enclaves and the garnet-bearing veins is lacking. Furthermore, the vein-forming event occurred after the thermal maximum, and therefore postdates initial prograde metamorphism of the carbonate rocks. It is notable that the widespread occurrence of magmatic hypersthene in gabbros to tonalites, a feature which has led to the description "granulite terrane" [Sharry, 1981], points to low H_2O activities during original igneous emplacement. The lack of orthopyroxene in partially melted biotite quartzofeldspathic paragneisses is suggestive of high H_2O activities during the thermal maximum for these rocks [e.g., Waters, 1988].

In Cretaceous, granulite-grade, deep-batholithic orthogneisses of Fiordland, New Zealand, Bradshaw [1989] describes garnet-bearing veins which bear some resemblance to those discussed here. Although the Fiordland rocks have seen a more complex P-T history than the Tehachapi Mountains orthogneisses, he attributes formation of the garnet-bearing vein assemblages (based on fluid-inclusion studies and reaction modeling) to the same process invoked here -- localized infiltration of CO_2-rich fluids resulting in hornblende breakdown. In Bradshaw's model system, pyroxene-free vein assemblages, which are the only kind observed in the Tehachapi Mountains, require that the system be open with respect to Na and Ca. The possibility of such behavior was suggested above for the study area to help account for variations in plagioclase composition.

b. Tectonic implications

Uplift -- The plutonic rocks of the Tehachapi Mountains were intruded in a dynamic tectonic environment [Sams, 1986; Saleeby et al., 1987; Sams and Saleeby, 1988]. The metamorphic assemblages described here formed both during and after the development

of high-temperature deformation fabrics; for example, some of the garnet-bearing veins in the metaigneous rocks cut across the near-solidus fabrics. The garnet-bearing veins, as well as the high-temperature fabrics, are in turn locally transposed by domainal mylonitic fabrics which developed under lower-grade metamorphic conditions, particularly along and near the north branch of the Garlock fault (Figure 2.2). As described above, these lower-grade fabrics have a dominant, shallow north dip in the vicinity of this fault. Since the mylonitic fabrics post-date garnet-bearing assemblages, the initial uplift event from 30 km to 15 km cannot be directly tied to the mylonitic deformation. It has been suggested, however, [Sharry, 1981] that uplift of the high-pressure rocks of the Tehachapi Mountains is related to underthrusting of the Rand Schist, which is exposed just across the north branch of the Garlock fault from the Tehachapi rocks (Figure 2.2). Seismic reflection work across the range by Malin et al. [in review] has revealed a major, shallowly north-dipping reflector which they interpret as a thrust separating the Rand Schist from the high-grade crystalline rocks of the present study. This hypothesized thrust projects to the surface along the north branch of the Garlock fault. Such a thrust may be related to the observed mylonitic deformation near the north branch of the Garlock fault, although the fault appears to now represent a recent, near-vertical reactivation related to the left-lateral transcurrent motion on the Garlock fault system. Sharry [1981] reports outcrops and drill-hole data which suggest such a thrust geometry near the convergence of the Pastoria thrust and the north branch of the Garlock fault. (The presence of the highest-pressure sample ("CORE") near the proposed thrust is suggestive of major displacements in this area.) If correct, these tectonic relationships are analogous to those common to other localities of Rand-Orocopia-Pelona-type schist bodies [Haxel and Dillon, 1978].

Temperatures of 530-630°C and pressures of 7.3-8.7 kbar have been reported for the conditions of metamorphism of the Rand Schist adjacent to the high-grade rocks of the study area [Sharry, 1981]. The Rand Schist was thus metamorphosed at the same deep

levels as the Tehachapi complex, although at lower temperatures. Sharry [1981] also reports that the highest temperatures in the Rand Schist block were attained closest to the north branch of the Garlock fault, suggestive of a temporal link between initial thrusting and metamorphism; such a link is suggested for the Rand-Orocopia-Pelona-type schists in general by Jacobson et al. [1988]. Combined with the new evidence for lower-pressure (4 kbar) metamorphism in the Tehachapi rocks, this implies that initial thrusting of the Rand Schist beneath the high-grade Tehachapi rocks may have taken place while the latter were still hot (>600°C) and before they had been uplifted to 15 km depths. Alternatively, the correspondence in pressures across the north branch of the Garlock fault could have resulted from a later coincidental juxtapositioning of two high-pressure blocks.

A minimum uplift rate for the crystalline rocks of the Tehachapi Mountains, calculated on the basis of exposure of the deep 100 Ma rocks at 52 Ma (earliest Middle Eocene -- Nilsen, 1987), is 0.6 mm/yr. Biotite K/Ar ages from Grapevine Canyon (summarized in Ross [1989]), from very near high-pressure samples GV-1a and GV-2 but 20 km from the low-pressure zone of the Tunis-El Paso Creeks area, are 86 and 87 Ma. In the Bear Valley Springs tonalite, 20 km on the other side of the low-pressure zone, Ross [1989] reports a biotite K/Ar age of 86 Ma. Since the lower-pressure rocks of the Tunis-El Paso Creeks area (4 kbar) record temperatures of ~590°C, well above biotite Ar blocking temperatures, it is unlikely that the K/Ar ages to the east and west were set while the rocks were still between 30 and 15 km deep. If uplift from 30 to <15 km took place before 87 Ma, this implies a relatively rapid uplift rate of >1.2 mm/yr. This rate compares favorably with those of some modern orogens as summarized by Zen [1988], as well as with rates determined by Zen for deep Cretaceous plutons of the northern Cordillera. If this uplift rate also applies to the structurally underlying Rand Schist, this estimate is consistent with the work of Jacobson et al. [1988], who summarize arguments for rapid uplift following metamorphism (pre-70 Ma) for all Rand-Orocopia-Pelona-type schists.

May [1989] has proposed a model of synplutonic Late Cretaceous tectonism in southern California related to the westward transport of a segment of the magmatic arc, now exposed in Salinia, along major low-angle faults. In the context of his model, the higher-temperature, steeply-dipping, west-to-north-striking, synplutonic deformation in the Tehachapi Mountains would be a manifestation of tectonism on the periphery of this "westward escaping arc segment." May [1989] draws a distinction between this event and the later, lower-temperature, multi-stage deformation (see below) associated with low-angle fault zones overlying the various Rand-Orocopia-Pelona schist bodies (or Baldy Terrane). However, the possible tectonic emplacement of the Rand Schist beneath the high-grade Tehachapi block at great depths, as described in the present study, may provide a link between these two events. In other words, since this underthrusting likely occurred soon after magmatism, it may provide evidence for a tectonic continuum between May's proposed Late Cretaceous synbatholithic tectonism and original underthrusting of Rand-Orocopia-Pelona schist bodies. Subsequent uplift may have been a result of isostatic adjustment after major underthrusting of the low-density metasedimentary rocks [Sharry, 1981]. Therefore, it is possible that uplift of the high-pressure rocks of the Tehachapi Mountains was a manifestation of an extensional event following crustal thickening, and some of the mylonitic features of the range (the kinematics of which lack detailed study) may result from this later event.

Malin et al. [in review] propose, based on interpretation of seismic reflectors beneath the Tehachapi Mountains, that uplift of the range resulted from crustal-scale tilting, with greatest uplift in the southeast. This scenario is plausible, but it is not reflected in the observed patterns of pressure determinations; that is, there is no consistent increase in pressures toward the southeast. Furthermore, based on the lower Al-in-hornblende pressures to the north reported in this study and in Ague and Brimhall [1988], uplift in the southernmost Sierra Nevada appears to have taken place on a longer

horizontal length scale (>75 km) than would be implied by block tilting within the confines of the Tejon embayment and the southern Tehachapi range.

Role of low-angle faults -- These proposed temporal relations contrast with those deduced by Silver and Nourse [1986] for low-angle faulting affecting the Rand Schist in the Rand Mountains, which would lie about 50 km east-northeast of the Rand Schist exposures in the main study area after removing 50 km of left-lateral offset on the Garlock fault [Ross, 1989]. Silver and Nourse [1986] conclude that low-angle fault motion postdates metamorphism of the schist and emplacement of a 79 Ma pluton. Silver [1986] correlates the multiple faulting events of the Rand Mountains with those observed on the north side of the Garlock fault, 50 km northeast of the present study area. This later date of faulting (post-79 Ma) could only hold for the Tehachapi Mountains if thrusting significantly post-dated the high-pressure metamorphism recorded on both sides of the thrust. This would be counter to the apparent contemporaneity of metamorphism and thrusting in the Tehachapi Mountains suggested by Sharry [1981]. Resolution of these differing scenarios for probably correlative tectonic assemblages awaits better age control on faulting and thermal events. It does seem clear that in both the Rand and Tehachapi ranges, the Rand Schist was metamorphosed before 79 Ma. Perhaps initial thrusting in the Tehachapis, accompanied by this high-pressure metamorphism, actually represents an event separated in time from a later, higher-level reactivation correlative with the faulting described by Silver [1983, 1986] and Silver and Nourse [1986]. Such a reactivation is proposed for the Rand Mountains by Postlethwaite and Jacobson [1987] and Nourse and Silver [1986], who describe multiple episodes of faulting with varying shear directions. Reactivation may be responsible for many of the lower-temperature deformational features in the Tehachapi Mountains, including the intense deformation and greenschist-grade retrograde metamorphism of the White Oak diorite gneiss along the north branch of the Garlock fault, cataclasis and mylonitization in the vicinity of the fault,

and scattered deformation elsewhere [Sams and Saleeby, 1988].

The role of the Pastoria thrust [Crowell, 1964] in the tectonic history of the area is still open to question, particularly since its spatial relationship to the probable thrust of the north branch of the Garlock fault is not established. The Pastoria thrust (Figure 2.2) brings lower-pressure, undeformed Cretaceous granitic rocks of contrasting petrologic and isotopic character [Ross, 1989] over the Tehachapi rocks along an apparently south-dipping fault. Therefore, this faulting event must have postdated intrusion, deformation, metamorphism, and a large part of the uplift of the Tehachapi rocks. If the Rand Schist were thrust beneath the high-pressure Tehachapi rocks while they were still at great depths, this would imply that the Pastoria thrust also postdates the original thrust contact above the Rand Schist. Perhaps this fault is analogous to the later faults in the Rand Mountains described by Silver and Nourse [1986] and Postlethwaite and Jacobson [1987]. The rocks of the upper plate have affinities with younger, higher-^{87}Sr/^{86}Sr, more granitic plutons of the eastern Sierra Nevada, implying appreciable post-intrusion westward transport. From west of the Tehachapi Mountains, in the San Emigdio Mountains, James [1986] describes the Pastoria thrust as paralleling and structurally overlying the supposed fault contact between a possible Rand Schist-correlative sliver and high-grade rocks similar to those discussed in the present work; he also implies a later age for the Pastoria thrust as compared to the schist-gneiss fault.

Conditions favorable for delamination -- The Tehachapi Mountains appear to represent a site of major deep-crustal delamination, manifested by underthrusting beneath, and uplift of, 30 km-deep Cretaceous batholithic rocks. Geophysical evidence suggests that the range has high seismic velocities at relatively shallow depths and no apparent root [Hearn and Clayton, 1986; Malin et al., in review]. Regardless of the tectonic setting responsible for deformation and uplift of the deep-seated rocks, it is clear that at depths of ~30 km, the southern Sierra Nevada batholith was susceptible to disruption.

As pointed out above, the average composition of the intrusive rocks is approximately tonalitic with an appreciable proportion of granite; thus quartz is a significant component. Combined with the prolonged high-temperature conditions, lasting at least from ~115 Ma (earlier zircon ages) to ~87 Ma (earliest biotite K/Ar ages), this would imply a weak, ductile middle crust susceptible for an extended period of time to ductile deformation and delamination from the deeper crust.

c. Similar mid-Cretaceous deep batholithic rocks in central and southern California

Similarities between the southern Sierra Nevada and plutonic and high-grade metamorphic rocks of the Salinian block of the central California coast, and in particular between the Tehachapi Mountains and the western Santa Lucia Range (inset in Figure 2.1), have been discussed in depth [e.g., Page, 1981; Ross, 1984, 1989; Mattinson and James, 1985; Silver and Mattinson, 1986; James and Mattinson, 1988]. These include the presence of orthopyroxene-bearing or "charnockitic" granitoids, upper amphibolite to granulite metamorphic grades, mid-Cretaceous timing of intrusion and metamorphism, and some textural and mineralogical similarities. In the Santa Lucia Range, Wiebe [1970] estimated metamorphic conditions of 4-6 kbar at >650°C in the northern part, while Hansen and Stuk [1989] determined 7.5-8.5 kbar at 750-820°C further to the south. These latter conditions are similar to those determined here for the Tehachapi Mountains, although in the Santa Lucia range, true granulite-facies assemblages are more common [Compton, 1960]. The deep-seated rocks of the two areas may have followed similar uplift histories: Mattinson [1978] used U/Pb isotopic data to infer that 104 Ma plutons of the central Santa Lucia Range had remained at >500°C for ~25 m.y., followed by rapid uplift and cooling. However, some features of the Santa Lucia rocks have closer affinity to more eastern components of the southern Sierra Nevada: marble and feldspathic quartzite compositions are more abundant than in the gneiss complex of the Tehachapi Mountains,

mafic intrusive lithologies are less abundant, and initial $^{87}Sr/^{86}Sr$ and $^{143}Nd/^{144}Nd$ ratios are higher and lower, respectively (compare Mattinson [1990] with Saleeby et al. [1987] and Pickett and Saleeby [1989]; see also Chapter 3). Therefore, it is not possible to draw a direct correlation between these two areas of high-pressure batholithic rocks; it is possible, however, that they represent exposures of similar depths from differing east-west positions within the regional Cretaceous batholithic belt. (Silver and Mattinson [1986] do note resemblances in radiogenic isotopic patterns between the two areas on a larger, regional scale.) Any correlations between these two areas would require an alternative interpretation of paleomagnetic data [Champion et al., 1984] which have formed the basis for calling on major (2500 km) relative transport of the Salinian block from the south.

The San Gabriel Mountains of southern California (inset in Figure 2.1) also bear evidence for exposure of deep-seated (20-30 km) Cretaceous plutonic rocks, albeit in a quite different pre-batholithic framework [Barth 1990]. These include rocks of the Cucamonga terrane of the southeastern San Gabriel Mountains, which consists of a narrow belt of granulite-grade orthogneisses and paragneisses which contrast compositionally, isotopically, and mineralogically with the Tehachapi rocks [May and Walker, 1989; Barth and May, in review; Barth et al., in review]. However, there are similarities in metamorphic histories. Barth and May [in review] estimate peak conditions at 105 Ma of 750°C and 8 kbar, followed by a period of isobaric cooling, then rapid decompression to conditions of 600°C and 5 kbar at 85 Ma. This pressure-temperature-time sequence is strikingly similar to the Tehachapi history discussed here. In the San Gabriels, uplift of the deep rocks is interpreted to precede underthrusting of the range by Pelona Schist [May and Walker, 1989; May, 1989], but in the Tehachapis evidence for the relationship between uplift and Rand Schist underthrusting is ambiguous. Better information about timing of tectonic events in the two areas is needed in order to try to discern any possible correlation of tectonism in the two areas. Of course, such a link is

made more difficult by the fact of their wide separation (~350 km) prior to San Andreas fault offset.

d. Implications for batholith structure

<u>Character of the deeper batholith</u> -- The first-order interpretation of the data presented in this paper is that the Sierra Nevada batholith extended to great depth, with voluminous magmas crystallizing at depths of at least 30 km. In overall compositional and isotopic terms [Sams, 1986; Saleeby et al., 1987; Sams and Saleeby, 1988; Pickett and Saleeby, 1989; Chapters 3 and 4] these magmas are not markedly different from those intruded at higher levels in the batholith. The average composition is roughly tonalitic to mafic tonalitic and the various lithologies, including the hypersthene tonalites and quartz diorites, have affinities with those along the western margin of the batholith to the north [Saleeby and Sharp, 1980] where shallower conditions are inferred [Ague and Brimhall, 1988; Saleeby, 1990; Knott et al., 1990]; thus the compositional character of the Tehachapi intrusive rocks may not necessarily reflect some intrinsic feature of the deeper reaches of a batholith. While it is true that there is an appreciable amount of gabbroic and dioritic rock at small and large scales, this component has perhaps been overemphasized at the expense of tonalitic to granitic lithologies [Hamilton, 1988; Ross, 1989]. Even voluminous cumulate gabbros like those in the Tehachapi Mountains are well-represented in the western batholith at higher original levels [Saleeby and Sharp, 1980; Knott et al., 1990].

On the other hand, in order to make general statements about whether or not the compositional character of the rocks of the Tehachapi Mountains is a function of their location in the deep batholith, it is necessary to place the Tehachapi magmas in the context of the well-known west-to-east isotopic and petrologic variations in the main part of the batholith [e.g., Kistler and Peterman, 1978]. Initial $^{87}Sr/^{86}Sr$ ratios and ε_{Nd} values for the intrusive rocks of the main study area [Saleeby et al., 1987; Pickett and Saleeby,

1989; Chapter 3] range from 0.7042 to 0.7054 and +2.6 to -0.8, respectively, placing them within the isotopic range observed for west-central intrusives of the batholith (west of the 0.706 isopleth), where tonalitic compositions prevail [Bateman et al., 1984; Saleeby et al., 1986, and references therein]. In contrast, the gabbroic to tonalitic rocks of the westernmost batholith have lower $^{87}Sr/^{86}Sr$ and higher ε_{Nd} [Knott, et al., 1990] than those in the Tehachapi Mountains, implying that, despite lithologic similarities, the rocks of the two areas do not occupy equivalent lateral positions in the west-to-east batholithic pattern. The Tehachapi Mountains suites also have a smaller proportion of mafic lithologies than the westernmost batholith [Saleeby and Sharp, 1980]. The affinity in isotopic character between the Tehachapi magmatic rocks and the west-central tonalitic belt also applies to the metamorphic frameworks of the intrusive rocks: in these two areas, the metamorphic pendants consist of thick continental margin sedimentary assemblages of the Kings sequence, with unknown basement [Saleeby et al., 1978, 1987]. (In contrast, the westernmost gabbroic to tonalitic belt intrudes the Kings-Kaweah ophiolite belt with only a thin veneer of western distal Kings sequence strata.) However, chemical data from the west-central tonalitic belt [Bateman et al., 1984] show this belt, in contrast to the Tehachapi igneous suites, to be more homogeneous and somewhat less mafic. Placed, then, in a proper context within the Sierra Nevada batholith, compositions of the intrusive rocks of the Tehachapi Mountains appear to reflect a deeper batholith which is more heterogeneous and somewhat more mafic than at higher levels. In addition, metamorphic framework rocks of the deep batholith are marked by high-temperature conditions throughout, with no decrease in grade away from intrusive rocks, and with common effects of partial melting.

The Sr, Nd, O, and zircon U/Pb isotopic systematics of the Tehachapi rocks [Saleeby et al., 1987; Pickett and Saleeby, 1989; Chapter 3] indicate that the entire compositional range of magmas shows evidence for mixing of depleted mantle-derived

magmas with appreciable components of old continental, probably metasedimentary, material. Extensive migmatization of metasedimentary rocks and the predominance of more refractory metasedimentary lithologies (quartzitic and calcareous) suggests that, at this level, much of the metamorphic framework of the batholith has been consumed by melting and mixing with the batholithic magmas. The rocks of the Tehachapi Mountains thus provide evidence for major reconstitution of the continental margin crust to great depths (>30 km) during batholith construction. This further implies that the preintrusive crust of the Sierra Nevada was already at least 30 km thick due to earlier episodes of tectonic thickening.

Other views of the deep Sierra Nevada batholith -- The batholithic rocks of the Tehachapi Mountains can be compared with compositions predicted by seismic modeling for subsurface rocks in the central batholith [Saleeby et al, 1986]. About 300 km to the north of the Tehachapi Mountains, near the latitude of Fresno, seismic models of the batholith crust predict a zone down to depths of 20-25 km of rocks with a p-wave velocity of 6.1 km/s, underlain by a zone with a velocity of 6.9 km/s. Since the granitoids at the surface in this area represent original depths of 5-15 km [Ague and Brimhall, 1988], this velocity boundary corresponds to original batholithic depths of 30-40 km. Velocities for Tehachapi rocks, which would lie at these depths in the batholith prior to uplift, can be estimated by referring to experimental velocities determined by Fountain et al. [1990] at 6 kbar for deep crustal rocks. Garnet-free rocks having SiO_2 > 60% all yield velocities of around 6.5 km/s, while garnet-bearing quartzofeldspathic rocks tended toward 6.9 km/s. Hornblende-rich mafic rocks, with and without garnet, lay mostly in the 7.1-7.4 km/s range. In the Tehachapi Mountains, garnet-free tonalites to granites predominate, but garnet-bearing felsic to mafic rocks are nevertheless found in appreciable numbers. Therefore, a rough estimate of the average p-wave velocity of Tehachapi rocks would lie somewhat above 6.5 km/s, perhaps as high as ~6.7 km/s. Such velocities are equivalent

to those in the vicinity of the boundary between 6.1 and 6.9 km/s as modeled in the central batholith, and this boundary lies at batholithic depths equivalent to those now exposed in the Tehachapi Mountains. Thus, the Tehachapi rocks most likely have seismic velocity characteristics consistent with their original location 30 km deep in the Sierra Nevada batholith.

Samples of the crust and mantle beneath the central Sierra Nevada batholith are found as xenoliths in Tertiary volcanic rocks [Domenick et al., 1983; Dodge et al., 1986, 1988]. At Chinese Peak [Dodge et al., 1986], along with pyroxenite and peridotite, the xenolith suite includes gabbros and "mafic granulites," many of which show some bulk chemical similarities to gabbros and diorites of the Tehachapi Mountains [Chapter 4], as well as rocks with gneissic textures. However, a major distinction between these xenoliths and Tehachapi rocks is the paucity in the former of hornblende and garnet and tonalitic to granitic lithologies. Dodge et al. [1986] estimate equilibration of these xenoliths at less than 10 kbar, but they have clearly had a different history from the Tehachapi rocks. Xenoliths from Big Creek [Domenick et al., 1983; Dodge et al., 1988] have more in common with rocks of the Tehachapi Mountains. Included are numerous examples of plagioclase ± hornblende ± pyroxene ± garnet rocks similar in mineralogy and texture to more mafic varieties of the Tehachapi intrusive rocks. However, correlatives of the common tonalite to granite gneisses of the Tehachapis are few; granitoid xenoliths of Big Creek are described as typical of those exposed at the surface in the area, and garnet is not mentioned as a constituent. No pressure information is available for the Big Creek crustal xenoliths, making direct comparisons difficult. In summary, these Sierran xenoliths share some compositional and textural features with the deep-batholith rocks of the Tehachapi Mountains, but direct correlation is not possible. The predominance of more mafic lithologies in the xenolith suites may be due to preferential sampling of the batholith at depths even greater than those now exposed in the Tehachapi Mountains [Saleeby et al.,

1986].

Dodge and Bateman [1988] describe the batholith levels exposed in the Tehachapi Mountains as representing a "lens of metaigneous hornblende-rich rocks" lying in the lower part of the upper half of the crust, underlain by a more mafic (to ultramafic) lower crust. This scenario is consistent with the results of the present study, although it is not clear that rocks of this level throughout the batholith necessarily show the same metamorphic and deformational fabrics as the Tehachapi rocks. In the Dodge and Bateman model, this 30 km-deep level would be the deepest part of the batholith with appreciable quartz contents; this is consistent with our view, discussed above, that syn- and post-intrusion conditions in the Tehachapi Mountains were favorable for delamination of the batholith crust. Such mid-batholithic levels may typically prove to be sites of major crustal disruption.

Deep rocks of other Cordilleran batholiths -- Zen [1988] summarizes information on deep-seated, epidote-bearing calcalkaline plutons from the Idaho and Coast batholiths of the northern Cordillera. These rocks are inferred to have crystallized at pressures of 6-8 kbar with average geothermal gradients of ~25-30°C/km, conditions similar to those in the Tehachapi Mountains. Lithologies, as in the Tehachapi Mountains, are dominantly quartz diorite to tonalite to granodiorite, and metamorphic framework rocks have supracrustal protoliths; gneissic foliation is not a ubiquitous feature. Relatively rapid average uplift rates (0.2 - 0.6 mm/yr) are responsible for exposure of these rocks, but apparently synplutonic deformation as observed in the Tehachapis is not a necessary component of the structural history. Zen [1988] emphasizes the necessity of thick (50-60 km) sialic crust for production of these deep plutons. Along with the results of this study, these occurrences show that, at least down to 30 km depths, Cordilleran batholiths and their framework rocks retain the basic lithologic character of the abundantly exposed higher levels of the batholiths. Apparently, variable but special tectonic circumstances are

necessary for exposure of such rocks.

2.8. Summary and Conclusions

1)   The 115-100 Ma intrusive rocks of the Tehachapi Mountains were emplaced at depths of ~25-30 km, making them the deepest exposed members of the Cretaceous Sierra Nevada batholith. These rocks represent the culmination of a regional-scale, oblique section through the batholith in its southern half [Saleeby, 1990].

2)   Localized subsolidus metamorphism of these intrusive rocks, as well as metamorphism of framework sedimentary rocks, occurred at these same depths (i.e., ~8 kbar) at around 700°C and, in the area between Tunis and El Paso Creeks, after ~15 km of uplift at ~600°C. Garnet-forming reactions in the metaigneous rocks were caused by the action of channelized flow of generally CO_2-rich fluids. However, volatile activities attendant on metamorphism were variable, precluding any pervasive fluid influx. The crystalline rocks of the Tehachapi Mountains do not properly constitute a "granulite" terrane, as most orthopyroxene occurrences are of igneous origin.

3)   Uplift from 30 to 15 km deep followed soon after intrusion and the 8 kbar metamorphism, and was probably completed by ~87 Ma, implying a minimum uplift rate of 1.2 mm/yr. Uplift to surface conditions was completed by ~52 Ma. Initial uplift may have followed underthrusting of the Rand Schist from what is now the southeast. Predominantly low-angle ductile deformation fabrics formed in response to underthrusting and to later reactivation in the vicinity of the thrust, which, in its latest phase of activity, represents a strand of the high-angle, brittle Garlock fault system.

4)   These pressure-temperature conditions and inferred uplift history resemble those

in the high-pressure, high-temperature metamorphic and plutonic rocks of the Santa Lucia Range, Salinia. However, contrasts in other geologic and geochemical characteristics preclude direct correlation between the two areas. Granulite-grade rocks of contrasting character in the southeastern San Gabriel Mountains have the same pressure-temperature-time history as the Tehachapi gneisses, perhaps reflecting parallel processes responsible for arc disruption.

5)   As compared with higher levels of similar isotopic character, the deep Sierra Nevada batholith, as exposed in the Tehachapi Mountains, is lithologically more heterogeneous and somewhat more mafic in average composition. Cumulate rocks are common, though not predominant, and metasedimentary rocks are typically migmatitic. The intrusive rocks at this deep level show the same isotopic evidence (see Chapter 3) for hybridization between mantle and continental crustal sources that is observed throughout the batholith.

6)   At 30 km depths, the Sierra Nevada batholith is still rich in quartz. This allows for a wide temperature range under which conditions are favorable for ductile deformation and possible delamination of the young batholithic crust. Thus, the middle to deep batholith may prove to be a common site of major tectonic disruption and transport.

References

Ague, J.J., and G.H. Brimhall, Magmatic arc asymmetry and distribution of anomalous plutonic belts in the batholiths of California: Effects of assimilation, crustal thickness, and depth of crystallization, *Geol. Soc. Amer. Bull., 100*, 912-927, 1988.

Armstrong, J.T., Quantitative analysis of silicate and oxide materials: Comparison of Monte Carlo, ZAF, and $\phi(\rho z)$ procedures, in *Microbeam Analysis - 1988*, edited by D.E. Newbury, pp. 239-246, San Francisco, San Francisco Press, 1988.

Barth, A.P., Mid-crustal emplacement of Mesozoic plutons, San Gabriel Mountains, California, and implications for the geologic history of the San Gabriel terrane, *Geol. Soc. Amer. Memoir 174*, 33-45, 1990.

Barth, A.P., and D.J. May, Mineralogy and pressure-temperature-time path of Cretaceous granulite gneisses, southeastern San Gabriel Mountains, southern California, *J. Meta. Geol.*, in review.

Barth, A.P., J.L. Wooden, and D.J. May, Sr, Pb, and Nd isotopic and geochemical systematics of mid-Cretaceous granulite gneisses, San Gabriel Mountains, southern California, *Contrib. Mineral. Petrol.*, in review.

Bateman, P.C., and J.P. Eaton, Sierra Nevada batholith, *Science, 158*, 1407-1417, 1967.

Bateman, P.C., F.C.W. Dodge, and P.E. Bruggman, Major oxide analyses, CIPW norms, modes, and bulk specific gravities of plutonic rocks from the Mariposa 1 x 2

sheet, central Sierra Nevada, California, *U.S. Geol. Survey Open File Rep. 84-162*, 50 pp., 1984.

Berman, R.G., T.H. Brown, and H.J. Greenwood, An internally consistent thermodynamic data base for minerals in the system $Na_2O-K_2O-CaO-MgO-FeO-Fe_2O_3-Al_2O_3-SiO_2-TiO_2-H_2O-CO_2$, *Atomic Energy of Canada Ltd. Technical Report 377*, 62 pp., 1985.

Blundy, J.D., and T.J.B. Holland, Calcic amphibole equilibria and a new amphibole-plagioclase geothermometer, *Contrib. Mineral. Petrol., 104*, 208-224, 1990.

Bradshaw, J.Y., Early Cretaceous vein-related garnet granulite in Fiordland, southwest New Zealand: a case for infiltration of mantle-derived CO_2-rich fluids, *J. Geol., 97*, 697-717, 1989.

Champion, D.E., D.G. Howell, and C.S. Gromme, Paleomagnetic and geologic data indicating 2500 km of northward displacement for the Salinian and related terranes, California, *J. Geophys. Res., 89*, 7736-7752, 1984.

Chipera, S.J., and D. Perkins, Evaluation of biotite-garnet geothermometers: application to the English River subprovince, Ontario, *Contrib. Mineral. Petrol., 98*, 40-48, 1988.

Clark, S.P., Handbook of physical constants, *Geol. Soc. Amer. Mem. 97*, 1966.

Compton, R.R., Charnockitic rocks of Santa Lucia Range, California, *Amer. J. Sci., 258*, 609-636, 1960.

Crowell, J.C., The San Andreas fault zone from the Temblor Mountains to Antelope Valley, southern California, *American Association of Petroleum Geologists and Society of Economic Paleontologists and Mineralogists, Pacific Sections Guidebook*, pp. 7-39, 1964.

Dodge, F.C.W., and P.C. Bateman, Nature and origin of the root of the Sierra Nevada, *Amer. J. Sci.*, *288-A*, 341-357, 1988.

Dodge, F.C.W., L.C. Calk, and R.W. Kistler, Lower crustal xenoliths, Chinese Peak lava flow, central Sierra Nevada, *J. Petrol.*, *27*, 1277-1304, 1986.

Dodge, F.C.W., J.P. Lockwood, and L.C. Calk, Fragments of the mantle and crust from beneath the Sierra Nevada batholith: xenoliths in a volcanic pipe near Big Creek, California, *Geol. Soc. Amer. Bull.*, *100*, 938-947, 1988.

Domenick, M.A., R.W. Kistler, F.C.W. Dodge, and M. Tatsumoto, Nd and Sr isotopic study of crustal and mantle inclusions from the Sierra Nevada and implications for batholith petrogenesis, *Geol. Soc. Amer. Bull.*, *94*, 713-719, 1983.

Edwards, R.L., and Essene, E.J., Pressure, temperature, and C-O-H fluid fugacities across the amphibolite-granulite transition, northwest Adirondack Mountains, New York, *J. Petrol.*, *29*, 39-72, 1988.

Ferry, J.M., and F.S. Spear, Experimental calibration of the partitioning of Fe and Mg between biotite and garnet, *Contrib. Mineral. Petrol.*, *66*, 113-117, 1978.

Fountain, D.M., M.H. Salisbury, and J. Percival, Seismic structure of the continental crust based on rock velocity measurements from the Kapuskasing uplift, *J. Geophys. Res., 95*, 1167-1186, 1990.

Fuhrman, M.L., and D.H. Lindsley, Ternary-feldspar modeling and thermometry, *Amer. Mineral., 73*, 201-215, 1988.

Ghent, E.D., Tremolite and H_2O activity attending metamorphism of hornblende-plagioclase-garnet assemblages, *Contrib. Mineral. Petrol., 98*, 163-168, 1988.

Ghent, E.D., and M.Z. Stout, Geobarometry and geothermometry of plagioclase-biotite-garnet-muscovite assemblages, *Contrib. Mineral. Petrol., 76*, 92-97, 1981.

Goldsmith, J.R., and R.C. Newton, Scapolite-plagioclase stability relations at high pressures and temperatures in the system $NaAlSi_3O_8$-$CaAl_2Si_2O_8$-$CaCO_3$-$CaSO_4$, *Amer. Mineral., 62*, 1063-1081, 1977.

Goodman, E.D., P.E. Malin, E.L. Ambos, and J.C. Crowell, The southern San Joaquin Valley as an example of Cenozoic basin evolution in California, in *The Origin and Evolution of Sedimentary Basins and their Energy and Mineral Resources, Geophysical Monograph 48, IUGG Vol. 3*, edited by R.A. Price, pp. 87-107, Amer. Geophys. Union, 1989.

Graham, C.M., and R. Powell, A garnet-hornblende geothermometer: Calibration, testing, and application to the Pelona Schist, southern California, *J. Meta. Geol., 2*, 13-31, 1984.

Hamilton, W., Tectonic setting and variations with depth of some Cretaceous and Cenozoic structural and magmatic systems of the western United States, in *Metamorphism and Crustal Evolution of the Western United States (Rubey Vol. VII)*, edited by W.G. Ernst, pp. 1-40, Englewood Cliffs, N.J., Prentice-Hall, 1988.

Hamilton, W., and W.B. Myers, The nature of batholiths, *U.S. Geol. Surv. Prof. Paper 554-C*, 30 pp., 1967.

Hammarstrom, J.M., and E. Zen, Aluminum in hornblende: an empirical igneous geobarometer, *Amer. Mineral., 71*, 1297-1313, 1986.

Hansen, E.C., and M.A. Stuk, Devolatilization reactions in the amphibolite to granulite facies transitional terrane around Cone Peak, Santa Lucia Range, California (abstract), *Geol. Soc. Amer. Abstract Progr., 21*, A277, 1989.

Haxel, G., and J. Dillon, The Pelona-Orocopia Schist and Vincent-Chocolate Mountain thrust system, southern California, in *Mesozoic Paleogeography of the Western United States: Pacific Coast Paleogeography Symposium 2*, edited by D.G. Howell and K.A. McDougall, Los Angeles, Society of Economic Paleontologists and Mineralogists, Pacific Section, pp. 453-469, 1978.

Hearn, T.M., and R.W. Clayton, Lateral velocity variations in southern California, Part I: results from the upper crust from Pg waves, *Bull. Seismol. Soc. Amer., 76*, 495-509, 1986.

Hodges, K.V., and F.S. Spear, Geothermometry, geobarometry and the Al_2SiO_5 triple point at Mt. Moosilauke, New Hampshire, *Amer. Mineral., 67*, 1118-1134, 1982.

Hoisch, T.D., Empirical calibration of six geobarometers for the mineral assemblage quartz + muscovite + biotite + plagioclase + garnet, *Contrib. Mineral. Petrol., 104*, 225-234, 1990.

Hollister, L.S., G.C. Grissom, E.K. Peters, H.H. Stowell, and V.B. Sisson, Confirmation of the empirical correlation of Al in hornblende with pressure of solidification of calc-alkaline plutons, *Amer. Mineral., 72*, 231-239, 1987.

Indares, A., and J. Martignole, Biotite-garnet geothermometry in the granulite facies: the influence of Ti and Al in biotite, *Amer. Mineral., 70*, 272-278, 1985.

Jacobson, C.E., M.R. Dawson, and C.E. Postlethwaite, Structure, metamorphism, and tectonic significance of the Pelona, Orocopia, and Rand Schists, southern California, in *Metamorphism and Crustal Evolution of the Western United States (Rubey Vol. VII)*, edited by W.G. Ernst, pp. 976-997, Englewood Cliffs, N.J., Prentice-Hall, 1988.

James, E.W., U/Pb age of the Antimony Peak tonalite and its relation to the Rand Schist in the San Emigdio Mountains, California (abstract), *Geol. Soc. Am. Abstract Progr., 18*, 121, 1986.

James, E.W., and J.M. Mattinson, Metamorphic history of the Salinian block: an isotopic reconnaissance, in *Metamorphism and Crustal Evolution of the Western United*

States (Rubey Vol. VII), edited by W.G. Ernst, pp. 938-952, Englewood Cliffs, N.J., Prentice-Hall, 1988.

Johnson, M.C., and M.J. Rutherford, Experimental calibration of the aluminum-in-hornblende geobarometer with application to the Long Valley caldera (California) volcanic rocks, *Geology, 17*, 837-841, 1989.

Kanter, L.R., and M.O. McWilliams, Rotation of the southernmost Sierra Nevada, California, *J. Geophys. Res., 87*, 3819-3830, 1982.

Kerrick, D.M., and G.K. Jacobs, A modified Redlich-Kwong equation for H_2O, CO_2, and H_2O-CO_2 mixtures at elevated pressures and temperatures, *Amer. J. Sci., 281*, 735-767, 1981.

Kistler, R.W., and Z.E. Peterman, Reconstruction of crustal blocks of California on the basis of initial strontium isotopic compositions of Mesozoic granitic rocks, *U.S. Geol. Survey Prof. Paper 1071*, 17 pp., 1978.

Knott, D.C., J.B. Saleeby, H.P. Taylor, Jr., and B.W. Chappell, Petrology of the Early Cretaceous Sierra Nevada batholith: the Stokes Mountain region, CA, *Eos Trans. Amer. Geoph. Union, 71*, 1576, 1990.

Kohn, M.J., and F.S. Spear, Two new geobarometers for garnet amphibolites, with applications to southeastern Vermont, *Amer. Mineral., 75*, 89-96, 1990.

Leake, B.E., Nomenclature of amphiboles, *Amer. Mineral., 63*, 1023-1052, 1978.

Malin, P.E., E.D. Goodman, Y.-G. Li, T.L. Henyey, and D.A. Okaya, Crustal-scale tilt-block tectonics beneath the Tejon embayment and Tehachapi Mts., California, in review, *J. Geophys. Res.*

Mattinson, J.M., Age, origin, and thermal histories of some plutonic rocks from the Salinian block of California, *Contrib. Mineral. Petrol., 67*, 233-245, 1978.

Mattinson, J.M., Petrogenesis and evolution of the Salinian magmatic arc, *Geol. Soc. Amer. Memoir 174*, pp. 237-250, 1990.

Mattinson, J.M., and E.W. James, Salinian block U/Pb age and isotopic variations: implications for origin and emplacement of the Salinian terrane, in *Tectonostratigraphic Terranes of the Circum-Pacific Region*, edited by D.G. Howell, pp. 215-226, Houston, Circum-Pacific Council for Energy and Mineral Resources, 1985.

May, D.J., Late Cretaceous intra-arc thrusting in southern California, *Tectonics, 8,* 1159-1173, 1989.

May, D.J., and N.W. Walker, Late Cretaceous juxtaposition of metamorphic terranes in the southeastern San Gabriel Mountains, California, *Geol. Soc. Amer. Bull., 101*, 1246-1267, 1989.

McWilliams, M.O., and Y. Li, Tectonic oroclinal bending of the southern Sierra Nevada batholith, *Science, 230*, 172-175, 1985.

Moecher, D.P., and E.J. Essene, Scapolite as a potential sensor of fluid composition in calc-silicates and granulites (abstract), *Geol. Soc. Amer. Abstract Progr., 17*, 666, 1985.

Newton, R.C., Metamorphic fluids in the deep crust, *Ann. Rev. Earth Planet. Sci., 17*, 385-412, 1989.

Newton, R.C., T.V. Charlu, and O.J. Kleppa, Thermochemistry of the high structural state plagioclases, *Geochim. Cosmochim. Acta, 44*, 933-941, 1980.

Nilsen, T.H., Stratigraphy and sedimentology of the Eocene Tejon Formation, western Tehachapi Mountains and San Emigdio Mountains, California, *U.S. Geol. Surv. Prof. Paper 1268*, 110 pp., 1987.

Nourse, J.A., and L.T. Silver, Structural and kinematic evolution of sheared rocks in the Rand "thrust" complex, northwest Mojave Desert, California, *Geol. Soc. Amer. Abstract Progr., 18*, 165, 1986.

Oterdoom, W.H., and W.D. Gunter, Activity models for plagioclase and CO_3-scapolites: an analysis of field and laboratory data, *Amer. J. Sci., 283-A*, 255-282, 1983.

Page, B.M., The southern Coast Ranges, in *The Geotectonic Development of California (Rubey Vol. I)*, edited by W.G. Ernst, pp. 329-417, Englewood Cliffs, N.J., Prentice-Hall, 1981.

Pakiser, L.C., and J.N. Brune, Seismic models of the root of the Sierra Nevada, *Science*, *210*, 1088-1094, 1980.

Perchuk, L.L., and I.V. Lavrent'eva, Experimental investigation of exchange equilibria in the system cordierite-garnet-biotite, in *Kinetics and Equilibrium in Mineral Reactions*, edited by S.K. Saxena, pp. 199-239, New York, Springer-Verlag, 1983.

Perkins, E.H., T.H. Brown, and R.G. Berman, PTX-SYSTEM: three programs for calculation of pressure-temperature-composition phase diagrams, *Comput. Geosci., 12*, 749-755, 1986.

Pickett, D.A., and J.B. Saleeby, Petrogenetic and isotopic studies of mid-crustal batholithic rocks of the Tehachapi Mountains, Sierra Nevada, California (abstract), *Geol. Soc. Amer. Abstract Progr., 21*, A197, 1989.

Pickett, D.A., and J.B. Saleeby, P-T-X conditions in the Tehachapi Mountains, Sierra Nevada, California -- Metamorphism and tectonic disruption in the deep Cretaceous batholith (abstract), *Geol. Soc. Amer. Abstract Progr., 22*, A30, 1990.

Plescia, J.B., and G.J. Calderone, Paleomagnetic constraints on the timing of rotation of the Tehachapi Mountains, California (abstract), *Geol. Soc. Amer. Abstract Progr., 18*, 171, 1986.

Postlethwaite, C.E., and C.E. Jacobson, Early history and reactivation of the Rand thrust, southern California, *J. Struct. Geol., 9*, 195-205, 1987.

Robie, R.A., B.S. Hemingway, and J.R. Fisher, Thermodynamic properties of minerals and related substances at 298.15 K and 1 bar (10^5 Pascals) pressure and at higher temperatures, *Bull. U.S. Geol. Surv.*, *1452*, 1979.

Ross, D.C., Possible correlations of basement rocks across the San Andreas, San Gregorio-Hosgri, and Rinconada-Reliz-King City faults, California, *U.S. Geol. Survey Prof. Paper 1317*, 37 pp., 1984.

Ross, D.C., Mafic gneissic complex (batholithic root?) in the southernmost Sierra Nevada, California, *Geology, 13*, 288-291, 1985.

Ross, D.C., The metamorphic and plutonic rocks of the southernmost Sierra Nevada, California, and their tectonic framework, *U.S. Geol. Survey Prof. Paper 1381*, 159 pp., 1989.

Saleeby, J.B., Progress in tectonic and petrogenetic studies in an exposed cross-section of young (~100 Ma) continental crust, southern Sierra Nevada, California, in *Exposed Cross Sections of the Continental Crust*, edited by M.H. Salisbury, pp. 137-158, Dordrecht, Holland, D. Reidel Publ. Co., 1990.

Saleeby, J.B., and W.D. Sharp, Chronology of the structural and petrologic development of the southwest Sierra Nevada foothills, California, *Geol. Soc. Amer. Bull.*, *91*, pt. I, 317-320, pt. II, 1416-1535, 1980.

Saleeby, J.B., S.E. Goodin, W.D. Sharp, and C.J. Busby, Early Mesozoic paleotectonic-paleogeographic reconstruction of the southern Sierra Nevada region, in *Mesozoic*

paleogeography of the western United States: Pacific Coast Paleogeography Symposium 2, edited by D.G. Howell and K.A. McDougall, pp. 311-336, Los Angeles, Society of Economic Paleontologists and Mineralogists, Pacific Section, 1978.

Saleeby, J.B., and others, Continent-ocean transect: corridor C2 central California offshore to the Colorado Plateau, *Geol. Soc. Amer. Centennial Continent-Ocean Transect #10*, 1986.

Saleeby, J.B., D.B. Sams, and R.W. Kistler, Geochronology and geochemistry of crystalline rocks of the southernmost Sierra Nevada, California, *J. Geophys. Res., 92*, 10443-10466, 1987.

Sams, D.B., U/Pb zircon geochronology, petrology, and structural geology of the crystalline rocks of the southernmost Sierra Nevada and Tehachapi Mountains, Kern County, California, Ph.D. thesis, 315 pp., California Institute of Technology, Pasadena, California, 1986.

Sams, D.B., and J.B. Saleeby, Geology and petrotectonic significance of crystalline rocks of the southernmost Sierra Nevada, California, in *Metamorphism and Crustal Evolution of the Western United States (Rubey Vol. VII)*, edited by W.G. Ernst, pp. 865-893, Englewood Cliffs, N.J., Prentice-Hall, 1988.

Schürmann, H.M.E., Granatführender Diorit aus der Sierra Nevada, Kalifornien [Garnet-bearing diorite from the Sierra Nevada, California], *Neues Jahrbuch für Mineralogie, Geologie und Paläontologie, 74*, pt. A, 225-250, 1938.

Selverstone, J., and C.P. Chamberlain, Apparent isobaric cooling paths from granulites: Two counterexamples from British Columbia and New Hampshire, *Geology, 18,* 307-310, 1990.

Sharry, J., The geology of the western Tehachapi Mountains, California, Ph.D. thesis, 215 pp., Massachusetts Institute of Technology, Cambridge, Massachusetts, 1981.

Silver, L.T., Paleogene overthrusting in the tectonic evolution of the Transverse Ranges, Mojave and Salinian regions, California (abstract), *Geol. Soc. Amer. Abstract Progr.,* 15, 438, 1983.

Silver, L.T., Evidence for Paleogene low-angle detachment of the southern Sierra Nevada (abstract), *Geol. Soc. Amer. Abstract Progr., 18,* 750, 1986.

Silver,L.T., and J.M. Mattinson, "Orphan Salinia" has a home, *Eos Trans. Amer. Geoph. Union, 67,* 1215, 1986.

Silver, L.T., and J.A. Nourse, The Rand Mountains "thrust" complex in comparison with the Vincent thrust-Pelona Schist relationship, southern California (abstract), *Geol. Soc. Amer. Abstract Progr., 18,* 185, 1986.

Spear, F.S., and K.L. Kimball, RECAMP - A FORTRAN IV program for estimating Fe^{3+} contents in amphiboles, *Comput. Geosci., 10,* 317-325, 1984.

Vielzeuf, D., and Holloway, J.R., Experimental determination of the fluid-absent melting relations in the pelitic system: consequences for crustal differentiation, *Contrib. Mineral. Petrol., 98*, 257-276, 1988.

Warren, R.G., B.J. Hensen, and R.J. Ryburn, Wollastonite and scapolite in Precambrian calc-silicate granulites from Australia and Antarctica, *J. Meta. Geol., 5*, 213-223, 1987.

Waters, D.J., Partial melting and the formation of granulite facies assemblages in Namaqualand, South Africa, *J. Meta. Geol., 6*, 387-404, 1988.

Wiebe, R.A., Relations of granitic and gabbroic rocks, northern Santa Lucia Range, California, *Geol. Soc. Amer. Bull., 81*, 105-116, 1970.

Zen, E., Tectonic significance of high-pressure plutonic rocks in the western Cordillera of North America, in *Metamorphism and Crustal Evolution of the Western United States (Rubey Vol. VII)*, edited by W.G. Ernst, p. 41-67, Englewood Cliffs, N.J., Prentice-Hall, 1988.

Zen, E., Plumbing the depths of batholiths, *Amer. J. Sci., 289*, 1137-1157, 1989.

CHAPTER 3

Nd, Sr, and Pb isotopic characteristics of Cretaceous intrusive rocks of deep levels of the Sierra Nevada batholith, Tehachapi Mountains, California

3.1. Introduction

Geologic interest in the Phanerozoic continental margin batholithic belts of the world centers largely on their importance to the study of the evolution and growth of the continental crust. Many workers are interested in the extent to which the generation and intrusion of the typically intermediate composition magmas of these belts reflect addition of new material to the crust versus recycling of pre-existing crust, and isotopic ratios are a useful tool for such estimations [Hurley et al., 1965; Allègre and Ben Othman, 1980; Hamilton et al., 1980]. In the Mesozoic Sierra Nevada batholith of California, isotopic and petrologic studies [Kistler and Peterman, 1973, 1978; Masi et al., 1981; DePaolo, 1981a; Ague and Brimhall, 1988; Chen and Tilton, 1991] have demonstrated with some confidence the action of at least two generalized end-member components in the generation of batholithic magmas -- depleted mantle-derived and continental crustal material. Kistler [1990] and Chen and Tilton [1991] argue that the nature of the continental end-member changes across the batholith -- from continent-derived metasedimentary rocks in the west to Proterozoic crystalline basement in the east. Differences of opinion persist, however, regarding whether the mixing of source end-members occurs largely within and throughout the batholith crust [e.g., DePaolo, 1981a] or in deep-crustal or mantle source regions [e.g., Kistler, 1990]. It would seem useful,

then, to be able to probe more deeply into the Sierra Nevada batholithic crust to search for evidence of such mixing processes. This paper reports the results of an isotopic study of the deepest exposed rocks of the batholith, those of the Tehachapi Mountains.

The Tehachapi Mountains lie at the southern end of the Sierra Nevada range in central California (Figures 3.1 and 3.2). South and west of the Cretaceous tonalite of Bear Valley Springs, the crystalline basement of the range is composed of gneisses representing Cretaceous calcalkaline intrusive rocks and their metamorphic country rocks [Sharry, 1981; Ross, 1985, 1989; Sams, 1986; Saleeby et al., 1987; Sams and Saleeby, 1988]. Pickett and Saleeby [1991] quantitatively demonstrated that these rocks represent batholithic magmas that were intruded at depths of ~30 km, making them the deepest exposed components of the Sierra Nevada batholith. This is in line with the scenario of Saleeby [1990] describing the southern half of the Sierra Nevada as an oblique section through the batholith crust, and also with the same such suggestion from the regional scale barometric data of Ague and Brimhall [1988]. The crystalline rocks of the Tehachapi Mountains therefore represent the culmination of this southward deepening; in fact, Ross [1985] has referred to the Tehachapi basement as a "batholithic root." Clearly, the Tehachapi rocks afford us a unique opportunity to observe the products of magmatism at deeper levels of the batholith. Here we discuss the Nd and Sr (and, to a lesser extent, Pb) isotopic characteristics of the rocks and discuss their significance in the context of the Sierra Nevada batholith as a whole. Preliminary results of this study have appeared in abstract form [Pickett and Saleeby, 1989].

3.2. Geologic Setting and Sampling

The Tehachapi Mountains are underlain by variably foliated gabbroic to granitic rocks which have intruded chiefly psammitic and calcareous metasedimentary assemblages (Figure 3.2). Sams and Saleeby [1988] and Pickett and Saleeby [1991]

Figure 3.1 - Basement geologic map of the southern Sierra Nevada with sample localities in the northern study area. Modified after Ross [1989], Sams [1986], and Sharry [1981]. Sample localities are from Sams [1986].
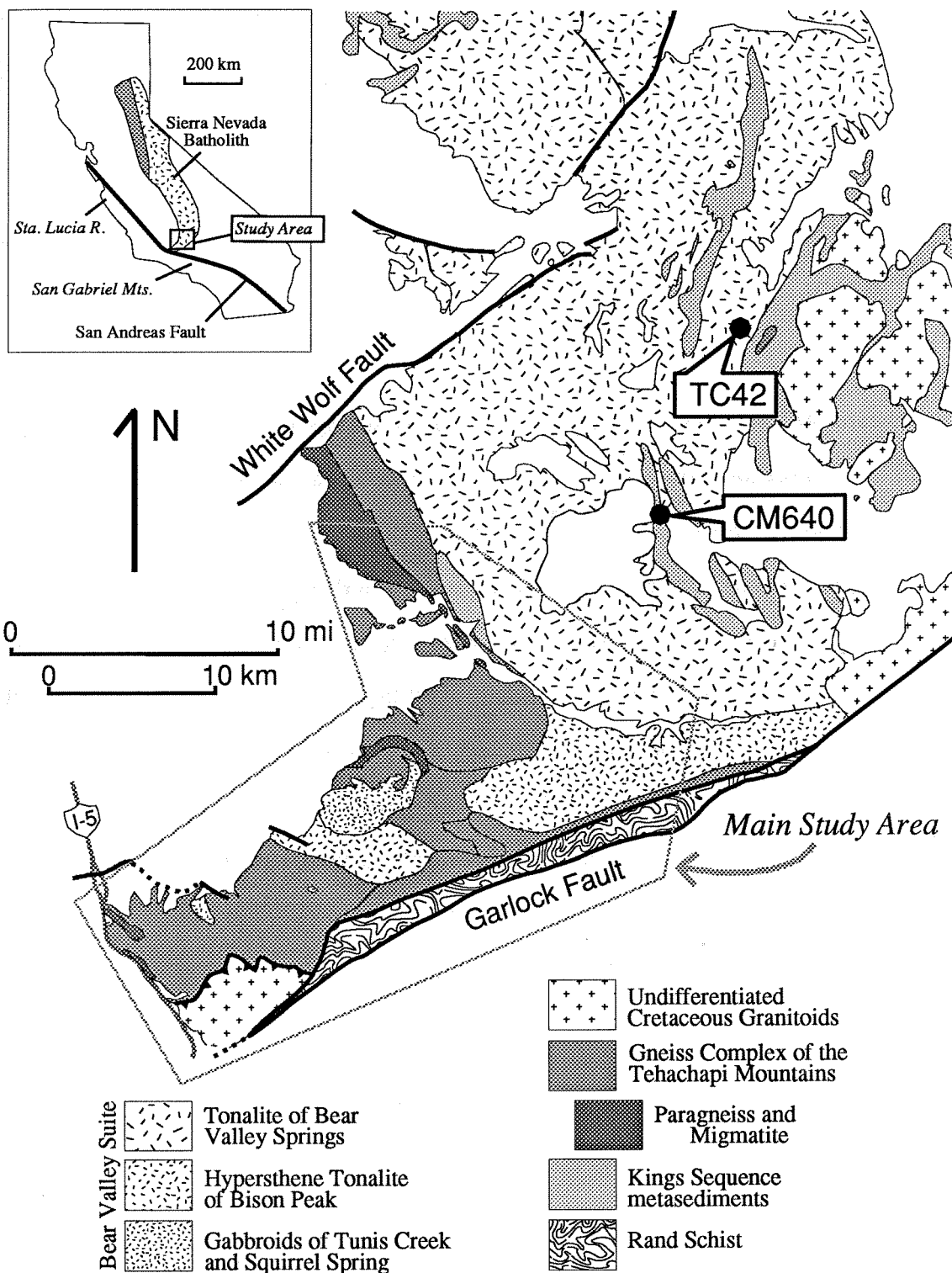
Fig. 3.1

Figure 3.2 - Basement geologic map of the main study area, Tehachapi Mountains, with sample localities. Modified after Sharry [1981] and Sams [1986], supplemented by new mapping. Sample localities for CM9 and PC175 from Sams [1986]. In the text, sample CM9 is not included in the "main study area." Units of the gneiss complex of the Tehachapi Mountains: T = tonalite gneiss of Tejon Creek, P = quartzofeldspathic gneiss of Pastoria Creek, W = diorite gneiss of White Oak, CP = paragneiss of Comanche Point, GP = migmatite of Grapevine Peak, GC = paragneiss of Grapevine Canyon. G = garnet-biotite tonalite of Grapevine (of the intrusive suite of Bear Valley). Smaller, sub-map-scale paragneiss bodies are not shown. For clarity, map patterns are omitted for the granitic rocks south of the Pastoria thrust (Figure 3.1).

Fig. 3.2

discuss the structural and tectonic setting of the Cretaceous rocks, and Goodman and Malin [1991] describe the Cenozoic tectonic history. To summarize: the rocks are variably foliated syntectonic intrusive rocks which, following intrusion, underwent localized subsolidus recrystallization and deformation at ~25-30 km depths, and were then uplifted to ~15 km while still fairly hot (probably by ~85 Ma). The rocks were uplifted, eroded, and exposed at the surface by mid-Eocene time (~50 Ma). A complex Cenozoic tectonic sequence, involving faulting,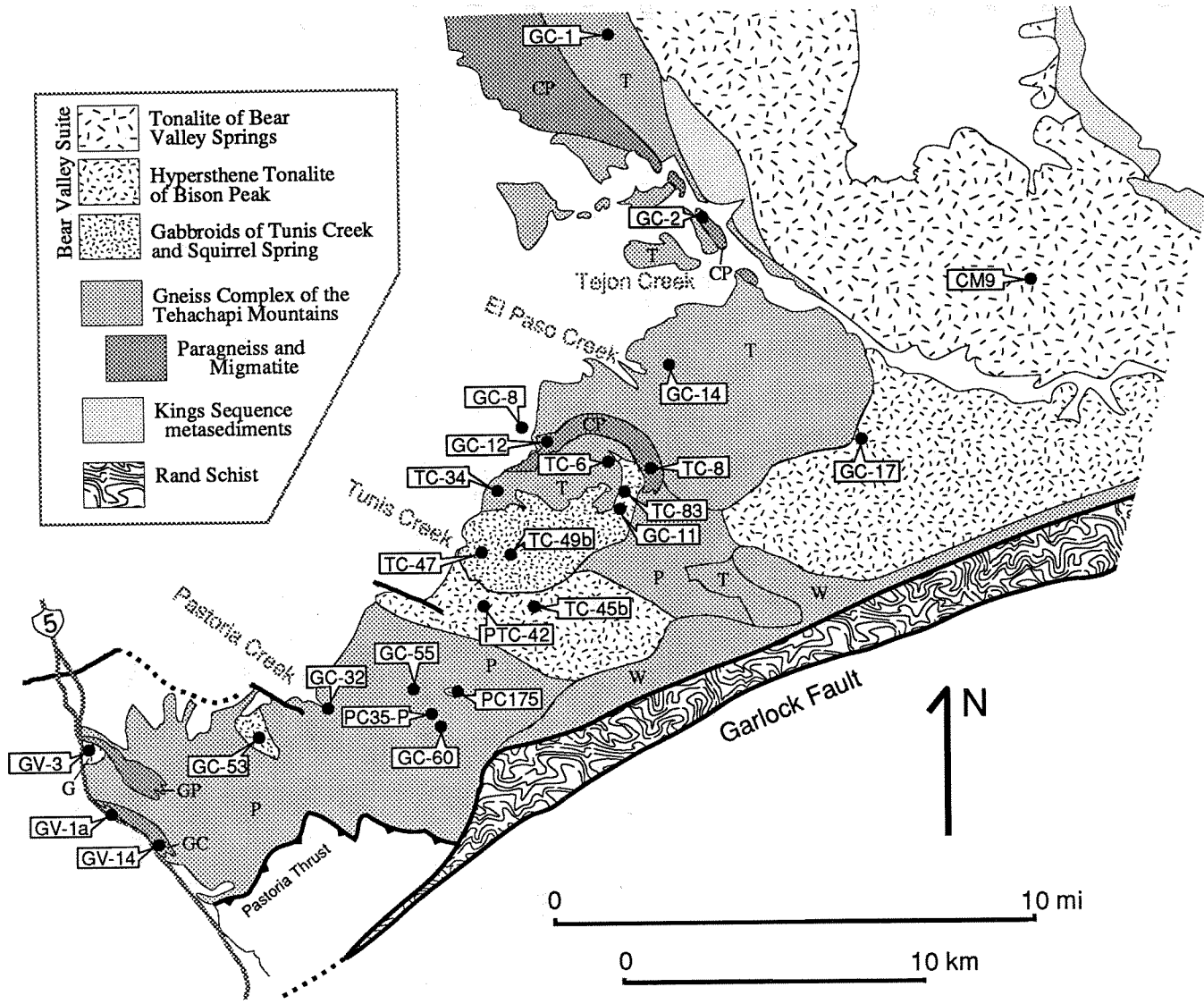 folding of overlying strata, volcanism, and rotation, is responsible for the present exposure of the Cretaceous rocks at the surface in the "tail" of the Sierra Nevada (Figure 3.1). The crystalline rocks of the Tehachapi range, as considered in this study, are bounded on the southeast by the Pastoria thrust and the north branch of the Garlock fault.

The Tehachapi crystalline rocks are weakly to strongly gneissic, showing effects of both high- and low-temperature deformation. They were divided by Saleeby et al. [1987] (with additions by Pickett and Saleeby [1991]) into two suites: the gneiss complex of the Tehachapi Mountains (herein also termed the "Tehachapi suite") and the intrusive suite of Bear Valley (or the "Bear Valley suite") (Figures 3.1 and 3.2). The lithologically diverse Tehachapi suite contains three orthogneiss units -- the ~115 Ma Tejon Creek tonalite gneiss, the ~115 Ma Pastoria Creek quartzofeldspathic gneiss, and the White Oak diorite gneiss -- as well as three paragneiss units -- the Comanche Point paragneiss, the Grapevine Canyon paragneiss, and the Grapevine Peak migmatite. The orthogneisses of the Tehachapi suite consist mainly of biotite and/or hornblende tonalites grading to biotite granites, with small-scale lithologic heterogeneities, including common dioritic layers. The igneous rocks of the generally less-deformed intrusive suite of Bear Valley (~100 Ma) are assigned to four units. The biotite- and/or hornblende-bearing tonalite of Bear Valley Springs constitutes a major batholith-scale pluton (Figure 3.1) which extends from the northern part of the main study area more than 60 km to the vicinity of Lake Isabella. It

grades on the south into the Bison Peak hypersthene tonalite; the northwestern portion of the Bear Valley Springs unit is termed the Mt. Adelaide phase (not distinguished on Figures 3.1 and 3.2). Also included in the Bear Valley suite are the gabbroids of Tunis Creek (norite to hornblende gabbro, commonly recrystallized) and the garnet-biotite tonalite of Grapevine.

The metasedimentary framework rocks consist of high-grade equivalents of quartz-rich clastic and calcareous, continental margin-type sedimentary assemblages with subordinate metavolcanic rocks. To the north (Figure 3.1) these are termed Kings Sequence, after Saleeby et al. [1978], and are correlated with similar metasedimentary pendants exposed throughout the southern Sierra Nevada. The higher-grade, more gneissic and migmatitic metasedimentary rocks of the main part of the study area (the Comanche Point and Grapevine Canyon paragneisses) are compositionally similar. These and similar rocks occur at many scales and are always structurally concordant with the intrusive rocks. The migmatite of Grapevine Peak is a major, mappable belt of migmatitic paragneiss showing apparent effects of both partial melting and magma injection.

Sampling for Nd and Sr isotopic analysis (Figures 3.1 and 3.2; Table 3.1) was motivated by the desire to represent the lithologic diversity of the igneous rocks of the two suites while allowing good areal coverage. Work was concentrated in areas south of the Bear Valley Springs tonalite batholith (Figure 3.1). Exposure is generally poor and surface weathering extensive, so many samples were collected from roadcut and canyon traverses. We also tried to avoid samples with extensive subsolidus deformation and alteration phases such as chlorite; this was most difficult to avoid in sampling granitic lithologies. Rejection of highly sheared rocks explains the paucity of samples from near the north branch of the Garlock fault [Pickett and Saleeby, 1991]. While both suites are dominated by tonalites, our desire for diversity has resulted in a collection which is not statistically representative of the proportions of each rock type. In addition, we collected a

disproportionate number of samples of the gabbroids of Tunis Creek, given our interest in the possible interaction between mafic magmas and their country rocks. The isotopic character of the framework metamorphic rocks is represented by five samples. Four of the samples were obtained from the Caltech collection from the Ph.D. work of Sams [1986]; these include CM640, CM9, TC42, and PC175. Published U-Pb zircon age data for these and other rocks from the area are reported in Sams [1986] and Saleeby et al. [1987]. In addition to our whole-rock initial isotopic ratio data, we report here new zircon U-Pb ages on two samples (Table 3.1) from Grapevine Canyon at the western edge of the study area, where previous age data were sparse. Four samples of intrusive rocks from the central study area were chosen for whole-rock common Pb isotopic analysis.

Sr and O isotope data for a number of rocks in the study area have been reported by Saleeby et al. [1987] and Kistler and Ross [1989]. Included in the Saleeby et al. [1987] report were data on three of the same samples used in the present study (CM640, CM9, and TC-42); in addition, new samples were collected from their localities for samples PC35 (our PC35-P), CM630 (GC-1), and WR643 (GC-14).

3.3. Analytical Procedures

The Rb-Sr and Sm-Nd data presented here are the first reported from this laboratory. Four samples (GC-1, GC-8, GC-11, GC-12) were analyzed in the laboratories of Professor G.J. Wasserburg using procedures summarized in Pickett and Wasserburg [1989]. The procedures for the other samples are as follows, with more detailed descriptions outlined in Appendix 2. Whole-rock samples (typically 2-3 kg) were broken by hammer into pieces a few cm across, splits of which were crushed into sand-sized fragments in a tabletop jaw crusher. About 100 g of this material was ground into fine powder in a WC shatterbox which was carefully cleaned between samples. 150-300 mg of this powder was spiked with ^{87}Rb, ^{84}Sr, and mixed ^{147}Sm-^{150}Nd tracer solutions prior to

Table 3.1 - Samples

	unit[1]	age[2]	lithology[3]	texture[4]
Intrusive suite of Bear Valley				
CM9[5]	BVS	100	bt-hb tonalite	protomylonitic
GC-8	TC	102	hb gabbro	massive
GC-11	TC	102	hy-hb gabbro	massive
GC-17	BP	102	hy-bt-hb tonalite	massive
GC-53	SS	102	hb gabbro	syn-magmatic
GV-1a[6]	(SS)	105	gt-hb metadiorite	granoblastic
GV-3[6]	G	101	gt-bt tonalite	syn-magmatic
PC175[5]	(TC)	102	troctolite	corona
PTC-42	BP	102	ep-hb-bt tonalite	protomylonitic
TC42[5]	BVS	98	bt-hb tonalite	protomylonitic
TC-45b	BP	102	hy-bt-hb qtz. diorite	syn-magmatic
TC-47	TC	102	cumm norite	massive
TC-49b	TC	102	hb gabbro	layered
TC-83	TC	102	gt-hb metagabbro	granoblastic
Gneiss complex of the Tehachapi Mountains				
GC-1	TJ	115	bt-hb tonalite	protomylonitic
GC-14	TJ	117	ep-bt leucotonalite	protomylonitic
GC-32	PC	113	ep-bt granodiorite	protomylonitic gneiss
GC-55	PC	117	bt-hb tonalite	orthomylonitic gneiss
GC-60	PC?	112	bt-hb diorite	gneiss or syn-magmatic?
PC35-P	PC	110	gt-bt granite	protomylonitic
TC-6	TJ	115	bt granite	massive
TC-34	TJ	115	bt tonalite	gneiss or syn-magmatic?
Metamorphic framework rocks				
CM640[5]	KS		bt-gr-ep qzfsp	gneiss
GC-2	CP		gt-mu-bt qzfsp	gneiss
GC-12	CP		gr-bt qzfsp	gneiss
GV-14	GC		gr-gt-mu-bt-pl-qz	gneiss
TC-8	CP		gr-gt-bt qzfsp	gneiss

[1] BVS = tonalite of Bear Valley Springs; TC = gabbroids of Tunis Creek; BP = hypersthene tonalite of Bison Peak; SS = gabbroids of Squirrel Spring; G = garnet-biotite tonalite of Grapevine; TJ = tonalite gneiss of Tejon Creek; PC = quartzofeldspathic gneiss of Pastoria Creek; KS = Kings Sequence; CP = paragneiss of Comanche Point; GC = paragneiss of Grapevine Canyon. Parentheses = tentative assignment. ? = may be TC or SS (see text).

[2] Ma. Assigned by correlation with dated samples except CM9 and TC42, which are from the original geochronological field samples [Saleeby et al., 1987].

[3] bt = biotite, hb = hornblende, hy = hypersthene, gt = garnet, ep = epidote, cumm = cummingtonite with thin hb rims, gr = graphite, mu = muscovite, pl = plagioclase, qz = quartz, qzfsp = quartz + two feldspars.

[4] "Protomylonitic gneiss" refers to a rock showing incipient mylonitic shear with textural evidence of a pre-existing gneissic fabric. "Gneiss" or "syn-magmatic" refers to metamorphic or igneous foliation, respectively, with an absence of finely recrystallized shear fabric. The distinction is often equivocal.

[5] From the thesis collection of D.B. Sams.

[6] New zircon and whole-rock isotope locality.

dissolution. The spikes (obtained from the laboratory of G.J. Wasserburg, Caltech) were calibrated against NIST SRM materials for Rb and Sr, and against a mixed Sm-Nd standard described in Wasserburg et al. [1981]. Dissolution procedures were of two types; the second technique eventually proved more dependable, although most samples were treated by the first. In 7-ml screw-top Teflon vials, HF (1-2 ml per 100 mg sample) and a small amount of HNO_3 were added after near-total evaporation of the tracer solutions. The vials were placed on a hot plate with the lid tightly closed for 2-4 days. This was followed by a similar treatment in concentrated HNO_3, sometimes followed by concentrated HCl. The sample was taken up in 1.5 N HCl and centrifuged to check for undissolved residue; such residue was then attacked in the same way. The other technique was analogous, but involved HF and $HClO_4$ in open Teflon beakers at room temperature. Chemical separation procedures were adapted from those described by DePaolo [1978]. Separation of Rb, Sr, and the bulk rare earth elements (REE) was performed on an aliquot of the sample using HCl elution in 1 cm-diameter, 15 cm-long columns of AG50W-X8 (100-200 mesh) resin. Separation of Sm and Nd was carried out on pressurized 0.15 cm-diameter, 30 cm-long columns of AG50W-X4 (-400 mesh) resin using 0.21 M 2-methyllactic acid with pH=4.65; automatic fraction collection was achieved with a turntable activated by a drop-counting sensor. The highest determined total procedural blanks were Rb - 12 pg, Sr - 220 pg, Sm - 7 pg, Nd - 19 pg.

Various filament loading techniques were employed before the most efficient and reliable were determined. Rb (2 ng) was loaded as phosphate on a thin film of silica gel on a flat Re filament, and Sr (300-500 ng) as chloride on a thick film of Ta_2O_5 powder on a flat Ta filament. For Sm, we employed the method of Noble et al. [1989], loading 30-50 ng of Sm as chloride on a thin film of platinized (10%) graphite on a flat Re filament; this method was unreliable for Nd, although some of the Nd measurements reported here were obtained in this way. The majority of Nd measurements reported in this paper were

obtained from triple filament assemblies (Re center, Ta sides) with 150-250 ng of Nd loaded on one side in HCl followed by H_3PO_4. The final, most efficient Nd method we adopted followed Walker et al. [1989], loading in HCl on 20-30 beads of AG50W-X8 (100-200 mesh) resin in a narrow strip on a flat Re filament, followed by a small amount of H_3PO_4. This method gave ionization efficiencies of greater than 1.2%.

Rb, Sr, Sm, and Nd concentrations were determined by isotope dilution, with isotopic compositions of Sr and Nd determined on the spiked runs. Mass spectrometric analyses were carried out on an automated VG Sector multicollector instrument fitted with adjustable 10^{11} Ω Faraday collectors and a Daly photomultiplier. The latter was used only for signal preparation and for a few Rb single-collector measurements on gabbroic rocks when the signal was weak. The majority of Rb analyses were obtained by static two-collector measuring with ^{87}Rb signal intensities of ~5x10^{-12} A and 100 ratios taken. Sm was also measured statically, with four collectors measuring the signals from masses 147, 148, 149, and 152, and with an exponential mass fractionation correction according to ^{149}Sm/^{152}Sm$\equiv$0.51686 [Wasserburg et al., 1981], ^{147}Sm intensity of ~2.5x10^{-12} A, and 100 ratios taken. Sr was measured with a four-collector peak-switching scheme ("multidynamic") which obviates the need for precise knowledge of differences in collector gains for measurement of ^{87}Sr/^{86}Sr. It was necessary, however, to obtain ^{84}Sr/^{86}Sr as a static, two-collector measurement in the same measuring routine. The mass fractionation correction (power law) was according to ^{86}Sr/^{88}Sr$\approx$0.1194, ^{88}Sr intensities were typically 4x10^{-11} A, Rb interference was monitored at mass 85, and 105 to 150 cycles were obtained, each cycle in effect involving two measurements of ^{87}Sr/^{86}Sr. Nd was measured by way of a five-collector, multidynamic scheme described in Patchett and Ruiz [1987] which allows determination of fully corrected values for ^{142}Nd/^{144}Nd, ^{143}Nd/^{144}Nd, ^{145}Nd/^{144}Nd, and ^{150}Nd/^{144}Nd. Sm interference was monitored at mass 147, which necessitated a small, offline adjustment since 147 was also the mass of our Sm spike isotope. Fractionation

was corrected (power law) according to $^{146}Nd/^{144}Nd \equiv 0.7219$, ^{144}Nd intensity was typically 1×10^{-11} A, and 105 to 150 cycles were obtained, each cycle in effect involving two measurements of $^{143}Nd/^{144}Nd$. For Sr, Sm, and Nd, the grand means of the ratios of interest were corrected by an offline program which adjusts for the spike contributions to both the fractionation correction and each individual ratio, and performs isotope dilution calculations.

Table 3.2 shows the results of measurements of standards during the course of this study -- results of individual standard runs are tabulated in Appendix 2. The within-run 2σ error for $^{87}Sr/^{86}Sr$ is typically ≤ 0.000014 (20 ppm), but external reproducibility, based on the range of results from multiple runs of the NBS 987 standard with the two extreme results discarded, is estimated to be ± 0.000018 (25 ppm). For $^{143}Nd/^{144}Nd$, the within-run 2σ error is typically ≤ 0.000010 (20 ppm), but runs of the La Jolla Nd standard suggest an external reproducibility of ± 0.000015 (30 ppm). A measurement of Caltech standard nNdβ yielded $\varepsilon_{Nd} = -13.97$, in accord with values reported in Wasserburg et al. [1981]. Some of the standards and samples were measured during a period when, due to inappropriate cup positioning, a number of the measured $^{150}Nd/^{144}Nd$ ratios were around 2-3‰ high. (The average $^{150}Nd/^{144}Nd$ in Table 3.2 does not include these runs.) The cup positioning was subsequently corrected. Calculations demonstrate that such errors in $^{150}Nd/^{144}Nd$ in the spiked samples measured during that period do not yield significant errors in the small age corrections involved, nor in the spike correction to the $^{143}Nd/^{144}Nd$ ratio.

Pb isotopic analyses were performed on whole-rock samples in the laboratory of Professor G.R. Tilton at U.C. Santa Barbara. Procedural details may be found in Grünenfelder et al. [1986]. Zircon U-Pb analyses were performed by J.B. Salceby at Caltech using procedures described in the footnotes to Table 3.3.

3.4. Results

a. Zircon ages

The Grapevine zircon samples (Table 3.3, Figure 3.3) yield interpreted intrusion ages of 101 and 105 Ma, which places them temporally in the intrusive suite of Bear Valley. This is somewhat surprising, given their location several km west of other members of the suite (Figure 3.2), and further demonstrates the lack of systematic age zonation in the Tehachapi Mountains [Saleeby et al., 1987]. While the diorite (GV-1a) ages are both concordant at 105 Ma, fractions from the tonalite (GV-3) show strong discordance with a well-defined intercepts of 1992 Ma and 101 Ma (Figure 3.3). Clearly, this rock inherited or incorporated Proterozoic zircon, as has been previously observed in some of the Tehachapi intrusive rocks [Saleeby et al., 1987]. On the other hand, such inheritance is not a ubiquitous indicator of the presence of old continental material in the intrusive rocks, which always show Nd and Sr evidence for such a component (see below).

The diorite is intrusive into rocks which we correlate with the older (115 Ma) quartzofeldspathic gneiss of Pastoria Creek. This new age raises the possibility that all of the diorites commonly found intermingling with and intruding into the rocks of the gneiss complex of the Tehachapi Mountains, including perhaps Sr-Nd sample GC-60 (Table 3.1), belong to the younger intrusive suite of Bear Valley. This is consistent with the overall more mafic composition of the younger suite.

b. Initial isotope ratios

Nd and Sr isotopic ratios of intrusive rocks from south of the Bear Valley Springs tonalite fall in a fairly restricted range; initial ε_{Nd} ranges from +2.9 to -0.9, while initial $^{87}Sr/^{86}Sr$ ranges from 0.70410 to 0.70602 (Tables 3.4 and 3.5, Figure 3.4). The two Bear Valley Springs tonalite samples, from north of the main study area, extend to lower ε_{Nd} (-1.9, -3.2) and higher $^{87}Sr/^{86}Sr$ (0.70574, 0.70641; see also Saleeby et al. [1987]). Overall, the new Sr data are consistent with the range of ratios reported in Saleeby et al. [1987].

Table 3.2 - Results of analysis of standards

standard	# runs	ratio for fractionation	ratios (± 2σ of mean)	
984 Rb	12		$^{85}Rb/^{87}Rb =$	2.6163 ± 19
987 Sr	24 [1]	$^{86}Sr/^{88}Sr \equiv 0.1194$	$^{87}Sr/^{86}Sr =$	0.710244 ± 5
			$^{84}Sr/^{86}Sr =$	0.056514 ± 10
nSmβ [2]	17	$^{149}Sm/^{152}Sm \equiv 0.51686$ [2]	$^{148}Sm/^{147}Sm=$	0.74964 ± 19
			$^{148}Sm/^{152}Sm=$	0.42049 ± 5
La Jolla Nd	33 [3]	$^{146}Nd/^{144}Nd \equiv 0.7219$	$^{142}Nd/^{144}Nd =$	1.14183 ± 2
			$^{143}Nd/^{144}Nd =$	0.511853 ± 3
			$^{145}Nd/^{144}Nd =$	0.348407 ± 1
			$^{150}Nd/^{144}Nd =$	0.236448 ± 13

[1] $^{84}Sr/^{86}Sr$ average based on 18 runs only.
[2] Wasserburg et al. [1981].
[3] $^{150}Nd/^{144}Nd$ average based on 10 runs only.
Individual runs are tabulated in Appendix 2.

Table 3.3 - Zircon U-Pb isotopic age data

Sample	Fraction†	Amount analyzed (mg)	Concentrations (ppm)		Atomic ratios				Isotopic ages (Ma)§		
			^{238}U	$^{206}Pb^*$	$\frac{^{206}Pb}{^{204}Pb}$	$\frac{^{206}Pb^*}{^{238}U}$	$\frac{^{207}Pb^*}{^{235}U}$	$\frac{^{207}Pb^*}{^{206}Pb^*}$	$\frac{^{206}Pb^*}{^{238}U}$	$\frac{^{207}Pb^*}{^{235}U}$	$\frac{^{207}Pb^*}{^{206}Pb^*}$
GV-1a	2/20 <45μ	0.3	207	3.0	252.9	0.01644(09)	0.1092	0.4821(15)	105.1	105.3	109±9
	2/20 45-62μ	1.2	222	3.2	1237	0.01641(10)	0.1085	0.4797(19)	105.0	104.6	98±10
GV-3	1/20 <45μ	0.4	939	13.6	4215	0.01671(09)	0.1212	0.5261(13)	106.8	116.1	312±7
	1/20 45-62μ	1.4	412	6.2	1423	0.01746(10)	0.1318	0.5479(11)	111.6	125.8	404±5
	1/20 62-80μ	3.0	467	7.4	1537	0.01826(11)	0.1488	0.5915(16)	116.7	140.9	572±6
	1/20 80-100μ	3.9	424	7.0	2964	0.01918(11)	0.1631	0.6171(15)	122.5	153.4	664±5

* Radiogenic; nonradiogenic correction based on 40 picogram blank Pb (1:18.78:15.61:38.50) and initial Pb compositions of $^{206}Pb/^{204}Pb$ = 18.84, $^{207}Pb/^{204}Pb$ = 15.64, and $^{208}Pb/^{204}Pb$ = 38.60 from the data of Table 3.6.

† Fractions separated by grain size and magnetic properties. Magnetic properties are given as nonmagnetic split at side/front slopes for 1.7 amps on Franz Isodynamic Separator. Samples hand-picked to 99.9% purity prior to dissolution. Dissolution and chemical extraction techniques modified from Krogh [1973].

§ Decay constants used in age calculation: $\lambda^{238}U$ = 1.55125 10^{-10}, $\lambda^{235}U$ = 9.8485 10^{-10} [Jaffey et al., 1971]; $^{238}U/^{235}U$ atom = 137.88. Uncertainties in $^{206}Pb^*/^{238}U$ and $^{207}Pb^*/^{235}U$ are given as "±" in last two figures. Uncertainties calculated by quadratic sum of total derivatives of ^{238}U and $^{206}Pb^*$ concentration and $^{207}Pb^*/^{206}Pb^*$ equations with error differentials defined as 1. isotope ratio determinations from standard errors (σ/√n) of mass spectrometer runs plus uncertainties in fractionation corrections based on multiple runs of NBS 981, 982, 983, and U500 standards; 2. spike concentrations from range of deviations in multiple calibrations with normal solutions; 3. spike compositions from external precisions of multiple isotope ratio determinations; 4. uncertainty in natural $^{238}U/^{235}U$ from Chen and Wasserburg [1981]; and 5. nonradiogenic Pb isotopic compositions from uncertainties in isotope ratio determinations of blank Pb and uncertainties in composition of initial Pb from estimates of regional variations and consideration of rock type.

Figure 3.3 - Concordia plot of zircon fractions from sample GV-3.
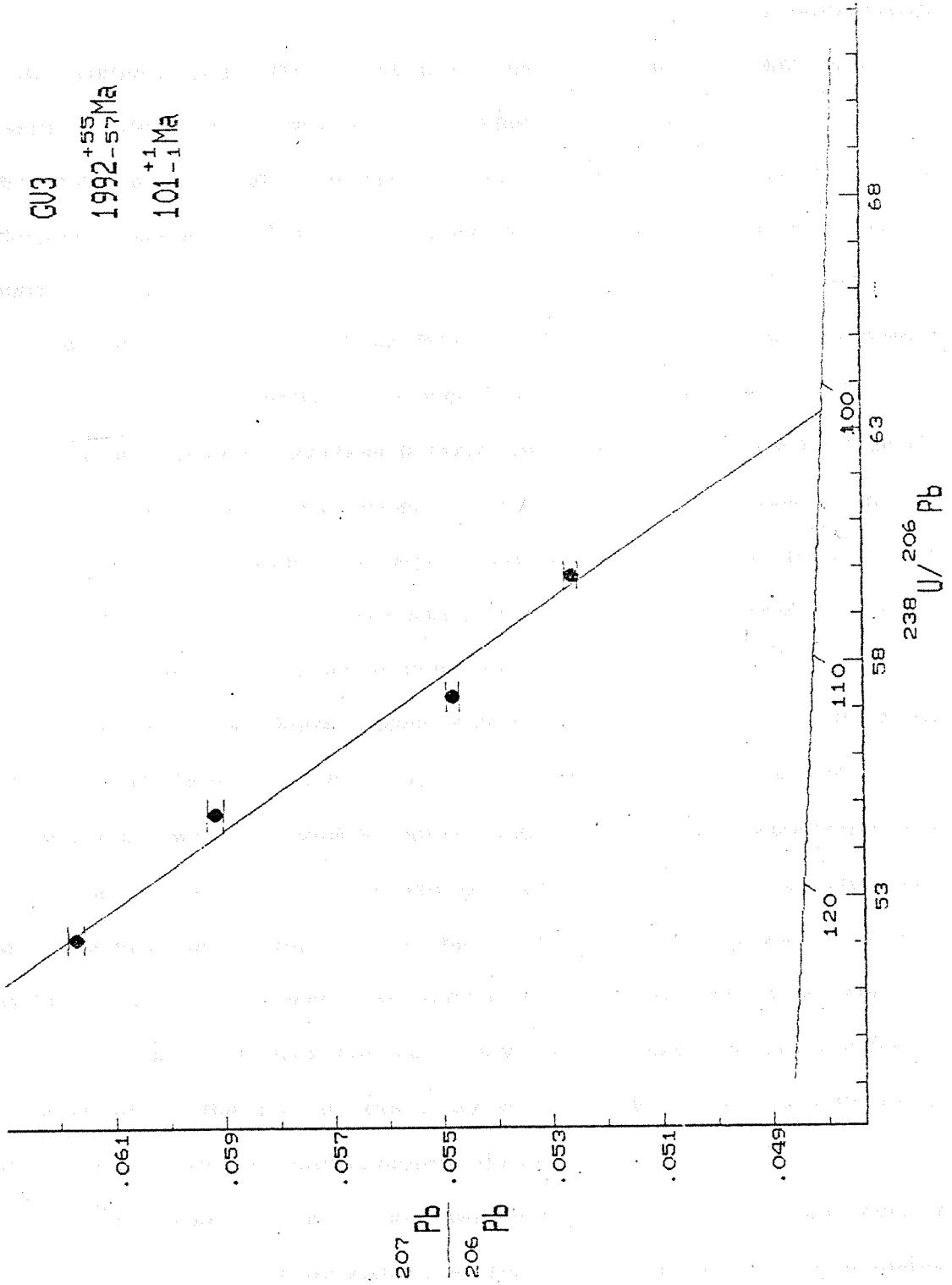
Fig. 3.3

The most striking feature of the data as plotted in Figure 3.4 is the general negative correlation between the two ratios, a feature common to rocks from continental margin granitoid batholiths [e.g., DePaolo, 1981a; McCulloch and Chappell, 1982; Pickett and Wasserburg, 1989]. The covariation is also reflected in the overall field of Nd and Sr isotopic ratios from throughout the Sierra Nevada batholith (Figure 3.4), into which most of the present samples fit. Three of the samples from the Tehachapi suite, all granites or granodiorites, show a departure from this pattern toward high $^{87}Sr/^{86}Sr$ and/or ε_{Nd}, particularly the two granites (TC-6 and PC35-P). This suggests the action of a distinct isotopic component in the genesis of the higher-SiO_2 rocks (see below).

In general, however, variations in isotope ratios are not reflected in the lithologic diversity of the sample suite. The histograms of Figure 3.5 reveal no consistent tendency for ε_{Nd} or $^{87}Sr/^{86}Sr$ to vary from one rock type to another. For instance, in the Bear Valley suite rocks (exclusive of the Bear Valley Springs tonalite samples), gabbros span the entire range of ε_{Nd}, overlapping values for the quartz diorite and tonalites.

In light of the well-known regular variations in Sr isotope ratios in the Sierra Nevada batholith [Kistler and Peterman, 1973, 1978; Kistler and Ross, 1990], it is interesting that it was not possible to contour either ε_{Nd} or $^{87}Sr/^{86}Sr$ on maps (Figures 3.6 and 3.7); ratios do not vary regularly with geographic position in the main study area south of the Bear Valley Springs tonalite. Figure 3.8 shows contours drawn in the north from the data of Kistler and Ross [1989], and it is clear that these cannot be extended into the main study area. The most that may be said about geographic variation within the main study area is that from the east to the west, there is a tendency for the lowest $^{87}Sr/^{86}Sr$ ratio of a given subarea to decrease (Figure 3.8).

The Pb isotope ratios for the four samples from the central study area define a rather small range (Table 3.6 and Figure 3.9). These ratios, along with the corresponding Sr values, fall plainly within data for the western province as defined by Chen and Tilton

[1991] based on Pb and Sr isotopic data from further north in the southern Sierra Nevada.

Nd and Sr isotope ratios of the five metamorphic rocks span a very wide range. The quartzite from the north (CM640) and two of the paragneisses from the central study area (TC-8, GC-12) have ratios reflective of a provenance of old continental crust (Tables 3.4 and 3.5, Figure 3.10). The other paragneisses (GC-2, GV-14), however, have much higher ϵ_{Nd} and lower $^{87}Sr/^{86}Sr$, but with high $^{87}Sr/^{86}Sr$ for a given ϵ_{Nd} relative to most igneous rocks, suggesting the influence of detritus from an arc volcanic source. It is thus possible that these particular metamorphic assemblages are roughly correlative with Mesozoic volcanic-sedimentary rocks that form portions of the western facies of the Kings sequence to the north [Saleeby et al., 1978]. Gneiss GC-2 has a $\delta^{18}O$ of 6.0 (Table 3.4), which is quite distinct from the paragneisses of demonstrably continental provenance. In spite of this apparent volcanic component, GC-2 and GV-14 are not distinct from the other paragneisses in terms of Rb, Sr, Sm, and Nd abundances and metamorphic mineral assemblages.

The new Rb-Sr data on samples CM640, CM9, and TC42 may be compared with the ratios reported on different pieces of the same samples in Saleeby et al. [1987]. Our Rb concentrations differ by 3 to 41%, Sr by 0.9 to 21%, and $^{87}Rb/^{86}Sr$ by 3 to 27%. These differences can probably be attributed to the small size (probably <300 g) of the samples available for each analysis, as well as to the rather high level of weathering (the original samples were not chosen with whole-rock isotopic analysis in mind). For CM9 and TC42, initial $^{87}Sr/^{86}Sr$ differ by 4.8 and 0.6 parts in 10^4 (ϵ units), respectively, the former being well outside the estimated uncertainty. CM640 is a metasedimentary rock, so the significance of $^{87}Sr/^{86}Sr$ at 100 Ma is unclear; the two measurements differ by 11 ϵ units. For these three samples, we prefer the new data because of the somewhat larger amount of sample used in crushing. For the three samples (GC-1, GC-14, and PC35-P) which are new field samples from localities in Saleeby et al. [1987] (respectively, CM630, WR643, and

Table 3.4 - Rb-Sr isotopic data

	Rb	Sr	$^{87}Rb/^{86}Sr$	$^{87}Sr/^{86}Sr$ (0)	$^{87}Sr/^{86}Sr$ (t)	$\delta^{18}O^1$
Intrusive suite of Bear Valley						
CM9	68.71	350.2	0.5641	0.707212	0.70641	9.1
GC-8[2]	0.249	394.8	0.00182	0.705070	0.70507	
GC-11[2]	1.13	473.4	0.00690	0.704991	0.70498	
GC-17	31.73	369.2	0.2471	0.705368	0.70501	
GC-53	2.05	543.2	0.0108	0.704332	0.70432	
GV-1a	2.84	315.5	0.0259	0.705009	0.70497	
GV-3	29.83	469.8	0.1825	0.705016	0.70475	
PC175	1.43	306.1	0.0134	0.704463	0.70444	
PTC-42	42.33	270.8	0.4495	0.705043	0.70439	
TC42	31.71	338.2	0.2695	0.706115	0.70574	9.1
TC-45b	22.84	406.8	0.1614	0.704767	0.70453	
TC-47	0.577	668.1	0.00248	0.704818	0.70482	8.4*
TC-49b	1.25	522.8	0.00686	0.705455	0.70545	
TC-83	1.28	543.7	0.00676	0.704907	0.70490	
Gneiss Complex of the Tehachapi Mts.						
GC-1[2]	49.44	299.3	0.4750	0.704961	0.70419	
GC-14	26.11	377.3	0.1990	0.705493	0.70516	
GC-32	36.29	374.6	0.2785	0.705170	0.70472	
GC-55	44.95	326.9	0.3954	0.705404	0.70475	
GC-60	2.20	415.3	0.0152	0.704120	0.70410	
PC35-P	139.2	52.24	7.673	0.718017	0.70602	10.0
TC-6	51.53	170.2	0.8704	0.706390	0.70497	
TC-34	39.25	510.2	0.2212	0.705051	0.70469	
Metamorphic framework rocks[3]						
CM640	45.42	108.9	1.201	0.725257	0.72355	17.4
GC-2	67.27	169.2	1.143	0.706662	0.70504	6.0*
GC-12[2]	69.20	240.8	0.8266	0.711293	0.71012	
GV-14	79.95	194.8	1.180	0.708496	0.70682	
TC-8	105.5	188.8	1.607	0.712706	0.71042	

Estimated 2σ uncertainties: $^{87}Rb/^{86}Sr$=2‰, $^{87}Sr/^{86}Sr$=0.025‰. For initial ratio, this does not include the age uncertainty. λ_{Rb}=1.42x10^{-11}a^{-1}.

[1] Saleeby et al. [1987], except * - new analyses by D.C. Knott, Caltech.
[2] Analyzed by DAP in the laboratory of G.J. Wasserburg, Caltech.
[3] $^{87}Sr/^{86}Sr$(t) calculated at 100 Ma.

Table 3.5 - Sm-Nd isotopic data

	Sm	Nd	$^{147}Sm/^{144}Nd$	$^{143}Nd/^{144}Nd(0)$	$\varepsilon_{Nd}(t)$	T_{DM}[1]
Intrusive suite of Bear Valley						
CM9	3.510	15.41	0.1377	0.512437	-3.2	
GC-8[2]	3.913	11.28	0.2098	0.512629	-0.4	
GC-11[2]	3.000	11.16	0.1626	0.512642	+0.5	
GC-17	3.594	15.13	0.1436	0.512615	+0.2	
GC-53	4.347	15.45	0.1701	0.512725	+2.0	
GV-1a	4.961	17.11	0.1753	0.512667	+0.9	
GV-3	2.834	14.56	0.1177	0.512585	0.0	
PC175	0.2185	1.003	0.1317	0.512614	+0.4	
PTC-42	3.640	15.86	0.1387	0.512691	+1.8	
TC42	3.129	13.30	0.1423	0.512505	-1.9	
TC-45b	4.426	17.94	0.1491	0.512683	+1.5	
TC-47	2.396	10.81	0.1340	0.512600	+0.1	
TC-49b	2.959	8.390	0.2132	0.512603	-0.9	
TC-83	4.630	16.30	0.1717	0.512661	+0.8	
Gneiss Complex of the Tehachapi Mts.						
GC-1[2]	4.481	18.04	0.1502	0.512668	+1.3	
GC-14	5.529	39.44	0.08475	0.512562	+0.2	
GC-32	0.7857	4.237	0.1121	0.512657	+1.6	
GC-55	5.216	21.36	0.1477	0.512644	+0.9	
GC-60	6.396	22.61	0.1710	0.512769	+2.9	
PC35-P	1.281	5.632	0.1375	0.512648	+1.0	
TC-6	3.543	24.85	0.08620	0.512673	+2.3	
TC-34	1.739	8.998	0.1168	0.512596	+0.4	
Metamorphic framework rocks[3]						
CM640	2.718	14.87	0.1105	0.511735	-16.5	1.93
GC-2	2.575	13.25	0.1175	0.512828	+4.7	0.37
GC-12[2]	2.346	11.72	0.1210	0.512190	-7.8	1.41
GV-14	3.444	15.24	0.1366	0.512552	-0.9	0.98
TC-8	5.621	28.10	0.1209	0.512272	-6.2	1.27

Estimated 2σ uncertainties: $^{147}Sm/^{144}Nd$=2‰; $^{143}Nd/^{144}Nd$=0.03‰ (0.3 ε). For initial ratio, this does not include the age uncertainty.

$\varepsilon_{Nd}(t)$ calculated as in DePaolo and Wasserburg [1976], but with $^{143}Nd/^{144}Nd_{CHUR}(0)$=0.512638, $^{147}Sm/^{144}Nd_{CHUR}$=0.1966, λ_{Sm}=6.54x10^{-12}a^{-1}.

[1] Method of DePaolo [1981b].

[2] Analyzed by DAP in the laboratory of G.J. Wasserburg, Caltech; 2σ uncertainty for $^{143}Nd/^{144}Nd$=0.05‰ (0.5 ε). $^{143}Nd/^{144}Nd$ recalculated to $^{146}Nd/^{144}Nd$=0.7219.

[3] $\varepsilon_{Nd}(t)$ calculated at 100 Ma.

Table 3.6 - Whole-rock Pb isotopic data

	U	Th	Pb	$^{206}Pb/^{204}Pb(0)$	$^{207}Pb/^{204}Pb(0)$	$^{208}Pb/^{204}Pb(0)$	$^{206}Pb/^{204}Pb(t)$	$^{207}Pb/^{204}Pb(t)$	$^{208}Pb/^{204}Pb(t)$
Intrusive suite of Bear Valley									
TC-45b	0.382	0.85	4.145	18.930	15.637	38.635	18.838	15.633	38.568
TC-47	0.080	0.17	1.070	18.934	15.665	38.716	18.859	15.661	38.664
TC-83	0.136	0.28	2.237	18.877	15.620	38.579	18.816	15.617	38.538
Gneiss complex of the Tehachapi Mts.									
TC-34	0.159	0.54	6.985	18.855	15.651	38.680	18.829	15.650	38.651

Figure 3.4 - Initial $^{87}Sr/^{86}Sr$ vs. initial ε_{Nd} for the intrusive rocks with "bulk earth" axes. Within the Bear Valley suite ("BV"), the two samples of the tonalite of Bear Valley Springs are distinguished ("BVS"), while within the Tehachapi suite ("TM"), granites and granodiorites are distinguished. Also shown is the field encompassing all published data on intrusive rocks of the Sierra Nevada batholith [DePaolo, 1981a; Domenick et al., 1983; Kistler et al., 1986; Dodge and Kistler, 1990; Knott et al., 1990]. This field extends slightly beyond the lower right boundaries of the diagram.
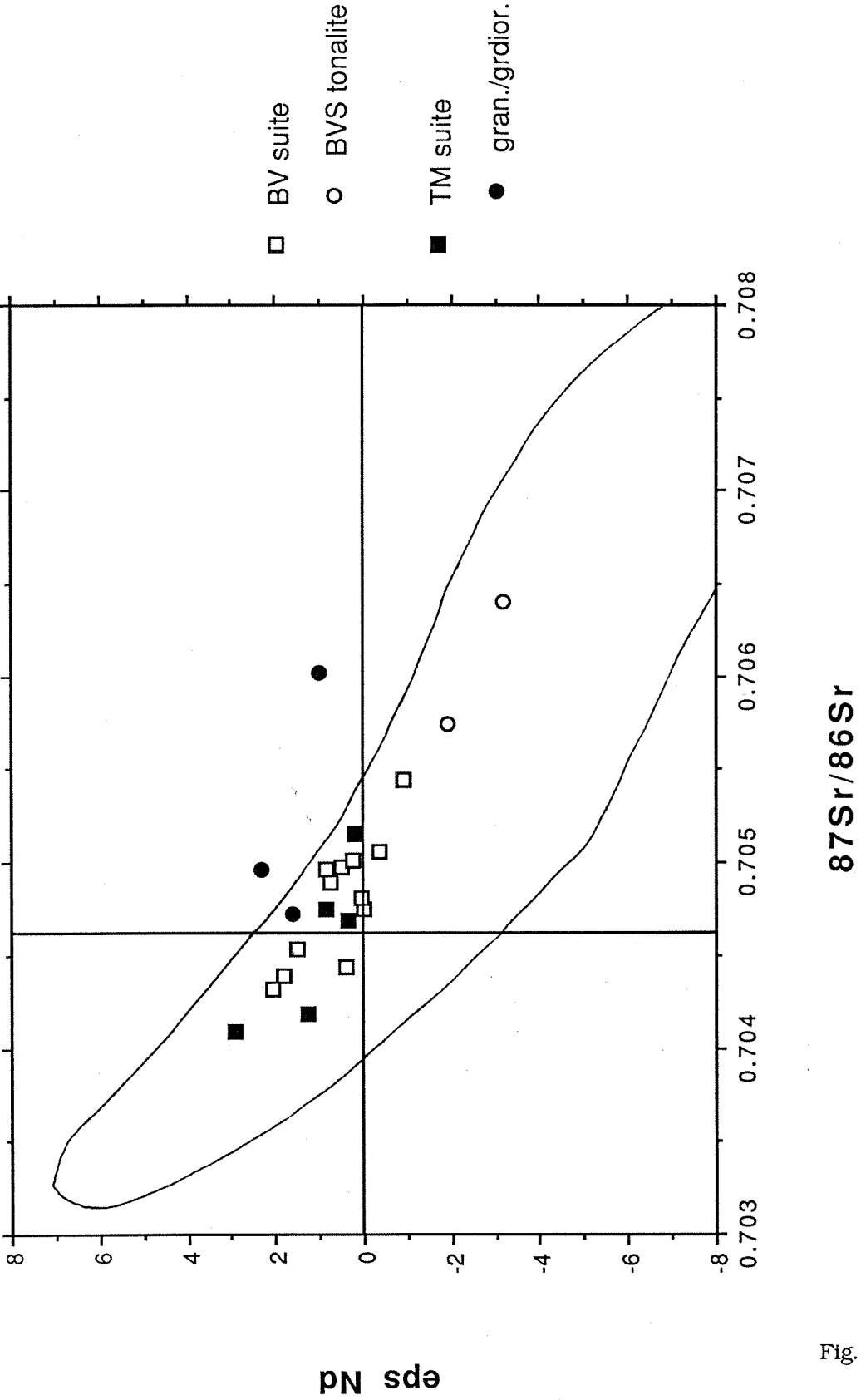
Fig. 3.4

Figure 3.5 - Histograms of initial Sr and Nd isotopic ratios in intrusive rocks from the main study area. Bear Valley Springs tonalites are not included. The Sr figures include additional data from Saleeby et al. [1987] and Kistler and Ross [1990].

Bear Valley Suite
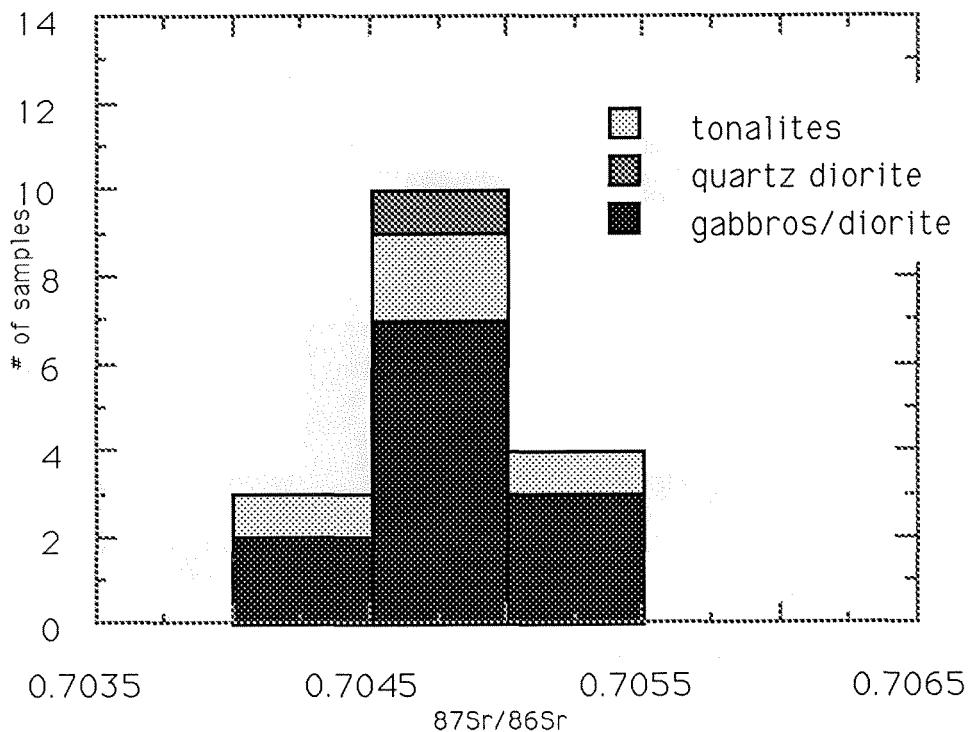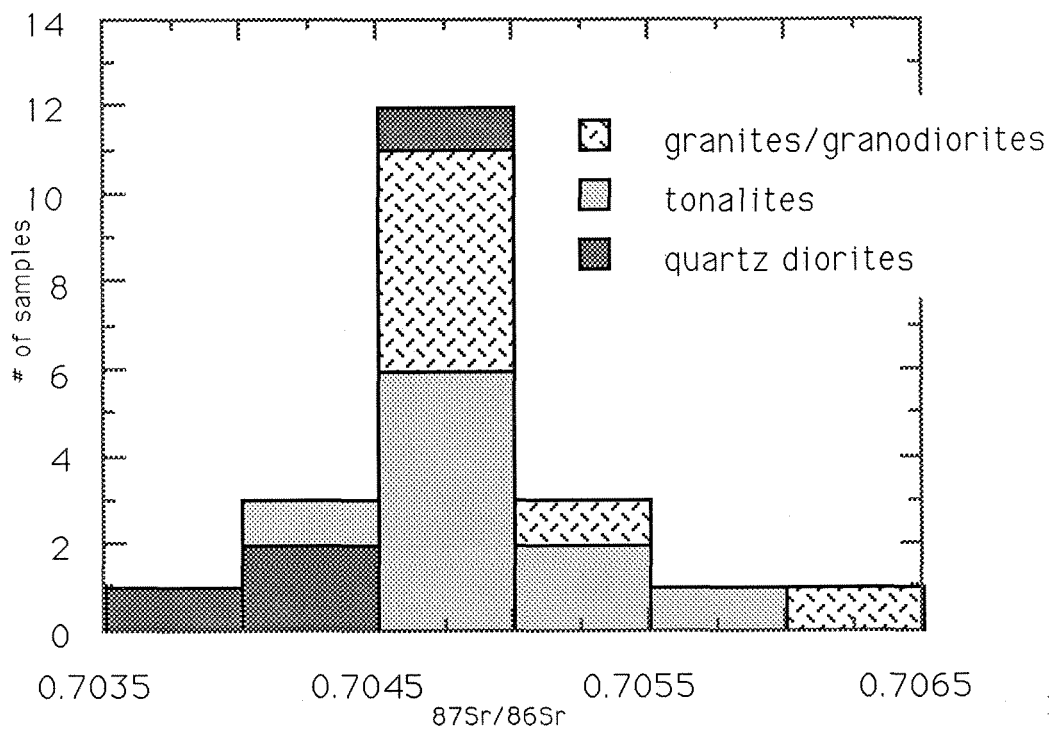
Tehachapi Suite

Fig. 3.5

Bear Valley Suite
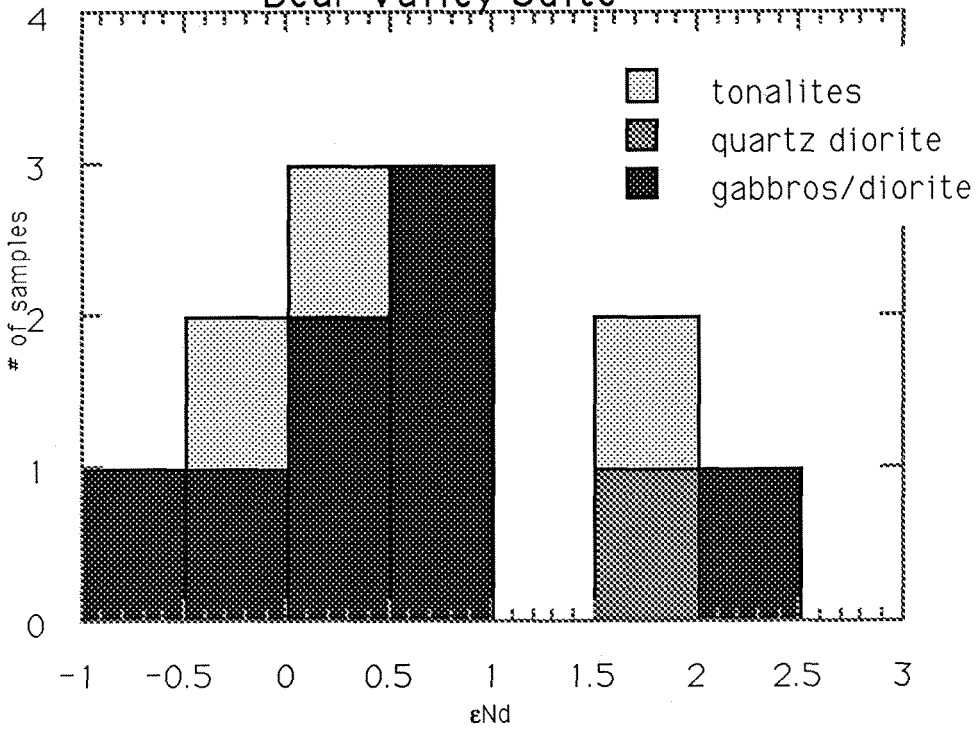
Tehachapi Suite
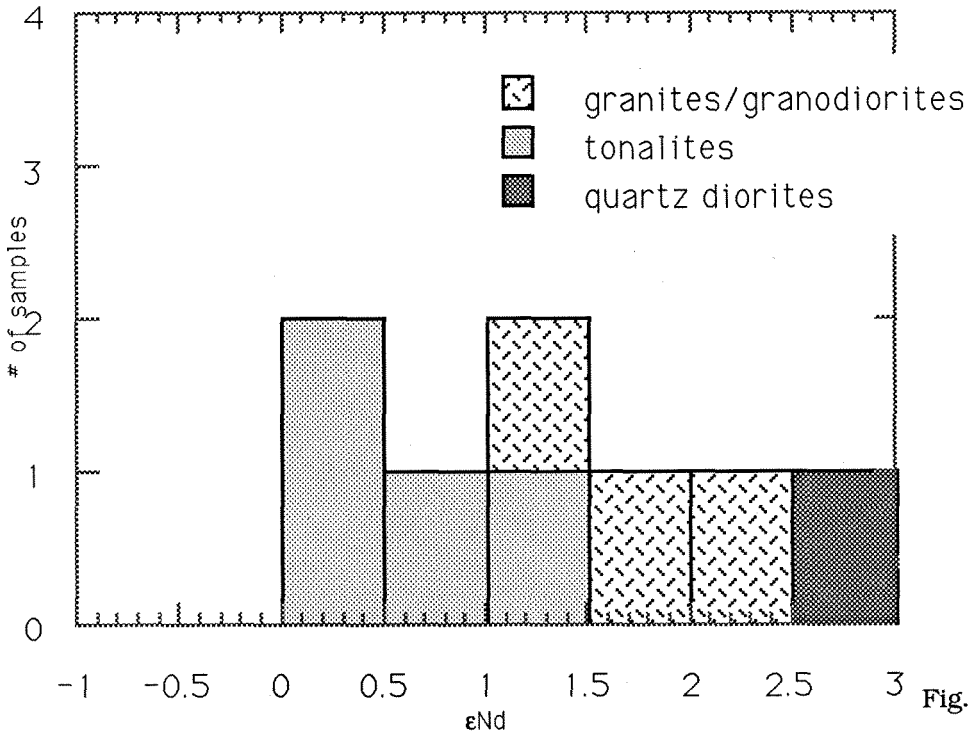
Fig. 3.5 (cont.)

Figure 3.6 - Map of initial ε_{Nd} in the main study area. Values for metamorphic framework rocks are calculated at 100 Ma. Units as in Figure 3.2.
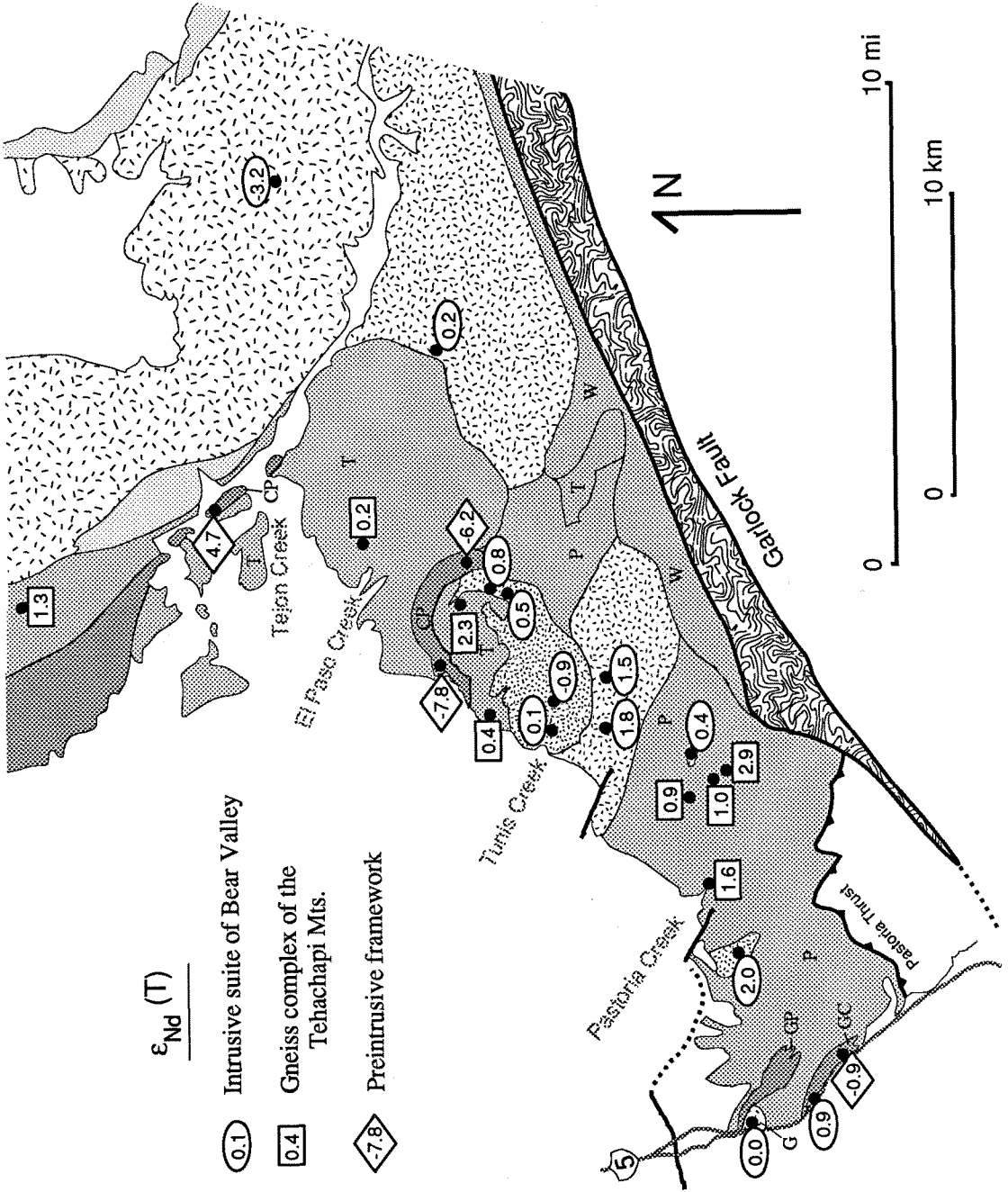
Fig. 3.6

<u>Figure 3.7</u> - Map of initial $^{87}Sr/^{86}Sr$ in the main study area. Values for metamorphic

framework rocks are calculated at 100 Ma. Units as in Figure 3.2.

-129-
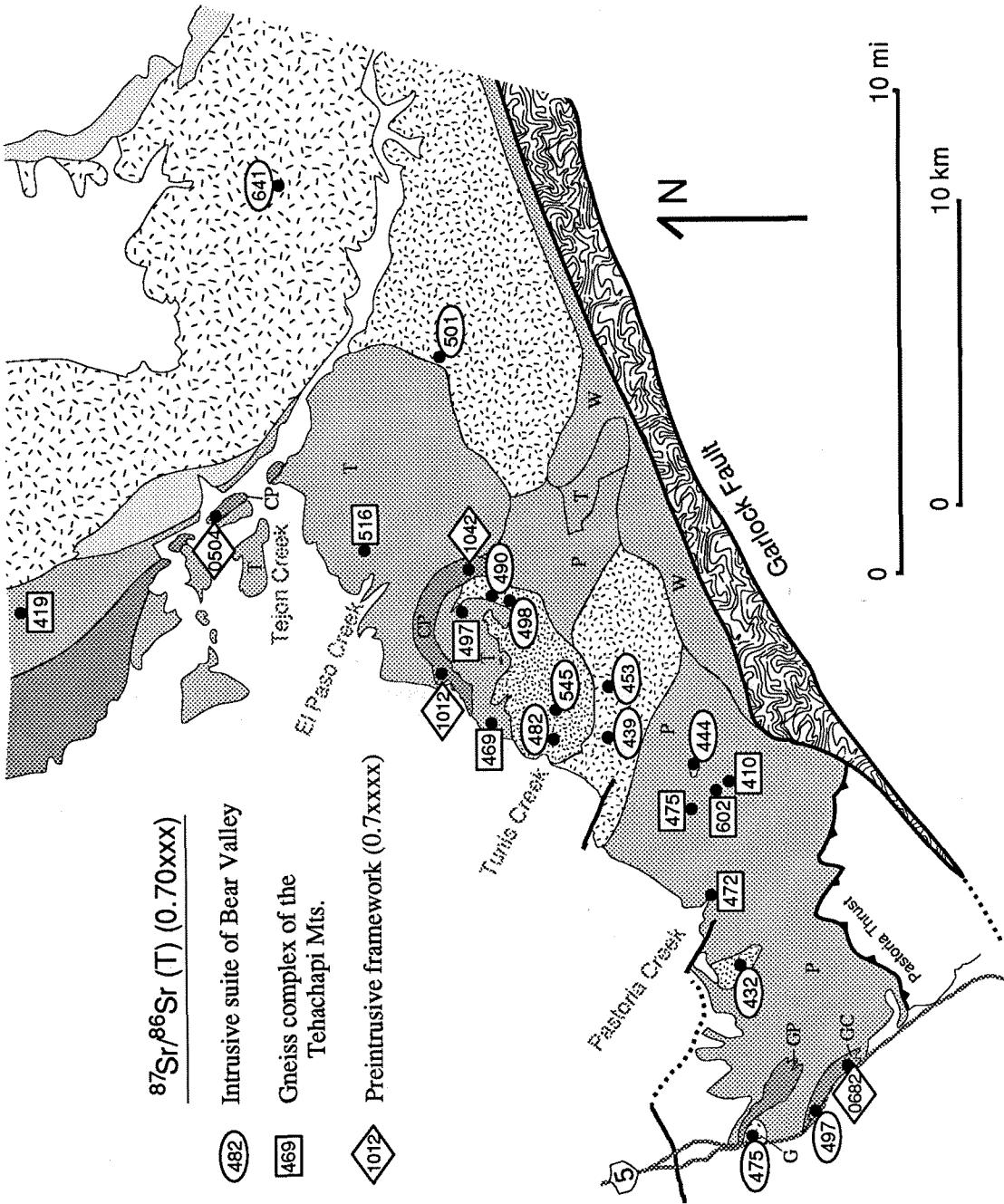
Fig. 3.7

Figure 3.8 - Map of initial $^{87}Sr/^{86}Sr$ in the southern Sierra Nevada. North of Tejon Creek, individual data localities from Kistler and Peterman [1978], Saleeby et al. [1987], and Kistler and Ross [1990] are shown, along with $^{87}Sr/^{86}Sr$ and ε_{Nd} values (boxes) for two samples, a tonalite and quartzite, from the present study. Isopleths of $^{87}Sr/^{86}Sr$ at 0.705 and 0.706 are drawn, but are poorly constrained in the southeast. (It is possible that the seven samples at 0.7059 to 0.7064 in the center of the map represent a local maximum; note the 0.7049 value to the east.) South of Tejon Creek, isopleths cannot be constructed, but variations in $^{87}Sr/^{86}Sr$ are shown for four different zones. Note the westward decrease in the lowest value in each zone. Ratios for granites are excluded because of possible secondary effects on $^{87}Sr/^{86}Sr$.

$^{87}Sr/^{86}Sr$ (T) (0.70xx)

0.70574
-1.9

0.72355
-16.5

48 - 52

44 - 54

41 - 52

36 - 50

Garlock Fault
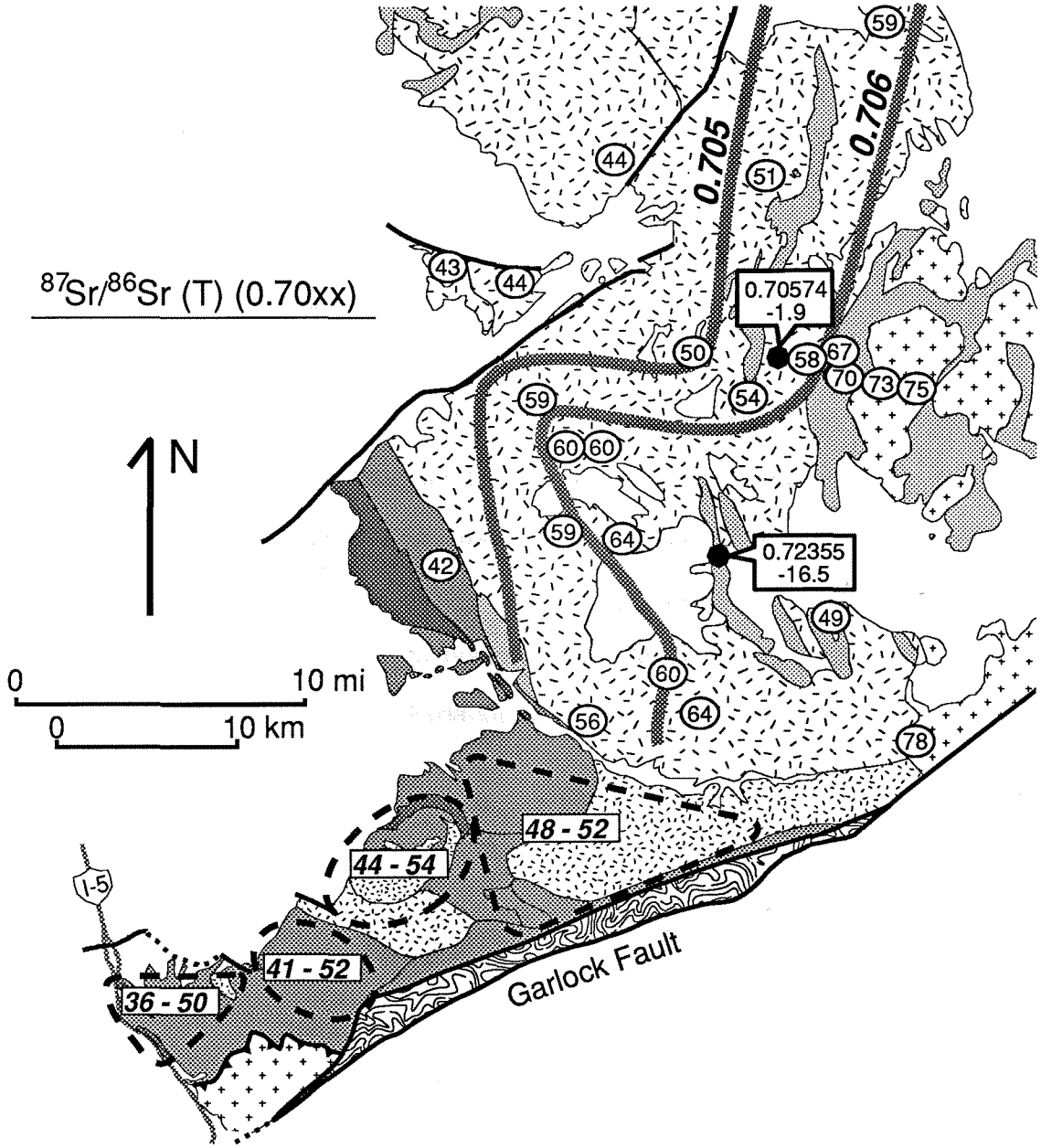
Fig. 3.8

Figure 3.9 - ^{208}Pb/^{204}Pb vs. ^{206}Pb/^{204}Pb for the four Tehachapi samples, with fields (western

and eastern) from Chen and Tilton [1991] for feldspars from Cretaceous granitoids in the

central Sierra Nevada batholith. Fields are dashed at high ^{206}Pb/^{204}Pb where western and

eastern fields overlap. Also shown are fields for "primitive arc" Pb [Doe and Zartman,

1979] and western U.S. area II metasedimentary Pb [Zartman, 1974]. Chen and Tilton

[1991] attribute the western variation to interaction between "primitive arc" and

metasedimentary components.
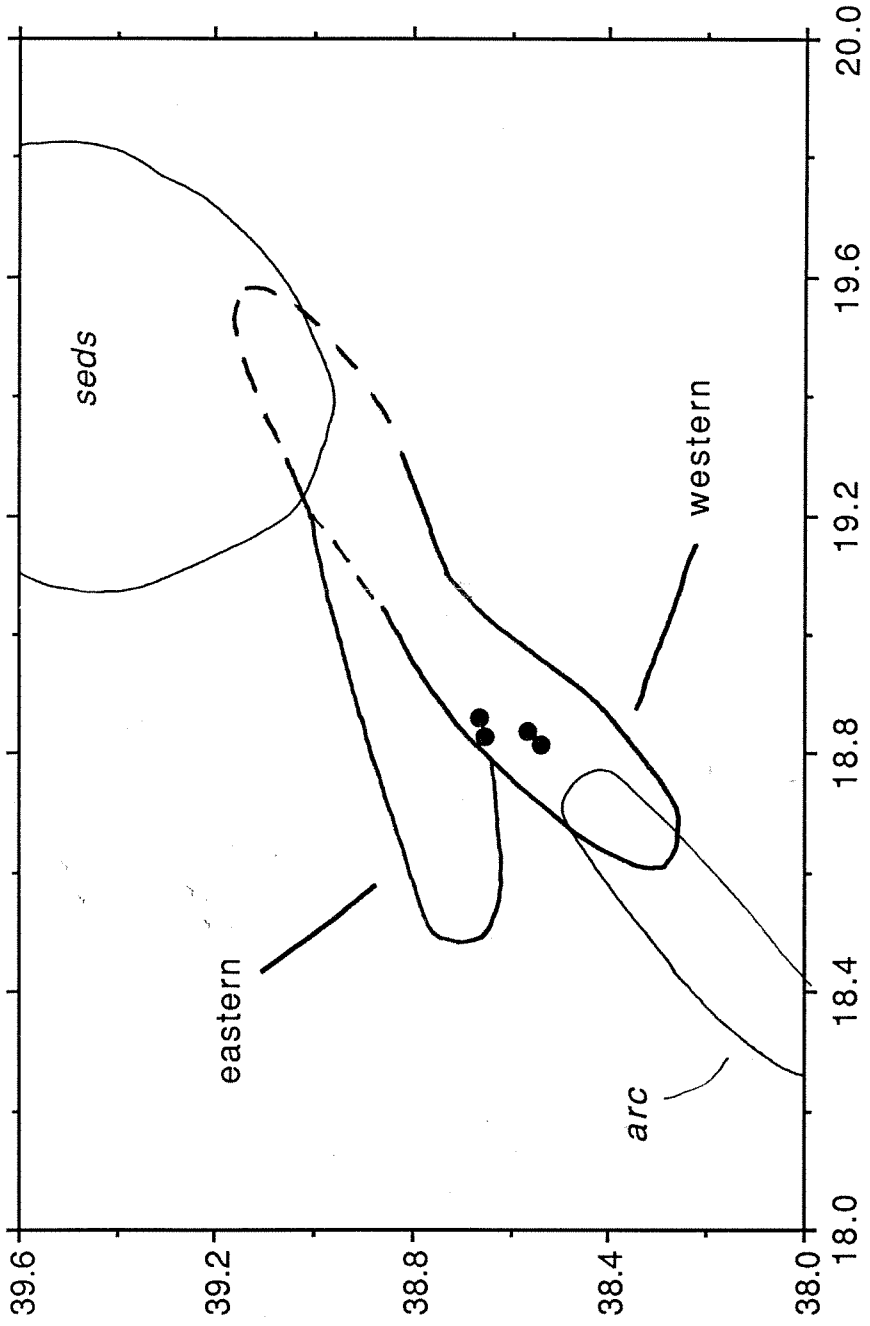
Fig. 3.9

Figure 3.10 - $^{87}Sr/^{86}Sr$ vs. ε_{Nd} for the intrusive rocks (initial ratios) and metamorphic framework rocks (at 100 Ma). Simple mixing curves are described in the text; tick marks are at 10, 30, 50, 70, and 90% metasedimentary component.
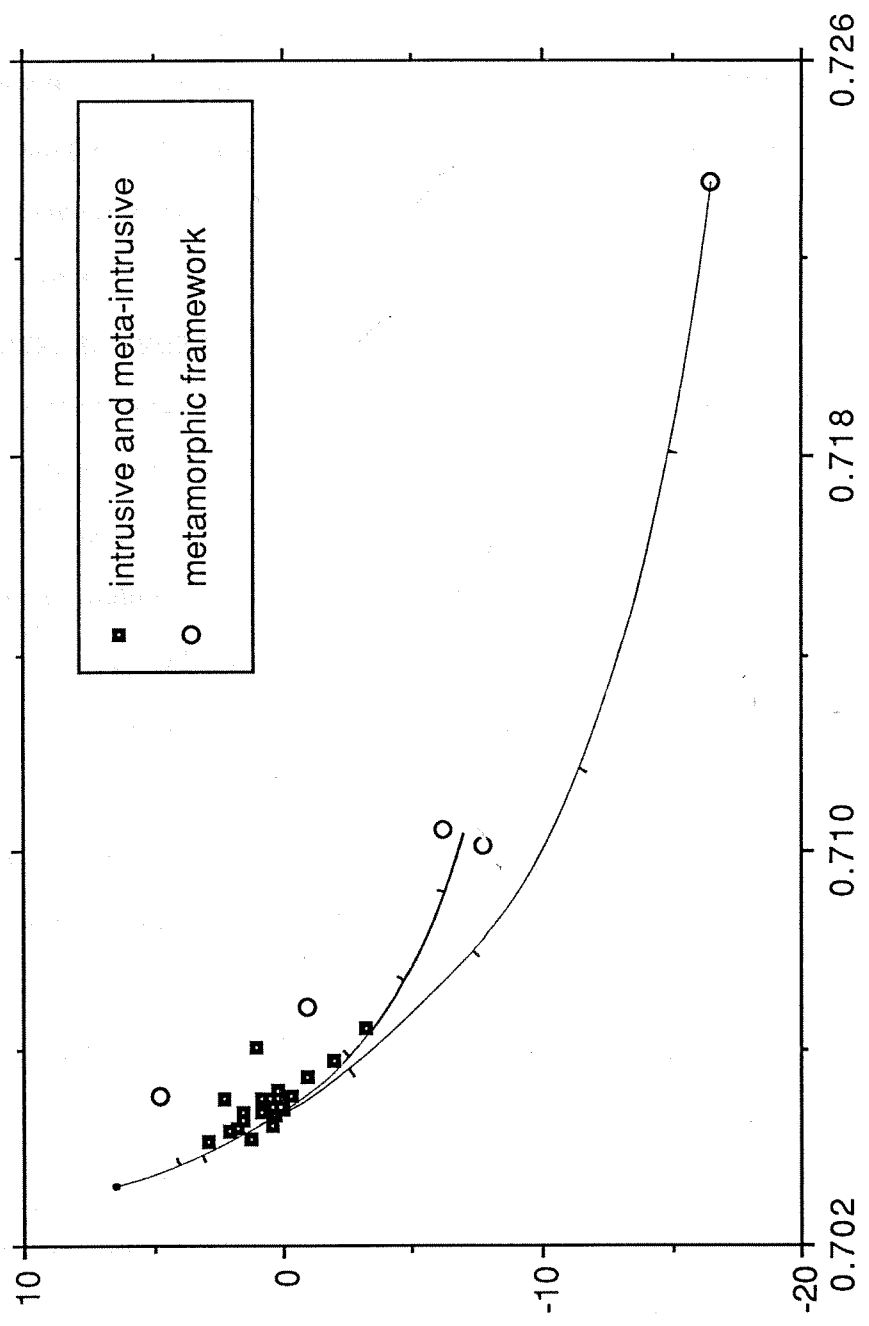
Fig. 3.10

PC35), such large concentration differences are more understandable. Rb differs by 7 to 37%, Sr by 3 to 16%, and $^{87}Rb/^{86}Sr$ by 12 to 21%. Agreement in $^{87}Sr/^{86}Sr$ is very good for two samples (0.3 ε for GC-14/WR643, and identical results for PC35-P/PC35) but worse for GC-1/CM630 (7.0 ε). Again, we prefer the new values, which are determined on larger, less altered samples. It is possible that some of the isotopic discrepancies are due to actual small-scale heterogeneity, but we have not sufficiently explored this possibility to be able to evaluate it.

c. Rb, Sr, Sm, and Nd concentrations

Rb concentrations in the intrusive rocks are low to moderate, with the exception of granite PC35-P (139 ppm), and display a strong bimodal distribution between gabbros/diorites and quartz diorites to granites (Table 3.4 and Figure 3.11). Tonalites (by far the most abundant lithology) in the main study area generally have lower Rb concentrations (Figure 3.11) and Rb/Sr ratios (Figure 3.12) than those in the Bear Valley Springs tonalite to the north. Sr concentrations in the main study area range, with the exception of the two granites (52 and 170 ppm), from 271 to 668 ppm. While the gabbros of the Bear Valley suite tend toward the highest Sr concentrations, tonalites from the two suites span similar ranges (overall 271-510 ppm). Rb and Sr concentrations and Rb/Sr ratios do not show coherent variation patterns with Sr and Nd isotopic ratios (Figure 3.12), demonstrating again a lack of correspondence between isotopic and chemical features in these intrusive rocks.

Nd concentrations (Table 3.5) are quite uniform in the Bear Valley suite, with all but one sample lying between 8.4 and 17.9 ppm. The one exception, PC175, is a recrystallized troctolite which probably owes its low Nd (1.0 ppm) to accumulation of olivine and plagioclase. Nd in the Bear Valley Springs tonalite to the north ranges to somewhat higher values (up to 26 ppm) [Ross, 1989]. Samples of the Tehachapi suite are more varied in their Nd contents (4.2 to 39.4 ppm).

Sm/Nd ratios (Figure 3.13) for most samples are <0.325, indicative of LREE (light rare earth element) enrichment, with rocks from the Tehachapi suite reaching the lowest Sm/Nd. Hornblende gabbros TC-49b and GC-8 have high Sm/Nd (0.353 and 0.347), reflective of LREE depletion. In fact, hornblende-bearing gabbros have the highest Sm/Nd among all samples, higher even than the more "primitive" troctolite PC175. This LREE depletion may be attributed to hornblende accumulation from gabbroic magmas with more LREE enriched patterns. Because of hornblende's relatively high K_D's for the REE in mafic to intermediate systems [Schnetzler and Philpotts, 1970; Arth, 1976], it is the dominant solid phase controlling REE distribution in these gabbros. This is true despite the presence of apatite, which has very high K_D's for the REE, in many of the gabbros. Using the relative REE concentrations in apatite and hornblende from a quartz diorite as reported by Fourcade and Allègre [1981] ($Nd_{ap}/Nd_{hb}=15.1$; $Sm_{ap}/Sm_{hb}=12.7$), we calculate that for a rock containing 40% hornblende and 0.5% apatite with all Nd and Sm in these two phases, 84% of the Nd and 86% of the Sm will reside in hornblende. Combined with other major and trace-element data (see Chapter 4), these high Sm/Nd ratios, as well as the aforementioned bimodality in Rb and Rb/Sr, confirm the cumulate origin of the gabbros. Because of the low Sm/Nd ratios in the hornblende-free gabbros and all other rock-types, it is apparent that the two suites are essentially characterized by LREE enrichment. This is in accord with REE concentrations reported by Ross [1989] on two Tehachapi suite rocks and several samples of the tonalite of Bear Valley Springs.

3.5. Discussion

a. Isotopic constraints on sources

The simplest interpretation of the covariation between ε_{Nd} and $^{87}Sr/^{86}Sr$ seen in the intrusive rocks (exclusive of granites TC-6 and PC35-P) is that they contain contributions from two end-member components, one characterized by high ε_{Nd} and low $^{87}Sr/^{86}Sr$, the

other by low ε_{Nd} and high $^{87}Sr/^{86}Sr$. In Figure 3.10 we model the isotopic trends resulting from mixtures between mantle-derived magmas and metasedimentary rocks. For the mantle end-member, we use $\varepsilon_{Nd}=+6.5$ and $^{87}Sr/^{86}Sr=0.7032$, which are the highest and lowest values, respectively, for Cretaceous Sierra Nevada intrusive rocks [Kistler and Peterman, 1973, 1978; DePaolo, 1981a]. Nd and Sr concentrations (10 and 360 ppm, respectively) are averages for noncumulate mafic rocks intruded into oceanic wall rocks in the western Sierra Nevada [Knott et al., 1990]. Two metasedimentary end-members are used: concentrations and ratios in one are averages of two paragneisses (TC-8 and GC-12) from the Comanche Point unit (Nd=20 ppm, Sr=215 ppm, $\varepsilon_{Nd}=-7.0$, $^{87}Sr/^{86}Sr=0.71027$), while the other uses values for the Kings sequence quartzite CM640 (Nd=15 ppm, Sr=109 ppm, $\varepsilon_{Nd}=-16.5$, $^{87}Sr/^{86}Sr=0.72355$). Both of these metasedimentary components contain Proterozoic continental material, as shown by Nd model ages (Table 3.5) and U/Pb zircon data [Saleeby et al., 1987]. Both mixing curves pass near the data array, with the curve involving Comanche Point paragneisses fitting slightly better. In fact, the Comanche Point rocks are the more appropriate end-member for the majority of the intrusive rocks given their location in the main study area (Figure 3.2). The mixing curve to these gneisses indicates a 15-35% contribution from this component to the Nd and Sr in the intrusive rocks of the main study area, with the Bear Valley Springs tonalites to the north indicating around 50%. These percentages are loosely constrained given the possible variability in end-member Nd and Sr concentrations as well as in isotopic ratios. Therefore, the Nd and Sr isotopic data are consistent with the hypothesis that the magmas of the Tehachapi and Bear Valley suites are mixtures between mafic mantle-derived magmas and continentally-derived metasedimentary rocks represented by the Comanche Point paragneisses. The higher $^{87}Sr/^{86}Sr$ ratios of the Bear Valley Springs tonalites just north of the study area may be due to a larger component of metasedimentary material (also reflected in the higher tonalite Rb concentrations and Rb/Sr ratios -- see Figures 3.11 and 3.12) or to higher

Figure 3.11 - Rb vs. Sr concentrations in ppm, with symbols as in Figure 3.4. Also shown

is the field of data on the Bear Valley Springs tonalite [Kistler and Peterman, 1978; Saleeby

et al., 1987; Kistler and Ross, 1990]; note the overall higher Rb in BVS tonalites relative

to tonalites from the main study area.
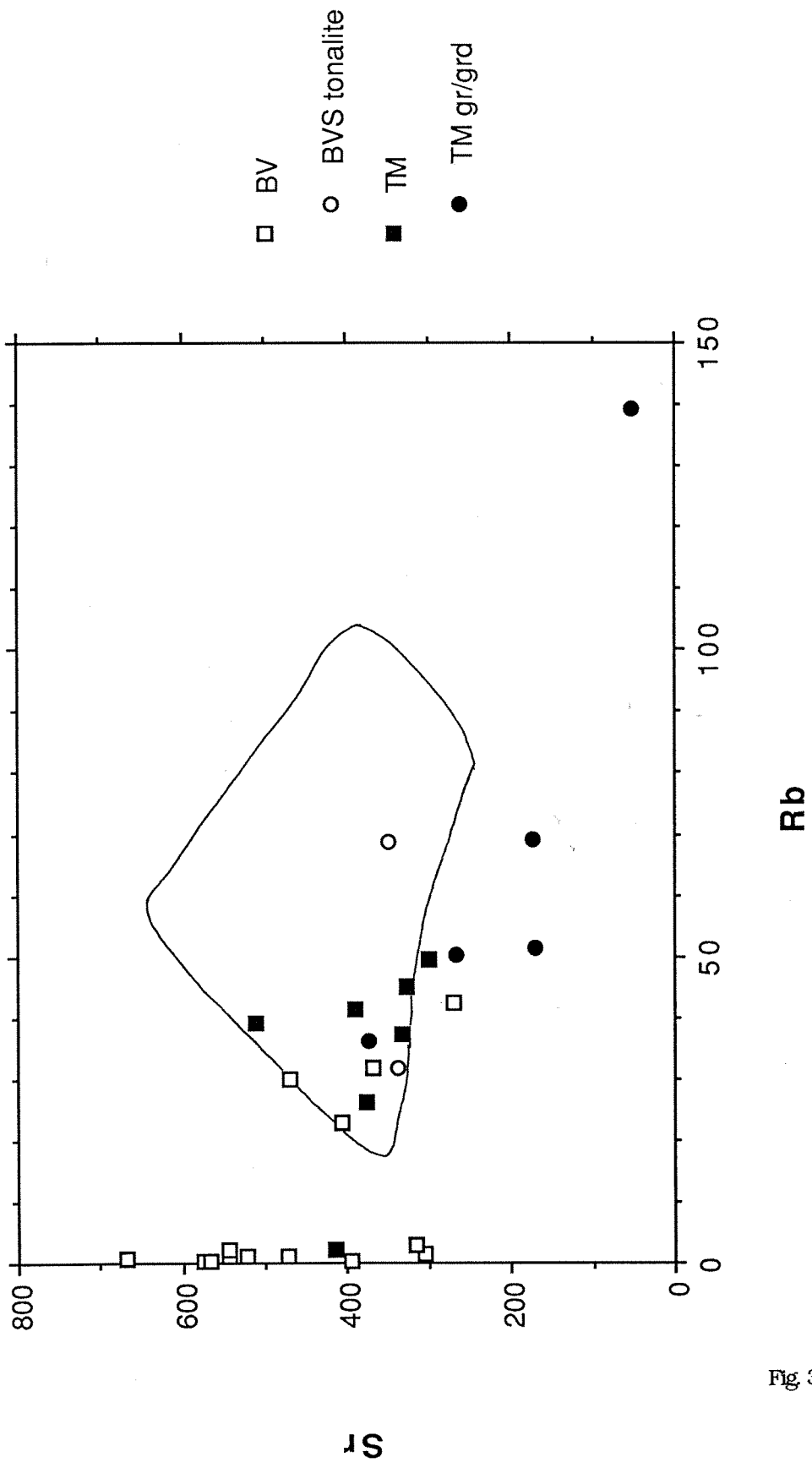
Fig. 3.11

Figure 3.12 - a) Sr (ppm) vs. initial $^{87}Sr/^{86}Sr$ for the intrusive rocks.

b) Rb/Sr (weight) vs. initial $^{87}Sr/^{86}Sr$ for the intrusive rocks, with the field of data for the Bear Valley Springs tonalite [Kistler and Peterman, 1978; Saleeby et al., 1987; Kistler and Ross, 1990]. Note the overall higher $^{87}Sr/^{86}Sr$ and Rb/Sr in the BVS tonalites relative to tonalites in the main study area. Granite PC35-P (TM suite) plots off to the right of the diagram (Rb/Sr=2.67, $^{87}Sr/^{86}Sr$=0.7060). Both diagrams display a lack of correspondence between isotopic and elemental parameters in the main study area.
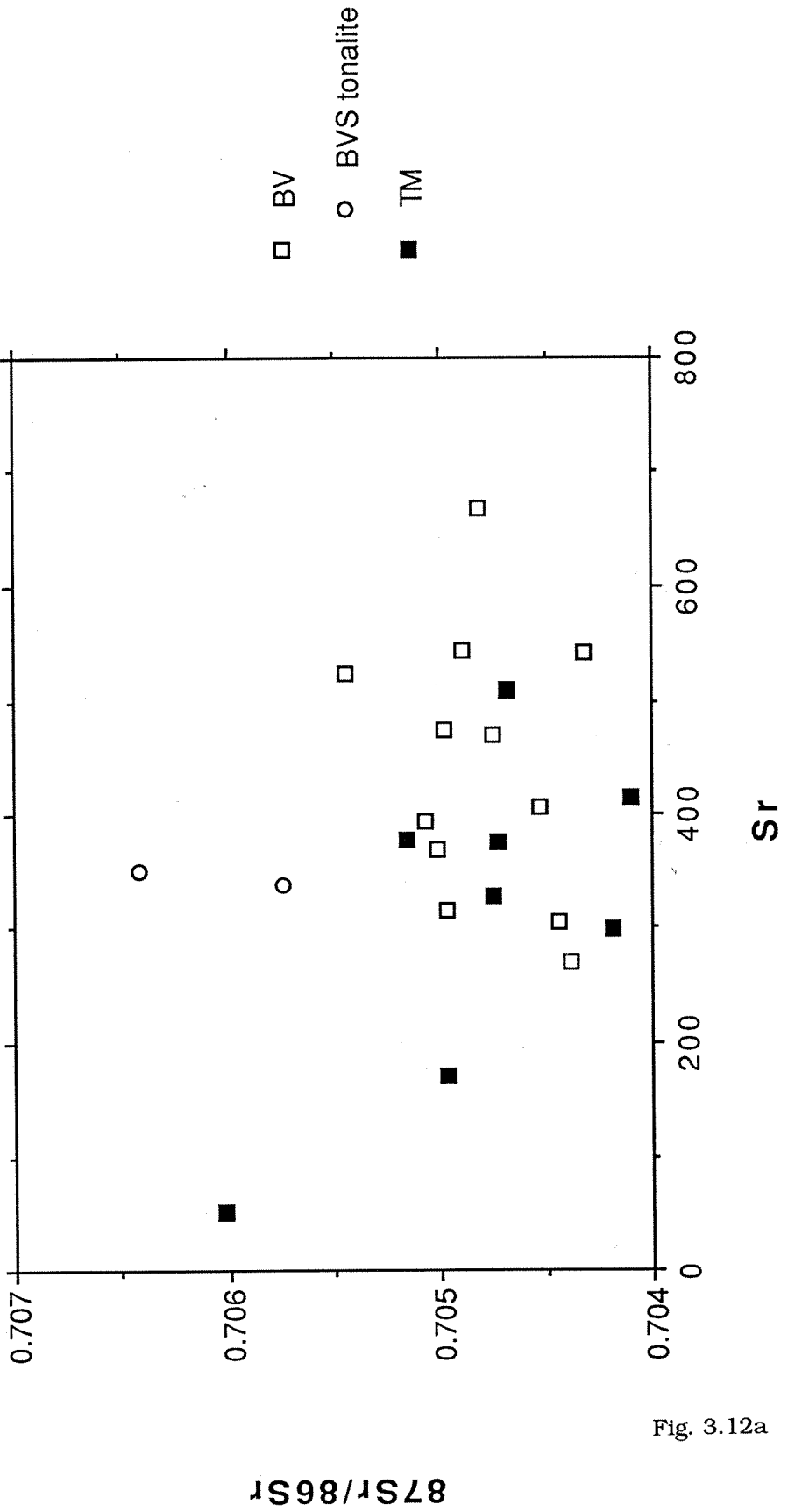
Fig. 3.12a
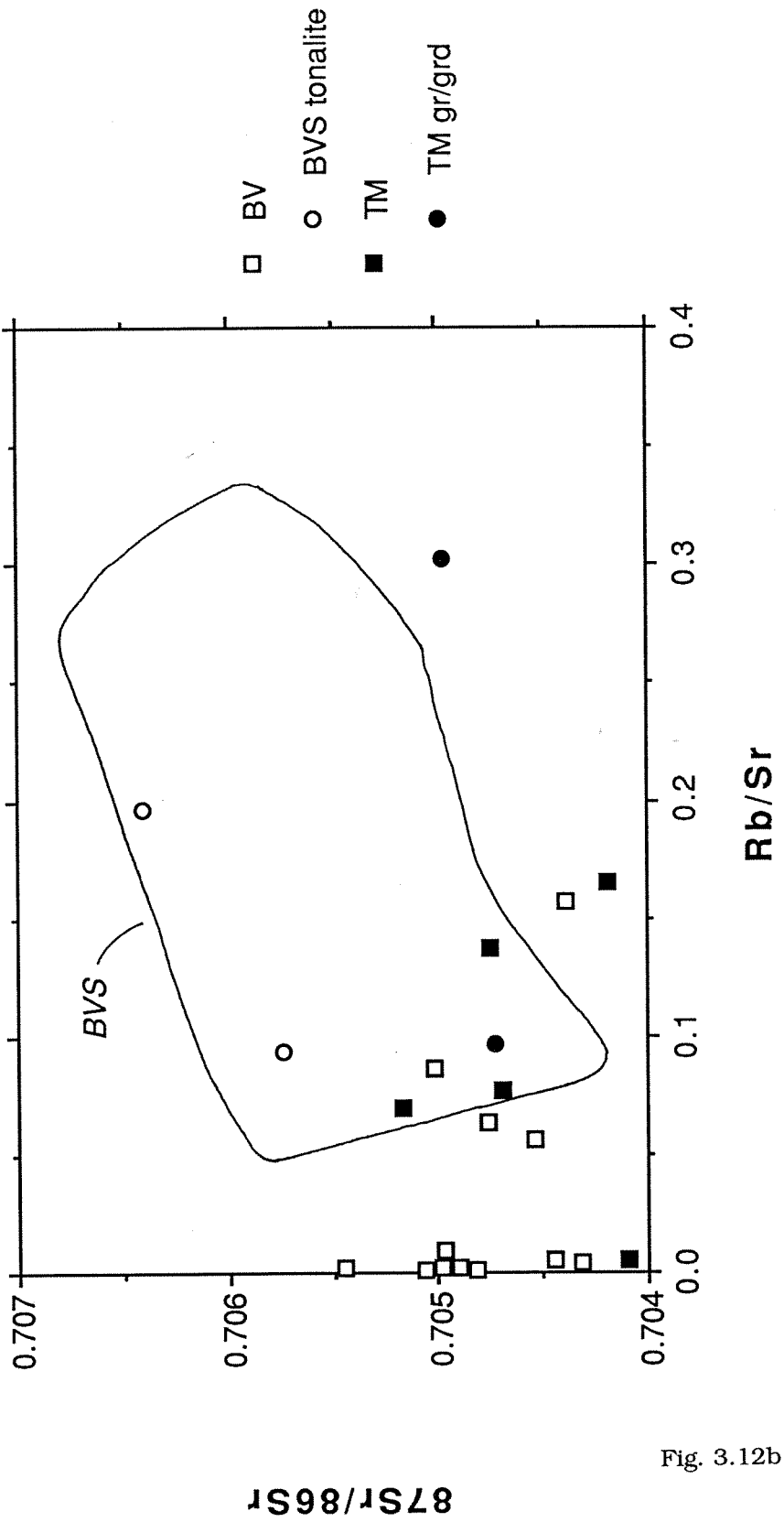
Fig. 3.12b

Figure 3.13 - Sm/Nd (weight) vs. initial ε_{Nd} for the intrusive rocks. Symbols as in Figure 3.4, except hornblende-bearing gabbros of the BV suite are distinguished and TM granites and granodiorite are not. Note the high Sm/Nd in the hornblende-bearing gabbros; the high-Sm/Nd TM sample is a hornblende diorite (GC-60) which may actually belong to the BV suite. The two hornblende-free gabbros (PC175 and TC-47) have low Sm/Nd like the tonalites.
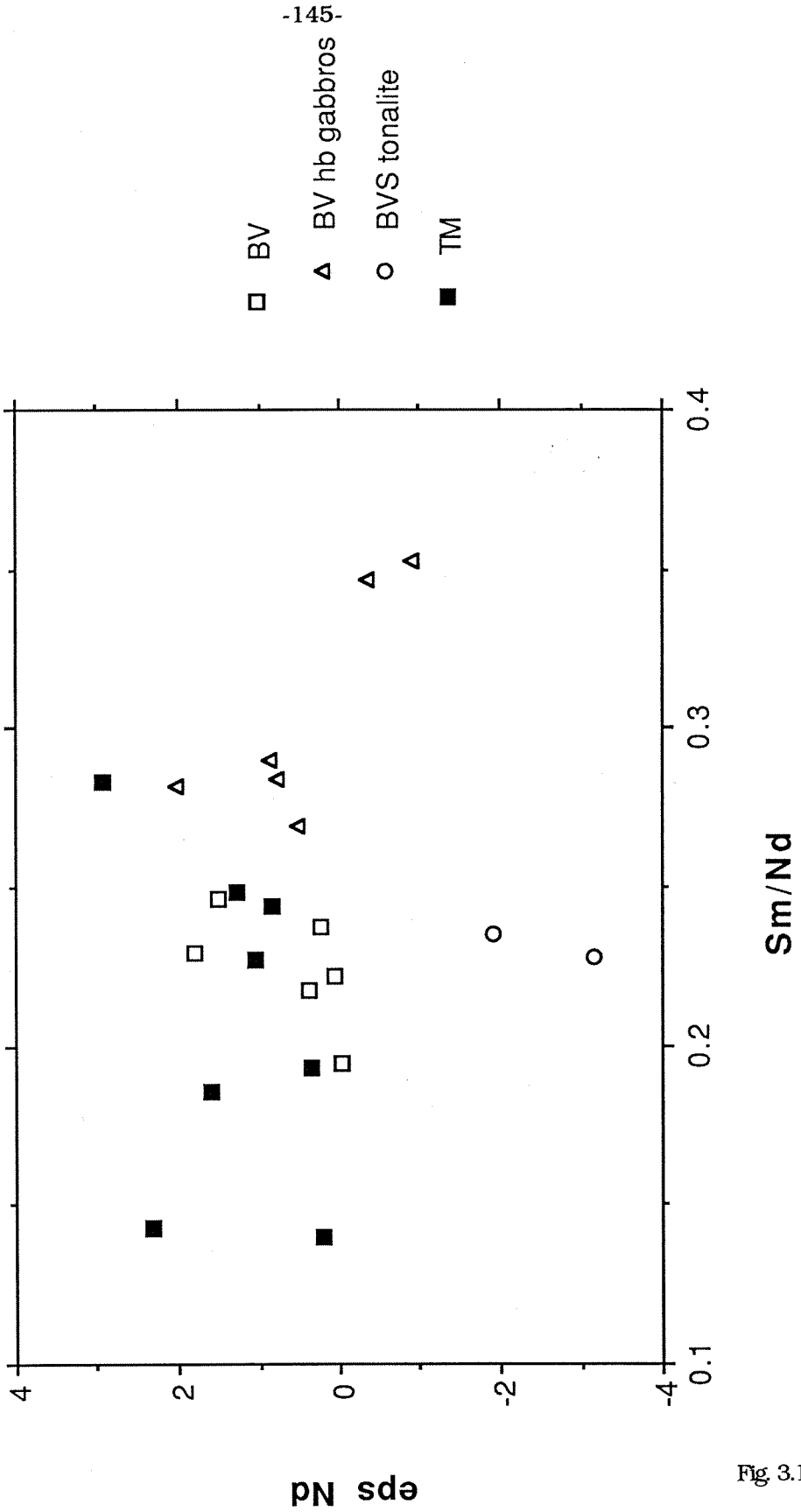
Fig. 3.13

$^{87}Sr/^{86}Sr$ ratios in the metasedimentary component as represented by CM640 [Saleeby et al., 1987] (see below).

The volcanic component apparent in the lower-$^{87}Sr/^{86}Sr$, higher-ε_{Nd} metamorphic rocks may be responsible for the relatively low $^{87}Sr/^{86}Sr$ (~0.710) and high ε_{Nd} (~-7) of the metasedimentary rocks of the main study area relative to other framework rocks such as quartzite CM640 (0.7236, -17), which is exposed in an area with higher-$^{87}Sr/^{86}Sr$, lower-ε_{Nd} intrusive rocks (e.g., Bear Valley Springs tonalites CM9 and TC42). As suggested by Saleeby et al. [1987], this distinction in preintrusive materials may be partly responsible for the contrasting Sr (and Nd) isotopic ratios in intrusive rocks from the two areas. In fact, the involvement of these volcanic components in the main study area lends strength to the mixing argument by allowing for less mixing of high-SiO_2 material to reach the observed Nd and Sr ratios. It should be noted, however, that the isotopic array defined by the majority of the intrusive rocks does not show a distinct trend toward the apparently volcanic-rich metamorphic rocks (see below).

This scenario involving mantle magma-metasediment mixing is consistent with the elevated $\delta^{18}O$ values for many of the intrusive rocks (Table 3.4 and Saleeby et al. [1987]) and with the presence in a number of the rocks of zircons displaying inheritance patterns with upper intercepts of 1400-2000 Ma (e.g., Figure 3.3), as originally suggested by Saleeby et al. [1987]. The Pb isotopic data are also consistent with this model. The Pb ratios for the four intrusive samples (Figure 3.9) fall among the "western" values of Chen and Tilton [1991], which they interpret as a mixing array between primitive arc magmas (less radiogenic Pb) and metasedimentary rocks (more radiogenic Pb). While overall the Pb data from the Sierra Nevada batholith require at least one additional end member [Silver, 1987; Silver and Chappell, 1988; Chen and Tilton, 1991], the data for the "western" rocks, which include the Tehachapi samples, are satisfied by such a two-component mixture.

Alternative explanations for the isotopic data must be considered. These include:

1. *The isotope ratios reflect mantle sources for the magmas.* In this scenario, quartz dioritic to granitic magmas must all originate by fractional crystallization of mantle-derived gabbroic magmas derived from an isotopically (Nd and Sr) heterogeneous mantle. There is evidence for some isotopic variation in the mantle beneath the Sierra Nevada to the north, at least during the Cenozoic [Van Kooten, 1981; Domenick et al., 1983; Mukhopadhyay et al., 1988]. However, basalts showing this heterogeneity are typically of strongly alkaline character in contrast to the calcic-calcalkaline batholithic rocks of the present study. Furthermore, there is no evidence linking the basalts' highly unique enriched mantle sources, or the sources of xenoliths of inferred cumulate origin [Mukhopadhyay et al., 1988], to Mesozoic processes. The most significant argument against this model is the observed high $\delta^{18}O$ values for the rocks (up to 10.9), with even gabbros reaching as high as 8.6. Such values are well above typical $\delta^{18}O$ for mantle-derived magmas (5-7; Kyser [1986]) and are too high to be attributed solely to fractionation effects [Taylor, 1968]. They require a component of material which has existed in a supracrustal environment at some point in its history.

2. *The ratios reflect variations in deep-crustal and/or upper mantle basaltic sources.* This type of model has been invoked by Gromet and Silver [1987] and Silver and Chappell [1988] for the Peninsular Ranges batholith in southern California. In the Tehachapi rocks, the oxygen isotopic data (see above) show that this model must involve a component of basaltic material which existed at some point in time at the earth's surface, e.g., MORB. The $\delta^{18}O$ values are not satisfied solely by sources originating as underplated deep-crustal gabbros. If the high-^{18}O component were altered oceanic crust [McCulloch et al., 1981], this would explain the overall correlation between $^{87}Sr/^{86}Sr$ and $\delta^{18}O$ observed in the area [Saleeby et al., 1987]. However, since alteration of oceanic crust does not observably affect the Nd isotope ratios, this model does not explain the Nd-Sr covariation. Since the

hypothesized oceanic basaltic sources would most likely have originated from a depleted mantle source, any variation in ε_{Nd} might reflect variation in the ages of the basalts. However, since MORB typically has LREE-depleted patterns [e.g., Sun et al., 1979], it would be difficult to generate the lower ε_{Nd} values observed, even given large amounts of time. In summary, the $\delta^{18}O$ data argue against mantle-derived gabbroic sources, and the ε_{Nd} values and anticorrelation with $^{87}Sr/^{86}Sr$ ratios argue against altered oceanic crustal sources.

It is clear that the combined Nd, Sr, O, and Pb data are best explained by the mixing model discussed above. However, mixing is not demonstrated by isotope-element concentration plots such as Figures 3.12 and 3.13. The more silicic intrusive rocks do not in general have the highest $^{87}Sr/^{86}Sr$ and lowest ε_{Nd} expected had they originated as magmas richer in the higher-SiO_2 metasedimentary end member (Figure 3.5). Also, gabbros located closer to partially melted metasedimentary rocks do not show trends towards more "continental" isotopic ratios; in fact, the gabbro with the highest $^{87}Sr/^{86}Sr$ and lowest ε_{Nd} (TC-49b) is from the deepest interior of the Tunis Creek body (Figures 3.6 and 3.7). An important conclusion from these observations is that, while the isotopic data demonstrate a mantle-metasediment mixing origin for the intrusive rocks, the mixing is not reflected in the bulk chemistry of the magmas. That is, genesis of the more chemically evolved magmas of the Tehachapi Mountains was not contingent on nor accompanied by crustal interaction. It follows that mixing between mantle-derived mafic magmas and continental-affinity metasedimentary materials must have taken place at levels deeper than 30 km, and that superposed crystal fractionation processes played the dominant role in producing the lithologic diversity observed in the Tehachapi igneous suites. Bulk-rock and mineral chemical data (see Chapter 4) support this conclusion and demonstrate that the magmas from which the gabbros accumulated were already quite evolved, making it more reasonable that they had mixed with large amounts of metasedimentary material

while maintaining their "gabbroic" character. (A metasedimentary component in the gabbroic rocks is further supported by the zircon inheritance pattern of a Tunis Creek gabbro [Saleeby et al., 1987]). Of course, had the mantle magmas had less "MORB-like" Nd and Sr isotopic ratios than the mantle component modeled above, the amount of metasedimentary component necessary to attain the ratios in the intrusive rocks would be lower [see also Saleeby et al., 1987].

In a general way, this model for batholith magmatism shares much with the "MASH" hypothesis of Hildreth and Moorbath [1988] relating to Andean magmatism in what is probably a modern tectonic analogue for the Cretaceous Sierra Nevada batholith. They envision the deep crust as the primary site of hybridization of arc magmas as mantle-derived magmas mix with crustal melts. Apparently, the analogous zone in the Sierra Nevada batholith lay at levels deeper than 30 km.

Dodge et al. [1986] have identified possible analogues of the metasedimentary component in a suite of deep crustal xenoliths from a Neogene trachybasalt flow in the central Sierra Nevada. These "high-alumina granulites" have the requisite high $^{87}Sr/^{86}Sr$ (0.7084-0.7107) and high $\delta^{18}O$ (7.7-13.4), and other geochemical features suggest that they may be residues after partial melting of metasedimentary protoliths. Interestingly, the $^{87}Sr/^{86}Sr$ ratios (at 104 Ma) of ultramafic xenoliths which Dodge et al. [1986] ascribe to deep batholith accumulation span a range (0.7044-0.7054) similar to the deep batholithic rocks of the Tehachapi Mountains. It is apparent that crustal interaction has affected the deep mafic precursors to these cumulates to the same extent as in the Tehachapi Mountains. (The higher $^{87}Sr/^{86}Sr$ of the batholithic rocks exposed in the area (~0.7074) indicates that higher-level assimilation of continental materials may have taken place as well.)

b. Isotopically "anomalous" granites

The Nd and Sr isotopic ratios for the three granite/granodiorites, in particular for

TC-6 and PC35-P, do not fall within the mixing trend defined by the other samples, but lie at relatively high $^{87}Sr/^{86}Sr$ for a given ε_{Nd} (Figure 3.4). This deviation could be due to either of two factors. First, the granitic magmas may have had primary Nd and Sr isotopic ratios lying in the main trend, and interaction with Sr-rich, Nd-poor fluids with high $^{87}Sr/^{86}Sr$ caused an increase in $^{87}Sr/^{86}Sr$ with ε_{Nd} unchanged. These fluids could have been similar to seawater, which has the appropriately large Sr/Nd and $^{87}Sr/^{86}Sr$ ratios that would yield a horizontal mixing trajectory in plots such as Figure 3.4. The fluids could have partly originated in sedimentary rocks which were subjected to dehydration metamorphism. Thermodynamic estimates by Pickett and Saleeby [1991] suggest that the intrusive rocks were subjected to a variety of metamorphic fluids in channelized flow regimes during the slow cooling expected in such a deep-seated environment. Studies concerned with the mobility of the REE in high-temperature fluids in the crust have failed to lead to consensus [summary in Grauch, 1989], but the evidence favors the rarity of mobility beyond the scale of a few centimeters [Seifert and Chadima, 1989]. Thus, it is plausible that subsolidus fluid interaction with the granites could have caused Sr isotopic shifts with little or no effect on Nd ratios. The unusual chemistry of PC35-P, in particular (see Chapter 4), with very high SiO_2, K_2O, and Rb, and low Ba and Sr, is suggestive of fluid involvement, as is evidence in this same rock for open-system, late-stage disturbance of zircon U/Pb systematics [PC35 in Saleeby et al., 1987]. While the incipient mylonitic fabric in PC35-P is a possible indication of some amount of fluid interaction, TC-6 is undeformed.

Alternatively, the distinct isotopic ratios of these rocks could reflect a high proportion of a source component from metamorphic rocks like GC-2 and GV-14 with a "volcanic" signature (i.e., relatively high $^{87}Sr/^{86}Sr$ for a given ε_{Nd} - see Figure 3.10). This is plausible, but there is no *a priori* reason to expect that the more silicic magmas would result from interaction with this particular class of metamorphic rocks. It would be

expected that other granites would show a stronger proportion of the higher-$^{87}Sr/^{86}Sr$, lower-ε_{Nd} metamorphic rocks (e.g., GC-12 and TC-8), which are also exposed in the vicinity of the granites. The data here and the Sr isotopic data of Saleeby et al. [1987] on other granites of the Tehachapi Mountains suite show no evidence for a stronger proportion of such metasedimentary material. The first hypothesis calling on fluid exchange of Sr, probably under subsolidus conditions, is the simpler and more plausible alternative. These rocks represent departures from the main petrogenetic trends which favor the processes described in the previous section.

c. Isotopic data within the context of batholith-wide variations

As noted above, the Nd, Sr, and Pb isotopic ratios of the Tehachapi intrusive rocks support an affinity with the western part of the main Sierra Nevada batholith. (This excludes rocks from south of the Pastoria fault, which have been transported from relatively farther east [Ross, 1989].) Whereas early Sr isotopic studies of the batholith [Hurley et al., 1965; Kistler and Peterman, 1973, 1978] led to the view, promulgated by the Nd study of DePaolo [1981a], that two source components for the magmas were sufficient, later O and Pb isotopic studies have revealed more complexity. The $^{18}O/^{16}O$ data of Masi et al. [1981], as adapted by Taylor [1988] and Kistler [1990], suggest that in the southern and western Sierra Nevada the continental component is metasedimentary (high $^{87}Sr/^{86}Sr$, high $\delta^{18}O$), while in the east-central batholith it is old crystalline igneous crust (high $^{87}Sr/^{86}Sr$, lower $\delta^{18}O$). On the basis of this distinction, as well as other geochemical and geological observations, Kistler [1990] sharply divides the metamorphic framework of the Sierra Nevada into two prebatholithic lithosphere zones: the Panthalassan (south and west) and North American (central) zones. The Pb isotopic data of Silver [1987] and Chen and Tilton [1991] show a peak in $^{206}Pb/^{204}Pb$, $^{207}Pb/^{204}Pb$, and $^{208}Pb/^{204}Pb$ ratios along the middle of the batholith, roughly corresponding to Kistler's lithospheric boundary. Chen and Tilton [1991] interpret this high-Pb-ratio line as a boundary between a western zone

where "primitive arc" or mantle-type low Pb isotope ratios increase to the east due to interaction with metasedimentary materials with high Pb ratios, and an eastern zone where lower $^{206}Pb/^{204}Pb$ and $^{207}Pb/^{204}Pb$ ratios reveal the presence of high-grade crystalline lower crust (Figure 3.9). The O and Pb isotopic data independently point to this generalized, spatially dependent, three-component model. Such spatial variations and sharp isotopic boundaries argue against the importance of sublithospheric mixing, such as in the subducted slab, in causing batholithic variability.

This three-component hypothesis of batholith-wide petrogenesis is also consistent with the sulfur isotopic data of Ishihara and Sasaki [1989] from the central batholith. They show that the western plutons, which, like the Tehachapi intrusive rocks, tend toward lesser magnetite abundance ("ilmenite series"), have low $\delta^{34}S$ values suggestive of a contribution from sedimentary materials. They deduce that this sedimentary component was most likely incorporated at great depths. Eastern plutons ("magnetite series"), on the other hand, have higher $\delta^{34}S$ values suggestive of purely "I-type" sources.

Within the western segment of the batholith, the eastward increase in $^{87}Sr/^{86}Sr$ [Kistler and Peterman, 1973, 1978; Kistler and Ross, 1990] can be explained as resulting from an eastward increase in the metasedimentary component in the magmas. However, a major conclusion of the present study is that crustal interaction is not strongly manifest at 30 km depths and was active at lower levels. This implies that to attribute the eastward isotopic gradient to greater metasedimentary component requires an eastward thickening of the prebatholithic crust. While this is possible, it may be simpler to attribute the eastward gradient to a gradient in the *average isotopic character* of the prebatholithic crust. This gradient is implied in the isotopic data on the metamorphic rocks of the Tehachapi Mountains, which reveal a contribution of detritus from a volcanic arc-like source with lower $^{87}Sr/^{86}Sr$ and higher ε_{Nd} in the more western metamorphic rocks. If the isotopic ratios of quartzite CM640 ($^{87}Sr/^{86}Sr=0.7236$, $\varepsilon_{Nd}=-17$) are representative of the

more "eastern" character of the western batholith framework, then the higher $^{87}Sr/^{86}Sr$ and lower ε_{Nd} of the Bear Valley Springs tonalite [Saleeby et al., 1987; this study] to the northeast of the main study area could reflect these more "eastern" ratios. On the other hand, the higher Rb and Rb/Sr in Bear Valley Springs tonalites as compared to tonalites in the main study area (Figures 3.11 and 3.12) seems to imply a *larger* metasedimentary component rather than interaction with an isotopically *different* component. (Note in Table 3.4 that the metamorphic rocks with more "volcanic" component are not distinct in terms of Rb or Rb/Sr.) Throughout the batholith, data on framework rocks are insufficient to fully evaluate the idea of west-to-east gradients, but, as mentioned above, there is a higher proportion of mafic to intermediate volcanic strata in the western facies of the Kings sequence prebatholithic assemblage [Saleeby et al., 1978].

In the context of the three-component batholith model, the intrusive rocks of the Tehachapi Mountains belong to that portion of the batholith where the evidence favors the mantle magma-metasediment mixing hypothesis. The lack of a west-to-east increase in the high-$^{87}Sr/^{86}Sr$, low-ε_{Nd} component in the main study area (Figures 3.6 and 3.7), in contrast to the fairly regular increase in same in the batholith to the north, may be attributed to several factors. 1) Fluid interaction such as that which may have affected the granites could have obliterated any map patterns of $^{87}Sr/^{86}Sr$ variation. This could be a factor, but ε_{Nd} values also fail to show a pattern. 2) There may have been extensive tectonic shuffling of different fault slices during events related to the deformation and/or subsequent uplift of the Tehachapi rocks [Pickett and Saleeby, 1991]. It is possible that some tectonic boundaries could remain unrecognized after extensive study because of poor exposure and lack of distinctive marker horizons, but zones of major relative motion within the boundaries of the study area have not been identified. 3) Proposed clockwise tectonic rotation of the Tehachapi Mountains block since the Cretaceous [McWilliams and Li, 1985] implies that the present northeast-southwest trend of the range (Figure 3.2) originated in

a north-south alignment. Thus, the isotopic patterns would be viewed in the context of *longitudinal* variations, which may not be as regular as transverse variations. Structural orientations in the study area [Pickett and Saleeby, 1991] are not completely consistent with the rotation hypothesis, which is partially subject to the uncertainties associated with paleomagnetic determinations on intrusive rocks. 4) It is possible that west-to-east isotopic variations are not present at these depths in the batholith. The geobarometric estimates of Pickett and Saleeby [1991] suggest that the higher-$^{87}Sr/^{86}Sr$, lower-ε_{Nd} tonalites of the Bear Valley Springs batholith were intruded at somewhat higher levels, limiting our knowledge of isotopic variability at the lowest levels observed (30 km). A lack of transverse gradients in the deep batholith is suggested by the xenolith study of Dodge et al. [1986] in the central Sierra Nevada, where deep-crustal, presumably syn-batholithic ultramafic cumulate rocks have less "evolved" Sr isotopic ratios than the corresponding upper crustal granodiorite (see above). The ultramafic rock $^{87}Sr/^{86}Sr$ ratios, in fact, are similar to those in the Tehachapi rocks. This observation suggests the possibility that at least some of the isotopic variability in the upper batholith is inherited at levels higher than 30 km. Full evaluation of this hypothesis is beyond the scope of this paper. A major impediment to such speculation is the uncertainty of exactly where the Tehachapi magmas lie within the context of the transverse geochemical variations in the batholith.

3.6. Conclusions

1)   Intrusive rocks of 101-105 Ma age reach farther west (to Grapevine Canyon) than previously recognized in the southernmost Sierra Nevada batholith.

2)   The Nd, Sr, Pb, and O isotopic ratios of the deep batholithic rocks of the Tehachapi Mountains, including cumulate gabbros, are consistent with an origin as mixtures between mafic mantle-derived magmas and metasedimentary rocks of continental provenance. There is also a possible metavolcanic component which could be responsible for keeping

$^{87}Sr/^{86}Sr$ relatively low and ε_{Nd} high.

3)   The Tehachapi rocks do not represent the actual sites of this hypothesized interaction, since chemical and isotopic characteristics do not vary systematically. Hybridization of these arc magmas took place in the deeper batholith (>30 km), and evolution of the varied intrusive lithologies is most strongly a function of fractionation processes.

4)   Rocks of the tonalite of Bear Valley Springs, to the north and east of the highest pressure rocks of the main study area, show isotopic and trace-element evidence for a larger metasedimentary component. It is unclear whether this is a function of vertical or lateral gradients in the batholith.

5)   The intrusive rocks display an affinity with the western segment of the main Sierra Nevada batholith, where other isotopic studies have suggested the involvement of the same two components.

References

Ague, J.J., and G. H. Brimhall, Magmatic arc asymmetry and distribution of anomalous plutonic belts in the batholiths of California: Effects of assimilation, crustal thickness, and depth of crystallization, *Geol. Soc. Amer. Bull., 100*, pp. 912-927, 1988.

Allègre, C.J., and D. Ben Othman, Nd-Sr isotopic relationship in granitoid rocks and continental crust development: a chemical approach to orogenesis, *Nature, 286*, pp. 335-342, 1980.

Arth, J.G., Behavior of trace elements during magmatic processes -- a summary of theoretical models and their applications, *J. Res. U.S. Geol. Survey, 4*, pp. 41-47, 1976.

Chen, J.H., and G.R. Tilton, Applications of lead and strontium isotopic relationships to the petrogenesis of granitoid rocks, central Sierra Nevada batholith, California, *Geol. Soc. Amer. Bull.*, in press, 1991.

Chen, J.H., and G.J. Wasserburg, Isotopic determination of uranium in picomole and subpicomole quantities, *Anal. Chem., 53*, pp. 2060-2067, 1981.

DePaolo, D.J., Study of magma sources, mantle structure, and the differentiation of the earth from variations of $^{143}Nd/^{144}Nd$ in igneous rocks, Ph.D. thesis, 360 pp., California Institute of Technology, Pasadena, Ca., 1978.

DePaolo, D.J., A neodymium and strontium isotopic study of the Mesozoic calc-alkaline granitic batholiths of the Sierra Nevada and Peninsular Ranges, California, *J. Geophys. Res., 86*, pp. 10470-10488, 1981a.

DePaolo, D.J., Neodymium isotopes in the Colorado Front Range and crust-mantle evolution, *Nature, 291*, pp. 193-196, 1981b.

DePaolo, D.J., and G.J. Wasserburg, Neodymium isotopic variations and petrogenetic models, *Geophys. Res. Lett., 3*, pp. 249-252, 1976.

Dodge, F.C.W., and R.W. Kistler, Some additional observations on inclusions in the granitic rocks of the Sierra Nevada, *J. Geophys. Res., 95*, pp. 17841-17848, 1990.

Dodge, F.C.W., L.C. Calk, and R.W. Kistler, Lower crustal xenoliths, Chinese Peak lava flow, central Sierra Nevada, *J. Petrol., 27*, pp. 1277-1304, 1986.

Doe, B.R., and R.E. Zartman, Plumbotectonics, the Phanerozoic, in *Geochemistry of Hydrothermal Ore Deposits (2nd ed.)*, edited by H.L. Barnes, pp. 22-70, New York, John Wiley and Sons, 1979.

Domenick, M.A., R.W. Kistler, F.C.W. Dodge, and M. Tatsumoto, Nd and Sr isotopic study of crustal and mantle inclusions from the Sierra Nevada and implications for batholith petrogenesis, *Geol. Soc. Amer. Bull., 94*, pp. 713-719, 1983.

Fourcade, S., and C.J. Allegre, Trace elements behavior in granite genesis: a case study - the calc-alkaline plutonic association from the Querigut complex (Pyrénées, France), *Contrib. Mineral. Petrol., 76*, pp. 177-195, 1981.

Goodman, E.D., and P.E. Malin, Evolution of the southern San Joaquin Basin and mid-Tertiary "transitional" tectonics, central California, *Tectonics*, in press, 1991.

Grauch, R.I., Rare earth elements in metamorphic rocks, in *Geochemistry and Mineralogy of Rare Earth Elements*, edited by B.R. Lipin and G.A. McKay, Mineral. Soc. Amer., *Reviews in Mineralogy, 21*, pp. 147-167, 1989.

Gromet, L.P., and L.T. Silver, REE variations across the Peninsular Ranges batholith: implications for batholithic petrogenesis and crustal growth in magmatic arcs, *J. Petrol., 28*, pp. 75-125, 1987.

Grünenfelder, M.H., G.R. Tilton, K. Bell, and J. Blenkinsop, Lead and strontium isotope relationships in the Oka carbonatite complex, Quebec, *Geochim. Cosmochim. Acta, 50*, pp. 461-468, 1986.

Hamilton, P.J., R.K. O'Nions, and R.J. Pankhurst, Isotopic evidence for the provenance of some Caledonian granites, *Nature, 287*, pp. 279-284, 1980.

Hildreth, W., and S. Moorbath, Crustal contributions to arc magmatism in the Andes of central Chile, *Contrib. Mineral. Petrol., 98*, pp. 455-489, 1988.

Hurley, P.M., P.C. Bateman, H.W. Fairbairn, and W.H. Pinson, Jr., Investigation of initial $^{87}Sr/^{86}Sr$ ratios in the Sierra Nevada plutonic province, *Geol. Soc. Amer. Bull., 76*, pp. 165-174, 1965.

Ishihara, S., and A. Sasaki, Sulfur isotopic ratios of the magnetite-series and ilmenite-series granitoids of the Sierra Nevada batholith -- A reconnaissance study, *Geology, 17*, pp. 788-791, 1989.

Jaffey, A.H., K.F. Flynn, L.E. Glendenin, W.C. Bentley, and A.M. Essling, Precision measurement of the half-lives and specific activities of ^{235}U and ^{238}U, *Phys. Rev., C4*, pp. 1889-1906, 1971.

Kistler, R.W., Two different lithosphere types in the Sierra Nevada, California, in *The Nature and Origin of Cordilleran Magmatism, Geol. Soc. Amer. Memoir 174*, edited by J.L. Anderson, pp. 271-281, 1990.

Kistler, R.W., and Z.E. Peterman, Variations in Sr, Rb, K, Na, and initial Sr^{87}/Sr^{86} in Mesozoic granitic rocks and intruded wall rocks in central California, *Geol. Soc. Amer. Bull., 84*, pp. 3489-3512, 1973.

Kistler, R.W., and Z.E. Peterman, Reconstruction of crustal blocks of California on the basis of initial strontium isotopic compositions of Mesozoic granitic rocks, *U.S. Geol. Survey Prof. Paper 1071*, 17 pp., 1978.

Kistler, R.W., and D.C. Ross, A strontium isotopic study of plutons and associated rocks of the southern Sierra Nevada and vicinity, California, *U.S. Geol. Survey Bull. 1920*, 20 pp., 1990.

Kistler, R.W., B.W. Chappell, D.L. Peck, and P.C. Bateman, Isotopic variation in the Tuolumne Intrusive Suite, central Sierra Nevada, California, *Contrib. Mineral. Petrol.*, *94*, pp. 205-220, 1986.

Knott, D.C., J.B. Saleeby, H.P. Taylor, Jr., and B.W. Chappell, Petrology of the Early Cretaceous Sierra Nevada batholith: the Stokes Mountain region, California, *Eos Trans. Amer. Geoph. Union, 71*, p. 1576, 1990.

Krogh, T.E., A low contamination method for hydrothermal decomposition of zircon and extraction of U and Pb for isotopic age determinations, *Geochim. Cosmochim. Acta, 37*, pp. 485-494, 1973.

Kyser, T.K., Stable isotope variations in the mantle, in *Stable Isotopes in High Temperature Geological Processes*, edited by J.W. Valley, H.P. Taylor, Jr., and J.R. O'Neil, Mineral. Soc. Amer., *Reviews in Mineralogy, 16*, pp. 141-164, 1986.

Masi, U., J.R. O'Neil, and R.W. Kistler, Stable isotope systematics in Mesozoic granites of central and northern California and southwestern Oregon, *Contrib. Mineral. Petrol.*, *76*, pp. 116-126, 1981.

McCulloch, M.T., and B.W. Chappell, Nd isotopic characteristics of S- and I-type granites, *Earth Planet. Sci. Lett., 58*, pp. 51-64, 1982.

McCulloch, M.T., R.T Gregory, G.J. Wasserburg, and H.P. Taylor, Jr., Sm-Nd, Rb-Sr, and $^{18}O/^{16}O$ isotopic systematics in an oceanic crustal section: evidence from the Samail ophiolite, *J. Geophys. Res., 86*, pp. 2721-2735, 1981.

McWilliams, M.O., and Y. Li, Tectonic oroclinal bending of the southern Sierra Nevada batholith, *Science, 230*, 172-175, 1985.

Mukhopadhyay, B., W.I. Manton, and D.C. Presnall, Petrographic, chemical, and isotopic constraints on the origin of garnet pyroxenite xenoliths from the Big Creek volcanic pipe, Sierra Nevada batholith (abstract), *Eos Trans. Amer. Geoph. Union, 69*, p. 1517, 1988.

Noble, S.R., P.C. Lightfoot, and U. Schärer, A new method for single-filament isotopic analysis of Nd using in situ reduction, *Chem. Geol., 79*, pp. 15-19, 1989.

Patchett, P.J., and J. Ruiz, Nd isotopic ages of crust formation and metamorphism in the Precambrian of eastern and southern Mexico, *Contrib. Mineral. Petrol., 96*, pp. 523-528, 1987.

Pickett, D.A., and J.B. Saleeby, Petrogenetic and isotopic studies of mid-crustal batholithic rocks of the Tehachapi Mountains, Sierra Nevada, California (abstract), *Geol. Soc. Amer. Abstract Progr., 21*, p. A197, 1989.

Pickett, D.A., and J.B. Saleeby, Thermobarometric constraints on the depth of exposure and conditions of plutonism and metamorphism at deep levels of the Sierra Nevada

batholith, Tehachapi Mountains, California, *J. Geophys. Res.*, in press, 1991. **See Chapter 2.**

Pickett, D.A., and G.J. Wasserburg, Nd and Sr isotopic characteristics of New Zealand granitoids and related rocks, *Contrib. Mineral. Petrol., 103,* pp. 131-142, 1989. **See Appendix 1.**

Ross, D.C., Mafic gneissic complex (batholithic root?) in the southernmost Sierra Nevada, California, *Geology, 13,* pp. 288-291, 1985.

Ross, D.C., The metamorphic and plutonic rocks of the southernmost Sierra Nevada, California, and their tectonic framework, *U.S. Geol. Survey Prof. Paper 1381,* 159 pp., 1989.

Saleeby, J.B., Progress in tectonic and petrogenetic studies in an exposed cross-section of young (~100 Ma) continental crust, southern Sierra Nevada, California, in *Exposed Cross Sections of the Continental Crust,* edited by M.H. Salisbury, pp. 137-158, Dordrecht, Holland, D. Reidel Publ. Co., 1990.

Saleeby, J.B., S.E. Goodin, W.D. Sharp, and C.J. Busby, Early Mesozoic paleotectonic-paleogeographic reconstruction of the southern Sierra Nevada region, in *Mesozoic paleogeography of the western United States: Pacific Coast Paleogeography Symposium 2,* edited by D.G. Howell and K.A. McDougall, pp. 311-336, Los Angeles, Society of Economic Paleontologists and Mineralogists, Pacific Section, 1978.

Saleeby, J.B., D.B. Sams, and R.W. Kistler, Geochronology and geochemistry of crystalline rocks of the southernmost Sierra Nevada, California, *J. Geophys. Res., 92*, pp. 10443-10466, 1987.

Sams, D.B., U/Pb zircon geochronology, petrology, and structural geology of the crystalline rocks of the southernmost Sierra Nevada and Tehachapi Mountains, Kern County, California, Ph.D. thesis, 315 pp., California Institute of Technology, Pasadena, California, 1986.

Sams, D.B., and J.B. Saleeby, Geology and petrotectonic significance of crystalline rocks of the southernmost Sierra Nevada, California, in *Metamorphism and Crustal Evolution of the Western United States (Rubey Vol. VII)*, edited by W.G. Ernst, pp. 865-893, Englewood Cliffs, N.J., Prentice-Hall, 1988.

Schnetzler, C.C., and J.A. Philpotts, Partition coefficients of rare-earth elements between igneous matrix material and rock-forming mineral phenocrysts, II., *Geochim. Cosmochim. Acta, 34*, pp. 331-340, 1970.

Seifert, K.E., and S.A. Chadima, Depletion of heavy rare-earth elements in metamorphic minerals from Adirondack anorthosites, *Geology, 17*, pp. 1004-1006, 1989.

Sharry, J., The geology of the western Tehachapi Mountains, California, Ph.D. thesis, 215 pp., Massachusetts Institute of Technology, Cambridge, Mass., 1981.

Silver, L.T., Lead isotopes and the petrogenesis of Cordilleran batholiths (abstract), *Geol. Soc. Amer. Abstract Progr., 19*, p. 845, 1987.

Silver, L.T., and B.W. Chappell, The Peninsular Ranges Batholith: an insight into the evolution of the Cordilleran batholiths of southwestern North America, *Trans. Roy. Soc. Edinburgh Earth Sci., 79,* pp. 105-121, 1988.

Sun, S.-S., R.W. Nesbitt, and A.Y. Sharaskin, Geochemical characteristics of mid-ocean ridge basalts, *Earth Planet. Sci. Lett., 44,* pp. 119-138, 1979.

Taylor, H.P., Jr., The oxygen isotope geochemistry of igneous rocks, *Contrib. Mineral. Petrol., 19,* pp. 1-71, 1968.

Taylor, H.P., Jr., Oxygen, hydrogen, and strontium isotope constraints on the origin of granites, *Trans. Roy. Soc. Edinburgh Earth Sci., 79,* pp. 317-338, 1988.

Van Kooten, G.K., Pb and Sr systematics of ultrapotassic and basaltic rocks from the central Sierra Nevada, California, *Contrib. Mineral. Petrol., 76,* pp. 378-385, 1981.

Walker, R.J., R.W. Carlson, S.B. Shirey, and F.R. Boyd, Os, Sr, Nd, and Pb isotope systematics of southern African peridotite xenoliths: implications for the chemical evolution of subcontinental mantle, *Geochim. Cosmochim. Acta, 53,* pp. 1583-1595, 1989.

Wasserburg, G.J., S.B. Jacobsen, D.J. DePaolo, M.T. McCulloch, and T. Wen, Precise determination of Sm/Nd ratios, Sm and Nd isotopic abundances in standard solutions, *Geochim. Cosmochim. Acta, 45,* pp. 2311-2323, 1981.

Zartman, R.E., Lead isotopic provinces in the Cordillera of the western United States and their significance, *Econ. Geol., 69*, pp. 792-805, 1974.

CHAPTER 4

Major and trace element constraints on petrogenesis of rocks of the deep Sierra Nevada batholith, Tehachapi Mountains, California

4.1. Introduction

In Chapters 2 and 3, it was shown that the Cretaceous intrusive rocks of the Tehachapi Mountains study area were intruded at great depths (30 km) and that their isotopic characteristics are suggestive of a hybrid origin. Here, we will examine the major and trace element concentrations of the rocks in an attempt to gain further understanding of the petrogenetic processes at work.

We have seen that the variations in isotope ratios among the rocks cannot be related to chemical variation by way of processes involving either simple mixing or combined mixing and fractionation. In other words, most of the igneous rock samples cannot be considered strictly cogenetic because their isotopic variability implies that they originated from different sources (or similar sources with varying amounts of hybridization as described in Chapter 3). Therefore, the consideration of petrogenetic pathways in this chapter is not meant to imply consanguinity among specific rocks. I am merely exploring possible pathways that affected the various magmatic systems to varying degrees. It is important to note that the igneous (and metaigneous) rocks as sampled here (Figures 4.1 and 4.2, Table 4.1) are not meant to be statistically representative of the chemical variations present in the Tehachapi Mountains. As noted in Chapters 2 and 3, while there is a larger proportion of mafic rocks in the younger Bear Valley suite and felsic rocks in the Tehachapi suite, both are dominated by tonalitic compositions. Sampling was oriented

CHAPTER 4

Major and trace element constraints on petrogenesis of rocks of the deep Sierra Nevada batholith, Tehachapi Mountains, California

4.1. Introduction

In Chapters 2 and 3, it was shown that the Cretaceous intrusive rocks of the Tehachapi Mountains study area were intruded at great depths (30 km) and that their isotopic characteristics are suggestive of a hybrid origin. Here, we will examine the major and trace element concentrations of the rocks in an attempt to gain further understanding of the petrogenetic processes at work.

We have seen that the variations in isotope ratios among the rocks cannot be related to chemical variation by way of processes involving either simple mixing or combined mixing and fractionation. In other words, most of the igneous rock samples cannot be considered strictly cogenetic because their isotopic variability implies that they originated from different sources (or similar sources with varying amounts of hybridization as described in Chapter 3). Therefore, the consideration of petrogenetic pathways in this chapter is not meant to imply consanguinity among specific rocks. I am merely exploring possible pathways that affected the various magmatic systems to varying degrees. It is important to note that the igneous (and metaigneous) rocks as sampled here (Figures 4.1 and 4.2, Table 4.1) are not meant to be statistically representative of the chemical variations present in the Tehachapi Mountains. As noted in Chapters 2 and 3, while there is a larger proportion of mafic rocks in the younger Bear Valley suite and felsic rocks in the Tehachapi suite, both are dominated by tonalitic compositions. Sampling was oriented

Figure 4.1 - Basement geologic map of the southern Sierra Nevada with one sample locality [Sams, 1986] in the northern study area. Modified after Ross [1989], Sams [1986], and Sharry [1981].
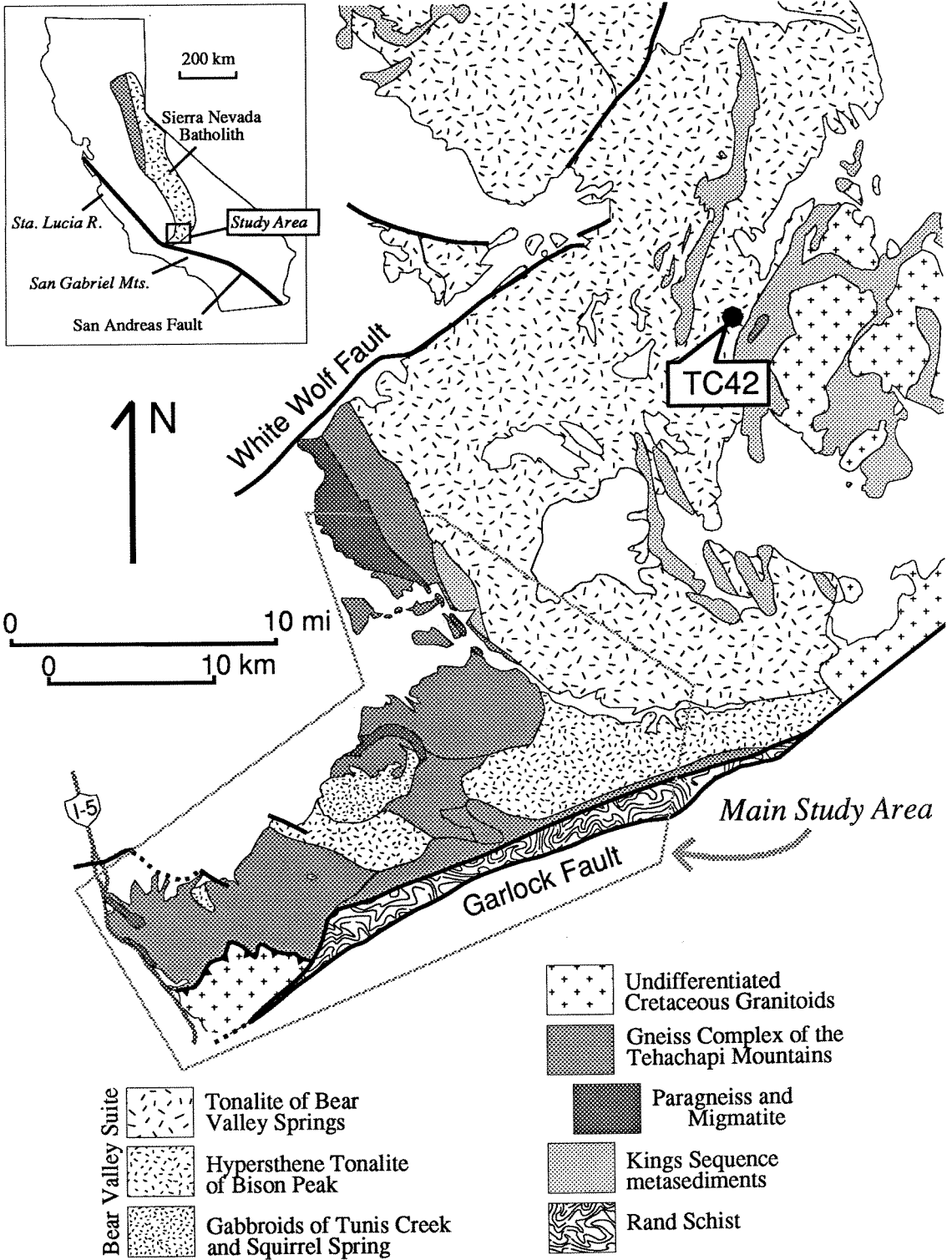
Fig. 4.1

Figure 4.2 - Basement geologic map of the main study area, Tehachapi Mountains, with sample localities. Modified after Sharry [1981] and Sams [1986], supplemented by new mapping. Sample localities for CM9 and PC175 from Sams [1986]. In the text, sample CM9 is not included in the "main study area." Units of the gneiss complex of the Tehachapi Mountains: T = tonalite gneiss of Tejon Creek, P = quartzofeldspathic gneiss of Pastoria Creek, W = diorite gneiss of White Oak, CP = paragneiss of Comanche Point, GP = migmatite of Grapevine Peak, GC = paragneiss of Grapevine Canyon. G = garnet-biotite tonalite of Grapevine (of the intrusive suite of Bear Valley). Smaller, sub-map-scale paragneiss bodies are not shown. For clarity, map patterns are omitted for the granitic rocks south of the Pastoria thrust (Figure 3.1).

Fig. 4.2

Table 4.1 - Samples

	unit[1]	lithology[2]	texture[3]
Intrusive suite of Bear Valley			
CM9[4]	BVS	bt-hb tonalite	protomylonitic
GC-8	TC	hb gabbro	massive
GC-11	TC	hy-hb gabbro	massive
GC-17	BP	hy-bt-hb tonalite	massive
GC-53	SS	hb gabbro	syn-magmatic
GV-3	G	gt-bt tonalite	syn-magmatic
PC175[4]	(TC)	troctolite	corona
PTC-42	BP	ep-hb-bt tonalite	protomylonitic
TC-9	TC	hy-hb gabbro	syn-magmatic
TC-19	TC	hb gabbro	syn-magmatic
TC42[4]	BVS	bt-hb tonalite	protomylonitic
TC-45b	BP	hy-bt-hb qtz. diorite	syn-magmatic
TC-47	TC	cumm norite	massive
TC-49b	TC	hb gabbro	layered
TC-83	TC	gt-hb metagabbro	granoblastic
Gneiss complex of the Tehachapi Mountains			
GC-1	TJ	bt-hb tonalite	protomylonitic
GC-14	TJ	ep-bt leucotonalite	protomylonitic gneiss
GC-32	PC	ep-bt granodiorite	protomylonitic gneiss
GC-33	PC	hb-bt granodiorite	protomylonitic gneiss
GC-43	PC	ep-bt granite	protomylonitic gneiss
GC-50	PC	bt tonalite	massive
GC-55	PC	bt-hb tonalite	orthomylonitic gneiss
GC-60	PC?	bt-hb diorite	gneiss or syn-magmatic?
PC35-P	PC	gt-bt granite	protomylonitic
TC-6	TJ	bt granite	massive
TC-12b	TJ	bt-hb diorite	gneiss or syn-magmatic?
TC-34	TJ	bt tonalite	gneiss or syn-magmatic?
Metamorphic framework rocks			
GC-2	CP	gt-mu-bt qzfsp	gneiss
GC-12	CP	gr-bt qzfsp	gneiss
TC-8	CP	gr-gt-bt qzfsp	gneiss

---

[1] BVS = tonalite of Bear Valley Springs; TC = gabbroids of Tunis Creek; BP = hypersthene tonalite of Bison Peak; SS = gabbroids of Squirrel Spring; G = garnet-biotite tonalite of Grapevine; TJ = tonalite gneiss of Tejon Creek; PC = quartzofeldspathic gneiss of Pastoria Creek; KS = Kings Sequence; CP = paragneiss of Comanche Point; GC = paragneiss of Grapevine Canyon. Parentheses = tentative assignment. ? = may be TC or SS (see text).

[2] bt = biotite, hb = hornblende, hy = hypersthene, gt = garnet, ep = epidote, cumm = cummingtonite with thin hb rims, gr = graphite, mu = muscovite, pl = plagioclase, qz = quartz, qzfsp = quartz + two feldspars.

[3] "Protomylonitic gneiss" refers to a rock showing incipient mylonitic shear with textural evidence of a pre-existing high-temperature fabric. "Gneiss" or "syn-magmatic" refers to metamorphic or igneous foliation, respectively, with an absence of finely recrystallized shear fabric. The distinction is often equivocal.

[4] From the thesis collection of D.B. Sams.

toward examining lithologic variability, so gabbros and granites are as well-represented as tonalites. Descriptions of the geologic setting, structural features, and units of the rocks may be found in Chapters 2 and 3.

4.2. Lithologic descriptions

a. Intrusive suite of Bear Valley

More detailed descriptions of most units described in this paper may be found in Sams [1986]. Lithologies represented in the intrusive suite of Bear Valley range from gabbro through tonalite, and their ages are 98-105 Ma. Mafic varieties are found in the gabbroids of Tunis Creek and Squirrel Spring, as well as in scattered smaller bodies of gabbro or diorite as represented by samples PC175 and GV-1a (Figure 4.2). The two major units are dominated by hornblende hypersthene gabbros variously bearing textural and structural evidence for crystal accumulation (rhythmic layering, poikilitic texture), annealing recrystallization (120 grain boundaries, zoned plagioclase rims), and near-solidus and subsolidus metamorphism (cummingtonite rims on hypersthene, cummingtonite exsolution patches in hornblende, felsic-haloed garnet -- Chapter 2). Ubiquitous accessories in the gabbros are ilmenite and apatite. Some gabbros, particularly in the northeastern "tongue" of the Tunis Creek body (Figure 4.2), have a foliation defined by preferred orientation of elongate hornblende and plagioclase grains, attributed by Sams [1986] and Sams and Saleeby [1988] to near-solidus magmatic flow. A few, small, isolated stocks intrusive into older gneisses (e.g., PC175 in Figure 4.2) contain troctolite with extensive reaction coronas between olivine and plagioclase containing orthopyroxene, amphibole, and spinel. Widespread, outcrop-scale bodies of hornblende gabbro and diorite intrusive into the older gneiss complex of the Tehachapi Mountains may be correlative with these gabbros, as suggested by the zircon age data of Chapter 3. Two biotite-hornblende diorites, GC-60 and TC-12b (Table 4.1), are tentatively

assigned to the gneiss complex of the Tehachapi Mountains because they occur as concordant, gneissose layers in the older tonalite gneisses and because of the presence of biotite (albeit subordinate to hornblende).

A distinctive intrusive unit of the Bear Valley suite is the hypersthene tonalite of Bison Peak (the "Bison Peak granulite" of Sharry [1981]), characterized by hypersthene-biotite-hornblende quartz diorites to tonalites with accessory ilmenite + apatite + zircon ± epidote. These rocks range texturally from unfoliated to gneissose (syn-magmatic preferred orientation) to mildly protomylonitic. Hypersthene is typically found near the centers of mafic aggregates with biotite and hornblende, but is in apparent texturally equilibrium with all phases.

A recently recognized unit of the Bear Valley suite, the garnet-biotite tonalite of Grapevine (Chapter 3), is found at the western end of the study area. The subtle foliation is defined by biotite preferred orientation. Textural evidence for garnet paragenesis is equivocal, but a biotite-garnet temperature from the unit (sample GV-2 in Chapter 2) suggests a subsolidus origin.

To the north of the main study area (Figure 4.2) lies the tonalite of Bear Valley Springs, a major, batholith-scale unit coeval with the other members of the Bear Valley suite. It consists mainly of tonalite with varying proportions of hornblende and biotite, with occurrences of hypersthene-bearing tonalite in its southern reaches [Sams, 1986; Ross, 1989]; accessory phases include apatite, epidote, sphene, zircon, ilmenite, and magnetite. While undeformed rocks with igneous flow fabrics predominate, textures reflecting ductile deformation with dynamic recrystallization of quartz are also common. The present study is concentrated on the rocks of the main study area, so only two samples of the Bear Valley Springs tonalite are considered.

b. Gneiss complex of the Tehachapi Mountains

Two 110-117 Ma orthogneiss units make up the bulk of this complex. The tonalite gneiss of Tejon Creek is a relatively homogeneous assemblage of biotite ± hornblende tonalites with very rare biotite granite. Accessory phases include those described above for the Bear Valley Springs tonalite, with prominent epidote, typically with allanite cores. The tonalites show a range of deformation fabrics, from apparently syn-magmatic flow foliation to protomylonitic shear. Biotite-hornblende diorites are common as outcrop-scale, concordant layers among the more abundant tonalite. Metamorphic garnet is formed locally (see Chapter 2). The quartzofeldspathic gneiss of Pastoria Creek has these same general characteristics, but granodioritic and granitic compositions are more abundant. The Pastoria Creek unit is thus quite heterogeneous, but tonalitic compositions prevail. Both granodiorite samples on Table 4.1 are on the border with tonalite in terms of feldspar proportions; in both cases, some of the alkali feldspar may have formed from subsolidus exsolution from plagioclase, suggesting that these were in fact primarily tonalites. In some of the granodiorite or granite gneisses, hornblende is present as an accessory phase in highly resorbed grains.

Also included in the gneiss complex of the Tehachapi Mountains are paragneisses which occur scattered as small selvages within the two orthogneiss units and as mappable units themselves: the paragneisses of Comanche Point and Grapevine Canyon and the migmatite of Grapevine Peak. These are high-grade, commonly migmatized quartzofeldspathic gneisses with biotite ± graphite ± garnet; muscovite is present as a secondary phase. For the purposes of discussion, the "Tehachapi suite" will refer to the igneous rocks of the gneiss complex of the Tehachapi Mountains to allow for comparison with the Bear Valley suite.

4.3. Analytical procedures

Major elements for 15 samples (Table 4.2) were measured on solutions by direct current plasma spectrometry. Well-characterized rock samples were used for preparation of standard solutions, and drift and dilution corrections were applied. Major elements for the remaining 15 samples were measured at the University of Southern California by X-ray fluorescence on fused glass discs. Trace elements (except Rb and Sr) for 24 samples were measured also at U.S.C. by XRF using pressed powder pellets. Rb and Sr concentrations are by isotope dilution (Chapter 3), except for samples TC-9, TC-19, GC-33, GC-43, GC-50, and TC-12b (XRF). For samples GC-2, GC-12, GC-11, GC-53, and GV-3, Ba was measured by DCP.

Mineral compositions (Table 4.3) were determined on a scanning electron microscope with an energy dispersive spectrometer. Data manipulation utilized the Tracor Northern MICROQ program with linear least-squares peak-fitting, with correction factors after Bence and Albee [1968]. Beam conditions were 15 keV and 100 pA, and count times were 100 seconds. Some mineral data are taken from electron microprobe analyses reported in Chapter 2. These include data from garnet-free zones in thin-sections showing the localized garnet crystallization described in Chapter 2; these are probably good estimates of primary igneous compositions.

4.4. Results

a. Major elements

SiO_2 contents reach extreme values at the high and low ends, with gabbros as low as 42.1 and 43.8 %, and granites as high as 76.2 and 79.4 %. Tonalites, the most abundant rock type, range from 59.7 to 67.2 % with the exception of the quartz-rich leucotonalite (73.8 %). On oxide variation diagrams (Figure 4.3), there are gaps in SiO_2 concentration on either side of the quartz diorite/tonalite field. Many elements (e.g., CaO,

Table 4.2. Major and trace element compositions

	Metamorphic rocks			Intrusive suite of Bear Valley											
	GC-2	GC-12	TC-8	CM9	GC-8	GC-11	GC-17	GC-53	GV-3	PC175	PTC42	TC-9	TC-19	TC42	TC45b
	†	†		†		†	†	†	†						†
SiO_2	72.41	72.17	73.40	62.82	43.77	47.28	59.72	49.20	66.73	42.06	67.17	46.18	44.92	58.86	56.55
TiO_2	0.23	0.59	0.55	0.76	1.44	1.42	0.82	1.39	0.68	0.10	0.59	1.80	1.28	0.79	0.86
Al_2O_3	15.10	13.52	12.51	16.87	20.82	20.65	17.80	21.00	17.11	19.83	16.24	21.46	24.01	16.87	19.83
FeO*	2.51	3.15	3.53	5.32	11.49	11.62	6.25	8.63	3.94	9.18	4.21	11.22	7.14	6.63	6.67
MgO	0.74	1.84	1.86	3.18	7.48	6.10	3.44	5.03	1.81	17.36	1.71	4.78	5.47	3.56	2.77
MnO	0.14	0.04	0.14	0.09	0.22	0.17	0.10	0.14	0.06	0.26	0.22	0.17	0.14	0.28	0.12
CaO	2.59	2.77	1.41	6.24	12.35	11.61	7.20	10.41	4.87	10.24	4.55	11.04	13.96	7.12	6.57
Na_2O	3.96	2.71	1.72	3.26	1.40	1.83	3.60	3.60	4.02	0.87	3.93	2.16	1.69	4.49	4.77
K_2O	2.27	2.12	3.70	1.86	0.08	0.21	1.13	0.29	1.25	0.05	1.35	0.09	0.11	1.29	0.90
P_2O_5	nd	nd	0.05	nd	0.02	nd	nd	nd	nd	0.01	0.10	0.31	0.09	0.12	nd
LOI	nd	nd	1.01	nd	0.64	nd	nd	nd	nd	1.39	0.72	0.17	0.85	1.73	nd
total	99.94	98.91	99.88	100.40	99.70	100.90	100.07	99.70	100.47	99.96	100.78	99.38	99.65	101.72	99.03
Rb	67.3	69.2	106	68.7	0.25	1.13	31.7	2.05	29.8	1.43	42.3	0.28	0.43	31.7	22.8
Sr	169	241	189	350	395	473	369	543	470	306	271	575	567	338	407
Ba	677	575	1651	544	nd	45.0	366	81.0	528	2.14	979	50.7	30.5	520	702
Y			27	20			21			2.6	21	13	9.6	20	25
Zr			159	111			122			31	159	71	63	125	250
Nb			25	22			21			15	21	18	17	20	21
Ta			0.96	bd			2.7			1.4	0.71		2.0	0.39	1.1
Hf			5.4	3.6			4.0			2.9	5.4	10.9	4.4	4.2	8.7
La			26.2	17.9			8.7			bd	7.9	16.8	7.3	16.5	18.6
U			3.2	0.29			0.14			0.022	0.18	0.019	0.020	0.14	0.11
Th			9.9	0.63			bd			bd	0.52	bd	bd	bd	bd
Pb			21	11.2			9.5			4.3	9.4	6.1	5.9	7.2	7.7
Ni			32	8.5			6.1			138	7.8	2.3	9.1	3.5	6.9
Cr			57	44			32			620	30	14	49	26	30

Table 4.2 continued

B.V. suite cont. | Gneiss complex of the Tehachapi Mountains

	TC-47	TC49b †	TC-83	GC-1 †	GC-14	GC-32 †	GC-33	GC-43	GC-50	GC-55 †	GC-60	PC35P †	TC-6 †	TC12b	TC-34 †
SiO$_2$	49.05	44.43	44.72	61.89	73.83	74.49	65.34	76.24	66.86	63.54	51.68	79.39	74.67	49.07	65.91
TiO$_2$	1.38	1.86	1.67	0.73	0.27	0.28	0.72	0.22	0.58	0.86	1.45	0.05	0.28	1.85	0.53
Al$_2$O$_3$	22.96	20.41	21.86	16.01	14.76	14.63	15.72	13.20	16.99	16.12	18.89	12.01	14.07	18.39	17.54
FeO*	8.13	10.71	11.57	5.98	1.86	1.90	5.18	1.78	3.43	6.24	9.70	0.62	1.73	10.40	2.75
MgO	4.03	7.45	4.32	4.01	0.56	0.55	1.52	0.46	1.47	1.80	3.95	0.09	0.49	4.78	1.26
MnO	0.16	0.14	0.24	0.11	0.22	0.02	0.21	0.21	0.16	0.10	0.21	0.02	0.02	0.26	0.04
CaO	10.95	13.19	12.21	6.76	3.79	3.31	4.54	1.79	4.50	5.17	8.57	0.71	1.99	10.06	4.43
Na$_2$O	2.70	1.59	2.94	3.26	3.75	4.01	4.07	3.21	4.20	3.88	3.96	3.04	3.35	3.70	3.99
K$_2$O	0.05	0.16	0.22	1.50	0.91	1.17	1.74	3.35	1.64	1.34	0.43	5.01	3.76	1.29	1.40
P$_2$O$_5$	0.38	nd	0.24	nd	0.05	nd	0.17	0.04	0.17	nd	0.21	nd	nd	0.21	nd
LOI	0.33	nd	0.20	nd	0.59	nd	0.68	0.51	0.86	nd	0.54	nd	nd	0.66	nd
total	100.10	99.93	100.20	100.24	100.59	100.35	99.88	101.00	100.00	99.06	99.58	100.94	100.36	100.66	97.86
Rb	0.58	1.25	1.28	49.4	26.1	36.3	50.3	69.0	41.2	45.0	2.20	139.2	51.5	37.5	39.3
Sr	668	523	544	299	377	375	267	173	391	327	415	52.2	170	334	510
Ba	33.1	51.4	46.1	446	353	469	613	1076	569	532	74.2	26.0	945	140	679
Y	4.9	15	21	27	9.5	5.5	39	11	7.7	32	41	19	8.6	29	7.3
Zr	56	57	67	125	123	99	168	102	128	184	131	57	180	90	118
Nb	15	18	20	23	17	17	26	20	18	24	25	24	18	23	17
Ta	1.2	1.2	2.3	bd	2.8	6.2	4.2	2.4	bd	bd	6.7	9.9	0.81	bd	bd
Hf	3.8	4.6	2.0	4.1	4.0	3.2	5.7	3.4	4.2	6.3	4.3	1.8	6.2	4.0	3.8
La	9.9	9.6	17.1	25.2	45.5	10.6	27.2	17.9	8.3	21.2	14.6	10.6	29.5	15.0	10.5
U	0.019	0.024	0.022	0.22	0.12	0.16	0.23	0.30	0.19	0.20	0.026	1.0	0.25	0.17	0.50
Th	bd	0.08	bd	3.0	11	bd	0.07	7.5	bd	1.3	bd	5.9	12	bd	bd
Pb	4.7	4.9	6.9	10.3	10.3	8.5	11.5	11.6	12.2	9.7	9.0	19.5	18.1	9.6	10.1
Ni	6.5	6.1	2.6	30	bd	bd	23	bd	0.81	2.1	3.8	bd	bd	11	1.5
Cr	15	44	15	113	6.6	6.6	78	6.6	7.5	11	21	6.5	6.7	54	7.6

bd = below detection limit; nd = not determined.
† Major elements by DCP; other samples by XRF.
Most Rb and Sr by isotope dilution (Chapter 3), most Ba by XRF; exceptions in text. Other trace elements by XRF.

Figure 4.3 - Variations of selected major element oxides with SiO_2 (weight percent). *Open squares* are intrusive suite of Bear Valley, exclusive of Bear Valley Springs tonalite, which are *open circles*; *closed squares* are igneous rocks of the gneiss complex of the Tehachapi Mountains. On the MgO plot, troctolite PC175 plots off the figure at 17.36 %.
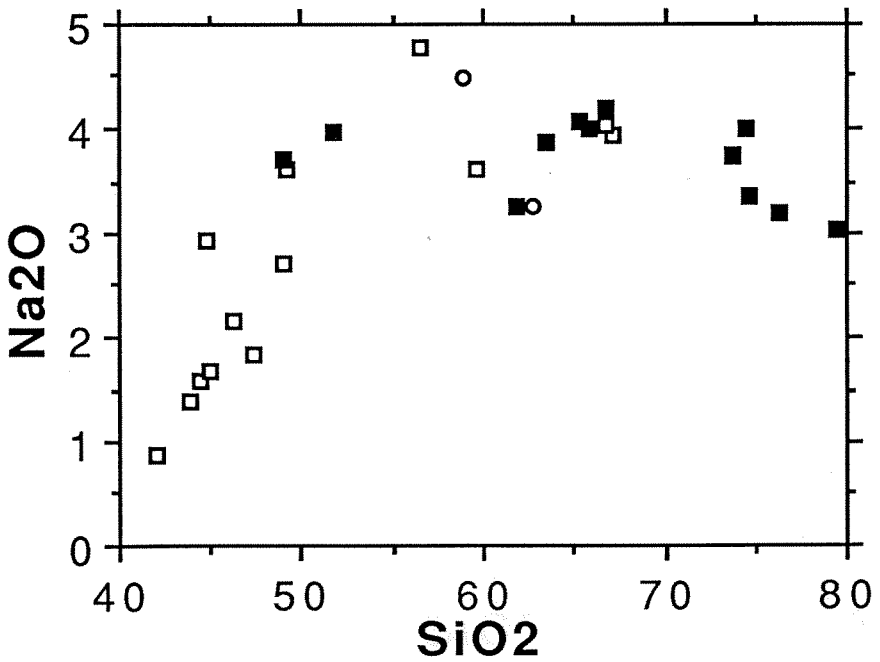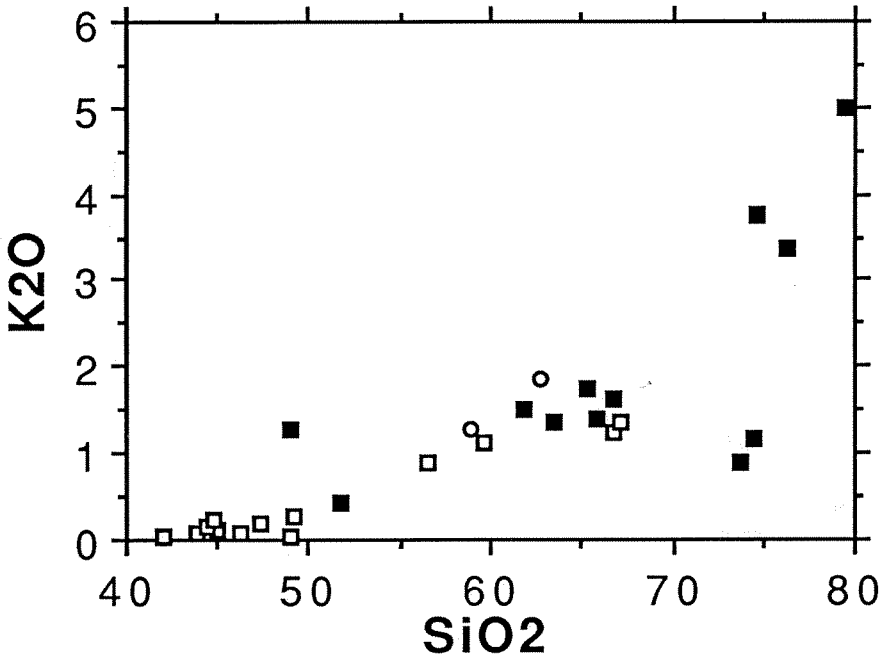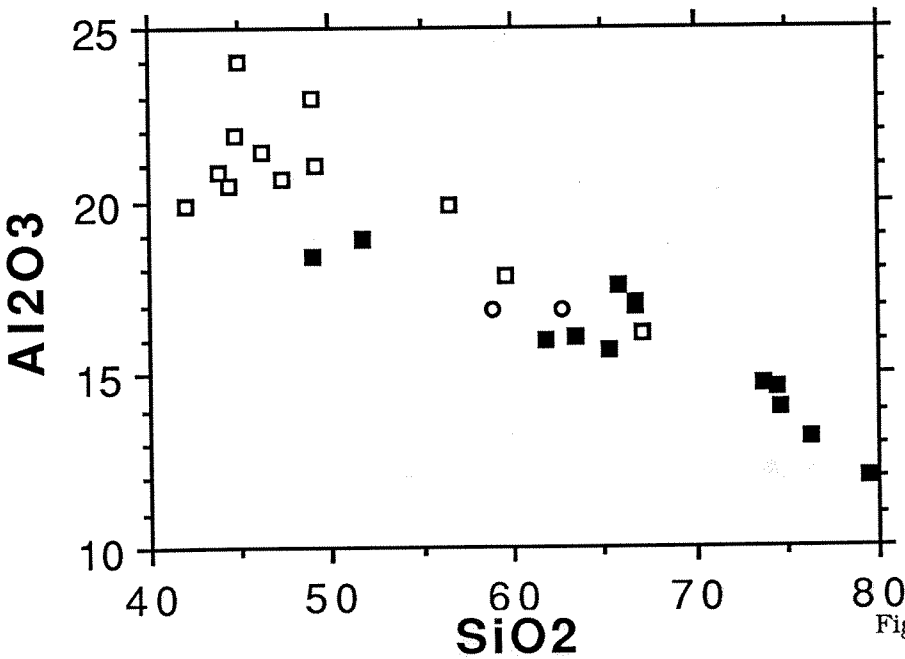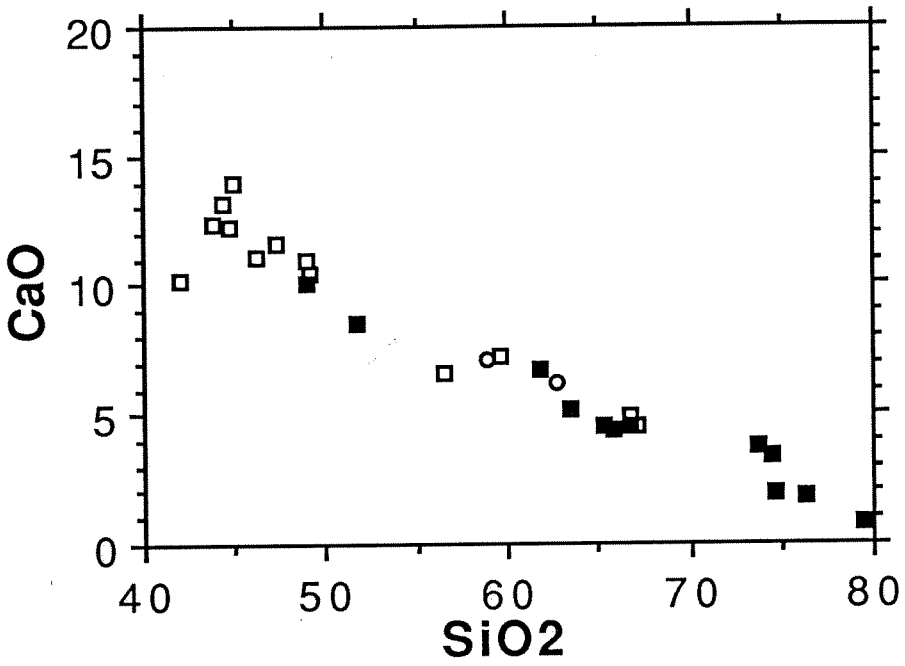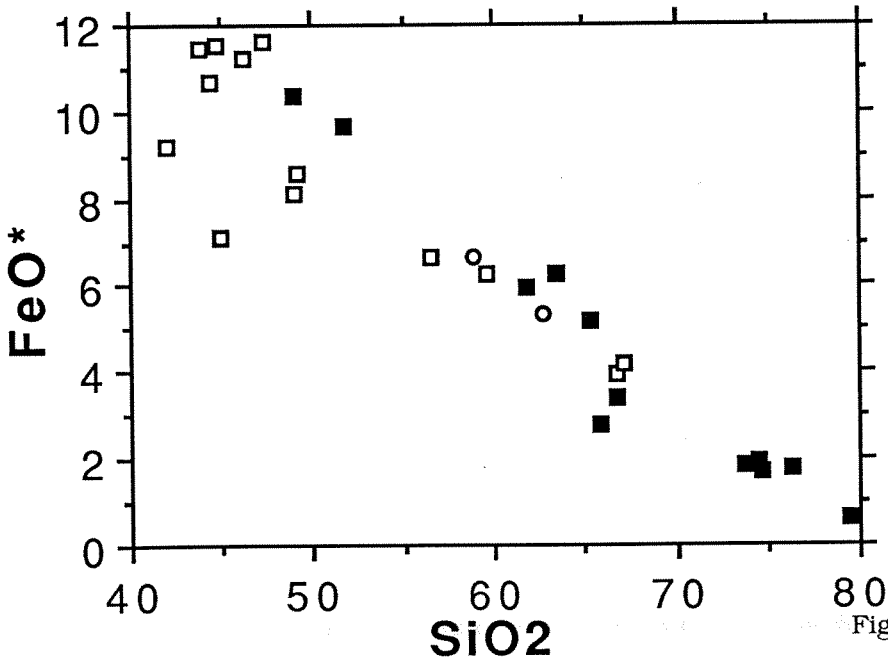
Fig. 4.3

Fig. 4.3 (cont.)
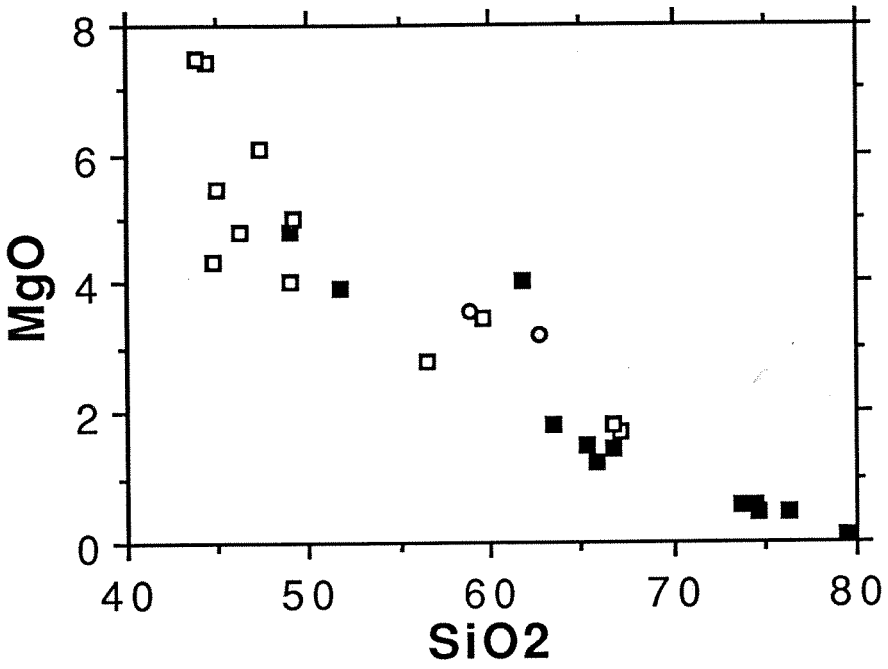
Fig. 4.3 (cont.)

FeO, TiO_2, MgO, Al_2O_3) show relatively smooth, though broad, variation patterns with SiO_2, but K_2O and Na_2O do not (Figure 4.3). K_2O is anomalously high in one diorite (at SiO_2=49 %), and at high SiO_2 there is an apparent bifurcation in concentration due to the low-K_2O, high-SiO_2 leucotonalite and granodiorite. Na_2O follows a convex-up pattern peaking at 4.8 % (at SiO_2=56.6 %). For CaO, Al_2O_3, MgO, and FeO, there is a pronounced dispersion in gabbro concentrations, with troctolite PC175 showing the largest deviations from the overall trend (e.g., MgO=17.4 %). CaO and Al_2O_3 reach particularly high values in the other gabbros (up to 14.0 and 24.0 %, respectively).

The suites are classified as calcic on the basis of an alkali-lime index of around 65. While the Bear Valley and Tehachapi suites obviously differ in the range of compositions (the former reaching more mafic rocks, the latter more felsic), they overlap completely in the tonalite fields, and both have similar patterns to those reported by Ross [1989] on many more samples from the tonalite of Bear Valley Springs. For nongabbro lithologies, both suites have major element variation patterns similar to Cretaceous batholithic rocks from the central Sierra Nevada [Bateman et al., 1984], which have similar age and isotopic characteristics to the Tehachapi rocks (Chapter 3), except that the Tehachapi tonalites are generally more sodic (Figure 4.4). Furthermore, the Tehachapi suites are more lithologically heterogeneous than the more tonalite-dominated central Sierra group of suites.

b. Trace elements

Trace element concentrations (Table 4.2) are highly variable in the suites and rarely show regular, monotonic variation patterns with SiO_2. Rb and Ba, for example (Figure 4.5), show a large increase in concentration between the gabbros and the more silicic rocks, and both show no pattern in the high-SiO_2 rocks; note the large spread in Rb and Ba in rocks with SiO_2>70 %. The gabbros are very poor in many large-ion lithophile elements (e.g., Ba, Rb, U, Th, Pb); in Chapter 3, I discussed their low Rb/Sr and high

Sm/Nd ratios in terms of a cumulate origin. The tonalites have moderate Rb, Ba, and Sr contents, but Rb and Rb/Sr tend to be lower in tonalites of the main study area than in those in the Bear Valley Springs tonalite (Chapter 3). Zr concentrations, presumably controlled to some extent by zircon solubility in rocks with SiO_2 > 50 %, increase from low values in the gabbros and, with two exceptions, remain in the range 99-184 ppm (Figure 4.6). One exception is the high-SiO_2 granite PC35-P, which is marked not only by low Zr, but also low Sr, Ba, and Hf, and high Rb, U, Pb, Y, Nb, Ta, and Sm/Nd (Chapter 3) relative to the other silicic rocks. Zr/Hf ratios (Figure 4.6) are remarkably constant for nongabbro lithologies, but the same may not be said for ratios involving Zr and Nb or Ta. Ni and Cr concentrations are fairly low throughout, even in the gabbros of probable cumulate origin; the obvious exception is the troctolite (Ni=138 ppm, Cr=620 ppm).

c. Mineral compositions

Plagioclase (Table 4.3) shows a gradual change in composition with rock type. Troctolite PC175 and hornblende gabbro TC-49b have very calcic plagioclase (An_{85-97}), while the other gabbros range from An_{67} to An_{46}. Tonalite plagioclase lies in the range An_{30-40}, while the most sodic examples are found in the granites and granodiorites (An_{22-31}). While these data are admittedly sparse, they serve to show the overall progression in plagioclase compositions.

For hornblende compositions, the SEM-EDS data assume all Fe as Fe^{2+}, while the microprobe values use the "average Fe^{3+}" option of the recalculation scheme of Spear and Kimball [1984]. It is possible, then, that actual Mg#'s are higher than shown on Table 4.3, particularly for SEM-EDS samples. For example, if Fe^{3+}/Fe^{2+} = 0.3 for TC-49b, the Mg# range becomes 64-58 rather than 58-51. The Fe^{3+}/Fe^{2+} ratios are probably not so high, given the evidence for relatively low f_{O_2} in the area (Chapter 2). Like plagioclase, hornblende shows a progression in composition with rock type, though less pronounced. Gabbros have the most Mg-rich hornblendes (Mg#=50-58), quartz diorite/tonalite Mg#'s

Figure 4.4 - Comparison of $Na_2O/(Na_2O + K_2O)$ vs. SiO_2 (wt. %) in Tehachapi Mountains igneous rocks with those from the central Sierra Nevada batholith, west of the $^{87}Sr/^{86}Sr$ = 0.706 isopleth. Central Sierra data from Bateman et al. [1984].
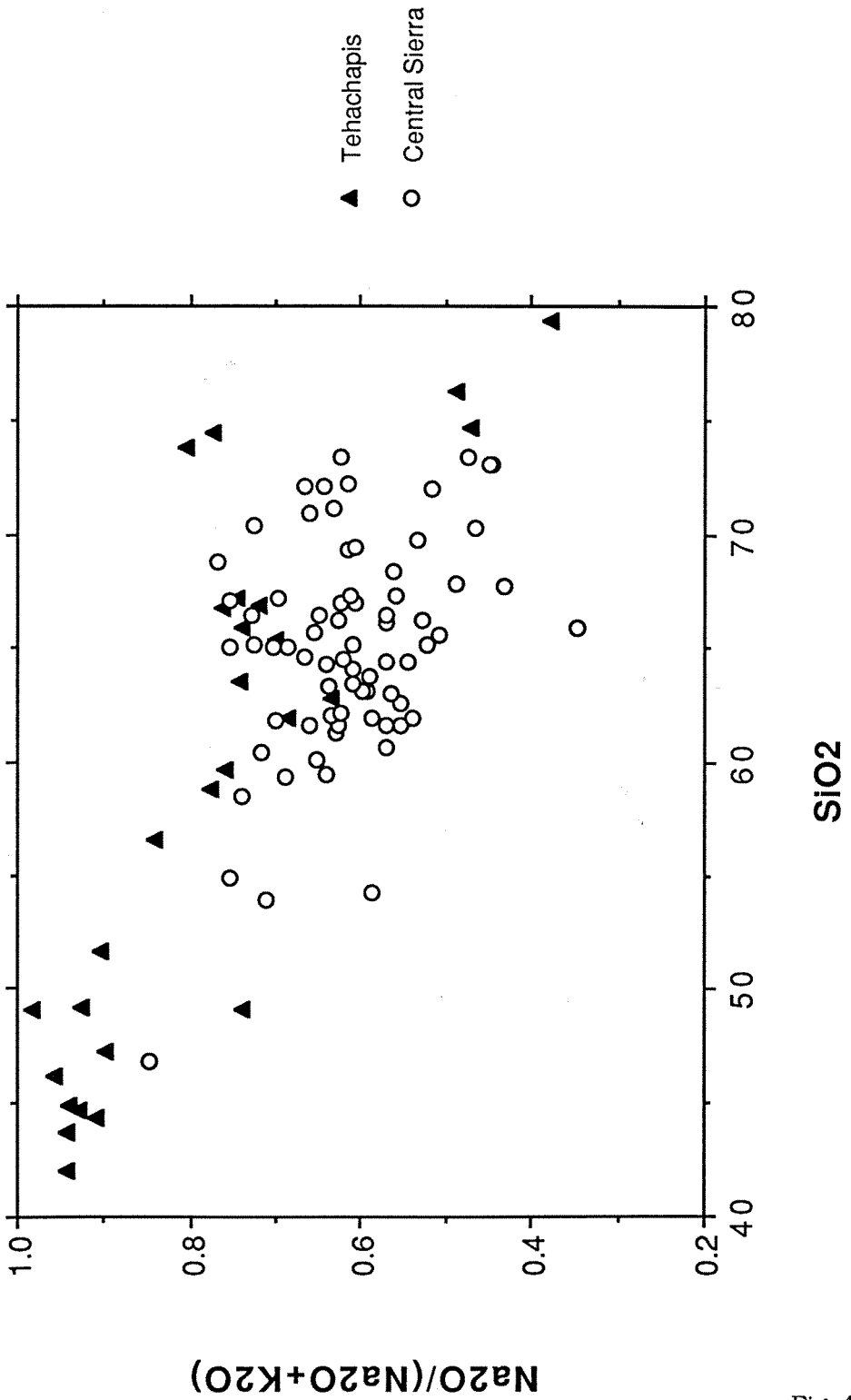
Fig. 4.4

Figure 4.5 - Variations of Ba and Rb (ppm) with SiO_2 (wt. %). Symbols as in Figure 4.3.

Note the large spread at high SiO_2.
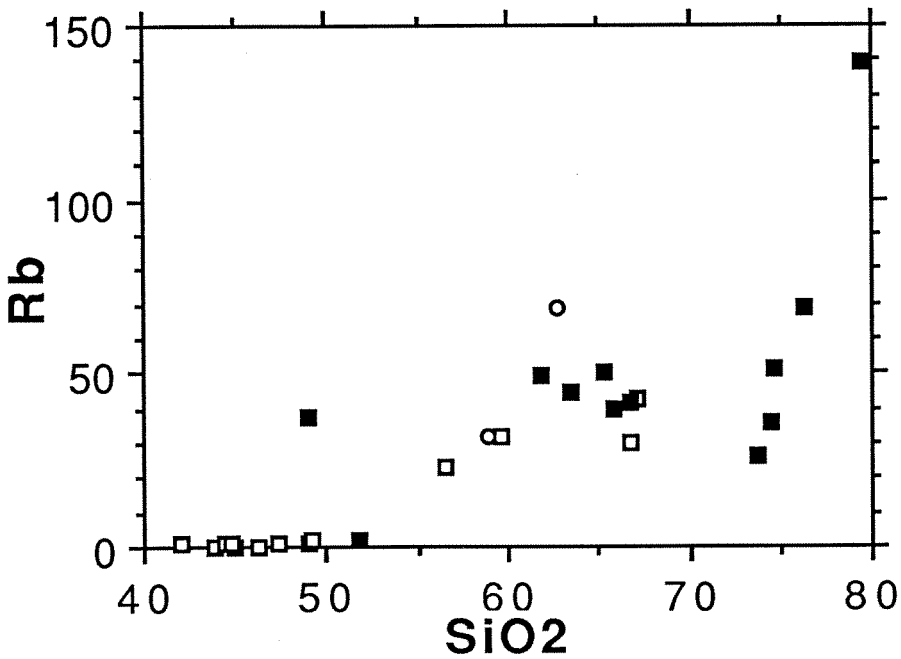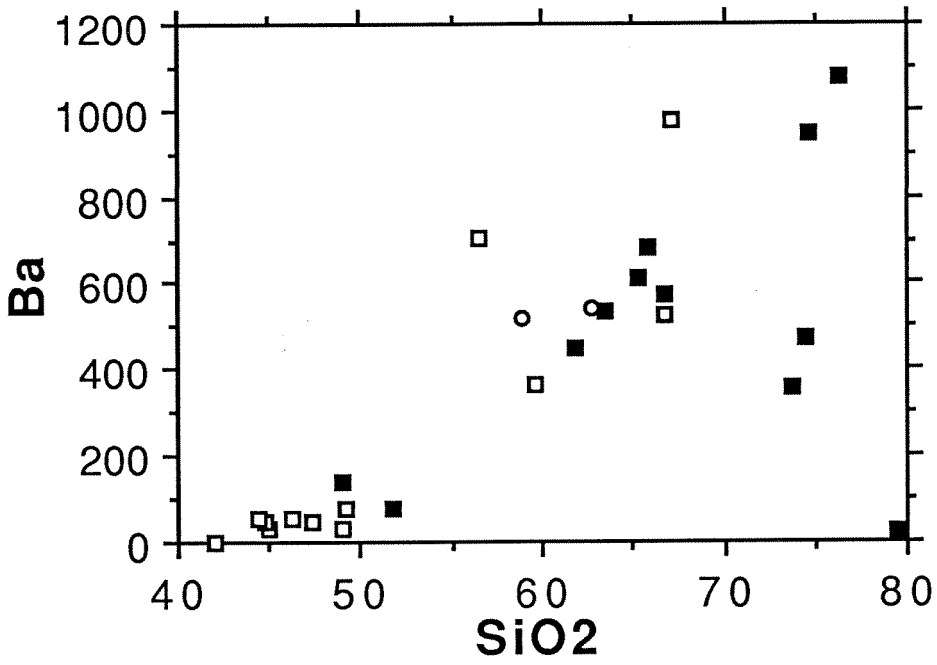
Fig. 4.5

Figure 4.6 - Variations in Zr and Zr/Hf (ppm) with SiO$_2$ (wt. %), with symbols as in Figure

4.3. *Square with dot* is garnet-bearing metagabbro TC-83.
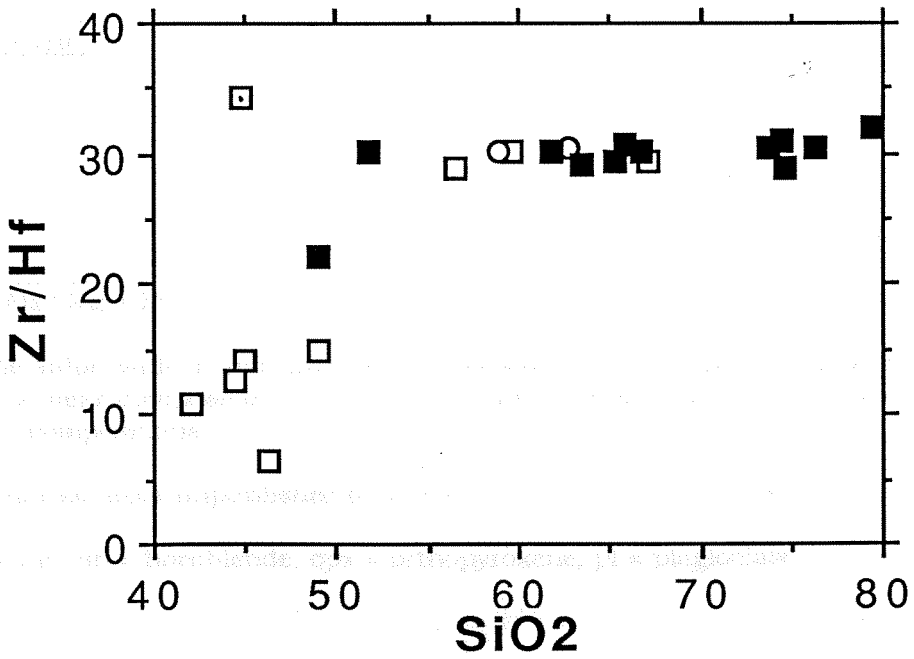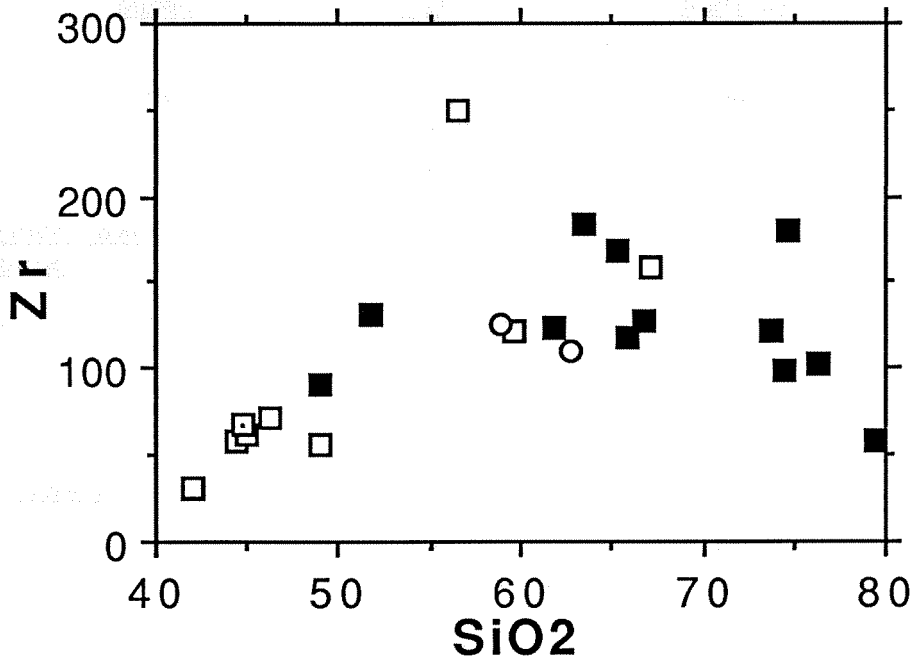
Fig. 4.6

Table 4.3.   Mean mineral compositional parameters from SEM-EDS analyses* and microprobe WDS analyses† (Chapter 2)

	Mg#(ol)	Mg#(hb)	Mg#(opx)	An(pl)
Gabbro				
PC175*	78	-	80	97
TC-49b*	-	58-51	-	85-90
TC-47*	-	50 (r)	52 (c)	58-67
"Metagabbro" away				
from garnet				
TC-83†	-	51 (r)	-	59 (r)
TC-2a†	-	53 (r)	-	63 (r)
GV-1a†	-	-	-	48 (c)
GC-46†	-	57 (r)	-	50-46
TC-2†	-	-	47	54 (r)
Quartz diorite,				
tonalite				
TC-45b*	-	46 (r)	46	35-32
GC-17*	-	53 (r)	53	40 (r)
WR27a†	-	49 (r)	-	-
TC-12a†	-	40 (r)	-	-
CM657†	-	29 (r)	-	-
"Metatonalite" away				
from garnet				
PC107a†	-	36 (r)	-	32 (r)
"CORE"†	-	33	-	33-30
Granodiorite,				
granite				
GC-33†	-	33 (r)	-	31 (r)
GC-16†	-	35 (r)	-	-
TC-6*	-	-	-	24-22

Mg# = Mg/(Mg + Fe^{2+})

A single value with (r) indicates rim composition, with (c) core composition, and with neither a mean composition from essentially unzoned minerals. Two values indicate core and rim compositions.

TC-2 analysis from unpublished data of C. Gallup.

ol = olivine, hb = hornblende, opx = orthopyroxene, pl = plagioclase

span a wide range from 29 to 53, and granodiorite/granite values are 33 and 35.

Orthopyroxene in the troctolite is bronzite (Mg#=80); the measured grains are contained within the corona structure between plagioclase and olivine, but their composition is consistent with equilibrium with the Fo_{78} olivine in this rock using the formula of Medaris [1969] for 700-900°C. Orthopyroxenes in the gabbros to tonalites are much more Fe-rich, straddling the hypersthene-ferrohypersthene boundary.

4.5. Discussion

a. Gabbros

The data presented here lend support to the idea, presented in Chapter 3 on the basis of Rb/Sr and Sm/Nd ratios, that the gabbroic rocks of the Tehachapi Mountains originated from accumulation of variable amounts of hornblende, calcic plagioclase, orthopyroxene, olivine, and ilmenite. This is evident in the very low concentrations of incompatible elements such as Ba, Rb, Zr, Pb, and K, but also in the high Al_2O_3, CaO, MgO, and FeO. Because many of the hornblende ± orthopyroxene gabbros have textures reflecting subsolidus recrystallization, there is some question whether these hornblende-rich rocks represent the primary cumulate igneous assemblages; after all, these rocks have been referred to as amphibolites and granulites [Sharry, 1981; Ross, 1989]. As discussed in Chapter 3, the high Sm/Nd ratios of the hornblende-bearing gabbros substantiate the importance of hornblende as a primary cumulate phase. Figure 4.7 shows further evidence of the primary nature of the hornblende. In plots of Al_2O_3 and CaO versus SiO_2, the bulk compositions of hornblende gabbros lie in the area of mixtures between hornblende and calcic plagioclase, while orthopyroxene-bearing gabbros are shifted toward orthopyroxene-plagioclase mixture compositions. Plagioclase accumulation is supported by the rather high Sr concentrations in the gabbros (306 to 668 ppm). Another suggestion is in the high K/Rb ratios of hornblende-bearing gabbros (Figure 4.8), since K would be less incompatible in hornblende than Rb [Gill, 1978]. The two gabbros lacking primary

hornblende (PC175 and TC-47) have the lowest K/Rb ratios because K and Rb are equally incompatible in plagioclase, orthopyroxene, and olivine. Thus, it is clear that the primary igneous cumulate phases are preserved in the gabbros, and we may use the minerals in order to attempt to gain information about their parent magmas.

For troctolite PC175, the olivine Mg# should reflect that in the melt with which it was in equilibrium. Using a K_D $((FeO/MgO)_{oliv}/(FeO/MgO)_{melt})$ value of 0.3 [Roeder and Emslie, 1970] yields a quite evolved Mg# for the melt of 52. This is consistent with the implication of the isotopic data (Chapter 3) that this gabbro has a significant crustal component, and demonstrates that it did not crystallize from a primary mantle melt. The coexistence of Fo_{78} olivine with very calcic plagioclase (An_{97}) bears a resemblance to relationships in cumulate nodules from the Lesser Antilles island arc [Arculus and Wills, 1980]. The authors distinguish this association from those in gabbros in other tectonic/plutonic settings and attribute the very high An content of the plagioclase to high H_2O activity.

Plagioclase compositions in the other gabbros indicate that they crystallized from more evolved magmas. Estimates of melt Mg#'s may be made from hornblende and orthopyroxene compositions. For hornblende, the K_D for Fe and Mg is apparently highly variable and sensitive to a number of parameters; we use a value of 0.375 based on a compilation by Gilbert et al. [1982]. For the TC-49b core Mg# (58), we calculate a melt Mg# of 34; if the hornblende Fe^{3+}/Fe^{2+} ratio is 0.3 (rather than zero), the hornblende Mg# is 64 and the calculated melt is 40. For a hornblende Mg# such as 46 in quartz diorite TC-45b, the melt value is 24; this corresponds to $(FeO/MgO)_{wt.}$ in the melt of 5.6, which is an unreasonably high value (the highest values among the samples are 3.5). We do not consider such calculations to be reliable without better constrained K_D's. Calculations based on orthopyroxene compositions yield equally unreasonable melt Mg#'s; the K_D is temperature dependent, and we use values from Barnes [1986] and calculated values from

Figure 4.7 - Variations in CaO and Al_2O_3 with SiO_2 in gabbros from the Tunis Creek unit. *squares* are hornblende-only gabbros, and *triangles* also contain orthopyroxene; the highest-SiO_2 gabbro has no hornblende. Also plotted as *circles* are average compositions of hornblende, orthopyroxene, and plagioclase (An_{90-60}) from the unit (data of this Chapter and Chapter 2), showing that the gabbros may be described as cumulate mixtures of plagioclase and the appropriate mafic phase(s).

Tunis gabbros
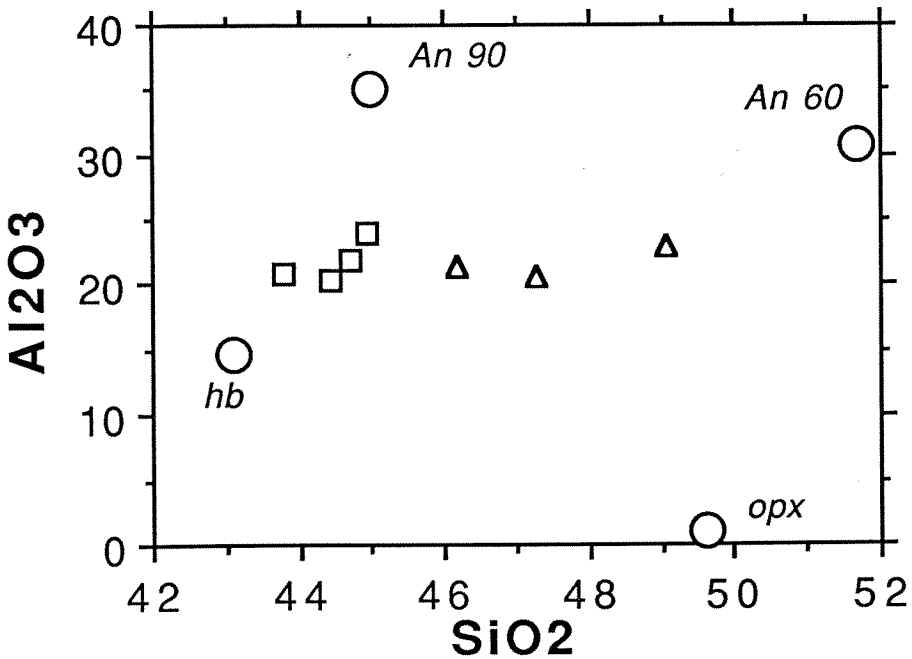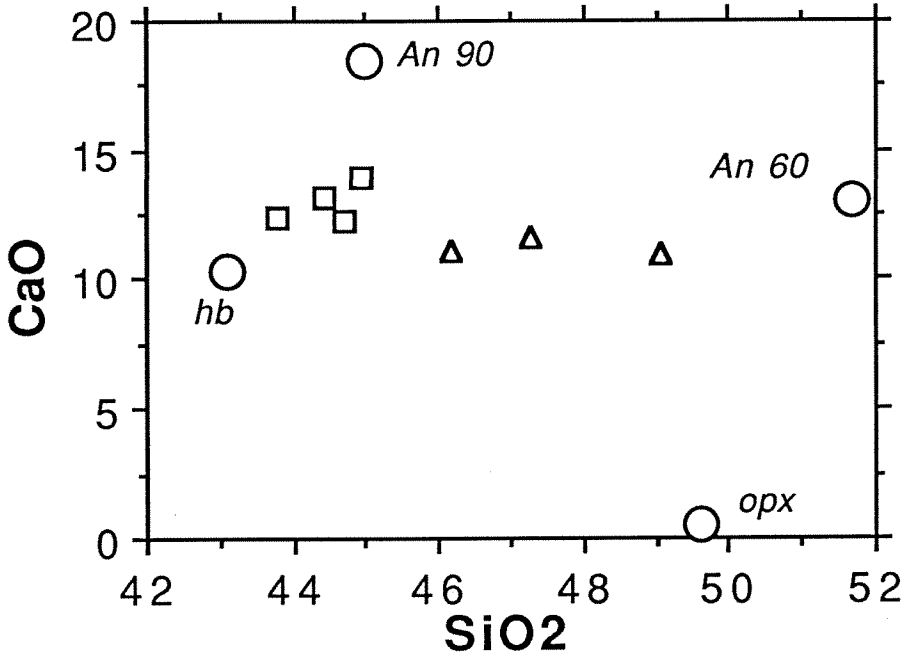
Fig. 4.7

Figure 4.8 - Log plot of K/Rb vs. K (ppm) which includes data from the area from Ross [1989] (including the Bear Valley Springs tonalite). "BV" = intrusive suite of Bear Valley, "TM" = igneous rocks of the gneiss complex of the Tehachapi Mountains. Note the deviation of the granites from the trend defined by the tonalites. "*T*" = TC-6; "*P*" = PC35-P. The low-K rocks are gabbros, with the two lowest-K being the hornblende-free samples (TC-47 and PC175).
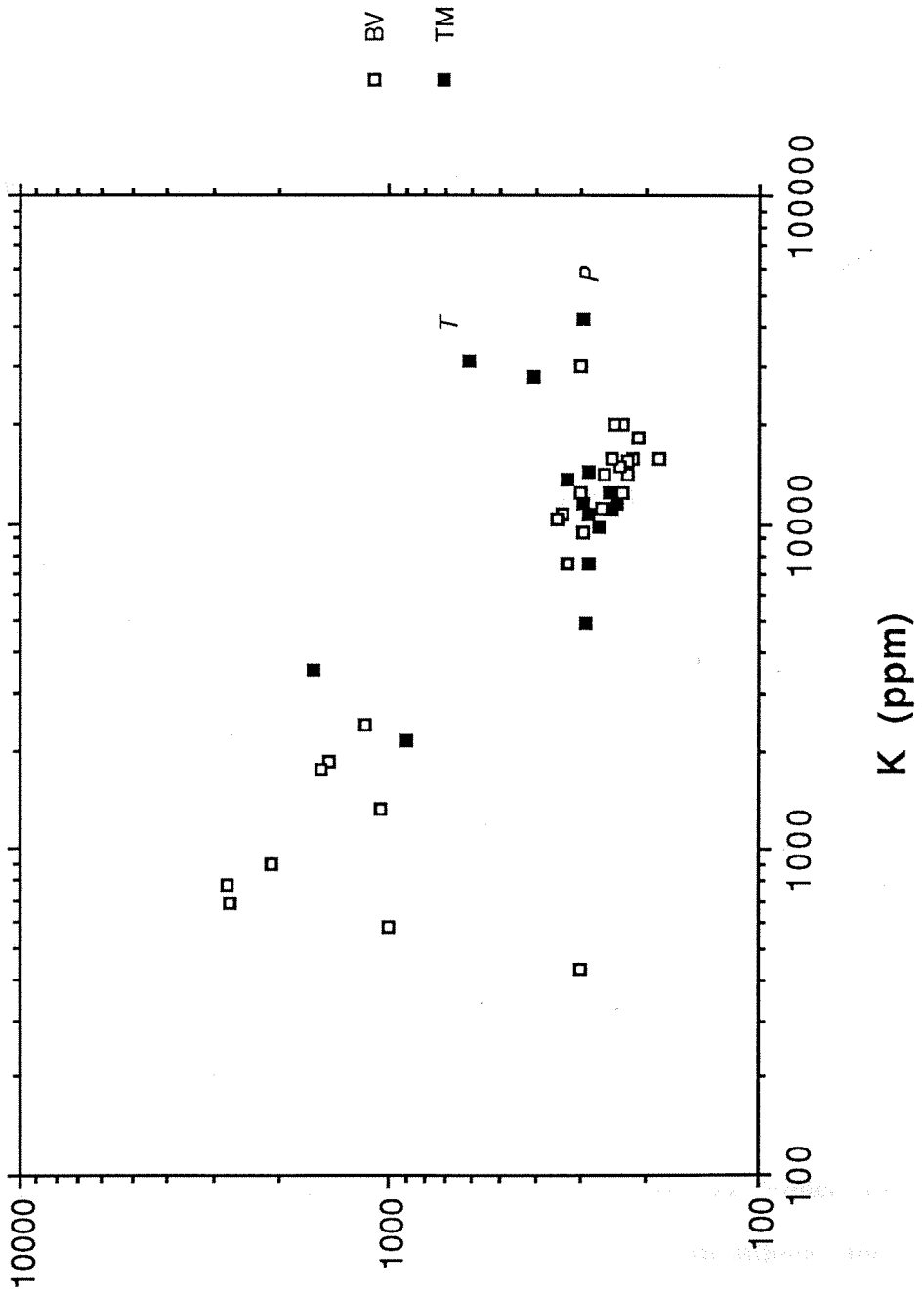
Fig. 4.8

the data of Grove and Juster [1989]. For norite TC-47, the calculated melt Mg# is 14 to 20, depending on temperature. We cannot fully explain the reasons for these apparently erroneous calculated compositions, but a large part of the problem most likely lies in the inappropriateness of the experimental conditions for those in the batholith. Such low Mg#'s are not unusual for hornblendes and orthopyroxenes in mafic and intermediate magmas from island arcs [Arculus and Wills, 1980; Gill, 1981] or elsewhere in the Sierra Nevada batholith [Mack et al., 1979]. Despite these uncertainties, it is clear that the Tehachapi gabbros accumulated from melts of rather evolved character, perhaps dioritic or quartz dioritic. The low Ni and Cr of the gabbros, exclusive of the troctolite, suggests that these magmas had previously undergone Ni and Cr depletion by olivine farctionation. Otherwise, the high partition coefficients for Ni and Cr in hornblende and orthopyroxene [e.g., Gill, 1978] would have resulted in higher concentrations.

One of the gabbros, TC-83, contains dispersed metamorphic garnets, and there are some indications of possible open-system behavior during the metamorphic event. These include high Y and Zr/Hf (Figure 4.6) relative to the other gabbros. More metamorphic samples are needed to fully evaluate the extent of element mobility.

b. Tonalites and granodiorites

Intermediate rocks from the two suites overlap in all chemical parameters (e.g., Figures 4.3 and 4.5-4.8) and, as mentioned above, their major element characteristics are like those in the central part of the Sierra Nevada batholith, with the exception of being more sodic (Figure 4.4). The only significant distinction in primary character between the two suites is the presence in the lower-Si intermediate rocks of the Bear Valley suite of orthopyroxene. The orthopyroxene, the smooth major element variations, and the systematic mineral chemical variations help establish a link between the gabbros and the Bear Valley tonalites. It therefore is likely that the tonalites of the two suites had similar origins, which involved fractionation from more mafic magmas. The tonalites lack critical

chemical features (low Y, high Sr/Y) that would support an eclogitic source [Defant et al., 1991], including a lack of HREE depletion in a few samples of tonalite gneiss and several from the Bear Valley Springs unit reported by Ross [1989]. Furthermore, the experimental data of Carroll and Wyllie [1990] preclude a garnet-bearing source for Sierra Nevada magmas in general, and the Tehachapi compositions follow the same general chemical trend (see Figure 7 in Carroll and Wyllie). In evaluating the hypothesis of a garnet-free gabbroic source for the tonalites, it is difficult to distinguish this process from fractional crystallization from such a gabbroic magma. The discussion of isotopic data in Chapter 3, however, favors the presence of mafic magmas which mix with crustal materials and subsequently fractionate.

The major and trace element data offer some clues pertaining to particular phases involved in this inferred fractionation. The lack of significant Rb enrichment in higher-SiO_2 members of the suites (Figure 4.5) implies that biotite must be a fractionating phase; no other mineral in these rocks has the same capability to inhibit such enrichment. The unusual chemical characteristics of diorite TC-12b (Table 4.2), including its high K_2O (1.3 %) and Rb (38 ppm) for such low SiO_2 (49 %), reflect accumulation of biotite along with hornblende; this rock thus lends credence to the plausibility of biotite fractionation. The two low-K_2O, -Rb, and -Ba but high SiO_2 rocks (Figure 4.3) may have been formed as a result of more pronounced biotite fractionation. The relative K_2O depletion cannot be attributed solely to dilution by quartz enrichment, by magmatic or subsolidus means, because not all elements show a similar depletion. The convex-up Na_2O pattern (Figure 4.3) is suggestive of fractionation of progressively more sodic plagioclase with higher SiO_2. The progressive lowering of Sm/Nd with increasing SiO_2 (not shown) can be attributed, like the high Sm/Nd in the gabbros, to the sorting of hornblende; this fractionation effect could be enhanced by the increasing abundance in the tonalites of LREE-enriched accessory phases such as allanite.

In summary, the chemical data are compatible with an origin for the tonalites as fractionates from more mafic magmas. The isotopic data (Chapter 3) point to the heterogeneity of these mafic parents throughout the two suites, so that consanguinity among the various samples is not implied by these conclusions. In fact, features such as the low-K_2O leucotonalite and granodiorite reveal variations in the fractionation processes as well.

c. Granites

The three granites (GC-43, PC35-P, and TC-6) are quite distinctive, particularly considering that the granodiorites are low in alkali feldspar. On Figure 4.8, the granites lie in a distinct field of K/Rb and K, suggesting an origin that is discontinuous with tonalite and granodiorite genesis. Furthermore, TC-6 and PC35-P are shifted to higher $^{87}Sr/^{86}Sr$ than the other igneous rocks without a corresponding decrease in ε_{Nd}, which was taken as a possible indication of a contribution of Sr from a fluid source (Chapter 3). However, the granites have quite variable trace element characteristics (Table 4.2, Figures 4.5 and 4.6). Using the methods and partition coefficients of Nabelek [1986], we find that separation of a 30 % batch partial or residual melt from an average biotite tonalite yields Rb, Sr, and Ba concentrations (87, 161, and 780 ppm, respectively) reasonably close to those in TC-6 (52, 170, and 945) and GC-43 (69, 173, and 1076). However, modeling of PC35-P concentrations (139, 52, and 26 ppm) was not successful, mainly due to the unusually low Ba. Nevertheless, calculations suggest that the low Ba and Sr contents could result from partial melting or extreme fractionation of a granite, with Rb still behaving relatively incompatibly if biotite is not too abundant. The low Zr of this granite could result from the presence of zircon in the partial melt residue; calculations of zircon solubility [Watson and Harrison, 1983] in PC35-P show that its Zr concentration (57 ppm) is appropriate for a zircon saturated melt at 720°C. The high Sm/Nd (0.227) of PC35-P compared to the other granitic rocks (Chapter 3) can be explained by the presence of

allanite in the residue [e.g., Miller and Mittlefehldt, 1982]. The unusual K/Rb ratios (Figure 4.8) cannot be easily explained by such models, but it is possible that K metasomatism may have been a factor; such fluid interaction could have resulted in the inferred isotopic shifts. However, such metasomatism would not likely cause the low Sr and Ba and high Rb in PC35-P, due to high mineral/fluid partition cofficients for Sr and Ba and low coefficients for Rb [e.g., Carron and Lagache, 1980].

4.6. Summary and conclusions

These discussions have illustrated the consistency of the chemical data for the Tehachapi igneous rocks with petrogenetic processes involving crystal sorting. We interpret fractionation to have acted on isotopically variable mafic to intermediate magmas which had formed from mixtures in the deepest batholith between mantle-derived magmas and metasedimentary rocks. It is the fractionation processes, rather than mixing, which have given rise to the various lithologies. Particular points of interest are as follows:

-- The gabbros are cumulates with hornblende being of primary igneous origin; i.e., these are not amphibolites. Parent magmas to these cumulates were quite evolved, with Mg#'s of at most 52, and the hornblende-bearing cumulates crystallized from magmas which had most likely been previously subjected to olivine fractionation.

-- Tonalites of the two suites are chemically similar, and are inferred, along with the granodiorites, to have formed from fractional crystallization of magmas analogous to the parents of the cumulates. Crystallization conditions may have been variable, yielding in some cases quartz-rich tonalites.

-- Two of the granites appear to have formed by fractionation of the more evolved biotite tonalites. The origin of the high-SiO_2 granite is enigmatic, but it may have formed by partial melting of granites. An important role for fluid interaction cannot be ruled out.

References

Arculus, R.J., and K.J.A. Wills, The petrology of plutonic blocks and inclusions from the Lesser Antilles island arc, *J. Petrol., 21*, pp. 743-799, 1980.

Barnes, S.J., The distribution of chromium among orthopyroxene, spinel, and silicate liquid at atmospheric pressure, *Geochim. Cosmochim. Acta, 50*, pp. 1889-1909, 1986.

Bateman, P.C., F.C.W. Dodge, and P.E. Bruggman, Major oxide analyses, CIPW norms, modes, and bulk specific gravities of plutonic rocks from the Mariposa 1 x 2 sheet, central Sierra Nevada, California, *U.S. Geol. Survey Open-file Report 84-162*, 50 pp., 1984.

Bence, A.E., and A.L. Albee, Empirical correction factors for the electron microanalysis of silicates and oxides, *J. Geol., 76*, pp. 382-403, 1968.

Carroll, M.R., and P.J. Wyllie, The system tonalite-H_2O at 15 kbar and the genesis of calc-alkaline magmas, *Amer. Mineral., 75*, pp. 345-357, 1990.

Carron, J.-P., and M. Lagache, Étude expérimentale du fractionnement des éléments Rb, Cs, Sr et Ba entre feldspaths alcalins, solutions hydrothermales et liquides silicatés dans le système Q.Ab.Or.H_2O à 2 kbar entre 700 et 800°C [Experimental study of the fractionation of Rb, Cs, Sr, and Ba between alkali feldspars, hydrothermal solution, and silicate melts in the system Q.Ab.Or.H_2O at 2 kbar and 700 to 800°C], *Bull. Minéral., 103*, pp. 571-578, 1980.

Defant, M.J., L.F. Clark, R.H. Stewart, M.S. Drummond, J.Z. de Boer, R.C. Maury, H. Bellon, T.E. Jackson, and J.F. Restrepo, Andesite and dacite genesis via contrasting processes: the geology and geochemistry of El Valle Volcano, Panama, *Contrib. Mineral. Petrol., 106*, pp. 309-324, 1991.

Gilbert, M.C., R.T. Helz, R.K. Popp, and F.S. Spear, Experimental studies of amphibole stability, in *Amphiboles: Petrology and Experimental Phase Relations*, edited by D.R. Veblen and P.H. Ribbe, Mineral. Soc. Amer., *Reviews in Mineralogy, 9B*, pp. 229-353, 1982.

Gill, J.B., Role of trace element partition coefficients in models of andesite genesis, *Geochim. Cosmochim. Acta, 42*, pp. 709-724, 1978.

Gill, J.B., *Orogenic Andesites and Plate Tectonics*, New York, Springer-Verlag, 390 pp., 1981.

Grove, T.L., and T.C. Juster, Experimental investigations of low-Ca pyroxene stability and olivine-pyroxene-liquid equilibria at 1-atm in natural basaltic and andesitic liquids, *Contrib. Mineral. Petrol., 103*, pp. 287-305, 1989.

Mack, S., J.B. Saleeby, and J.E. Farrell, Origin and emplacement of the Academy Pluton, Fresno County, California, *Geol. Soc. Amer. Bull., Part II, 90*, pp. 633-694, 1979.

Medaris, L.G., Jr., Partitioning of Fe^{++} and Mg^{++} between coexisting synthetic olivine and orthopyroxene, *Amer. J. Sci., 267*, pp. 945-968, 1969.

Miller, C.M., and D.W. Mittlefehldt, Depletion of light rare-earth elements in felsic magmas, *Geology, 10*, pp. 129-133, 1982.

Nabelek, P.I., Trace-element modeling of the petrogenesis of granophyres and aplites in the Notch Peak granite stock, Utah, *Amer. Mineral., 71*, pp. 460-471, 1986.

Roeder, R.L., and R.F. Emslie, Olivine-liquid equilibrium, *Contrib. Mineral. Petrol., 29*, pp. 275-289, 1970.

Ross, D.C., The metamorphic and plutonic rocks of the southernmost Sierra Nevada, California, and their tectonic framework, *U.S. Geol. Survey Prof. Paper 1381*, 159 pp., 1989.

Sams, D.B., U/Pb zircon geochronology, petrology, and structural geology of the crystalline rocks of the southernmost Sierra Nevada and Tehachapi Mountains, Kern County, California, Ph.D. thesis, 315 pp., California Institute of Technology, Pasadena, California, 1986.

Sams, D.B., and J.B. Saleeby, Geology and petrotectonic significance of crystalline rocks of the southernmost Sierra Nevada, California, in *Metamorphism and Crustal Evolution of the Western United States (Rubey Vol. VII)*, edited by W.G. Ernst, p. 865-893, Englewood Cliffs, N.J., Prentice-Hall, 1988.

Sharry, J., The geology of the western Tehachapi Mountains, California, Ph.D. thesis, 215 pp., Massachusetts Institute of Technology, Cambridge, Mass., 1981.

Spear, F.S., and K.L. Kimball, RECAMP -- A FORTRAN IV program for estimating Fe^{3+} contents in amphiboles, *Comput. Geosci.*, *10*, 317-325, 1984.

Watson, E.B., and T.M. Harrison, Zircon saturation revisited: temperature and composition effects in a variety of crustal magma types, *Earth Plan. Sci. Lett.*, *64*, pp. 295-304, 1983.

CHAPTER 5

SUMMARY

The objectives of this study were to investigate the evidence for a deep-batholith setting for the intrusive rocks of the Tehachapi Mountains, and then to discuss the isotopic and chemical features of the rocks in the context of this setting. In Chapter 2, it was shown that these rocks indeed crystallized at depths of 25-30 km, making them the deepest exposed rocks of the Cretaceous Sierra Nevada batholith. The rocks were subjected to syn-magmatic and subsolidus deformation and flow, as well as recrystallization, localized garnet-forming metamorphism (8 kbar), and lower-temperature retrograde metamorphism. Uplift is inferred to have followed soon after intrusion, with a 4 kbar garnet-forming event imprinted on the Tunis Creek area. Low-temperature ductile deformation affected much of the area throughout its subsolidus history. It is thus demonstrated that the deep Sierra Nevada batholith is a regime capable of extensive deformation (due to the abundance of quartz) and delamination from the deeper crust. This observation has implications for models of the tectonic history of the batholith, while the particular history of the Tehachapi Mountains block is important for models of the tectonic development of southern California.

Isotopic and chemical characteristics of these intrusive rocks, which are dominantly tonalitic but range from gabbro to granite, are best explained by their sources having consisted of mixtures of mantle-derived mafic magmas and metasedimentary rocks of old continental and, possibly, earlier Mesozoic volcanic arc provenance. In this model, the gabbros are cumulates from relatively evolved gabbroic to tonalitic magmas which had risen from the deeper batholith regime of isotopic hybridization, and the tonalites to

granites are products of fractional crystallization without further assimilation. This implies that, in general, batholithic magmas obtain their "hybrid" isotopic character in the deepest crust and high-level crustal interaction is of minor importance. This conclusion is independent of the particular petrogenetic model employed.

The deep (but not *deepest*) Sierra Nevada batholith as revealed in the Tehachapi Mountains is dominated by tonalite, but is apparently more heterogeneous than higher levels, with an appreciable amount of cumulate gabbros in bodies of considerable size (up to 4 x 7 km) and as intermingled magmas at outcrop scale. These gabbros are probably more abundant at deeper levels, where we would also expect to find gabbroic rocks which have seen less interaction with the pre-existing crust. It appears, then, that the process of building higher levels of the batholith involves some amount of homogenization of these chemically, but not isotopically, distinct magma types but also, of course, a diminution in the abundance of residual cumulate material.

These observations may have implications for the genesis of continental margin magmatic arcs in general. The mixing-type pattern exhibited by Sr and Nd isotopic ratios in the Tehachapi rocks is a common feature in such settings, and numerous workers have discussed the compelling evidence for a continental crustal component in arc magmas. What the Tehachapi study suggests is that this interaction is, by and large, a deep process, and that higher-level fractionation processes may obscure the chemical imprints while preserving the isotopic.

In Appendix 1 is a study of batholithic intrusive rocks in New Zealand, in a tectonic setting analogous to that of the Sierra Nevada batholith. These rocks also bear the isotopic signature of crustal interaction, and detailed modeling, while suggestive of metasedimentary sources for the crustal component, reveals the difficulty of seeing through magmatic processes to the chemical character of the ultimate source. An interesting result of the study is the recognition of isotopic differences between the two

major intrusive episodes that affected this portion of the New Zealand block. The Mesozoic episode appears to have involved a lesser input of crustal melts than in the Paleozoic magmas, possibly because the earlier episode depleted the crust in just those low-melting temperature materials which supply the crustal signature. Such a model does not appear applicable to the southern Sierra Nevada, where the association of plutonic rocks of vastly different ages is less pronounced; but it would be of interest to search for similar cases of juxtapositioning of plutonic belts throughout the world.

Continental margin granitoid batholiths are typically emplaced in crustal settings of transitional character, where outboard craton edges give way to marginal sedimentary prisms which in turn give way to more ensimatic sedimentary and volcanic assemblages. Seen in this way, it is not surprising that the magmas generated and emplaced in this setting should reflect its hybrid character.

APPENDIX 1

Neodymium and strontium isotopic characteristics

of New Zealand granitoids and related rocks

Note: A revised and shortened version of this chapter, coauthored with Professor Gerald

J. Wasserburg, was published as Pickett and Wasserburg (1989).

A1.1. Introduction

New Zealand occupies a crustal block unique in its dimensions and isolation. It

exhibits petrologic, tectonic, and stratigraphic associations typical of Phanerozoic mobile

belts found in marginal regions of continents. However, New Zealand presently lacks a

corresponding cratonic interior as well as any exposed Precambrian basement rocks.

Therefore, many questions remain regarding the age and nature of the underlying

crystalline crust, and if and how such crust is distributed among the surrounding

submerged plateaus.

To address these questions, we have made a reconnaissance-scale isotopic study

of New Zealand granitoids from this crustal block, as felsic magmatism has been shown

commonly to reflect the character of the crust in which it has formed. We have

attempted to ascertain the degree of involvement of recycled, remobilized crustal

materials in felsic magmatism throughout New Zealand's history, and to place

constraints on the types of petrogenetic processes that may facilitate crustal involvement

in granitoid generation. Comparison is made between similar rock associations in New

Zealand, Australia, and Antarctica, which are thought to have been proximal in

Gondwanaland. Preliminary results have appeared in abstract form (Pickett et al., 1986).

A1.2. Geologic setting

Granitoids are exposed on the South Island and Stewart Island of New Zealand, and in the offshore region on the Snares, Auckland, and Bounty Islands (Figure A1.1). On the South Island, granitoids are restricted to the western Tasman metamorphic belt (Landis and Coombs, 1967) or Foreland Province (Aronson, 1965), and are not found in the late Paleozoic to Mesozoic Wakatipu belt (Landis and Coombs, 1967) or Geosynclinal Province (Aronson, 1965) to the east. In West Nelson and Westland, the granitoids are intruded into three belts of Early Cambrian to Early Devonian sequences of continental margin sediments and volcanic rocks (Nathan, pp. 68-79, and Grindley, pp. 80-99, in Suggate et al., 1978). Exposures of paragneisses and orthogneisses of the Charleston Metamorphic Group (Nathan, 1975) are found mainly in the western coastal area. The rocks were long thought to represent the Precambrian basement to the Paleozoic strata, and Adams (1975) reported a 666 m.y. Rb-Sr whole-rock isochron on the unit. However, recent U-Pb zircon data (D. Kimbrough, pers. commun.) are more consistent with a Cretaceous igneous and metamorphic age for the gneisses. Thus, the question of the presence of Precambrian crystalline rocks remains unresolved. Aronson (1968), however, has reported a middle Proterozoic age (1.48 b.y.) on detrital zircons, demonstrating the existence of Precambrian sources for the sedimentary Greenland Group of the Foreland Province.

Relationships are more complex and less understood in the remote Fiordland region (Grindley, pp. 100-110, in Suggate et al. 1978; Mattinson et al. 1986), which appears to represent deeper levels of exposure than the West Nelson-Westland region, which is offset from it along the Alpine Fault. Western Fiordland consists mainly of complexly deformed metaplutonic and metasedimentary rocks, while in the east the

Figure A1.1a. New Zealand and its associated submarine plateaus, defined by the 2000 m isobath, after Cullen, p. 3, in Aronson (1965). Shown are localities for two samples from Campbell Plateau islands and two from the southern South Island. FL = Fiordland, WL = Westland, WN = West Nelson, TVZ = Taupo Volcanic Zone. On the South Island, the heavy line is the Alpine Fault, and the dashed line is the Median Tectonic Line (Landis and Coombs 1967).

1b. Pre-Late Cretaceous geology of West Nelson and northern Westland, South Island, after Tulloch and Brathwaite (1986) and Mason and Taylor (1987), showing sample localities. Despite the location of sample AR-16 in the Karamea Suite unit, it is here considered to be Cretaceous in age (see text). The unpatterned patch between the Glenroy-Rotoroa unit and the Alpine Fault contains Permian strata.

Fig. A1.1a

b

Mid-Cret. & younger sed. rocks
E.K. Rahu Suite granitoids
E.K. Separation Pt. Suite granitoids
K.? Glenroy Meta. Complex +
Rotoroa Mafic Complex
D Riwaka Mafic Complex
D-C Karamea Ste. granitoids
Undiff. granitoids

NE-16
NE-19
NE-3
NE-13

Westport

N
50 km

AR-16
NE-4

Greymouth
33-RO
32-RO
Hokitika
12-RO
WL-2

€→D Lower Pz. sed. rocks
(Greenland Gp. shaded)
p€?K?Charleston Meta. Gp.
? and Fraser Fm.(in south)

ALPINE   FAULT

AR-23G

Fig. A1.1b

intrusives are relatively undeformed and appear to have been emplaced at higher levels.

Pre-granitoid rocks on Stewart Island and the Snares Islands (Watters, pp. 111-112, in Suggate et al. 1978) are represented by isolated schists and amphibolites. In the Auckland and Bounty Islands, no pre-intrusive rocks are exposed, although graywacke has been dredged from the shelf floor near the Bounty Islands (Wasserburg et al., 1963).

Comprehensive summaries of the granitoids of New Zealand and pertinent geochronologic data may be found in Tulloch (1983), and in Tulloch and Brathwaite (1986). Although early Mesozoic ages have been reported, granitoid plutonism is dominated by two episodes: Devonian-Carboniferous (mainly 380-330 m.y.) and Cretaceous (mainly 130-100 m.y.), in accord with the pioneering geochronologic work of Aronson (1965, 1968). With the exception of the 185 m.y.-old Bounty Islands granodiorite (BIG) (Wasserburg et al., 1963), the present study is confined to rocks from these two episodes. Tulloch (1983) classifies the majority of the granitoids into three groups based on petrography and geochemistry (Figure A1.1b). The Karamea Suite (Devo-Carboniferous) is characterized by biotite and two-mica granites to tonalites. The Cretaceous Rahu Suite is dominated by biotite granite and granodiorite, with lesser muscovite occurrences. The Cretaceous Separation Point Batholith lies on the eastern margin of the Tasman belt and consists of an assemblage of biotite hornblende granites to quartz diorites.

A1.3. Samples and analytical procedures

Samples were chosen to represent the spectrum of compositional types from the two main intrusive episodes and for wide geographic coverage (Figure A1.1, Table A1.1). In general, it was also desired that the units sampled have relatively well-established ages. Thus, in the north, the well-dated Rameka Gabbro (NE-16) of the Riwaka Complex

and the Karamea two-mica granite exposed at the Oparara Quarry (NE-3) provide compositional end-members of the Paleozoic episode. In Westland, geographic diversity is provided by the Waitaha River biotite granite (AR-23G) and the two-mica granite near Mt. McLean (WL-17) (associated with the "Quartz Hill" pegmatite, muscovite age of 357 m.y., (Aronson, 1968)). These three granites are characteristic of the Karamea Suite.

For the Cretaceous rocks, mafic members are represented by a hornblende-bearing mafic phase of the Pearse Granodiorite, Separation Point Batholith (NE-13) and the Thirsty Creek metanorite (WL-2). This latter unit is probably Cretaceous in age, based on its undeformed nature in a Cretaceous mylonite zone (Tulloch and Brathwaite, 1986; Mason and Taylor, 1987). Three Cretaceous granites from West Nelson-Westland were studied. The two-mica Buckland Granite, Lower Buller Valley (NE-4) is constrained in age to between 110 and 99 m.y. by Adams and Nathan (1978), and preliminary U-Pb zircon work by D. Kimbrough (pers. commun.) suggests a 120 to 100 m.y. age. AR-16 is Aronson's (1968) "Buller Granite," a two-mica granite apparently correlative with the O'Sullivans Granite (Roder, 1984). Roder (1984) suggests a Carboniferous age for the O'Sullivans Granite, but Aronson (1968) obtained a well-defined 110 m.y. Rb/Sr internal isochron on AR-16. The two-mica Rotomanu granite (32-RO) has yielded a 70 m.y. K/Ar biotite age (Mason, 1961), reflecting uplift, and has been assigned by Tulloch and Brathwaite (1986) to the Cretaceous Rahu Suite. SF-4 is a sample of the biotite-bearing Pomona Granite, which lies in the eastern Fiordland belt of unmetamorphosed intrusives (Mattinson et al., 1986).

In the interest of examining the extension of New Zealand crustal characteristics out onto its surrounding shelf, granites from islands on the Campbell Plateau were also studied. The Auckland Islands biotite microgranite (82242) is exposed over a small area at the base of a Miocene basaltic shield volcano (sample 30142/7779 of Gamble and Adams (1985)), and has yielded a K/Ar biotite age of 93 m.y. (Denison and Coombs,

Table A1.1 - Sample localities and ages

		N.Z. Grid Reference[a]	Age (m.y.) [ref.]	T(m.y.)[b]
Mesozoic Granites				
AR-16	Whale Flat, Buller R.	S25/631701	110 (Rb/Sr) [1]	110
NE-4	Lower Buller Gorge at Ohikanui River	S31/199612	110-99 (K/Ar) [2]	105
32-RO	Rotomanu, south of railroad station	K32/899383	70 (K/Ar) [3]	115
SF-4	Pomona Island, Lake Manapouri	S149/566088	115-100 (Rb/Sr) [1]	115
82242	Musgrave Point, Auckland Island	50°49.5'S, 166°02.5'E	93 (K/Ar) [4]	115
BIG	Bounty Islands	~ 47°40'S, 179°E	185 (K/Ar, Rb/Sr) [5]	185
Mesozoic Mafic Rocks				
NE-13	Motueka River near Pearse Stream	S13/207348	120-115 (U/Pb) [6]	115
WL-2	Inlier on Thirsty Cr., near Rotomanu	K32/912374	Cretaceous [7, 8]	115
Paleozoic Granites				
NE-3	Quarry, Oparara R.	S12/601384	345 (Rb/Sr) [1]	345
AR-23G	Ellis Cr. Quarry, Waitaha River	S64/334139	351 (Rb/Sr) [1]	351
WL-17	Mt. McLean, near Arawata River	S97/601940	357 (Rb/Sr) [1]	357
Paleozoic Mafic Rock				
NE-16	Pikikiruna Range, on Rameka Track	S8/270718	367 (K/Ar) [9]	367
Metasediments				
NE-19	Pikikiruna Range, near Takaka Hill	S13/243597	Ordovician [10] 107 (K/Ar meta.) [9]	355, 115
12-RO	Inlier on Thirsty Cr., near Rotomanu	K32/922375	?	355, 115
33-RO	Hill south of Kangaroo Lake	K32/911416	Cambro-Ordovician [11]	355, 115

[a] The two Campbell Plateau samples are located by latitude-longitude. The localities with the prefix K32 are from a 1:50,000 map grid; the others are from a 1:63,360 grid.
[b] The ages to which isotopic ratios were corrected.
References: 1 - Aronson 1968; 2 - Adams and Nathan 1978; 3 - Mason 1961; 4 - Denison and Coombs 1977; 5 - Wasserburg et al. 1963; 6 - D. Kimbrough, pers. commun.; 7 - Tulloch and Brathwaite 1986; 8 - Mason and Taylor 1987; 9 - Harrison and McDougall 1980; 10 - Suggate et al. 1978; 11 - Adams 1975.

1977). The Bounty Islands biotite granodiorite (BIG) has yielded biotite K/Ar and Rb/Sr ages of 185 m.y. (Wasserburg et al., 1963) and thus is evidence for granitoid-bearing continental crust extending out to the eastern edge of the Campbell Plateau.

It is of interest to isotopically characterize the crust through which the granitoids were intruded. Since the make-up of this crust is unknown, the best guess is represented by the Paleozoic sedimentary rocks of the South Island. Sample 33-RO is a representative of the Cambrian(?)-Ordovician Greenland Group graywackes which underlie a major portion of the West Nelson-Westland region (Figure A1.1b) (Suggate et al., 1978; Adams, 1975; Nathan, 1976). Sample 12-RO is a sillimanite-almandine-biotite gneiss from near Rotomanu, which has strong similarities to paragneisses in the Charleston Metamorphic Group. Mason and Taylor (1987) place this rock in the Fraser Formation. Finally, NE-19 is a sample of the Pikikiruna Schist (quartz-muscovite-biotite-garnet), which is intruded by the Separation Point Batholith and has a probable protolith age of pre-Late Ordovician (Grindley, pp. 80-99, in Suggate et al. 1978) and a K/Ar metamorphic age of 107 m.y. (Harrison and McDougall, 1980). These sedimentary units (as exposed) may not directly participate in granite generation, but rather, may be representative of the material which comprises the crust of the region.

Samples of up to 2 kg of rock were broken down to ~0.5 cm pieces and well-mixed splits of these were crushed with a stainless steel mortar and pestle to yield 20 g of powder. A 200-400 mg split of this powder was taken for analysis. To ensure complete dissolution, powders were either (1) dissolved in HF + HNO_3 in teflon bombs at 180°C, or (2) dissolved in HF + $HClO_4$ in open teflon beakers, with any residue from centrifugation of the solution then receiving the bomb treatment. Concentrations of Rb, Sr, Sm, and Nd were determined by isotope dilution, and Sr and Nd isotopic ratios were determined on the same runs as the concentration determinations. Procedural details are described elsewhere (Papanastassiou and Wasserburg, 1973; Papanastasiou et al.,

1977; DePaolo and Wasserburg, 1976). Splits of the powders (except for sample AR-16) were analyzed by X-Ray Assay Laboratories, Inc. for elemental concentrations. Major elements, Zr, and Ba, were determined by x-ray fluorescence for all samples. For selected samples, REE (La, Ce, Nd, Sm, Eu, Tb, Yb, Lu), Sc, Cr, Cs, Th, and U were determined by neutron activation analysis, and V, Mn, Ni, Zn, and Pb by direct current plasma spectrometry.

A1.4. Results

The Rb/Sr and Sm/Nd isotopic and concentration data are presented in Tables A1.2 and A1.3. Following DePaolo and Wasserburg (1976), the isotopic data are presented in ε notation. Correction to the initial isotopic composition at a "formation" time T (AE) is: $\varepsilon_{Nd}(T) \approx \varepsilon_{Nd}(0) + Q_{Nd}f^{Sm/Nd}T$. Here, $f^{Sm/Nd} = [(^{147}Sm/^{144}Nd)_m/(^{147}Sm/^{144}Nd)_{CHUR}] - 1$. Analogous formulae hold for $\varepsilon_{Sr}(T)$. Decay constants used are $\lambda_{Sm} = 6.54 \times 10^{-12}$ yr^{-1} and $\lambda_{Rb} = 1.42 \times 10^{-11}$ yr^{-1}. Model system parameters used are: $(^{143}Nd/^{144}Nd)^o_{CHUR} = 0.511847$; $(^{147}Sm/^{144}Nd)^o_{CHUR} = 0.1967$; $Q_{Nd} = 25.13$ AE^{-1}; $(^{87}Sr/^{86}Sr)^o_{UR} = 0.7045$; $(^{87}Rb/^{86}Sr)^o_{UR} = 0.0827$; $Q_{Sr} = 16.67$ AE^{-1}. Initial $(^{87}Sr/^{86}Sr)^T$ values are also shown, calculated according to the standard decay equation. The T^{Nd}_{CHUR} model age indicates the time when the material would have separated from a source with chondritic Sm/Nd ratio, assuming no change in its Sm/Nd ratio throughout its history since, calculated by: T^{Nd}_{CHUR} (AE) $= [(\varepsilon_{Nd}(0))/Q_{Nd}f^{Sm/Nd})]$ (McCulloch and Wasserburg, 1978). The T^{Nd}_{DM} indicates the time of separation from an evolving depleted mantle, and is calculated by determining T from the equation $\varepsilon_{Nd}(0) - Q_{Nd}f_{Nd/Sm}T = 0.25T^2 - (3T + 8.5)$ (DePaolo, 1981a).

The range in Nd isotopic values is roughly the same for both the Paleozoic and Mesozoic intrusive rocks, with $\varepsilon_{Nd}(T) = +2.7$ to -11.0. This range is similar to many obtained from Phanerozoic granitoid batholiths (e.g. DePaolo, 1981b; McCulloch and

Chappell, 1982), and clearly indicates the involvement of ancient, LREE-enriched continental crustal components. This is also consistent with the high range of ε_{Sr} values of -4 to +282 ($^{87}Sr/^{86}Sr$ = 0.70410-0.72390), with the Paleozoic granites all having higher values than the Mesozoic. Thus, the crustal components must have had elevated Rb/Sr ratios for long periods of time. On ε_{Nd}-ε_{Sr} plots (Figure A1.2), there is observed with the intrusive rocks a correlation between lower ε_{Nd} and higher ε_{Sr}, with the Mesozoic data lying near a mixing hyperbola between a model depleted mantle-derived magma and the Greenland Group sedimentary rock (see below). The Paleozoic rocks do not follow the mixing curve as well.

The three Devo-Carboniferous granites all have $^{87}Sr/^{86}Sr$ > 0.709, in accordance with the summary of data on some Karamea samples in Tulloch and Brathwaite (1986), while the Paleozoic mafic rock (ME-16) has distinctly lower ε_{Sr} and higher ε_{Nd}. The Pearse Granodiorite (NE-13) lies in the range of their Separation Point Batholith data (<0.7045), and the Pomona Granite (SF-4) lies near their boundary between the Separation Point samples and that of the Rahu Suite (0.7050-0.7085). The Pomona Granite, however, is unique among the granitoids in its high ε_{Nd}. The O'Sullivans and Buckland Granites (AR-16, NE-4) lie in the Rahu Suite range, while the Rotomanu granite (32-RO) at 0.7089, is beyond it. It is of interest to note that, if the O'Sullivans Granite is > 335 m.y. old as Roder (1984) concludes, its initial $^{87}Sr/^{86}Sr$ would have to be < 0.7021, which seems excessively low for a granite of any kind. Either AR-16 is a different unit from that which Roder sampled, and is not O'Sullivans Granite, or his conclusion is erroneous. At any rate, it is clear that AR-16 is most probably a Cretaceous rock belonging to the Rahu Suite.

The two granites dated only by K/Ar, Rotomanu (32-RO) and Auckland Islands (82242), have had their initial ratios calculated at 115 m.y. It is clear that they are not Paleozoic granites heated later during Cretaceous activity because their $^{87}Sr/^{86}Sr$ ratios

Table A1.2 - Rb, Sr, Sm and Nd concentrations (ppm) and parent-daughter ratios

	Rb	Sr	^{87}Rb/^{86}Sr[a]	f$^{Rb/Sr}$	Sm	Nd	^{147}Sm/^{144}Nd[b]	f$^{Sm/Nd}$
Mz Granites								
AR-16	183.2	348.6	1.516	+17.3	4.36	23.35	0.1130	-0.426
NE-4[c]	140.4	547.2	0.7402	+7.95	1.940	10.75	0.1092	-0.445
	136.7	526.2	0.7492	+8.06	1.747	9.790	0.1079	-0.451
32-RO	191.9	297.9	1.858	+21.5	3.66	17.23	0.1285	-0.347
SF-4	112.1	43.39	7.452	+89.1	2.971	16.54	0.1087	-0.448
82242	193.4	74.37	7.502	+89.7	4.720	20.89	0.1366	-0.306
BIG	176.0	135.3	3.753	+44.4	3.035	14.24	0.1289	-0.345
Mz Mafic								
NE-13	5.07*	1803	0.00808*	-0.902	7.223	35.40	0.1234	-0.373
WL-2	17.7*	602.4	0.0847*	+0.024	1.974	9.600	0.1244	-0.368
Pz Granites								
NE-3	187.9	152.6	3.550	+41.9	8.031	37.71	0.1288	-0.345
AR-23G	184.0	179.9	2.950	+34.7	5.834	30.37	0.1162	-0.409
WL-17	201.0	102.4	5.662	+67.5	7.212	28.98	0.1505	-0.235
Pz Mafic								
NE-16	40.2*	1070	0.1085*	+0.312	4.752	22.15	0.1297	-0.341
Metasediments								
NE-19	59.94	39.96	4.326	+51.3	1.922	9.509	0.1223	-0.378
12-RO	264*	199.4	3.8*	+45	5.084	26.20	0.1174	-0.403
33-RO	88*	55.21	4.6*	+55	6.08	32.51	0.1130	-0.426

[a] 2σ error is smaller than 2‰, except "*".
[b] 2σ error is smaller than 3‰.
[c] Replicate performed on different powder split.
* Rb determined only from aliquot run. 2σ error on ^{87}Rb/^{86}Sr is smaller than 1%, except 12-RO and 33-RO, around 3%.

Table A1.3 - Rb-Sr and Sm-Nd isotopic data

	^{87}Sr/^{86}Sr	^{87}Sr/^{86}Sr(T)	ε_{Sr}(T)	^{143}Nd/^{144}Nd	ε_{Nd}(0)	ε_{Nd}(T)	T_{CHUR}(Ma)	T_{DM}(Ma)
Mz Granites								
AR-16	0.70931(3)	0.70690	+35.9	0.511570(15)	-5.4(0.3)	-4.2	500	1030
NE-4	0.70742(6)	0.70632	+27.6	0.511525(21)	-6.3(0.4)	-5.1	560	1060
	0.70746(3)	0.70634	+27.9	0.511535(21)	-6.1(0.4)	-4.9	540	1040
32-RO	0.71200(3)	0.70896	+65.2	0.511431(16)	-8.1(0.3)	-7.1	930	1460
SF-4	0.71703(4)	0.70485	+6.9	0.511920(21)	+1.4(0.4)	+2.7	-	500
82242	0.72002(4)	0.70776	+48.3	0.511490(20)	-7.0(0.4)	-6.1	910	1500
BIG	0.71802(3)	0.70815	+54.9	0.511538(21)	-6.0(0.4)	-4.4	690	1280
Mz Mafic								
NE-13	0.70411(3)	0.70410	-3.8	0.511846(20)	0.0(0.4)	+1.1	-	700
WL-2	0.70744(4)	0.70730	+41.5	0.511490(17)	-7.0(0.3)	-5.9	760	1300
Pz Granites								
NE-3	0.72800(5)	0.71057(9)	+92.5(1.3)	0.511444(19)	-7.9(0.4)	-4.9	910	1450
AR-23G	0.72681(3)	0.71207	+113.4	0.511224(18)	-12.2(0.4)	-8.6	1190	1610
WL-17*	0.75205(4)	0.72327	+273.4	0.511179(20)	-13.1(0.4)	-11.0	1450	1830
Pz Mafic								
NE-16	0.70491(3)	0.70434	+3.8	0.511751(20)	-1.9(0.4)	+1.3	220	920
Metasediments								
NE-19 (115)	0.73800(3)	0.73093	+377.1	0.511080(22)	-15.0(0.4)	-13.9	1580	1960
(355)		0.71614	+171.3			-11.6		
12-RO (115)	0.72754(3)	0.7213(2)	+240(3)	0.511260(17)	-11.5(0.3)	-10.3	1140	1570
(355)		0.7082(7)	+59(10)			-7.9		
33-RO (115)	0.75004(4)	0.7425(2)	+542(3)	0.511240(21)	-11.9(0.4)	-10.6	1110	1530
(355)		0.7268(7)	+323(10)			-8.1		

Errors of measured ratios are 2σ of the mean. ^{87}Sr/^{86}Sr is normalized to ^{86}Sr/^{88}Sr = 0.1194. ^{143}Nd/^{144}Nd is normalized to ^{146}Nd/^{142}Nd = 0.636151. Errors for time-corrected ratios are approximately the same as for measured values, with noted exceptions. Errors do not include age uncertainties. T's used are from Table A1.1.

* WL-17 has an unusually high Sm/Nd, which is not reflected in the overall REE pattern (Figure A1.4). This results in probably unrealistically high model ages (T_{CHUR} = 2220 m.y., T_{DM} = 2620 m.y.). The model ages here were calculated by assuming $f^{Sm/Nd}$ = -0.4 for the source prior to crystallization at 357 m.y.

Figure A1.2. Initial ε_{Nd} vs. ε_{Sr} for all samples in the Devo-Carboniferous (a) and the Cretaceous (b). The three metasediments are represented on both diagrams. Shown are simple mixing curves between the Greenland Group graywacke (33-RO) and a model depleted mantle-derived magma (DM, see text) with tick marks representing percent graywacke. Note the exceptional position of the Mt. McLean granite on the Devo-Carboniferous plot. In the Cretaceous case, any of the metasediments could provide a suitable mixing end-member.
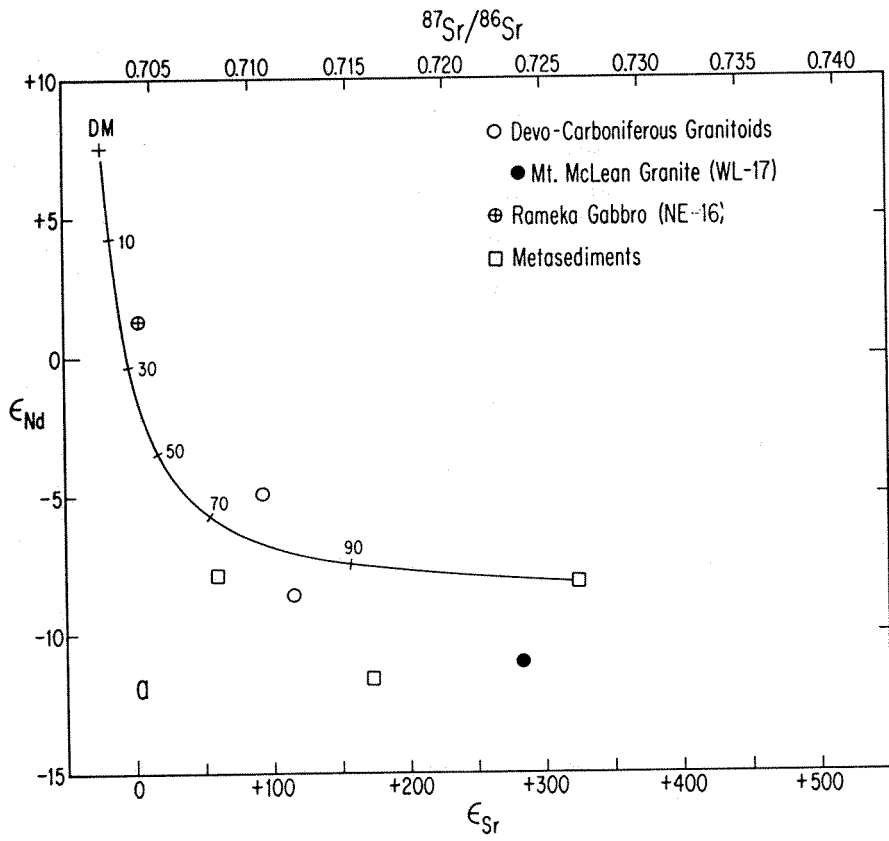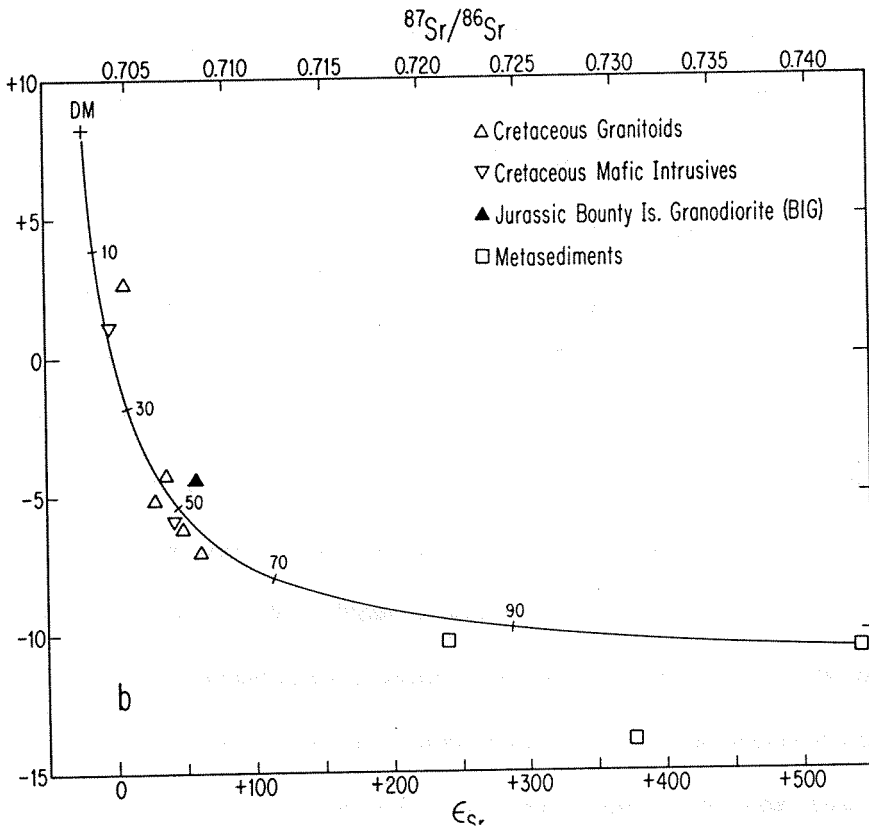
Fig. A1.2a

Fig. A1.2b

calculated for 355 m.y. are much too low (0.702 and 0.682, respectively). The metanorite (WL-2) was also calculated at 115 m.y., and gives surprisingly low ε_{Nd} and high ε_{Sr}.

The three metasediments display the high ε_{Sr} and low ε_{Nd} values reflecting a continental provenance. The T_{DM} model age of 1530 m.y. for the Greenland Group bulk rock sample (33-RO) is similar to the detrital zircon age of 1480 m.y. reported by Aronson (1968) on the Greenland Group. The $^{87}Sr/^{86}Sr$ ratio of 33-RO (0.75004) places it in the low end of the range of values previously reported for Greenland Group samples by Adams (1975) (0.734 to 0.986). The paragneiss (12-RO) has a virtually identical ε_{Nd} as the Greenland Group rock, but a much lower ε_{Sr}. Nevertheless, a mixing curve between it and a mantle magma (not shown in Figure A1.2b) also passes near the array of Mesozoic intrusive rock data. Thus, both metasedimentary rocks from the Rotomanu area are acceptable from isotopic considerations as continental crustal components involved in Cretaceous granitoid genesis. The Pikikiruna Schist sample (NE-19) has the least evolved $\varepsilon_{Nd}(0)$ (-15.0), and also is a suitable crustal component. The T_{DM} model age of 1960 m.y. points to a rather ancient continental provenance, indicating that the sedimentary strata of the Eastern Belt of West Nelson, as well as the Western Belt sediments, formed in proximity to an exposed ancient craton. Since the Cretaceous mafic intrusives generally lie within the range of isotopic values for the granitoids, the degree of contribution to them from crustal sources is not grossly different. Thus, it is clear that the trace element characteristics of the mafic rocks are not dominated by a depleted mantle source.

When the isotopic ratios of the metasediments are corrected to 355 m.y. (Figure A1.2a), their relationship to the Devo-Carboniferous intrusives is unlike that observed in the Cretaceous. The mixing curve between 33-RO and a depleted mantle-derived magma does not follow the granite data, and none of the sediments alone could act as a suitable continental component involved in generation of all the granites. For example, the paragneiss (12-RO) has too low an ε_{Sr} to be representative of any major crustal component

active at this time. Nevertheless, it is not difficult to imagine that there were continental sources available that could result in the observed isotopic ratios in the intrusive rocks. For example, the ε_{Nd} of NE-19 and the ε_{Sr} of 33-RO are similar to the values for the Mt. McLean granite (WL-17). It is apparent that the granites have a similar range of isotopic values as the pre-intrusive sedimentary rocks, in sharp contrast to the case in the Cretaceous. The Rameka Gabbro shows a stronger affinity with a depleted mantle source than the granites, but still must contain a substantial crustal component.

Major and trace element data are shown in Table A1.4. The granitoids are generally high SiO_2, low CaO rocks. Most lie near the alumina saturation boundary between peraluminous and metaluminous magma types $[(Al_2O_3)/(Na_2O + K_2O + CaO)mol. = 1]$, with the Rotomanu (32-RO) and Mt. McLean (WL-17) granites showing the most peraluminous characteristics (values of 1.15 and 1.04, respectively). All three Devo-Carboniferous granites have $K_2O > Na_2O$ (wt.%), in accordance with Tulloch's (1983) Karamea Suite classification. Three Mesozoic granitoids have $Na_2O > K_2O$ (BIG, NE-4, SF-4), while two do not (32-RO, 882242). The two most peraluminous granites (32-RO, WL-17) are also the most potassic; these qualities may be indicative of a sedimentary influence on the source (Chappell and White 1974). The metanorite (WL-2) has major element features typical of an orthopyroxene-bearing magma, while the other two mafic rocks bear indications of a cumulate origin (consistent with textural evidence). These include the very low SiO_2 and high total Fe of the Rameka Gabbro (NE-16) and the high Al_2O_3 and Na_2O, perhaps indicative of plagioclase accumulation, in the mafic phase of the Pearse Granodiorite (NE-13). The three metasediments are strongly aluminous. 33-RO is quite similar in major and trace element composition to the average Greenland Group graywacke (Nathan 1976), while 12-RO is much more pelitic in chemistry. The chemistry of the Pikikiruna Schist (NE-19) is dominated by quartz.

There is considerable variation in trace element characteristics among the

Table A1.4 - Major and trace element concentrations (weight percent and ppm, respectively)

	NE-4	32-RO	SF-4	82242	BIG	NE-13	WL-2	NE-3	AR23G	WL-17	NE-16	NE-19	12-RO	33-RO
SiO_2	72.1	71.5	73.1	75.2	75.0	52.2	48.6	70.6	68.8	72.8	42.9	87.8	61.0	74.9
TiO_2	0.14	0.18	0.21	0.25	0.19	1.17	0.78	0.45	0.35	0.11	2.09	0.28	0.90	0.63
Al_2O_3	15.0	14.9	14.1	12.6	13.2	18.3	15.5	14.1	15.3	14.3	16.8	5.56	16.5	11.3
Fe_2O_3*	0.90	1.18	1.15	1.50	1.26	7.19	13.0	2.99	2.81	0.84	14.4	2.06	7.47	3.93
MnO	0.01	0.02	0.04	0.02	0.04	0.08	0.11	0.04	0.04	0.01	0.14	0.30	0.05	0.02
MgO	0.24	0.43	0.28	0.37	0.38	4.22	9.68	0.93	0.73	0.38	5.80	0.64	3.94	1.86
CaO	0.95	1.23	0.39	1.03	1.39	7.53	8.45	1.99	3.10	0.69	11.4	0.24	1.56	0.27
Na_2O	5.33	3.10	5.50	3.40	4.12	5.65	1.61	3.41	3.46	3.23	2.40	0.53	2.37	2.28
K_2O	3.75	5.23	4.65	4.78	3.87	1.10	0.50	4.35	3.74	6.63	1.05	1.47	3.69	2.12
P_2O_5	0.07	0.32	0.04	0.07	0.06	0.49	0.06	0.16	0.13	0.13	0.35	0.13	0.14	0.17
L.O.I.	0.70	1.08	0.47	0.70	0.47	1.08	0.93	0.47	1.16	0.70	1.70	0.85	1.70	2.23
Sum	99.2	99.2	99.9	99.9	100.0	99.0	99.2	99.5	99.6	99.8	99.0	99.9	99.3	99.7
Ba	1150	860	560	210	460	730	140	580	570	330	290	530	490	410
Zr	50	60	230	110	90	50	30	180	170	80	40	30	180	260
La	24.2	50.2	40.6	23.3	-	32.4	10.3	-	-	40.3	-	-	55.3	45.1
Ce	30	60	54	44	-	53	22	-	-	70	-	-	92	79
Nd	13	21	20	20	-	34	11	-	-	25	-	-	39	31
Sm	2.12	4.53	3.73	5.38	-	7.44	2.35	-	-	7.60	-	-	8.60	7.35
Eu	1.15	1.03	0.38	0.79	-	2.47	0.80	-	-	0.66	-	-	0.59	0.65
Tb	0.4	0.8	0.7	0.9	-	0.7	-	-	-	1.0	-	-	1.2	1.2
Yb	0.90	0.83	2.13	2.92	-	1.44	1.05	-	-	0.39	-	-	3.25	3.59
Lu	0.19	0.14	0.40	0.49	-	0.29	0.15	-	-	0.06	-	-	0.52	0.57
Cs	13.8	16.0	3.7	-	-	-	1.8	-	-	6.8	-	-	14.6	6.4
Pb	34	30	14	-	-	2	2	-	-	64	-	-	12	14
Th	8.1	11	19	-	-	0.4	1.5	-	-	18	-	-	16	13
U	3.0	5.0	3.8	-	-	-	0.4	-	-	4.8	-	-	3.0	3.0
Ni	17	18	41	-	-	44	140	-	-	27	-	-	61	37
Cr	49	51	71	-	-	77	380	-	-	55	-	-	190	110
Sc	1.5	4.0	3.5	-	-	19	34	-	-	2.9	-	-	23	11
V	8	12	10	-	-	150	300	-	-	4	-	-	130	58
Zn	49	48	34	-	-	140	150	-	-	28	-	-	180	73

Estimated uncertainties for the major elements are generally < 2%; uncertainties are worse for those making up less than 1 weight percent. Estimated uncertainties for the trace elements are generally < 10%, but up to 15% for the REE.

granitoids. For example, Figure A1.3 shows the wide range in Ba and Sr. On the other hand, all of the granitoids have Rb in the relatively restricted range of 110-200 ppm. The four granites for which Cr and Ni were measured all show high concentrations for these two elements, while all but one (SF-4) have high Pb concentrations. The levels of these three elements are similar to those for Australian "S-type" granites (Chappell 1984). As expected, the transition metals are generally quite higher, and incompatible elements such as Th and U quite lower, in the mafic samples than in the granitoids. The unusually high Sr concentrations in mafic samples NE-13 and NE-16 partly reflect high plagioclase contents, but must also point to high Sr concentrations in their parent magmas. Similar high Sr contents have been reported from Cretaceous mafic rocks in Fiordland (McCulloch et al. 1987).

The REE patterns for five granites, two metasediments and two mafic intrusives are shown in Figure A1.4. The two metasediments have very similar patterns, which are also similar to Nathan's (1976) Greenland Group average with the exception of their large Eu anomalies. Sample NE-13 has rather high REE concentrations for a mafic rock, with a suggestion of middle REE enrichment related to its high hornblende content. WL-2 has low REE concentrations consistent with its basaltic character, and a LREE enrichment typical of arc basaltic magmas (Taylor 1977). The granites all have enriched, and roughly similar, LREE patterns, with concentrations lower than the metasediments. Three have strong Eu anomalies, one (32-RO) has a weaker Eu anomaly, and one (NE-4) has a positive Eu anomaly and significantly lower LREE. Feldspar accumulation could account for the features of the latter two granites, consistent with their high Ba and Sr concentrations (see Figure A1.3). The five granites show variable amounts of HREE depletion, with $(Ce/Yb)_n$ varying from 3.9 to 45. (Since the granites have roughly parallel LREE patterns, the $(Ce/Yb)_N$ ratio is taken here as an indicator of HREE depletion rather than LREE enrichment.)

A1.5. Discussion

a. Isotopic data

The $^{143}Nd/^{144}Nd$ ratios of the granitoids have implications for the crustal history of their source regions. The TCHUR model ages (Table A1.3) for the Mesozoic rocks range up to 930 m.y., with the Paleozoic rocks up to 1450 m.y. The T_{DM} model ages are probably a better indicator of crustal residence times (DePaolo 1981a), and range up to 1500 m.y. for Mesozoic and 1830 m.y. for Paleozoic granitoids. Even considering the uncertainties implicit in the model age calculation, it is clear that the Nd in most of these igneous rocks is dominated by Proterozoic continental crustal Nd. This is evidence for large amounts of crustal recycling having taken place during batholith construction in New Zealand, as has been found elsewhere (e.g. DePaolo 1981b; Allegre and Ben Othman 1980). This observation is supported by the widespread evidence in New Zealand granitoids for inheritance of 1000-1500 m.y.-old zircons (U-Pb data of D. Kimbrough, pers. commun.).

The covariation of initial Nd and Sr isotopic ratios (Figure A1.2), particularly in the Mesozoic rocks, is suggestive of generation of the rocks by mixing between two components. Figure A1.2b shows a curve generated by a simple mixture between a postulated magma derived from a depleted mantle (Sr = 450 ppm, $^{87}Sr/^{86}Sr$ = 0.7028, Nd = 14 ppm, ε_{Nd} = 8.2) and a Greenland Group sedimentary rock (Sr = 61 ppm, $^{87}Sr/^{86}Sr$ = 0.7425, Nd = 37 ppm, ε_{Nd} = -10.6). Concentrations in the mantle component are typical for island arc volcanic rocks (Basaltic Volcanism Project 1981; Von Drach et al. 1986) and are similar to values in McCulloch and Chappell's (1982) model for southeast Australian granites. Mantle isotopic ratios are calculated from DePaolo's (1981a) depleted mantle evolution model. The crustal end-member Sr and Nd concentrations are represented by average values for Greenland Group rocks (Nathan 1976) and are similar to sample 33-RO; ε_{Sr} and ε_{Nd} used for this component are those measured on 33-RO. Clearly, the Mesozoic intrusives fall near this calculated curve, and their Nd and Sr isotopic ratios are thus

Figure A1.3. Ba and Sr concentrations of the rocks, with curves showing partial melting and assimilation-fractional crystallization (AFC) paths. Symbols are as in Figure A1.2, with the closed square representing the average Greenland Group (Nathan 1976). The open square is 33-RO. The thick solid, dashed, and dotted lines show concentrations in 5 to 30 percent equilibrium partial melts ("EPM") of the average Greenland Group rock according to models 1, 2, and 3, respectively (Table A1.5). The curves labeled "mix" bound a region of mixtures between the metasediments or their partial melts and the DM magma; only a few intrusives lie in or near this region. The other curves show melt evolution paths resulting from AFC processes of varying parameters (DePaolo 1981c), as follows. a: $r = 0.85$, $D_{Sr} = 2$, $D_{Ba} = 0.25$; b: $r = 1.5$, $D_{Sr} = 0.5$, $D_{Ba} = 0.25$; c: $r = 1.5$, $D_{Sr} = D_{Ba} = 0.1$; d: $r = 0.85$, $D_{Sr} = 0.5$, $D_{Ba} = 0.25$; e: $r = 0.85$, $D_{Sr} = D_{Ba} = 0.1$. An example of the effect of invoking higher assimilation/crystallization ratios (r) is seen by comparing curves c and e.

Fig. A1.3

Figure A1.4. Chondrite-normalized rare-earth element concentrations of selected granitic,

mafic intrusive, and metasedimentary rocks.

Fig. AT.4
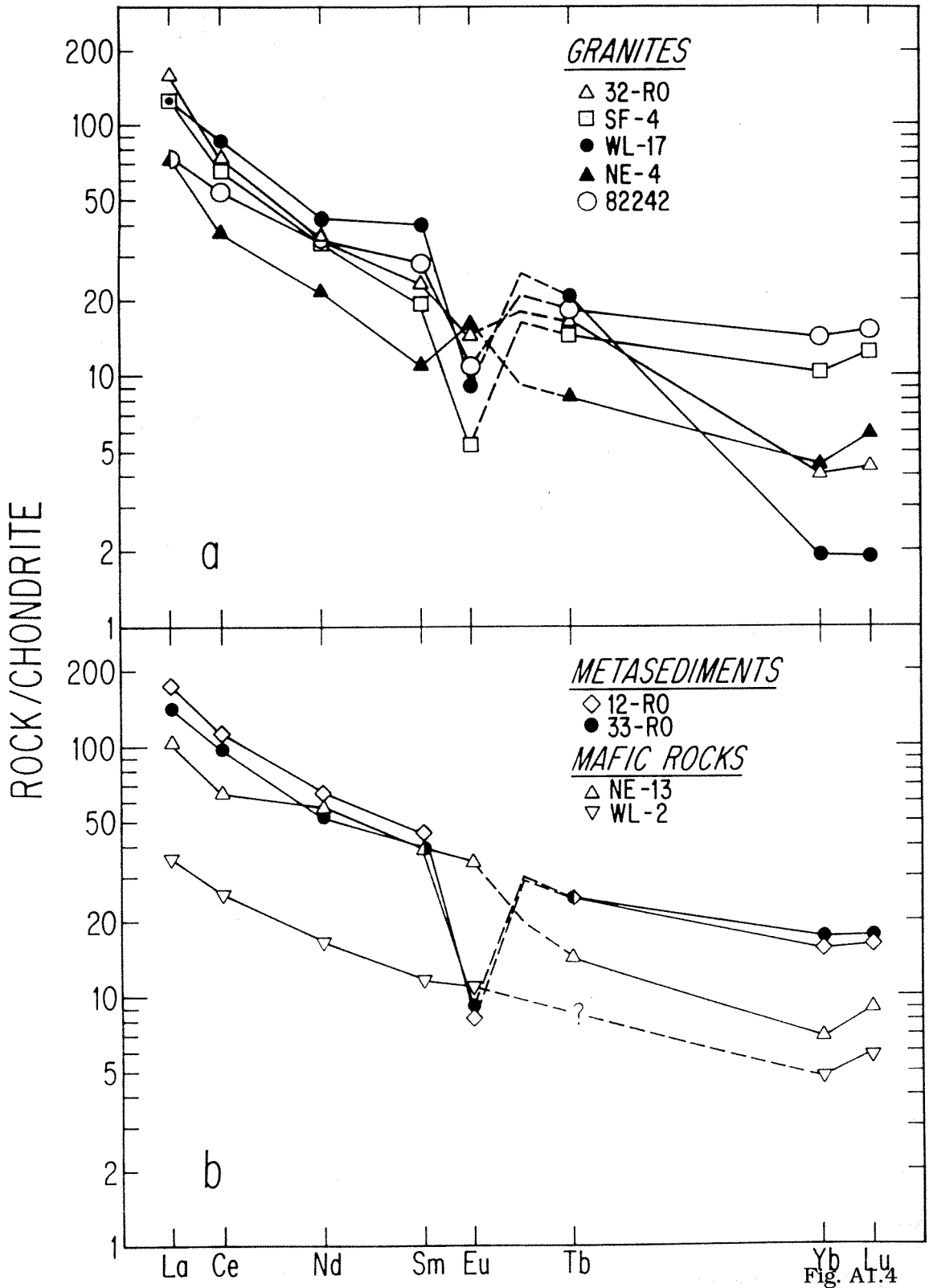
consistent with simple mixing. The range in Nd model ages would then reflect this mixing, rather than real source ages. It seems unlikely that the variation in Mesozoic initial isotopic ratios reflects separate sources for each pluton, distinguished by varying crustal residence times. It would be fortuitous to produce a Nd-Sr mixing-type array from this process, as we would expect much scatter in the ε_{Sr} values due to the potentially high variability of Rb/Sr ratios in crustal sources. Only one of the granitoids, the 357 m.y.-old Mt. McLean granite (WL-17), indicates that it might be a pure melt product of old crustal sedimentary rocks, due to its markedly high ε_{Sr} and low ε_{Nd}.

However, simple mixing is inconsistent with other compositional parameters. There is no simple correlation between ε_{Nd} and Nd concentration, for example, nor ε_{Sr} with Sr (Figure A1.5). Since the two model end-members have quite distinct SiO_2 contents, one would expect a correlation between isotopic parameters and SiO_2 content. This is not observed. Trace element concentrations also do not show linear covariation, nor are granite REE patterns intermediate between the model end-members (see Figure A1.6b). There must be other variable processes at work. Constraints may be placed on granitoid evolutionary pathways by applying petrogenetic modeling to the intrusive rocks, with particular emphasis on the Mesozoic suite.

b. Modeling

A model of mixing between materials of mantle and crustal parentages to explain granitoid Sr isotopic ratios was proposed by Hurley et al. (1965). With the recognition of a depleted mantle source and the study of Nd isotopic systematics in igneous rocks, mixing models involving Nd and Sr were given by DePaolo and Wasserburg (1976, 1979). In these and many later isotopic approaches, bulk mixing of end members was proposed, but no consideration was given to the involvement in these mixing processes of partial melting with concomitant element fractionation. The simplest variation on a mixing model

would then be to involve only a partial melt of the crustal end-member as the component to be mixed with the mantle-derived magma. The most appropriate choice in New Zealand for the continental participant is the thick assemblage of early Paleozoic continental margin sedimentary rocks. The Greenland Group is the most widespread and the largest unit, consisting of a Lower Paleozoic turbiditic assemblage of graywacke and subordinate argillite. The average chemical composition of Greenland Group rocks as reported by Nathan (1976) was used in calculations. Two extreme scenarios for the behavior of the trace elements will be considered: (1) the partial melt is in complete chemical and isotopic equilibrium with the residual phases until it is removed for mixing with the mafic magma; and (2) the partial melt is separated from the residue on formation, and isotopic equilibrium between the melt and residue is not attained. Third, we will consider models combining bulk assimilation of a crustal melt with simultaneous fractional crystallization of the invading mafic magma.

Equilibrium partial melting - To construct reasonable mineral assemblages for the starting sedimentary composition for possible melting conditions, we applied the AFM diagram as utilized by Reinhardt (1968) for high grade pelitic rocks. The minerals involved are quartz, alkali feldspar, plagioclase, and oxides (always present), plus sillimanite, cordierite, biotite, garnet, and hypersthene (Table A1.5). Metamorphic reactions mainly result in diminution of the biotite field at higher grades. Thus, a range of relative abundances of the minerals can be ascertained, with biotite less important, and hypersthene more important, in "dryer," higher grade conditions. Furthermore, garnet will be favored over cordierite at higher pressures. Plagioclase would generally be subordinate to alkali feldspar because of the Greenland Group's relatively high K_2O and low Na_2O and CaO contents. Following Winkler (1979), the partial melt is produced essentially from the breakdown of roughly equivalent portions of quartz, alkali feldspar, and plagioclase. Biotite, if present, does not contribute to the melt until late in the melting sequence (i.e.,

Figure A1.5. ε_{Sr} vs. Sr plot of Cretaceous intrusives, showing mixing and AFC curves resulting from interaction between DM and average Greenland Group graywacke (Nathan 1976). Symbols are as in Figure A1.3. The range in possible Sr concentrations of graywacke equilibrium partial melts (Table A1.5) is shown extending from the average graywacke data point ("EPM"), and it can be seen that mixing curves to all possible melts will lie quite near the simple mixing curve shown. Intrusive rock data points do not lie in this region. Also shown are mixing curves to nonequilibrium partial melts (NPM) for assemblages #1 and #3. All mixing curves have tick marks at 70% sediment. Parameters of the four AFC curves are as follows. a: $r = 0.85$, $D_{Sr} = 2$; b: $r = 1.5$, $D_{Sr} = 0.1$; c: $r = 0.85$, $D_{Sr} = 0.25$; d: $r = 0.85$, $D_{Sr} = 0.01$.
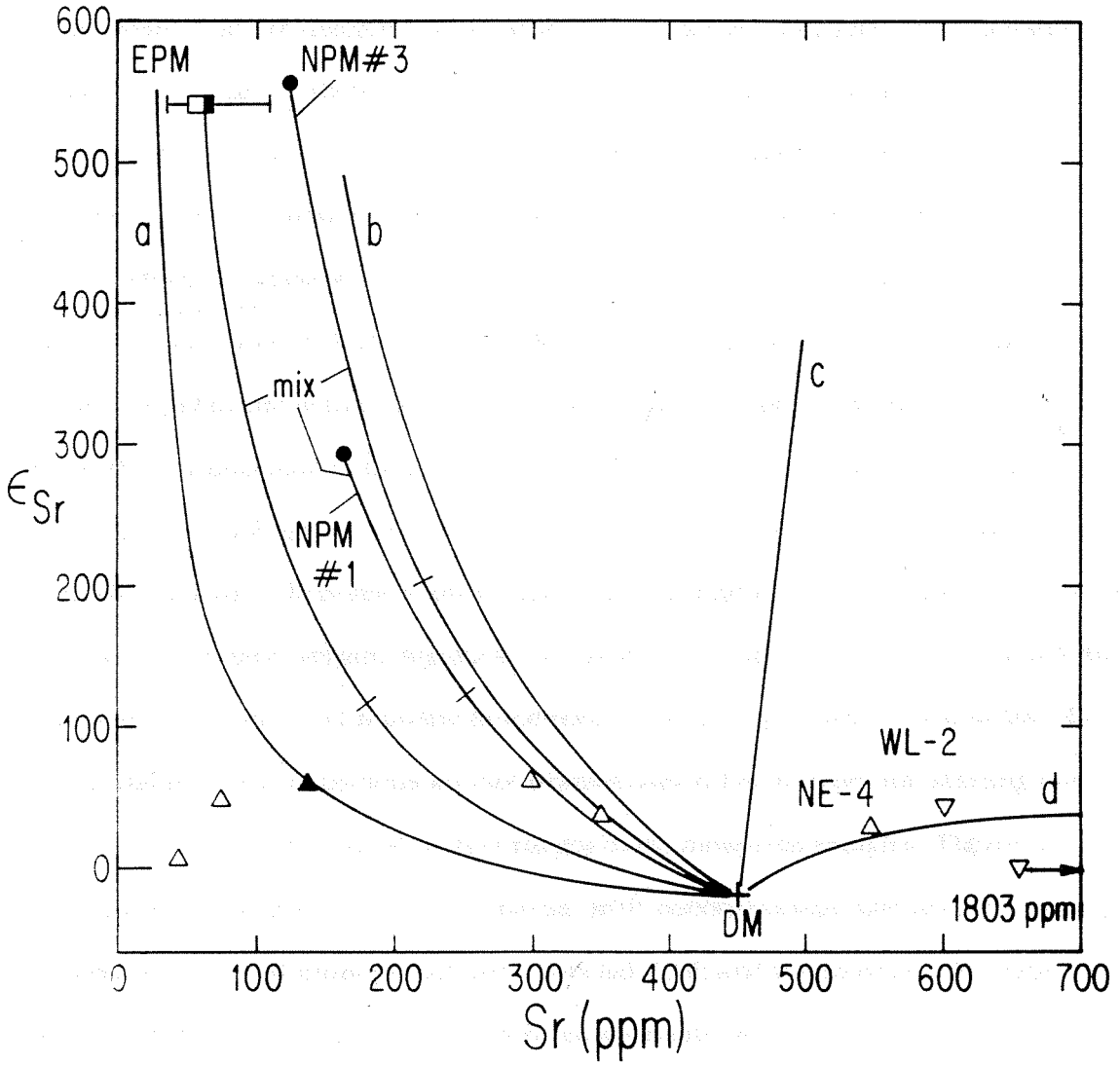
Fig. A1.5

after 30% melting). This melting model is similar to that of Clemens and Wall (1981) for so-called "S-type" granites, except that they propose a possible biotite breakdown early in the melting sequence. Mineral-melt partition coefficients were chosen from a variety of sources (Arth 1976, Condie 1978, Hanson 1978, Irving and Frey 1978, Reid 1983, Giraud et al. 1986), and are assumed to be constant. Partition coefficients for sillimanite were assumed to be zero. Melting equations are from Shaw (1970) for equilibrium nonmodal melting. For this model, ε_{Sr} and ε_{Nd} in the melts are taken as equal to those in the starting material. These have been calculated at 115 m.y. ago (Table A1.3).

Melting models were done for Rb, Sr, and Ba, as their distribution is dominantly dependent on major phases. Table A1.6 shows the calculated concentrations in partial melts in equilibrium with three different mineral assemblages. The importance of biotite to the Rb concentration in the melts is clearly shown, with the model involving 23% biotite being the only one giving melt Rb concentrations similar to the starting concentration. Therefore, mixtures between a low Rb mafic magma and partial melts from a biotite-free residue would tend toward significantly higher Rb concentrations than would those involving partial melts with biotite in the residue (or, for that matter, bulk melts). Sr and Ba partial melt concentrations are not dramatically different from the starting material, particularly within the context of their ranges in the measured samples. Figures A1.3 and A1.5 show the ranges of Ba and Sr partial melt concentrations and arrays of mixtures between these equilibrium partial melts (labeled EPM) and the model mafic magma (DM). Models involving mixing between these components would constrain the Ba and Sr contents and ε_{Sr} of the resultant rocks to rather limited ranges.

The same melting models were also applied to the REE, but this is highly dependent on the behavior of accessory minerals. Despite recent advances in the understanding of solubility and diffusion characteristics of some accessories (Watson and Harrison 1984), it is still difficult to predict how much of these phases were present and

whether or not they will behave as residual in a partial melt system. For each model residual assemblage, REE patterns were calculated with apatite and zircon as accessory residual phases (0.4 and 0.04%, respectively), with or without monazite as an additional phase (0.02%). Monazite, like allanite, partitions the LREE very strongly (Mittlefehldt and Miller 1983) and may be a common refractory phase in metasedimentary source rocks (Sawka et al. 1986). As seen in the calculated partial melt REE patterns of Figure A1.6, the presence and amount of monazite will affect whether there is a LREE enrichment or depletion on partial melting. The major minerals have a limited effect on the LREE melt pattern; i.e., all three model assemblages give similar results.

The HREE patterns are more informative concerning source characteristics, since their distribution in melting systems is much less dependent on accessory phases (Figure A1.6a). The models involving garnet (assemblage #2, Figure A1.6b) show marked Yb depletions, virtually independent of the degree of melting, while the garnet-free assemblage (Figure A1.6a) leaves the HREE relatively unaffected. Figure A1.6b shows Taylor's (1977) REE pattern for an average island arc magma, which is here used for the REE pattern of the mantle mafic magma. The range of expected REE contents for mixtures between this model magma and a partial melt is highly dependent on the presence of monazite and garnet. Given the uncertainty in monazite (or allanite) behavior, we can only constrain the LREE values, for all three model residual assemblages, to between the island arc pattern and the stippled area on Figure A1.6b. For the HREE, the range in Yb is quite limited for garnet-free systems (between 10 and 25 times chondritic), but extends to markedly lower values (2 times chondritic) with garnet present. In sum, while LREE concentration patterns cannot be well-constrained by these models, the HREE would be useful in illustrating a mixing origin for the granitoids if garnet were present as a residual phase during partial melting of the model sedimentary end-member. Granitoid HREE contents would then be limited to between the "island arc" pattern and the HREE depleted pattern

Table A1.5 - Mineral assemblages (%) of three models of partial melting of graywacke

	Qz	Kf	Pl	Bt	Cd	Sl	Gt	Hy	Ap	Zr
#1	43	10	12	23	6	6			0.4	0.04
#2	35	23	10	3	17		12		0.4	0.04
#3	38	26	10		5		20	1	0.4	0.04

Qz = quartz, Kf = alkali feldspar, Pl = plagioclase, Bt = biotite, Cd = cordierite, Sl = sillimanite, Gt = garnet, Hy = hypersthene, Ap = apatite, Zr = zircon.

Table A1.6 - Equilibrium partial melting calculations

		Rb	Sr	Ba
Starting concentration		159	61	510
#1: Bt + Sl + Cd	5%	185	50	244
	30%	151	108	281
#2: Cd + Gt + Bt	5%	551	36	303
	30%	331	58	363
#3: Gt + Cd + Hy	5%	728	37	318
	30%	387	61	385

Melt trace element concentrations (ppm) for three models of 5% and 30% partial melting of the average Greenland Group sediment (Nathan 1976).

Table A1.7 - Nonequilibrium partial melting calculations

	Rb (ppm)	Sr (ppm)	$^{87}Sr/^{86}Sr$ (115 Ma)
Model 1			
Plagioclase	7.8	319	0.7217
Alkali feldspar	128	176	0.7310
Melt	45	165	0.7250
Model 3			
Plagioclase	35	240	0.7233
Alkali feldspar	583	133	0.7797
Melt	206	124	0.7434

Figure A1.6a. REE pattern of the average Greenland Group rock (Nathan 1976) and calculated values for a 30% partial melt of this average in equilibrium with a garnet-absent residual assemblage (Table A1.5). LREE values for the melt are highly dependent on the presence or absence of monazite (or allanite).

6b. REE diagram showing relationships between a calculated garnet-present 30% partial melt of the average Greenland Group rock (Table A1.5), a model mantle-derived island arc magma (Taylor 1977) and the range of values reported here for granites (excluding NE-4). Note the similarity in HREE contents between the partial melt and the low end of the granite range. It appears possible to produce most of the granite range from mixing between the partial melt and the island arc magma.
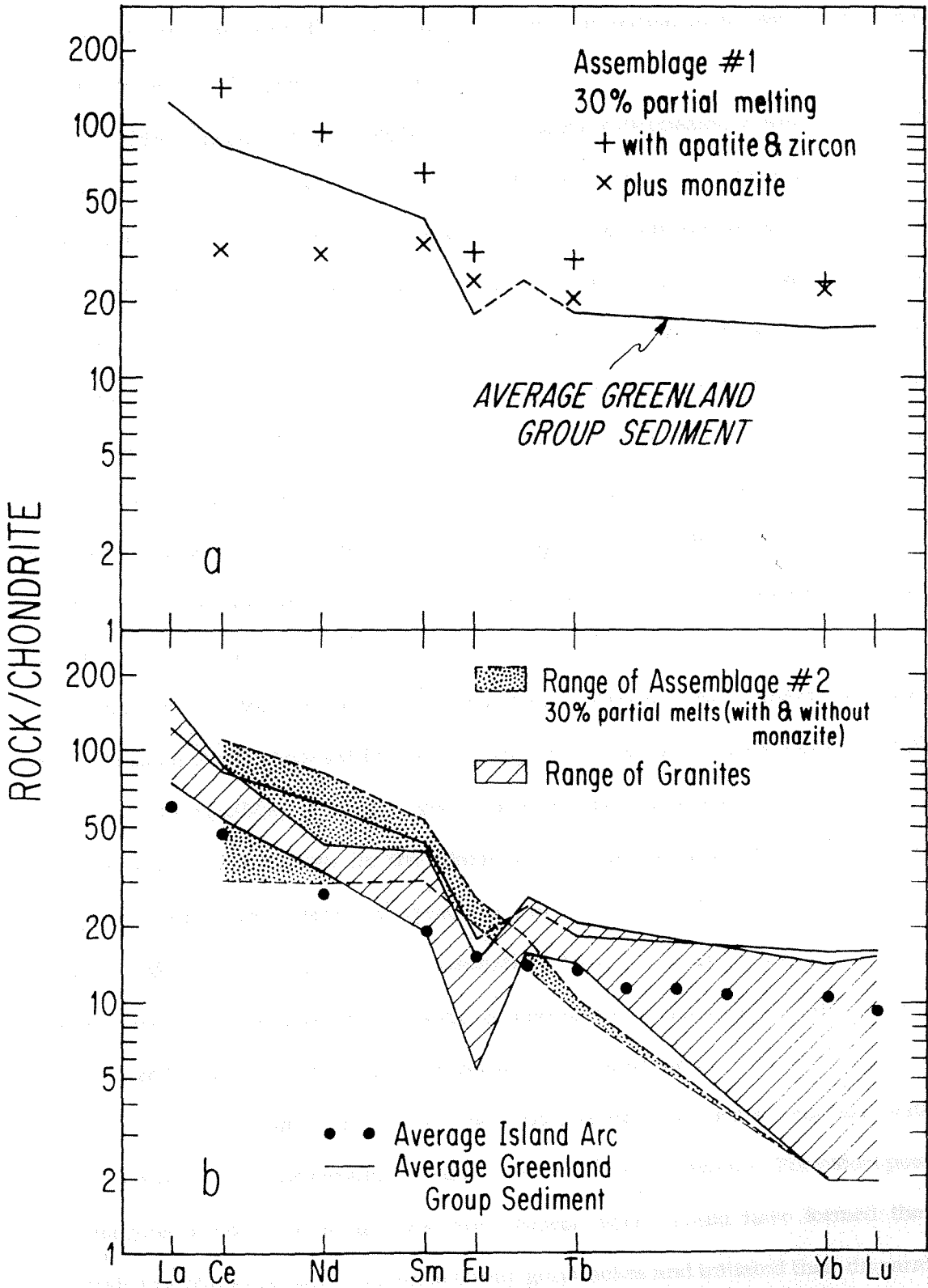
Fig. A1.6

in Figure A1.6b. Without the influence of garnet, the partial melts would have HREE contents similar to the "island arc" magma.

Nonequilibrium partial melting - In the preceding discussion, it was assumed that crystal-melt equilibrium was fully maintained, and that this resulted in isotopic equilibrium. We now consider a scenario in which equilibrium is not attained. The extreme end-member model would assume that the trace elements in a partial melt come only from those materials that are melted, i.e., from plagioclase and alkali feldspar (the trace element contents of quartz are taken as negligible). Thus, for the case of Sr, the Sr concentration and $^{87}Sr/^{86}Sr$ ratio of a partial melt (up to 30%, after which other minerals become involved in melting) result only from a combination of these parameters in the two feldspars. It is necessary, then, to derive reasonable values for Rb and Sr concentrations in these two minerals for the model metagraywacke. Since such values can be quite variable, it is necessary to calculate the distribution of these two elements as reflecting equilibrium at the time of formation of the two feldspars. Thus, mineral Rb and Sr concentrations were calculated for Models 1 and 3 with the same distribution coefficients used above for equilibrium melting, given the same starting whole-rock concentrations. The resulting concentrations for the feldspars are shown in Table A1.7. These values compare favorably with literature values (e.g. Aronson 1968). The lower Rb contents in Model 1 reflect the presence in that assemblage (Table A1.5) of biotite, which strongly concentrates Rb. The lower Sr in Model 3 reflects the abundance of feldspars in that assemblage (Table A1.5), diluting the feldspar Sr concentrations.

If the two feldspars existed in the model source rock for a long time without isotopic equilibration, they would have quite different $^{87}Sr/^{86}Sr$ values. The oldest possible metamorphic event in Westland and West Nelson which could have formed the two minerals in metamorphosed Greenland Group graywackes and initiated their disparate Sr evolution paths was at 438 m.y. ago (Adams et al. 1975). $^{87}Sr/^{86}Sr$ in our graywacke

(33-RO) at that date is calculated as 0.7213. Calculated values for $^{87}Sr/^{86}Sr$ for the feldspars and resulting melts are shown in Table A1.7 and Figure A1.5 (NPM). Model 1, the "wetter," biotite-rich assemblage, gives a lower melt $^{87}Sr/^{86}Sr$ ratio because of the lower Rb/Sr of the feldspars. The "dryer," more alkali feldspar-rich Model 3 gives a higher $^{87}Sr/^{86}Sr$ (similar to the equilibrium case) because of the absence of a Rb-enriched phase like biotite and the resulting high Rb/Sr in the feldspars. Both models give Sr concentrations higher, and Rb concentrations lower, than equilibrium partial melts.

Shown in Figure A1.5 are calculated mixing curves between these two partial melts and the DM magma. These are similar to the mixing curve to the equilibrium partial melt, but are shifted to higher Sr concentrations. Indicated on the curves for comparison are Sr and ε_{Sr} values for mixtures containing 70% of the sedimentary partial melt end-member. These show that, for a given amount of mixing between the two end-members, the nonequilibrium models give ε_{Sr} values similar to, or higher than, mixtures in the equilibrium case (despite the much lower ε_{Sr} of the Model 1 nonequilibrium end-member melt).

Analogous calculations were performed for the REE, and no significant differences between the three model assemblages were found. As would be expected due to the relatively low affinity of the REE for the feldspars, with the exception of Eu (Arth 1976), the partial melts arising from the feldspars and quartz would be low in most REE (e.g., less than 8 ppm in Nd), but would have marked positive Eu anomalies. In addition, there would be no significant change in slope in the HREE pattern as a result of melting. Any mixture between these postulated melts and the DM magma should reflect these REE characteristics. The ε_{Nd} (115 m.y.) values of the calculated melt 3 range between -10.4 and -13.4, in comparison to the whole-rock value of -10.6 of our Greenland Group sample (Table A1.3).

<u>Assimilation-fractional crystallization</u> - As Taylor (1980) and DePaolo (1981c) have pointed out, the model of a simple mixture between a mafic magma and a crustal melt is merely an end-member case for the more realistic and general process of combined assimilation-fractional crystallization (AFC). Figures A1.3 and A1.5 show curves for the results of AFC involving the DM magma and the average Greenland Group sediment, representing widely varying conditions and partitioning of Ba and Sr, using the equations of DePaolo (1981c). For the Sr-ε_{Sr} diagram, involvement of a partial, rather than total, melt of the sedimentary component will leave the curves only slightly changed, with a shift to lower ε_{Sr} if the fractional melting model is employed; on the Ba-Sr plot, all the curves will be rotated counterclockwise, toward the partial melt compositions. This will not affect the general conclusions.

It is apparent that any number of pathways on these diagrams may be obtained by choice of appropriate values for r (the rate of assimilation divided by the rate of crystallization) and D (bulk partition coefficient for the element on crystallization); however, there are factors at work which place constraints on these variables. For example, lower in the crust where the contaminant sedimentary rock may be at high temperatures previous to assimilation, r is likely to be around 1 and D_{Sr} will be low (DePaolo 1981c), resulting in pathways, such as curves "c" and "d" in Figure A1.5, leading to increased Sr concentration over the starting mafic magma. To get decreasing Sr on assimilation, it is necessary to have either high r - low D_{Sr} or low r - high D_{Sr} (curves "a" and "b" in both Figures A1.3 and A1.5). Further, to maintain a mixing-type path on an ε_{Nd}-ε_{Sr} plot (Figure A1.2b) requires either that D_{Sr} and D_{Nd} be of similar magnitude or that r be high (DePaolo 1981c). A high D_{Nd} is not likely unless hornblende or LREE-enriched accessories such as monazite are fractionally crystallizing from the magma. Higher in the crust, where more heat is necessary to melt the metasediments and plagioclase fractionation is more likely to be important, low r and high D_{Sr} may result. For Rb, AFC calculations with r < 1 will

always give large Rb enrichments, since D_{Rb} will likely remain relatively small throughout most of the assimilation process.

c. Comparison with data

Equilibrium partial melting - It is clear from Figures A1.3 and A1.5 that Ba and Sr concentrations and Sr isotopic ratios do not follow any mixing curves, and the addition of the partial melt consideration (rather than bulk melting) does not help the mixing hypothesis to explain the data. The array of mixing curves to partial melts is still too narrow. This does not imply that partial melting was never at work in the genesis of these rocks. In fact, the location of the Mt. McLean granite (WL-17) in Figure A1.3 is consistent with its having been produced by about 30% partial melting of a metasedimentary assemblage intermediate between models 1 and 2. This is consistent with its very high $^{87}Sr/^{86}Sr$ (Figure A1.2a). The Rb content of WL-17 (196 ppm) is most consistent with the model involving 23% biotite in the residue (#1). The other models, with 3 and 0% biotite, respectively, gave Rb values in the melt that were much higher (see Table A1.6). Since it is apparent that WL-17 is the granite with the most "sedimentary" character, and since almost all granites have Rb contents restricted to below 200 ppm, it seems likely that, in general, any partial melting involved 10-20% biotite as a residual phase. This is because biotite is the only likely phase that will concentrate Rb relative to a melt, and keep the melt Rb concentration down to the levels observed.

The range of granite LREE data (Figure A1.6b) is ambiguous. As the granites generally have Ce, Nd, and Sm lower than the Greenland Group average, this is suggestive that monazite or allanite may be present and residual during partial melting of the model metasedimentary end-member. However, La and Ce depletion would be expected to exceed Nd depletion, since distribution coefficients for these phases increase dramatically toward La. Since this is not observed in the granites, it is more likely that LREE-enriched

accessory phases, if present, have not been significantly separated from the partial melt, resulting in largely unaffected LREE patterns. None of the melting models explain the marked Eu anomalies observed in the granites compared with the average sediment, suggesting either that the average Greenland Group composition may be too deficient in feldspar components to serve as the sedimentary end-member source rock, or that the granites have experienced later feldspar fractionation.

The granites show a large range in HREE patterns, with some showing the low Yb characteristic of the garnet-present partial melt models. The Mt. McLean granite (WL-17) has a Yb depletion identical to the melt in equilibrium with 12% garnet, which further supports the idea that it is entirely a partial melt of sedimentary rocks. The marked depletion of Yb relative to Tb argues against hornblende as a major residual or fractionated phase. Most of the granites have HREE patterns between Taylor's (1977) island arc values (representing magmas rising from the mantle and interacting with the crust) and the garnet-partial melt values (Figure A1.6b), supportive of the partial melt-mixing hypothesis. This is illustrated further in Figure A1.7, where the Ce/Yb ratio is used as an indication of the involvement of garnet, and thus of the contribution of the sedimentary partial melt. Sample WL-17 is used as the partial melt end-member in Figure A1.7, which shows a general decrease in ε_{Nd} with increased Ce/Yb in the granites, along a calculated mixing curve. (Although WL-17 is Paleozoic, its ε_{Nd} of -11 is appropriate as a model of a sedimentary melt in the Cretaceous.) The Auckland Islands sample (82242) is an exception. It is notable that all these granites have similar SiO_2 contents. Thus, if the mixing hypothesis is correct, later evolution of these mixtures to granite compositions has not significantly affected Ce/Yb ratios. Similar Eu- and HREE-depleted patterns have been obtained on undated granitoids from Westland (Mason and Taylor 1987), including rocks from the complex Fraser Formation, as well as from west of the Fraser Fault.

Overall, the REE patterns of the granites are consistent with their having been

produced from mixtures between an island arc-type magma and a partial melt of Greenland Group-type sedimentary rocks with at least 12% residual garnet, indicative of moderate to high pressures. The LREE abundances suggest either only minor amounts of LREE-enriched accessory phases in the residue (but sufficient to prevent LREE enrichment in the melt relative to the original sedimentary rock) or retention of these phases in the separated melt. The restriction of Rb to less than 200 ppm in the intrusive rocks requires the presence in such a model system of about 10-20% biotite as a residual phase. Patterns of Ba and Sr concentrations and Sr isotopic ratios in the intrusive rocks are not, in general, satisfied by this partial melt-mix model.

Nonequilibrium partial melting - The Sr-ε_{Sr} mixing arrays produced by this model (Figure A1.5), like that for the equilibrium case, do not fit the data any better than the simple mixing case, particularly considering the high Sr concentrations of the calculated melts. This is true despite the wide range in possible ε_{Sr} values for the partial melt end-member. For the REE, there is no indication of the involvement of low-REE, high-Eu, flat-HREE melts as calculated. In fact, the granitoids show LREE concentrations similar to the sediments, generally have negative Eu anomalies, and display some HREE depletion (Figure A1.6).

Assimilation-fractional crystallization - It is not surprising that the intrusive rocks (Figures A1.3 and A1.5) do not follow any particular AFC pathway, but constraints may be placed on the involvement of this process in petrogenesis. Only one granitoid and the three mafic samples have higher Sr contents than the model mafic end-member, showing AFC conditions probable deep in the crust (curves "c" and "d" in Figure A1.5). The granite, the Buckland Granite (NE-4), along with the Rotomanu granite (32-RO) may have had their trace element characteristics affected by feldspar accumulation, as discussed above. The other five granites in Figure A1.3 lie in the vicinity of simple mixtures and high r trends (curve "b"). Alternatively, they could reflect lower r, higher D_{Sr} conditions (curve "a").

Figure A1.7. ε_{Nd} vs. chondrite-normalized Ce/Yb ratio for four Cretaceous granites and the Early Carboniferous Mt. McLean granite (WL-17), showing partial melt-mixing pathways. Partial melting of the average graywacke (closed square) results in a large increase in Ce/Yb in the melt at constant ε_{Nd}, due to Yb depletion resulting from separation of refractory garnet. Despite its age, the Mt. McLean granite (closed circle) is taken to represent the resulting partial melt because of its appropriate isotopic and REE characteristics (see text). Shown is the curve followed by mixtures between such a melt and the model mantle melt (DM).
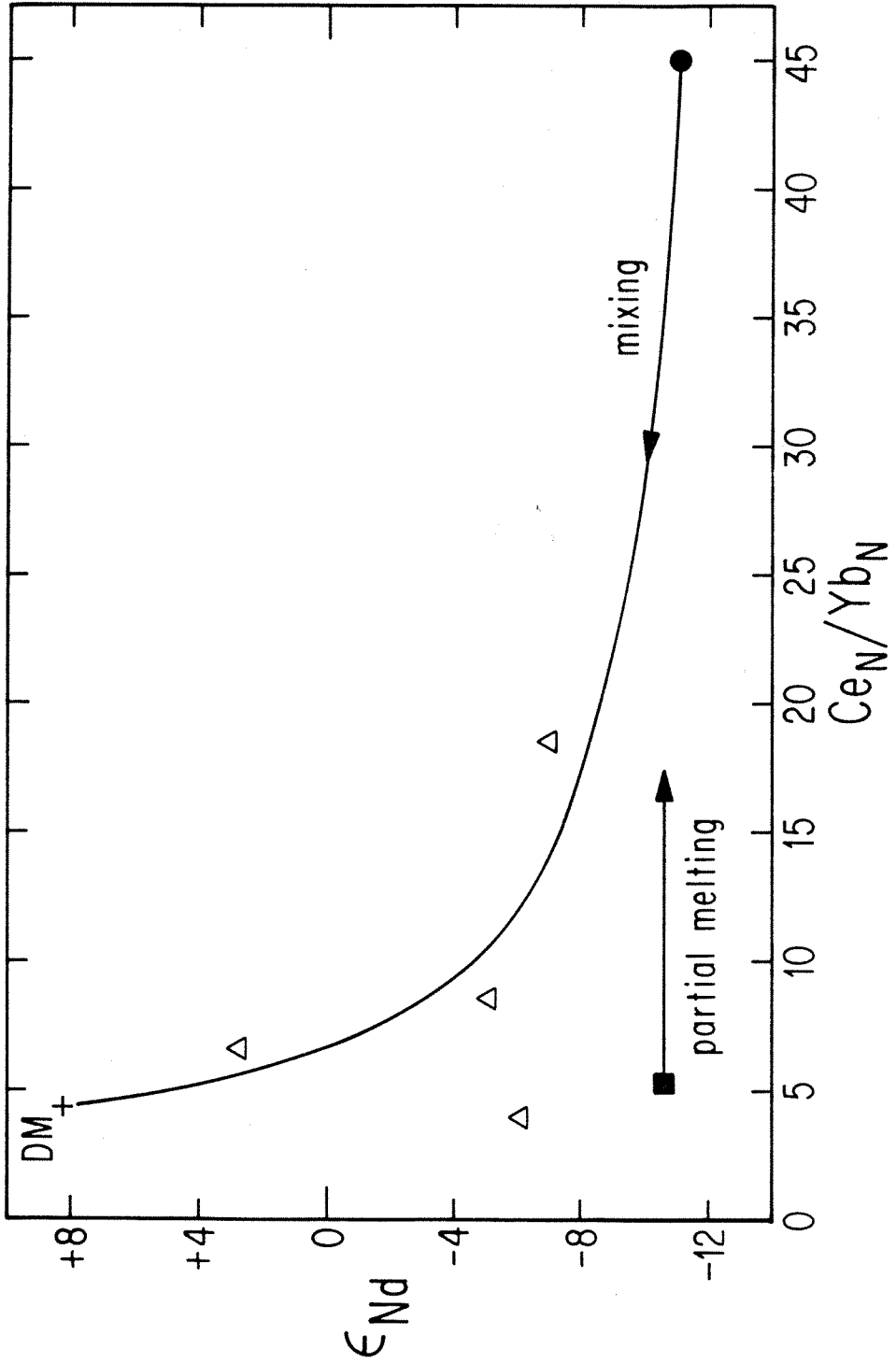
Fig. A1.7

The four granites in Figure A1.5, excluding NE-4 and 32-RO, show no pattern at all, except that they all lie to lower Sr concentrations and higher ε_{Sr} than the model mantle magma. The granites with the lowest Sr concentrations are suggestive of low r (< 0.85), but high D_{Sr} (~2), reasonable values for higher level crustal interaction (DePaolo 1981c). However, the simple mixture-type array on the ε_{Nd}-ε_{Sr} plot (Figure A1.2b) does not allow such a high D_{Sr} unless D_{Nd} is also very high (~2). This is unreasonable, particularly since the granite REE patterns show no evidence of major hornblende fractionation, and do not show the LREE depletion that would result from, say, monazite fractionation. Thus, the ε_{Nd}-ε_{Sr} array seems to require high assimilation rates (i.e., high values for r), which result in magmas approaching the chemical and isotopic characteristics of simple mixtures. Also, the high Rb contents that would result from low-r AFC are not observed, further supporting the call for high assimilation/crystallization ratios. This would be likely for the situation of an already rather warm middle to lower crust further heated by injection of basaltic magmas. The inconsistency of the Sr concentrations with this model (Figure A1.5) could be due to wide variations in the Sr contents of the mantle magmas, or to alteration of Sr contents by post-mixing fractionation.

The three mafic rocks (WL-2, NE-13, NE-16) show evidence for AFC at lower assimilation rates (r < 0.85) with low D_{Sr} (< 0.1), but the possibility of a cumulate origin for NE-13 and NE-16 limits interpretation. Although NE-13 does lie on the ε_{Nd}-ε_{Sr} apparent simple mixing curve (Figure A1.2b), its high Nd concentration also indicates possible AFC activity. The Thirsty Creek metanorite (WL-2) is more puzzling in that Figure A1.5 supports an AFC origin, but its low Nd concentration is not consistent with its quite low ε_{Nd} value of -5.9. Also, this rock must have received significant amounts of crustal Sr and Nd without significantly altering its whole-rock chemistry. Perhaps it began with extremely low REE contents, underwent AFC with a high Nd crustal melt, and had its $^{143}Nd/^{144}Nd$ ratio easily pulled down. Contamination of this basaltic magma is supported

by the presence of xenoliths of mylonitized granodiorite (Tulloch and Brathwaite 1986).

d. Petrogenesis

It can be seen that the chemical and isotopic characteristics of the Cretaceous intrusive rocks may be explained by AFC processes, of varying parameters but probably having high assimilation rates, acting on island arc-type mafic magmas ascending into the middle or lower crust and interacting with partial melts of the thick, lower Paleozoic sedimentary assemblages. It is difficult to infer a more detailed petrogenesis consistent with all the isotopic and trace-element data. Although trace element contents may have been altered by later fractional crystallization, it is clear that simple mixing alone fails to explain the data; both major and trace element features of the intrusives (e.g., Sr in Figure A1.5) are too removed from simple mixing trajectories to have resulted solely from post-mixing fractionation. The Rb and HREE concentrations of the intrusive rocks, however, do suggest the presence of biotite and garnet in the partial melt source.

Although not discussed in detail, the few Paleozoic intrusives studied are also consistent with such a partial melting-mixing scenario (with the Mt. McLean granite, in fact, appearing to be formed solely from a partial melt), but may require more variation in the crustal end-member isotopic ratios (Figure A1.2a). This leads to an interesting question regarding the Cretaceous rocks. In his Rb-Sr study of the Greenland Group, Adams (1975) reports wide variation in the Rb/Sr and $^{87}Sr/^{86}Sr$ ratios of the sediments. If his $^{87}Sr/^{86}Sr$ ratios are calculated back to 115 m.y. ago, there is a large range in values, mostly from 0.731 to 0.840, with an average of 0.785 (ε_{Sr} = 1150). It is not clear whether Adams' samples are representative of the unit, or if samples were chosen for a large range of Rb/Sr ratios. Thus, the significance of this average is unclear; it may be too high. A mixing curve in ε_{Nd}-ε_{Sr} space from this average does not lie near the intrusive rock values. It would seem that, had sediments of such a large range of $^{87}Sr/^{86}Sr$ ratios been involved

in the mixing giving way to the Cretaceous intrusives, these intrusives would show much more dispersion from the simple mixing line of Figure A1.2b. It appears that the crustal end-member had Sr isotopic ratios more uniform than, and in the lower range of, the Greenland Group sediments. It is possible that metasediments in the mix regions had undergone some sort of Sr isotopic homogenization prior to or during the melting episode, possibly involving large amounts of fluid transport of Sr.

It is possible that the continental component involved in granite genesis actually consists of ancient crystalline rocks, rather than just sediments derived from such crust. However, the sedimentary involvement is suggested by the generally low CaO and high Cr and Ni of the granites (Chappell 1984), and the presence of garnet in the source. A few of the granites do lend themselves to Chappell and White's (1974) division of I- and S-types (e.g. 32-RO and WL-17 would clearly be termed S-types), but the classification does not generally appear to apply. Rather, the observed isotopic variation is here proposed to represent a continuum resulting from mixing-type processes. The data do not suggest a clear-cut "I" versus "S" distinction.

The existence in New Zealand of sediments derived from Precambrian sources is evident, but the question of the involvement of ancient crystalline rocks beneath the South Island cannot be completely addressed. If there are no primary Proterozoic crystalline rocks in New Zealand, then the Antarctic and Australian cratons, which were adjacent, would provide appropriate sources for the Proterozoic source material evident in New Zealand sediments and in the later derived igneous rocks.

The superimposition of the Cretaceous batholith over the older Paleozoic belt raises the question of the involvement of remobilized Paleozoic intrusives in Cretaceous plutonism. The few Paleozoic samples studied here have a wide range in initial ε_{Nd} and ε_{Sr}, and these would be even more dispersed in Cretaceous time. The regular covariation of the Cretaceous Nd and Sr isotopes reported here argue against major contributions by

individual Paleozoic intrusives, which would have resulted in a larger scatter of the Cretaceous data. Perhaps the Paleozoic magmas had so completely migrated upward out of what would become the middle to lower crust zones in the Cretaceous that they would have left little or no imprint on the later plutonism, either as sources or contaminants. In addition, it is unlikely that the Cretaceous granitoids could have been derived from further melting of the residues of the Paleozoic source rocks. These depleted residues would still have ε_{Sr} values much higher than the Cretaceous granitoids.

An extensive Early Cretaceous calc-alkaline orthogneiss terrane (the Wester Fiordland Orthogneiss-WFO) is exposed on the South Island in Fiordland, and may represent a deeper level of exposure than the sample localities of the present work (Mattinson et al. 1986). McCulloch et al. (1987) report ε_{Nd} and ε_{Sr} on six 120 m.y.-old (magmatic age) dioritic orthogneisses from the WFO, as well as on two gabbronorites from the Early Cretaceous Darran Complex to the northeast. These are shown with the results from this study in Figure A1.8. McCulloch et al. (1987) explain the Sr isotopic homogeneity and Nd isotopic heterogeneity as resulting from the extraction of the WFO magmas from low Rb/Sr, mafic sources with crustal residence times ranging from 100 to 300 m.y. before formation of the WFO magmas. It is notable, however, that their array lies across the mixing curve invoked in the present work. To place the WFO magmas with the model framework of this work implies that the vertical Nd-Sr array is a fortuitous result of data scatter due to variations in mixing end-members. Resolution of these differences awaits further study. The similarities in isotopic ratios and Sr and REE concentrations between our diorite sample from the Pearse Granodiorite (NE-13) and the WFO dioritic orthogneisses (Figure A1.8) may point to an affinity between the Separation Point batholith intrusives and the WFO magmas. On the other hand, the Pomona Granite (SF-4) from the Eastern Fiordland Belt shows little evidence for kinship with the Western Fiordland rocks.

High pressure metamorphism in the WFO records a rapid post-magmatic ($\sim$120

m.y.) crustal thickening event which may have contributed to production of crustal melts. These melts may then have mixed at structural levels above the Fiordland levels, resulting in granitoids of the type in the present study. The melting process is hinted at by the occurrence of migmatized metapelitic bodies in the WFO (Mattinson et al. 1986).

Comparison of the Paleozoic and Mesozoic reveals that the older granites all have significantly higher ε_{Sr}, and extend to lower values of ε_{Nd} (Figure A1.2). This distinction is made all the more striking by the fact that the continental participants available in the Mesozoic had $^{87}Sr/^{86}Sr$ ratios ranging to much higher values than they had during the Paleozoic magmatism. Perhaps there was a fundamental difference in the overall mechanisms of granite generation between the two episodes. The Cretaceous episode may have involved a more significant input of mantle-derived mafic magmas which mixed with crustal melts, whereas the Devo-Carboniferous plutonism was dominated by crustal melting. This distinction may be analogous to that espoused by Chappell (1984) between Paleozoic southeastern Australian and Mesozoic Cordilleran plutonism. It must be mentioned, however, that McCulloch and Chappell (1982) obtained a nicely covariant, mixing-type Nd and Sr isotopic data set (typical of Mesozoic plutonism, e.g. New Zealand) for rocks from two Paleozoic Australian granite batholiths, suggesting that perhaps such a distinction need not be so sharp. In fact, their data appear to argue more against an "I" versus "S" dichotomy, and more for a mixing-dominated scenario (Gray 1984).

e. Comparisons with Australia and Antarctica

The New Zealand crustal block is generally believed to have been connected to Western Antarctica and Australia as part of the Gondwanaland supercontinent (Figure A1.9). The separation of New Zealand from the main Gondwana mass is estimated to have begun about 80 m.y. ago, according to studies of sea-floor magnetic anomaly patterns (Molnar et al. 1975). There are major episodes of granitic plutonism identified in Marie

Byrd Land and northern Victoria Land during the Devo-Carboniferous and the Cretaceous (Grindley and Davey 1982; Cooper et al. 1982), but published Nd and Sr isotopic data are sparse. For the Paleozoic rocks, Vetter et al. (1983) give ratios of 0.710 to 0.718 on 360 m.y.-old granites in northern Victoria Land. Recently, Borg et al. (1987) have reported Nd-Sr isotopic data on northern Victoria Land granitoids; two of New Zealand Paleozoic granitoids lie within their reported isotopic ranges, suggestive of similar source characteristics. In particular, the northern Karamea granite (NE-3) shows more affinity with the Admiralty intrusives, while the Waitaha River granite (AR-23G) resembles the older Granite Harbor intrusives. From Marie Byrd Land (Figure A1.9), Adams (1987) reports Sr initial ratios of 0.704-0.706 for 345-380 m.y.-old granitoids in the Ford Ranges. These ratios are distinctly lower than those in New Zealand and northern Victoria Land, suggesting different granitoid sources and/or petrogeneses in Paleozoic Marie Byrd Land. The New Zealand Paleozoic results also lie near the Nd-Sr isotopic pattern for the Paleozoic granites of the Lachlan Fold Belt, Australia (McCulloch and Chappell 1982). The Mt. McLean granite (WL-17) has quite higher ε_{Sr} and lower ε_{Nd}, but lies roughly on an extrapolation of the Australian pattern. These similarities support the proximity of New Zealand to Gondwanaland in Paleozoic times, as shown in reconstructions such as that of Kamp (1986) (Figure A1.9). Although the alignment of pre-rift tectonic belts between New Zealand, S.E. Australia, and northern Victoria Land is problematic due to the outboard position of New Zealand, there are strong similarities in pre-intrusive histories (Grindley and Davey 1982; Cooper et al. 1982), as well as in granitoid isotopic signatures.

Cretaceous granitoids are not found in the adjacent sections of Australia and Victoria Land, but are common in Marie Byrd Land, West Antarctica (Cooper et al. 1982). Once again, the Antarctic isotopic data are sparse, with reported initial $^{87}Sr/^{86}Sr$ ratios ranging between 0.7054 and 0.7061 (Halpern 1968; Halpern and Wade 1979; Adams 1987), easily within the range of New Zealand values. As suggested by Halpern (1968),

Figure A1.8. Comparison of ε_{Nd}-ε_{Sr} values for the New Zealand Cretaceous intrusives to the range of values for basaltic to rhyolitic Quaternary extrusives of the Taupo Volcanic Zone (TVZ) (McCulloch et al. 1986) and to Early Cretaceous intrusives of the Western Fiordland Orthogneiss (WFO) and the Darran Complex (DC) (McCulloch et al. 1987). Symbols as in Figure A1.2b. The mixing curve is the same as that shown in Figure A1.2b.

Fig. A1.8

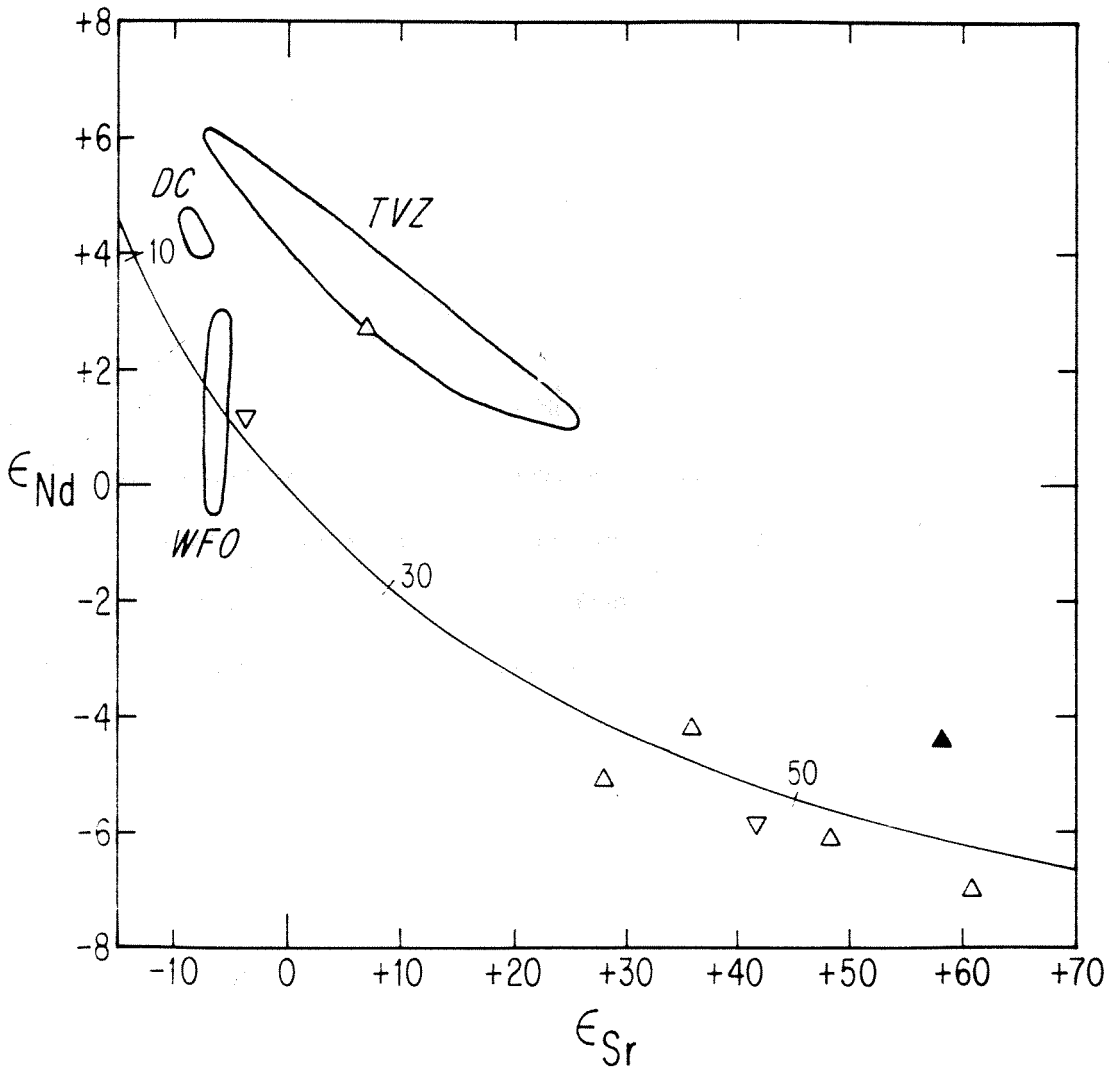Figure A1.9. Pre-drift reconstruction of New Zealand, Australia, and Antarctica of Kamp (1986), with known areas of granitoid occurrence shaded. The dotted line represents the Campbell Magnetic Anomaly System (Davey and Christoffel 1978), thought to represent a major tectonic boundary. LFB = Lachlan Fold Belt, AI = Auckland Islands, BI = Bounty Islands. Other abbreviations as in Figure A1.1.
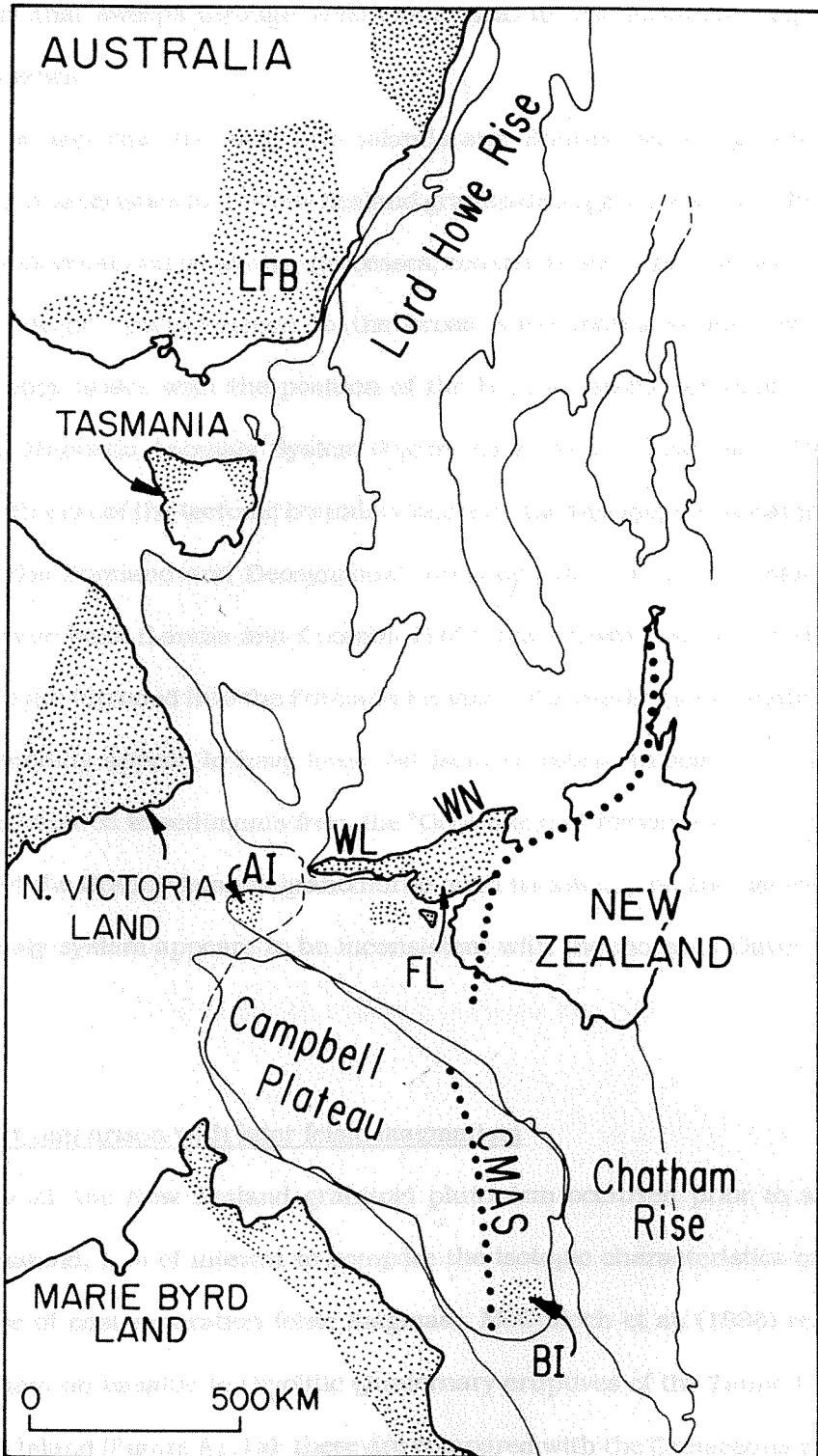
Fig. A1.9

it appears that New Zealand can be placed within the belt of Cretaceous "Andean" plutonism that sweeps through West Antarctica, up the Antarctic Peninsula, and into South America.

The fact that the Auckland Islands and Bounty Islands granites have similar isotopic characteristics to the New Zealand granitoids suggests that they formed within the same type of crust and by similar processes, consistent with the extension of New Zealand crustal geologic characteristics to the broad surrounding submerged plateaus. An inconsistency arises with the position of the Bounty Islands granodiorite north of the Campbell Magnetic Anomaly System (Figure A1.9) which Davey and Christoffel (1978) equate with part of the tectonic boundary between the two major crustal provinces of New Zealand, the Foreland and Geosynclinal (Aronson 1965) or the Tasman and Wakatipu metamorphic belts (Landis and Coombs 1967), respectively. All the other New Zealand granitoids are intruded into the Foreland Province, the pre-intrusive sedimentary rocks of which generally appear to have lower Nd isotopic ratios, indicative of an older crustal history, compared to sediments from the "Geosynclinal" Province (McCulloch 1986). The position of the Bounty Islands granodiorite, with its low ε_{Nd}, on the "geosynclinal" side of the anomaly system appears to be inconsistent with the model of Davey and Christoffel (1978).

f. Comparison with later felsic magmatism

As all the New Zealand granitoid plutonism occurred prior to separation from Gondwanaland, it is of interest to compare the isotopic characteristics of the granitoids with those of post-separation felsic magmas. McCulloch et al. (1986) report Sr and Nd isotopic data on basaltic to rhyolitic Quaternary eruptives of the Taupo Volcanic Zone of the North Island (Figure A1.1a); these are compared with the Cretaceous intrusive data in Figure A1.8. These magmas are decidedly more "oceanic" in isotopic character as

compared to the pre-rift magmas of the South Island. This is possibly due to a difference in the isotopic character of the crustal end-member involved in petrogenesis, since two samples of Taupo country rock give ε_{Nd} of -1 and +1, while the granitoids of the South Island may have seen crust with much lower ε_{Nd} values. But this increase in oceanic character from the Mesozoic to the Cenozoic may have broader implications for the evolution of the New Zealand crust. The thinning and foundering of the crust that have accompanied its rifting and isolation since the late Cretaceous may have resulted in increased infiltration into the lower crust of mafic magmas that lead to chemical insulation of, and thus to lessening interaction with, old continental crustal materials. This trend is analogous to one observed in andesites on the margin of the Japan Sea over the past 30 m.y. (Nohda and Wasserburg 1986). The aforementioned contrast between the Paleozoic and Mesozoic granitoids, the former being more "continental" in character, may push the trend in a general way farther back in time. In addition to chemical insulation, another factor involved may be the progressive decrease in the amount of old material in the lower crust available to later magmatic episodes, as it is continually remobilized to higher crustal levels. Thus, the isotopic character of Phanerozoic felsic magmas in New Zealand may reflect a progressive transition in the overall chemical character and average "age" of the lower to middle crust, toward a younger and more mafic identity.

A1.6. Conclusions

(1) The Nd and Sr isotopic ratios of New Zealand granitoids and sedimentary rocks reflect the presence and remobilization of large amounts of Proterozoic continental crustal material in the crust of the South Island and the Campbell Plateau during the Phanerozoic.

(2) These granitoids resulted from mixtures of mantle-derived magmas and continental crustal materials. The Mesozoic data are generally consistent with

assimilation-fractional crystallization processes acting on island arc-type mafic magmas at high assimilation rates, involving mixing with partial melts of biotite- and garnet-bearing metasedimentary rocks, perhaps followed by fractional crystallization towards granite compositions. This later fractionation may have, in some cases, altered trace element patterns, obscuring evidence for the formational process. Nevertheless, it is clear that simple mixing fails to explain the data. Regional-scale isotopic variations in the crustal end-member must have been limited, as evidenced by the lack of wide dispersion from the ε_{Nd}-ε_{Sr} mixing trajectory of data from widely spaced sample locations. Crustal melting may have been facilitated by high thermal conditions promoted by crustal thickening, as well as by heat transfer via the mantle-derived magmas. The data do not rule out the possible involvement of primary crystalline Proterozoic crustal rocks.

(3) Despite these generalized petrogenetic conclusions, the data clearly point to the difficulty of reconciling isotope and chemical data into a coherent, consistent model for granitoid genesis, particularly in terms of the large range of concentrations of some trace elements (e.g., Ba and Sr). This is a pervasive, fundamental problem in igneous petrology.

(4) Models of Sr behavior during melting-mixing processes show that nonequilibrium partial melting can result in melts with $^{87}Sr/^{86}Sr$ ratios significantly lower than the starting whole rock. These models do not, however, provide a better fit to the data.

(5) New Zealand granitoids have source regions similar to those in southeastern Australia, and in northern Victoria Land and Marie Byrd Land in Antarctica, supportive of their pre-rift proximity on the margin of Gondwanaland.

(6) Isotopic data suggest a general diminution of "continental" influence in felsic magmatism from the Paleozoic to the Mesozoic and, perhaps, to the Cenozoic, possibly reflecting the changing character of the New Zealand lower to middle crust. Continual mafic infiltration and underplating and remobilization of less refractory continental

materials to the upper crust may be responsible for this contrast.

References

Adams CJD (1975) Discovery of Precambrian rocks in New Zealand: age relations of the Greenland Group and Constant Gneiss, west coast, South Island. Earth Planet Sci Lett 28: 98-104

Adams CJ (1987) Geochronology of granite terranes in the Ford Ranges, Marie Byrd Land, West Antarctica. N Z J Geol Geophys 30: 51-72

Adams CJD, Harper CT, Laird MG (1975) K-Ar ages of low grade metasediments of the Greenland and Waiuta Groups in Westland and Buller, New Zealand. N Z J Geol Geophys 18: 39-48

Adams CJD, Nathan S (1978) Cretaceous chronology of the Lower Buller Valley, South Island, New Zealand. N Z J Geol Geophys 21: 455-462

Allegre CJ, Ben Othman D. (1980) Nd-Sr isotopic relationship in granitoid rocks and continental crust development: a chemical approach to orogenesis. Nature 286: 335-342

Aronson JL (1965) Reconnaissance Rb-Sr geochronology of New Zealand plutonic and metamorphic rocks. N Z J Geol Geophys 8: 401-423

Aronson JL (1968) Regional geochronology of New Zealand. Geochim Cosmochim Acta 32: 669-697

Arth JG (1976) Behavior of trace elements during magmatic processes - a summary of theoretical models and their applications. J Res U S Geol Surv 4: 41-47

Basaltic Volcanism Study Project (1981) Basaltic Volcanism on the Terrestrial Planets. Pergamon Press, New York, 1286 p

Borg SG, Stump E, Chappell BW, McCulloch MT, Wyborn D, Armstrong RL, Holloway JR (1987) Granitoids of northern Victoria Land, Antarctica: implications of chemical and isotopic variations to regional crustal structure and tectonics. Amer J Sci 287: 127-169

Chappell BW (1984) Source rocks of I- and S-type granites in the Lachlan Fold Belt, southeastern Australia. Phil Trans R Soc London A310: 693-707

Chappell BW, White AJR (1974) Two contrasting granite types. Pacific Geol 8: 173-174

Clemens JD, Wall VJ (1981) Origin and crystallization of some peraluminous (S-type) granitic magmas. Can Mineral 19: 111-131

Condie KC (1978) Geochemistry of Proterozoic granitic plutons from New Mexico, USA. Chem Geol 21: 131-149

Cooper RA, Landis CA, LeMasurier WE, Speden IG (1982) Geologic history and regional patterns in New Zealand and West Antarctica - their paleotectonic and paleogeographic significance. In: C Craddock (ed) Antarctic Geoscience. University of Wisconsin Press, Madison WN, pp 43-53

Davey FJ, Christoffel DA (1978) Magnetic anomalies across Campbell Plateau, New Zealand. Earth Planet Sci Lett 41: 14-20

Denison RE, Coombs DS (1977) Radiometric ages for some rocks from Snares and Auckland Islands, Campbell Plateau. Earth Planet Sci Lett 34: 23-29

DePaolo DJ (1981a) Neodymium isotopes in the Colorado Front Range and crust-mantle evolution in the Proterozoic. Nature 291: 193-196

DePaolo DJ (1981b) A neodymium and strontium isotopic study of the Mesozoic calc-alkaline granitic batholiths of the Sierra Nevada and Peninsular Ranges, California. J Geophys Res 86: 10470-10488

DePaolo DJ (1981c) Trace element and isotopic effects of combined wallrock assimilation and fractional crystallization. Earth Planet Sci Lett 53: 189-202

DePaolo DJ, Wasserburg GJ (1976) Nd isotopic variations and petrogenetic models. Geophys Res Lett 3: 249-252

DePaolo DJ, Wasserburg GJ (1979) Petrogenetic mixing models and Nd-Sr isotopic patterns. Geochim Cosmochim Acta 43: 615-627

Gamble JA, Adams CJ (1985) Volcanic geology of Carnley volcano, Auckland Islands. N Z J Geol Geophys 28: 43-54

Giraud A, Dupuy C, Dostal J (1986) Behaviour of trace elements during magmatic processes in the crust: application to acidic volcanic rocks of Tuscany (Italy). Chem Geol 57: 269-288

Gray CM (1984) An isotopic mixing model for the origin of granitic rocks in southeastern Australia. Earth Planet Sci Lett 70: 47-60

Grindley GW, Davey FJ (1982) The reconstruction of New Zealand, Australia, and Antarctica. In: C Craddock (ed) Antarctic Geoscience. University of Wisconsin Press, Madison WN, pp 15-29

Halpern M (1968) Ages of Antarctic and Argentine rocks bearing on continental drift. Earth Planet Sci Lett 5: 159-167

Halpern M, Wade FA (1979) Rubidium-strontium geochronology of plutonic igneous rocks from Hobbs and Walgreen coasts, Marie Byrd Land. Antarctic J U S 14 (no. 5): 18-19

Hanson GH (1978) The application of trace elements to the petrogenesis of igneous rocks of granitic composition. Earth Planet Sci Lett 38: 26-43

Harrison TM, McDougall I (1980) Investigation of an intrusive contact, northwest Nelson, New Zealand - I. Thermal, chronological and isotopic constraints. Geochim Cosmochim Acta 44: 1985-2003

Hurley PM, Bateman PC, Fairbairn HW, Pinson WH Jr (1965) Investigation of initial $^{87}Sr/^{86}Sr$ ratios in the Sierra Nevada plutonic province. Geol Soc Amer Bull 76: 165-174

Irving AJ, Frey FA (1978) Distribution of trace elements between garnet megacrysts and host volcanic liquids of kimberlitic to rhyolitic composition. Geochim Cosmochim Acta 42: 771-787

Kamp PJJ (1986) Late Cretaceous-Cenozoic tectonic development of the southwest Pacific region. Tectonophys 121: 225-251

Landis CA, Coombs DS (1967) Metamorphic belts and orogenesis in southern New Zealand. Tectonophys 4: 501-518

Mason B (1961) Potassium-argon ages of metamorphic rocks and granites from Westland, New Zealand. N Z J Geol Geophys 4: 352-356

Mason B, Taylor SR (1987) High grade basement gneisses and granitoids in Westland, New Zealand. J Roy Soc N Z 17: 115-138

Mattinson JM, Kimbrough DL, Bradshaw JY (1986) Western Fiordland orthogneiss: Early Cretaceous arc magmatism and granulite facies metamorphism, New Zealand. Contrib Mineral Petrol 92: 383-392

McCulloch MT (1986) Crustal evolution in New Zealand: Nd-Sr isotopic constraints. (Abstract) In: Abstracts, International Volcanological Congress, New Zealand, p 17

McCulloch MT, Bradshaw JY, Taylor SR (1987) Sm-Nd and Rb-Sr isotopic and geochemical systematics in Phanerozoic granulites from Fiordland, Southwest New Zealand. Contrib Mineral Petrol 97: 183-195

McCulloch MT, Chappell BW (1982) Nd isotopic characteristics of S- and I-type granites. Earth Planet Sci Lett 58: 51-64

McCulloch MT, Froude D, Perfit MR, Cole JW (1986) Petrogenesis of lavas from the Taupo Volcanic Zone: isotopic and geochemical constraints. (Abstract) In: Abstracts, International Volcanological Congress, New Zealand, p 179

McCulloch MT, Wasserburg GJ (1978) Sm-Nd and Rb-Sr chronology of continental crust formation. Science 200: 1003-1011

Mittlefehldt DW, Miller CF (1983) Geochemistry of the Sweetwater Wash Pluton, California: implications for "anomalous" trace element behavior during differentiation of felsic magmas. Geochim Cosmochim Acta 47: 109-124

Molnar P, Atwater T, Mammerickx J, Smith SM (1975) Magnetic anomalies, bathymetry, and tectonic evolution of the South Pacific since the Late Cretaceous. Geophys J Roy Astr Soc 40: 383-420

Nathan S (1975) Sheets S23 and S30 Foulwind and Charleston, Geological Map of New Zealand 1:63360. N Z Dept Sci Ind Res, Wellington

Nathan S (1976) Geochemistry of the Greenland Group (Early Ordovician), New Zealand. N Z J Geol Geophys 19: 683-706

Nohda S, Wasserburg GJ (1986) Trends of Sr and Nd isotopes through time near the Japan Sea in northeastern Japan. Earth Planet Sci Lett 78: 157-167

Papanastassiou DA, DePaolo DJ, Wasserburg GJ (1977) Rb-Sr and Sm-Nd chronology and genealogy of basalts from the Sea of Tranquility. Proc 8th Lunar Sci Conf: 1639-1672

Papanastassiou DA, Wasserburg GJ (1973) Rb-Sr ages and initial strontium in basalts from Apollo 15. Earth Planet Sci Lett 17: 324-337

Pickett DA, Mason BH, Wasserburg GJ (1986) Nd and Sr isotopic characteristics of New Zealand granitoids and related rocks. (Abstract) Geol Soc Amer Abs Prog 18: 718

Pickett, DA, Wasserburg GJ (1989) Nd and Sr isotopic characteristics of New Zealand granitoids and related rocks. Contrib Mineral Petrol 103: 131-142

Reid F (1983) Origin of the rhyolitic rocks of the Taupo Volcanic Zone, New Zealand. J Volc Geotherm Res 15: 315-338

Reinhardt EW (1968) Phase relations in cordierite-bearing gneisses from the Gananoque area, Ontario. Can J Earth Sci 5: 455-482

Roder GH (1984) Karamea Batholith. In: RP Suggate (ed) Sheet M29AC - Mangles Valley, Geological Map of New Zealand 1:50000. N Z Dept Sci Ind Res, Wellington

Sawka WN, Banfield JF, Chappell BW (1986) A weathering-related origin of widespread monazite in S-type granites. Geochim Cosmochim Acta 50: 171-175

Shaw DM (1970) Trace element fractionation during anatexis. Geochim Cosmochim Acta 34: 237-243

Suggate RP, Stevens GR, Te Punga MT (eds) (1978) The Geology of New Zealand. Government Printer, Wellington, 820 p

Taylor HP Jr (1980) The effects of assimilation of country rocks by magmas on 18O/16O and $^{87}Sr/^{86}Sr$ systematics in igneous rocks. Earth Planet Sci Lett 47: 243-254

Taylor SR (1977) Island arc models and the composition of the continental crust. In: M Talwani and WC Pitman III (eds) Island Arcs, Deep Sea Trenches, and Back-Arc Basins. Amer Geophys Union, Maurice Ewing Ser 1: 325-335

Tulloch AJ (1983) Granitoid rocks of New Zealand - a brief review. Geol Soc Amer Memoir 159: 5-20

Tulloch AJ, Brathwaite RL (1986) Granitoid rocks and associated mineralization of Westland - West Nelson, New Zealand. N Z Geol Surv Record 13: 65-92

Vetter U, Roland NW, Kreuzer H, Ho;hndorf A, Lenz H, Besang C (1983) Geochemistry, petrography and geochronology of the Cambro-Ordovician and Devonian-Carboniferous granitoids of northern Victoria Land, Antarctica. In: RL Oliver, PR James, JB Jago (eds) Antarctic Earth Science. Cambridge University Press, Cambridge, pp 140-143

Von Drach V, Marsh BD, Wasserburg GJ (1986) Nd and Sr isotopes in the Aleutians: multicomponent parenthood of island-arc magmas. Contrib Mineral Petrol 92: 13-34

Wasserburg GJ, Craig H, Menard HW, Engel AEJ, Engel CG (1963) Age and composition of a Bounty Islands granite and age of a Seychelles Island granite. J Geol 71: 785-789

Watson EB, Harrison TM (1984) What can accessory minerals tell us about felsic magma evolution?: a framework for experimental study. Proc 27th Int Geol Cong 11: 503-520

Winkler HGF (1979) Petrogenesis of Metamorphic Rocks, 5th ed. Springer-Verlag, New York, 348 p

APPENDIX 2

Detailed laboratory procedures

Compiled in collaboration with Diane Clemens Knott

I. Rb-Sr AND Sm-Nd CHEMISTRY

Note: These procedures are modified after those described in DePaolo (1978) and Russ (1974).

A. Spiking Samples

(1)   Make calculations of amounts of spikes needed for a reasonable weight of particular sample (usually less than 200 mg). First must estimate concentrations of Rb, Sr, and Nd in the sample based on previous runs, chemical analyses of other rocks in the same suite, or guesswork. If know concentrations of some REE (say, Ce and La), you can normalize these to chondritic values and assume straight REE slope from La to Nd. Calculate the normalized Nd concentration, then unnormalize in order to make a guess of ppm Nd in the sample.

Try to choose a sample size such that you dissolve approximately 2000 ng of Nd (e.g., 200 mg of a sample with 10 ppm Nd; this is a comfortable maximum amount of sample to dissolve). With your estimates for concentrations of Rb, Sr, and Nd use the following equations to determine the amount (in nmol) of spike isotope desired. W = weight of sample in grams;   C = estimated concentration of element.

^{87}Rb = 18.41 x W (g) x C (ppm)   [satisfies spiked $(85/87)_M$ = 0.4]

^{84}Sr = 0.172 x W (g) x C (ppm)   [satisfies spiked $(88/84)_M$ = 40]

^{150}Nd = 0.39 x W (g) x C (ppm)   [satisfies $150_T = 150_S$]

^{147}Sm = 2.99 x W (g) x C (ppm)   [satisfies $147_T = 3$ x $(147)_S$]

Subscript notation: M = measured; T = tracer/spike; S = sample.

Since we generally are using mixed spikes for Sm and Nd, there is no need to do the Sm calculation - optimize only for Nd.

Then look at the concentrations of available spikes (Table A2.1) and choose a spike such that you need on the order of 1 g of spike to give you the desired number of nmol.

At this writing, there is only one spike for Sr. You may need to adjust the amount of sample to optimize the amounts of spikes used. Try to avoid having to weigh out less than 0.5 g of spike solution.

Convert nmol of spike isotope to grams of spike solution, then convert desired g of spike to ml (using rough estimate of 1 ml = 1.05 g). Record desired weights and volumes of each spike on a separate piece of paper. Repeat process for all other spikes.

(2)   In clean lab, get a clean teflon beaker or screw-top vial (round-bottomed), rinse once with $2xH_2O$ and once with 1.5N HCl, picking up excess water drops. Rinse acid down sink. If using a beaker, make a parafilm cover from a 1.5 wide section of parafilm, cut off corners, write sample number on a colored dot, stick dot on parafilm cover, and cover beaker with clean side down. Alternatively, write directly on parafilm or on screw-top lid. Screw-top vials can be used instead of beakers if the total volume of spikes is less than about 6 ml. In this case make sure to rinse the lid as well. Add a squirt of 1.5N HCl to the beaker until the bottom is half covered (bottom of screw-top vial would be almost covered).

(3)   Using the pass-through, pass beaker and 1.5N HCl squirt bottle into center lab. Bring sample vial into center lab (i.e., do not bring vial of powder into clean lab). Place a large kimwipe on clean work surface next to balance.

(4)   Wear gloves. Label a page of notebook with the sample number, leaving an extra page between samples. Pour contents of vial (or about 3 Tbs) onto weighing paper and roll sample around. It is reasonable to assume powder homogeneity if the shatterbox was used. However, if worried about powder heterogeneity make splits by quartering pile, taking two opposite quarters, making a new pile, rolling this around, quartering again and

Table A2.1 - Spike Concentrations

Rb: sRb(1) ^{87}Rb = 402.10 nmol/g 85/87 = 0.0089

 sRb(2) ^{87}Rb = 220.45 nmol/g 85/87 = 0.0089

 sRb(3) ^{87}Rb = 5.8218 nmol/g 85/87 = 0.0089

Sr: sSr(1) ^{84}Sr = 2.9406 nmol/g 86/84 = 0.000583

   87/84 = 0.000090

   88/84 = 0.000407

Nd/Sm: sNd/Sm(1) ^{150}Nd = 2.8881 nmol/g

   ^{147}Sm = 4.5210 nmol/g

 sNd/Sm(2) ^{150}Nd = 0.15963 nmol/g

   ^{147}Sm = 0.4366 nmol/g

 sNd/Sm(3) ^{150}Nd = 0.92116 nmol/g

   ^{147}Sm = 1.4407 nmol/g

Blank Spike: BS-1 (calculated by gravimetry only; 24-Aug-88)

 ^{87}Rb = 1.79x10^{-4} nmol/g

 ^{84}Sr = 2.74x10^{-4} nmol/g

 ^{150}Nd = 5.21x10^{-5} nmol/g

 ^{147}Sm = 1.42x10^{-4} nmol/g

These values should be recalibrated annually (see separate section).

so on until you have the desired amount of sample. Put a clean piece of weighing paper on the balance pan. Make a "scooper" out of a diagonally creased piece of weighing paper or use a metal spatula. Roughly note the weight of the paper (knob on balance backwards/counterclockwise) in order to figure what weight of paper plus sample should be. Scoop sample onto weighing paper while watching scale. Each time scoop from a different section of the pile. Add and remove powder until proper weight is achieved. Now close the balance door, record the weight of sample plus paper, turn balance off and on again and check weight. Turn balance off, reset zeros, and pour sample into clean labeled beaker or vial. Do not let any sample get outside of the beaker. Use enough drops of 1.5N HCl to rinse sample to the bottom of the beaker, then swirl; if using vial, screw closed and swirl to rinse walls. Now weigh the weighing paper (and any clinging sample) and take the difference as the actual amount of sample to be dissolved. Turn balance off, then reweigh. Set scale to zero. If you are far from your desired sample weight, recalculate the weights of spikes to be added.

(5)   Return remaining sample powder to vial and clean work surface. If weighing more than one sample, use new gloves and kimwipes for each.

(6)   Pass beaker, notebook, and calculations into clean lab. In the clean lab, get the large adjustable pipet, pipet stand, and a number of clean pipet tips held in the lid of their container, and move all to the balance table. (Cover pipet container mouth with a kimwipe or a clean glove.) Use gloves and only handle the wide end of each tip.

(7)   Remove plastic box containing spike working and weighing vials from the acid "bread box". For first spike, set pipet for desired number of ml and gently pipet up spike from larger working vial. No bubbles allowed. Empty pipet into the small labeled weighing

vial, eject last drop from pipet, close weighing vial, and weigh (first on x100 scale - lever CCW - in order to set fine scale). Then weigh on fine scale (lever CW) adjusting zeros in last two decimal places with knob on right-hand side. Turn off scale, reweigh, record weight, turn off scale and reset right-hand knob to zero. Pour spike into sample vial without touching the two vials and swirl gently to mix with the powder. Weigh the empty vial (twice, as always) and subtract from first weight in order to get weight of spike added to sample. Screw on spike vial lids as tight as possible and return vials to clear plastic box. Discard pipet tip. Repeat procedure with remaining spikes (usually in the order Rb, Sr, Sm/Nd). In order to reduce the number of pipet tips used, spike all samples requiring the same spike simultaneously but carefully. When finished, replace plastic balance cover. Keep track of sample and spike weights and other calculations on a "sample sheet."

B. Dissolution of Samples

Note: The details of these procedures are frequently in a state of flux. Check with an experienced user before proceeding.

(1)   Begin evaporation. After swirling, put uncovered beakers (vials) on hot plates in evaporation hood, one sample per 1/2 of each hot plate. Turn on hot plates to approximately the 2.5 setting (center hot plate needs to be set about one unit higher). Place lids/labels on ledge in front of the corresponding sample on a piece of parafilm. Heat to near dryness, but still fluid - try to avoid completely drying as sample will form crust on the beaker which could flake off (from static electricity) and be blown away. One way to avoid losing sample in this way is to carefully add a few drops of HF to the dried sample before removing it from the hot plate. 1 ml takes about 1 hour to evaporate when starting with a cool hot plate.

(2)   Begin dissolution. Wear gloves and glasses, and be careful with these dangerous acids. Remove samples from evaporation hood and turn off hot plates. At this time, transfer any sample in a beaker to a screw-top vial. Clean and label the vial as described in step A.(2), carefully pour sample into the vial while under the evaporation hood, rinse the beaker with 1.5N HCl, and pour rinse into screw-top vial. (You may now need to dry down some more.) Go to hood next to acid "bread box". Add approximately 1-2 ml concentrated HF per 100 mg of sample or fill to base of raised square pattern on side of vial. Do not touch squirt bottle to sample vial and do not set down lid to vial during this time. Add a "long" squirt of conc. HNO_3. Put a piece of parafilm on the base of the vial, tightly screw on lid, remove parafilm, shake vigorously and place sample on teflon sheet on hot plate (setting = 2) under hood for approximately two days. During this period, check often and shake vigorously. If you have a Si-rich sample may decide to dissolve for one day, dry down sample, and repeat HF + HNO_3 dissolution procedure. Alternative method: after adding HF, add half this amount of conc. $HClO_4$ (not HNO_3). Use a 30 ml beaker with parafilm lid, or if using vial, do not tightly close lid. Let sample sit at room temperature a few days, checking and swirling periodically.

(3)   Let the vial cool before opening. Before opening, swirl to get acid off inside walls and lid. When first opening vial, hold base with a kimwipe to catch any drops of acid which may have condensed on the threads. If there are drops on the inside walls of the vial, gently tap the vial on the counter or rinse down the drops with some 1.5N HCl. Evaporate sample under laminar flow hood so that the fluorides can escape. Note that the hot plate does not produce an even temperature so samples may not evaporate at the same rate. The color of the dried sample should be orange to brown; whiteness indicates the possible presence of fluorides or other residues. If the sample is white, you may repeat the HF plus HNO_3 step. After the sample has completely evaporated, and while still in the

evaporation hood, add a few drops of HNO_3 to wet sample. Remove sample and place in acid hood. Redissolve sample in 2-3 ml of conc. HNO_3. Let dissolve on hot plate for a few days, tightly covered. Periodically shake sample. This step should attack any solid or gel residues which may have formed. <u>Alternative</u> method: dry down $HF-HClO_4$ solution in beaker after a few days at room temperature. Add $HClO_4$ and HF in reverse proportions (say, 1 ml $HClO_2$ and 0.5 ml HF per 100 mg sample), let sit for 1-2 days, swirling periodically.

(4)   Dry sample down in the evaporation hood. Measure 5 ml of 1.5N HCl using the 10 ml graduated cylinder which is kept in the CAT column hood. (Make sure to rinse the cylinder with 1.5N HCl before use.) Add to sample. Tightly screw on vial lid, shake well and place on the hot plate for one hour. Cool to room temperature. To speed up cooling, remove the lid and place sample in the evaporation hood on a cool hot plate. If using open beaker, only heat 1.5N HCl solution for about 15 min. so as not to evaporate acid.

(5)   Clean work surface and lay down a fresh sheet of quilted paper. Set out a clean quartz pipet, bulb, and pipet stand as well as a clean 30 ml PE (polyethylene) bottle and a clean, large plastic centrifuge tube for each sample. Label the stand, bottle, and tube with colored dots; cover dots with clear tape. Rinse pipet three times with 2x H_2O - after each rinse, wipe top with kimwipe and push liquid out with bulb. Rinse centrifuge tube twice with H_2O and once with 1.5N HCl.

(6)   Shake or swirl sample to suspend residue, if any. Pour suspension into the labeled centrifuge tube. Rinse vial with 1 ml 1.5N HCl and pour into centrifuge tube (skip this if you know you will have to go through another dissolution step). Screw lids on tightly and repeat for other sample.

(7)   Visually check that the two centrifuge tubes contain identical volumes of solution. Add 1.5N HCl to balance volumes as needed.

(8)   Place tubes in opposite positions in centrifuge. Close and slowly raise to full power setting, and let run for 5 min. Watch for wobbles. Meanwhile, weigh the PE bottles and record weight in notebook under heading "TR soln #1" (TR = total rock).

(9)   Very gently remove tubes from centrifuge (using blue forceps if necessary) and set in rack. Move to work surface. With quartz pipet, carefully transfer clear supernate from centrifuge tube to PE bottle without disturbing any residue in the bottom of the tube. Close PE bottle and weigh. Difference in weight equals TR solution #1. Look carefully at the bottom of the centrifuge tube for any undissolved residue. If you see any, proceed with step (10). If the sample is totally dissolved, skip to step (13).

(10)   Attacking the residue: Under the hood, pour approximately 2 ml of conc. HNO_3 into centrifuge tube with residue. Close and shake to suspend residue. Pour into original teflon screw-top vial. Rinse centrifuge tube with about 1 ml HNO_3 and add rinse to vial (you may want to pipet it into the vial). Tightly screw lid on vial. Shake vial and place on hot plate on setting #2. Continue heating and shaking overnight. Meanwhile, store sample pipets in glass tubes: rinse tube twice with 2x H_2O, cover base with one square of parafilm, label tube with colored dot then insert pipet. Store this in the glass cabinet until it is next needed. Alternative: Transfer residue from centrifuge tube to vial or beaker with 1.5N HCl. Heat to near dryness, then add 1-2 ml conc. $HClO_4$. Let sit at room temperature for most of a day, swirling occasionally.

(11)   Dry down sample (HNO_3 or $HClO_4$) and redissolve in 3 ml 1.5N HCl. Heat in closed vial for one hour (15 min. if in open beaker) and cool to room temperature. Inspect to see whether all residue has dissolved.

(12)   Repeat steps (6) through (9), except label the weights as "T.R. soln #2". Hopefully no residue remains at this point. If, however, there is still residue, repeat steps (10) and (11) then steps (6) through (9) labeling these weights as "T.R. soln #3". This makes a maximum of three dissolutions in HNO_3 or $HClO_4$. You may decide it is necessary to attack again with HF. Add to rest of dissolved sample and weigh again.

(13)   Calculate how much sample you want to put through the column. (Meanwhile, you should be preparing the columns for use - see below.) This calculation is usually based on the Nd content and usually equals about one third to one half of the total dissolved sample. Roughly, you want 600-1000 ng Nd (1000 ng is optimal) and 15,000 to 30,000 ng Sr (e.g., if T.R.=200 mg sample at 10 ppm Nd, take 1/2 sample for column). If you are only doing Rb-Sr on the sample, you only need 1000 ng Sr and a few ng Rb; however, increasing the amount of sample decreases the amount of Sr solution you will have to evaporate for filament loading. Estimate the volume needed and weigh the T.R. solution in its bottle before aliquoting (it may have changed since you last weighed it). Shake the T.R. solution well to ensure homogeneity and use the calibrated pipet to measure the proper amount of sample into a beaker or vial (you may use the original dissolution vessel if it is clean and free of residue). You may carefully pour solution from the bottle to the vial or beaker instead - it is not important to aliquot exactly the correct amount. Weigh the T.R. solution after removing the aliquot to get a precise weight of sample used. Dry the aliquot down in the evaporation hood. Redissolve in 2 ml 1.5N HCl, using the small graduated cylinder. Close tightly and heat 1/2 hour (15 min. if open beaker) to aid

dissolution, and cool to room temperature with the lid tightly screwed on. For the sake of efficiency, you should be completing these steps on the morning of Day 2 in the procedure for cation column elution (see below).

(14)   Since you never change the resin in the cation columns you want to be exceptionally careful that you never put any solid residue on the resin, as this could affect the elution and/or the blank. To avoid this possibility, we centrifuge the 2 ml sample solution before loading on the column. Take a tapered, narrow, quartz glass centrifuge tube and label with a colored label and cap it with a small square of parafilm. Carefully pour the 2 ml solution into the centrifuge tube and centrifuge for 5 min. (perform on two samples at a time to maintain centrifuge balance). You should be completing this step while the 10 ml 1.5N HCl is passing through the cation columns - see Day 2 below.

C. Elution of Rb, Sr, and bulk REE

Day 1

(1)   It is best to perform the elutions in pairs. Label CAT columns with colored dots corresponding to samples. Make sure you have enough 1.5N, 2.5N, and 4N HCl for the elution. Move portable hood with CAT columns against hood containing quartz acid still, open the rear panels, and raise the clear front panel half-way.

(2)   The night preceding the elution, place the large waste beaker under the column and run approximately 100 ml of 6N HCl through each column. This corresponds to filling the column reservoir bulb with acid -- pour the acid directly into column. Position beaker and adjust column height so that drops run smoothly down inside wall of beaker (no splashing), but don't let column tip touch the beaker. Always replace the cap on the top of the column when you are not adding acid or sample to the column. Record in notebook

as shown in Table A2.2. You will want to check off time and date as each step is completed.

Day 2

(3)   The next morning, completely remove the clear front hood panel. Empty the used 6N HCl into waste bottle kept under acid still hood. Place waste beaker back under column. With 1X H_2O wipe the work surface and lay down a quilted Crew Wipe in front of the column stand. Use the small graduated cylinder and add 10 ml of 1.5N HCl to each column.

(4)   Rinse the quartz pipet used in the dissolution procedure twice with 2X H_2O. When all the 1.5N HCl has passed into the resin, pipet the centrifuged sample from quartz centrifuge tube (from step B.(14) above) into the column. Try to avoid getting any sample in the reservoir or high on the walls of the column. *Gently* press the pipet tip against the wall less than a couple of inches above the resin and let the sample run down from this point. This procedure minimizes disruption of the top surface of the resin.

(5)   Put 2 ml of 1.5N HCl in each centrifuge tube as a rinse and run for 5 min. in the centrifuge. After the sample solution has passed completely into the resin, pipet the rinse acid into each column, simultaneously rinsing the walls of the column by moving the pipet tip around while expelling the acid

(6)   Get the sample beakers or vials that were used for weighing and dissolution, as long as they are free of residue. Rinse with 2x H_2O, followed by 1.5N HCl. Clean pipets by rinsing 3 times with 2x H_2O (use squirt bottle to fill pipet, dry around the top of the pipet with a kimwipe, and use the bulb to force the water out). Put a few ml of 1.5N HCl

into the beaker, take up in pipet as a final rinse, and discard acid into waste beaker under column.

(7)   Note: acid measurements in the following steps are correct only for CAT column #1 and are subject to change (see section on column calibration). Measure 42 ml of 2.5N HCl in the large graduated cylinder. Pour some of this into the sample beaker, replace lid on graduated cylinder, and carefully pipet some of the acid from the beaker into the column, washing down the walls of the column and avoiding disturbance of the top of the resin as before. Replace cap on top of the column and let all acid pass through the resin. Repeat twice to ensure that all sample is washed off the walls and is in the resin. Pipet in enough acid to fill the column to within 2 inches of the reservoir and pour the remainder of the 42 ml from the sample beaker and the graduated cylinder into the column. Adjust waste beaker so that drops run down the side of the beaker in order to avoid splashing. Then wait about one hour for all acid to sink beneath the top of the resin. Meanwhile, label two 60 ml PE bottles (for Sr, REE) and one 30 ml PE bottle (for Rb) per sample. These should be dry; do not rinse them. If you wish to check yields (see section on column calibration), weigh these bottles before and after elution.

(8)   After all acid has passed into resin, rinse off the outside of the lower end of the cation column with 2x H_2O into waste beaker. Position Rb collection bottle (30 ml polyethylene) under column. Raise the column by holding the reservoir, place inverted glass cover beaker (with hole in base) over PE collection bottle, and lower column through hole into neck of collection bottle (do not touch the cover beaker with the column tip). The tapered tip of the column should only be partially below the rim of the bottle so that air can escape easily.

Table A2.2: Example of lab book record for Rb and Sr elution

CAT-1

6-Aug-89

    18:00   6N HCl   100 ml   [cleans column]

7-Aug-89

    10:08   1.5N HCl 10 ml   [conditions column]

    10:24   (2) ml   "Sample number"

    10:30   2 ml   [sample rinse/column rinse]

    11:12   2.5N HCl 42 ml

    12:01   22 ml   Rb

    12:32   16 ml   [20 ml for CAT-2]

    13:04   50 ml   Sr

    14:11   4N HCl   25 ml

    15:16   60 ml   REE

    17:30   6N HCl   100 ml   [cleans column]

(9)   Using large graduated cylinder, pour 22 ml of 2.5N HCl into top of column. You do not need to pipet in this fraction as sample is far within resin column by now.

(10)   Wait approximately 1/2 hour. When the acid has all passed through the resin, raise the column and remove and cap the Rb collection bottle. Replace with waste beaker. Pour in 16 ml of 2.5N HCl.

(11)   When this fraction has all passed through the resin, remove waste beaker and insert Sr collection bottle (60 ml PE). Use inverted cover beaker and position column as in step (8). Pour in 50 ml of 2.5N HCl.

(12)   Put 2.5N bottle back into "bread box" and remove squeeze bottle of 4N HCl (this keeps you from using the wrong acid). When acid has all passed through the resin, remove and cover Sr collection bottle. Reposition waste beaker under column and pour 25 ml of 4N HCl into column.

(13)   When acid has all passed through the resin, position REE collection bottle (60 ml PE) underneath column as for Rb and Sr. Pour in 60 ml of 4N HCl.

(14)   When acid is beneath top of resin, remove and cover REE collection bottle; the elution is completed. Place waste beaker under column. To clean the column, fill the reservoir bulb with approximately 100 ml 6N HCl. This step will be repeated the night before you next use the column.

(15)   When acid is through column, place 30 ml bottle of 2x H_2O below column and lower column tip into bottle. This keeps the resin from drying. Empty out and rinse the waste

beakers. Replace front cover of portable hood, close back, and roll back into place away from acid hood.

D. Elution of Sm and Nd

Day 1

(1)   Prepare the REE solution (from the cation column) for separation of Sm and Nd. The usual amount of sample to use corresponds to 500 ng Nd, although smaller amounts could be fine (down to about 150 ng). Rinse a 30 ml teflon beaker with 2X H_2O and 1.5N HCl, and cover with parafilm. Weigh the REE bottle, record, and pour desired proportion (often) into beaker. Weigh bottle and calculate difference; this is the amount of sample to be dried down and eluted in the REE column. Place beaker in the evaporation hood and evaporate until nearly dry (small yellow drop remaining). Try to let it finish drying in air (covered) so that sample is not overdry and hard; the sample should be easy to redissolve.

(2)   Begin preparing the REE column early enough in the day so that you can complete the process 6 1/2 hours later. Wipe REE column work area, including column holder and turntable with 1X H_2O. Place quilted Crew Wipe on work counter next to column. Place a pipet holder on wipe. Wear gloves.

(3)   Loosen bolts holding the column holder to the stand, raise holder, and place plastic waste beaker underneath. Remove top and bottom flanges. Rinse bottom flange with 1X H_2O followed by 2X H_2O, especially around the nipple hole, and place on top of the inverted top flange (both on wipe).

(4)   Remove REE column from large acid-filled storage tube. To do this, hold the tube with a kimwipe, slightly below and away from the label, and carefully pour acid into the

labelled bottle (we recycle this acid -- it is diluted to   concentrated). Make sure you don't

lose the teflon nipple. In order to get all the acid out of the column, hold the tube upright

and then drain again. Repeat as needed.

(5)   Rinse column in the tube three times with 1X H$_2$O. Again, don't lose the nipple.

Make sure that during each rinse the column fills with water and is properly rinsed.

(6)   Get a clean glove with which to handle the column and nipple (don't wear the

glove). Remove both pieces from the acid tube by holding the glove over the open end and

tipping the tube: catch the nipple in the clean glove, let the column slide approximately

eight inches out, then place the glove and nipple on the Crew Wipe. Pull the column out

of the tube, taking care not to touch the bottom of the column with your gloved hand.

(7)   Rinse the column once with 1X H$_2$O then three times with 2X H$_2$O. Hold column

horizontally and rotate around axis in order to ensure that the capillary and reservoir are

rinsed. Dry the outside with a kimwipe, paying special attention to the ground glass ball

joint at the top of the column; do not dry the lower end of the column. Mark with a black

pen the scratch on the capillary 3 cm down from the reservoir.

(8)   Rinse the blue plastic forceps with 2X H$_2$O. Gently pick up the nipple with the

forceps and rinse with 2X H$_2$O. Place nipple firmly in the well in the bottom flange of the

column holder, with the tip protruding out the bottom. Get the plastic box containing filter

paper from the cabinet. If necessary, cut a circle of paper using the metal tool and plastic

guide. With the white tweezers, place a piece of filter paper in the nipple. Wet this with

one drop of 2X H$_2$O. Screw the bottom flange containing the nipple onto the column

holder, not letting the protruding nipple tip touch any surfaces (do not screw on completely for column REE-2 because this column is slightly too long for the holder).

(9)   Insert column into the holder from the top, being careful not to touch the tip of the column to anything (it helps to guide the column with a finger while you hold it with the other hand). Press column to seat in the nipple and gently screw on top flange; the black mark should be in front. Lower column assembly onto drop sensor bracket, and place the waste beaker under the column; this may require raising the column assembly and drop sensor.

(10)   Fill the column reservoir approximately 2/3 full with 2X H_2O from a squeeze bottle. Keep the ball joint dry. With the corner of a folded kimwipe, apply a small dot of silicone grease around the base of the ball joint in a thin but continuous swath. Check that the pressure line is ready, i.e. that the bottom bottle is less than 1/2 full. If not, lower the top bottle to be below the other and open the stopcock until the bottom bottle is nearly empty. Close the stopcock and return the bottles to their normal positions, securing the cord which holds them in place.

(11)   Attach pressure line socket joint to ball joint on column and move it around to spread out the grease. Attach the holding clamp and open stopcock to apply pressure until all air is forced from beneath the water in the column capillary. Close stopcock and remove the socket joint from the column (always remember to close the stopcock first).

(12)   Get the adjustable pipet, the labeled PE bottle containing the "REE pipet tip," and the screw-top vial containing the REE resin (larger resin stock bottle is in the "bread box"). Swirl resin and fill pipet with 1.2 ml of resin. Steadying the pipet with the opposite hand,

expel resin into the reservoir. The tip of the pipet does not need to be inserted into the reservoir. Completely fill the reservoir with 2X H_2O from the squeeze bottle so that all resin is washed from the walls. Return pipet tip to labeled bottle.

(13)   Cover top of column with inverted beaker cap and let resin settle for <u>one hour</u>. Put away all equipment except 2X H_2O and pipet stand.

(14)   Find a quartz pipet with a relatively small reservoir and long capillary. Rinse this with 2X H_2O. By this time the resin should have settled so that the upper level is above the top of the capillary. (If the resin level is below the top of the capillary, add a little more resin and let settle again.) Using the pipet, remove excess resin to just above the top of the capillary and discard excess into waste beaker. Then pipet out excess water from reservoir until it is even with the top of the resin. Rinse down the sides of the reservoir with a few drops of MLA (2-methyllactic acid) from the dropper bottle, and then remove this acid with the pipet.

(15)   Using the graduated cylinder labeled "MLA", pour approximately 11 ml of MLA into reservoir and re-cover the column. The MLA serves to condition the resin for the elution. Remember to keep the ball joint dry.

(16)   Remove the waste beaker from the turntable, turn on power on drop counter control, and depress the "Home" button at each turntable position until you reach the "H" position and the "Home" and "Start" lights are both on. At these settings, the turntable will not move in response to the drop counter. (Note: If the proper combination of lights won't turn on, check electric connections, turn power off, and try again.) Place waste beaker back under column. Push the reset button on the LCD counter display. Attach

the pressure line socket joint, open the stopcock, and record "time, 0 ml, MLA - pressure on" in lab book (Table A2.3). (Write out the format before beginning so all you have to do later is record the drops and the time at the appropriate points.) Leave for five hours.

(17)   After five hours the counter should read at least 130 drops. Do not leave the pressure on for much longer, as the resin will dry out if the reservoir is drained of all the MLA. You may have trouble if more than 200 drops have come out at this point; if so, add more MLA to reservoir. Remove pressure line as before, put cover beaker on column, replace parafilm on pressure line socket, and let column sit overnight.

Day 2

(18)   Record the number of drops - it should be near 200 at this point. If much lower, apply more pressure provided that there is sufficient MLA in the column to avoid drying the resin. Check numbers on thumbwheel switches on drop counter control box (e.g., so that Sm is collected in the second position on REE-1 between drops 30 and 39, etc.). Replace the plastic waste beaker under the column with the 7 ml waste vial, which fits in the well in the turntable in the "H" (home) position. Lower the column holder assembly so that the drop sensor is just above the level of the plexiglass turntable cover.

(19)   Using the pipet, remove resin from the column until the top of the resin is even with the marked scratch. Hopefully there won't be any residue in the reservoir. If so, you can wash this down with more MLA. Remove MLA to top of resin.

(20)   Rinse the pipet you used the previous day three times with 2X H_2O, ensuring that there is no resin inside the pipet. With the pipet, fill capillary of column above resin with 2X H_2O from small vial. This is a delicate procedure which requires practice to perform

Table A2.3: Example of Lab Book Record for Sm and Nd Elution

<u>REE - 1</u>

Sample #

11-Jan-89	12:30	0	MLA - pressure on
	17:38	127	Pressure off
12-Jan-89	9:39	192	resin to mark
	9:44	193	H_2O
	9:49	195	Sample [in 2 drops HCl]
	9:54	197	2 drops 0.75N HCl
	9:59	199	MLA
	10:00	0	
		30-39	Sm
		59-72	Nd

smoothly (see step 22). Apply pressure to the column until water level is approximately 1 mm above top of resin (after 1-2 drops have passed). Don't let the resin go dry. Remove pressure.

(21)   Meanwhile, put 2 drops of 0.75N HCl on dried REE sample in beaker. Ideally these drops should always be the same size: invert the bottle at a 45°angle and put a drop or two in the waste beaker before adding the drops to the sample. Note that the sample should not be excessively dried and hard. Stir with the tip of the pipet to help dissolve the sample.

(22)   Add sample to column capillary above the resin with pipet. Confine the sample to the capillary; if some gets in the reservoir and does not enter the resin with the rest of the sample, your elution curve may spread out, decreasing your yield and increasing Sm interference. The best method is to place the pipet tip just above the resin, then squeeze out sample gently while slowly pulling pipet up through capillary. Ensure that no air bubbles are in the capillary. If there is not enough room to fit all sample solution in the capillary, add the sample in steps. Apply pressure to column until the solution is just above the resin.

(23)   While waiting, add 2 more drops of 0.75N HCl to the beaker on the spot where the sample was. Stir with pipet tip to clean. When the last of the sample is near the top of the resin, remove the pressure and pipet in the rinse HCl from the beaker into the capillary. Apply pressure.

(24) Thoroughly clean beaker and pipet with 2X H_2O, followed by a few drops of MLA. Meanwhile, keep an eye on the column. Remove pressure when the HCl is just above the top of the resin.

(25) Place a few drops (5-6) of MLA in the beaker on the side opposite to where the dried sample was (you should not be putting any traces of sample in the column now). Fill capillary with MLA using pipet. Apply pressure. Watch for the next drop. After it has fallen, reset the LCD counter to zero. Push the "Start" button and the red light next to the first thumbwheel should come on. At this point, the "Start" light should be off and the "Home" light should remain on. The turntable should be oriented so that the "H" position is below the column. Drop counter control of the turntable is now activated and the elution has begun. Record the time. Keeping an eye on the column, get two clean snap-cap vials, empty and rinse them, label the lids with sample name and "Sm" or "Nd", and place in the appropriate turntable wells. Position #2 = Sm, #4 = Nd; there should be a reusable waste vial in #3.

(26) When the MLA is just above the resin, remove the pressure, put a few drops of MLA into the beaker, and again fill capillary using pipet. You can add a little extra MLA to rinse down any resin or sample that might have splashed into the reservoir. Apply pressure until acid is just above resin.

(27) Fill capillary with MLA a third time in the same way. Then pour in 6 ml of MLA. Apply pressure. Elution continues for 2-3 hours until Sm and Nd have been collected. Turntable will move in response to the drop counter according to the settings on the control box. It is alright to leave the column going longer than necessary, as long as the resin doesn't go dry.

(28) When elution is complete, remove pressure and correctly cap the Sm and Nd vials as you remove them from the turntable. Empty vials from "H" and #3 positions into waste beaker.

(29) Unscrew top flange and remove column from holder. Holding the column in your hand with the lower end over the waste beaker, apply pressure until the resin is expelled into waste beaker, quickly turning off the pressure as the column is emptied. Wipe the grease off the ball joint. Rinse the column three times, inside and out, with 1X H_2O. Remove the ink mark with acetone. Gently place the column, inverted, into the appropriate storage tube (hold tube horizontal and push the column to the bottom). Screw the top flange back on the column holder. Raise the column holder off the drop sensor bracket, unscrew the bottom flange, and remove the nipple with the blue forceps. Remove the filter paper and discard. Rinse nipple with 1X H_2O and drop into storage tube with column. Rinse the bottom flange with 1X H_2O and screw on base of column support.

(30) Fill acid tube with the reserved recycled HNO_3 from the labelled bottle. Place inverted beaker over tube and stand tube in large beaker to store.

(31) Put away all equipment and dirty ware and turn off control box. Rinse waste beakers with 1X H_2O.

II. FILAMENT LOADING

A. Loading Rb

(1)   Calculate how much Rb sample solution you need in order to load 2 ng Rb on the filament. If this is more than ~10 microliter (μl), dry it down in a snap-cap vial to a small drop. Otherwise, you will load it directly from the bottle.

(2)   Work in center lab under hood. Pass hat and samples into center lab.

(3)   Place bead with a single Re filament in center pair of sockets of loading stage. Adjust pipet to a volume of 1 μl greater than the sample, but at least 5 μl. Clean a new pipet tip by pipeting this volume of the following solutions, discarding each into waste beaker and gently knocking off any excess drops: (a) concentrated HNO_3; (b) W1 (water); (c) repeat W1; (d) W2.

(4)   Load 2 μl of silica gel suspension on filament. You want a short (3 mm), even layer in the center of the filament. Turn on the power source and push the button for the center socket. Move the dial so that the power setting is at 1.5. Put a small amount of gel on the filament and let this partially dry for a few seconds; try to avoid touching the filament with the pipet tip. If desired, support the pipet with the opposite hand. Repeat until finished.

(5)   Shake the sample bottle. Using pipet, put 2.0 μl of 0.5N H_3PO_4 on the inside lid of the sample bottle or vial in a position where it can be distinguished from sample drops. Put 1 μl of this on the gel on the filament, drying between drops.

(6)   Take up the appropriate volume of Rb solution from drops on the inside of the lid (or from the vial in 1 µl 1.5N HCl if evaporation was necessary) and dry on filament drop by drop.

(7)   Load the 1 µl of 0.5N H_3PO_4 left on the lid on the filament and dry. Never put a pipet tip which has touched sample into any other container, such as those for acids or loading media. To avoid confusion, immediately discard tip when finished with sample.

(8)   Turn off room and hood lights. Turn up the power source slowly until the center of the filament begins to glow orange. Immediately turn the power down to zero. The filament is ready for analysis.

(9)   The Rb standard is in the PE bottle labeled "nRb(AAA)" in hood. Load 1.2 µl (equivalent to 2 ng Rb) directly onto filament in same way.

B. Loading Sr

(1)   Dry down in a snap-cap vial an amount of the Sr solution equivalent to about 1000 ng Sr.

(2)   Inspect Ta single filament bead from the side. The Ta is stiff and may have warped. Push with pipet tip to straighten if necessary (and discard pipet tip).

(3)   Clean a pipet tip as for Rb. Turn on the filament power and set to about 1.5. Shake up container of Ta_2O_5 powder (suspended in water), and take approximately 0.5 µl (depending on suspension concentration) and load this on the filament. This will be a

more solid white than the silica gel spot on the Rb filament. The dried powder should be quite thin; if not, use clean water from the pipet to take up and discard the excess.

(4)   Put a drop of 1.5N HCl on the lid of the Sr sample vial. Put 3 µl on the dried sample, stir with pipet tip to dissolve, and load 1-1.5 µl of this (330-500 ng Sr) onto the filament in small increments. Take filament to 2.0 to complete loading.

(5)   The Sr standard is "987 Sr". Dry down approximately 150 µl in the labeled snap-cap vial in the evaporation hood. Dissolve this in HCl as in (4) and load on filament.

C. Loading Sm

(1)   Dry down Sm sample in evaporation hood, checking for condensed drops of MLA on walls of vial. Make sure the sample and vial walls are completely dry; mixing MLA and HCl produces a white substance which is difficult to dissolve.

(2)   Loading is on platinized (10%) carbon on a single Re filament. Clean a pipet tip as always. Shake Pt-C vial and pipet 0.5 µl Pt-C slurry onto filament. Dry at 1.3. You should have an even, thin layer confined to the center 3 mm or so of the filament. To remove excess, take up a little 3x H_2O (in the unlabelled squeeze bottle) in the pipet, place on the filament, and take up some of the Pt-C.

(3)   Place a drop of 1.5N HCl on the inside lid of the Sm vial and pipet 3 µl onto the dried sample. Help it dissolve by stirring with the pipet tip and sucking the solution in and out of the pipet. Set pipet to 1.5 µl (so that you are loading the sample) and incrementally dry this amount on the Pt-C on the filament. Final drying is at 2.0. Save the remaining sample.

D. Loading Nd

(1)   Evaporate Nd sample as in Sm step (1).

(2)   Loading is on resin beads (AG50W-X8, 100-200 mesh; i.e., that used in the cation columns) on a Re filament. After cleaning pipet tip, dry 0.5 µl of resin suspension on filament with current at 1.3. Should have a thin strip of ~20 beads in a single layer along the center of the filament.

(3)   Pipet 1 µl 0.5N H_3PO_4 onto the inside lid of the Nd vial.

(4)   Place a drop of 1.5N HCl on the inside lid of the Nd vial, away from the H_3PO_4 drop, and pipet 3 µl onto the dried sample. Help it dissolve by stirring with the pipet tip and sucking the solution in and out of the pipet. Set pipet to 1.5 µl (so that you are loading the sample) and incrementally dry this amount on the resin.

(5)   Pipet H_3PO_4 from lid onto sample. Dry at 2.0. Save remaining sample.

III. MASS SPECTROMETER ANALYSIS

<u>Note</u>: As runs can vary in quality, these are rough guidelines. With experience, the user will gain the flexibility necessary to get the most from each sample.

A. Rb

(1)   Rb is run in the static mode with mass 85 in Low 1 and 87 in High 1. It is therefore necessary to precede the analysis with a cup setup to "Rb Static," followed by a cup calibration with "L1-H1." One cup calibration should suffice for a day.

(2)   Preheat to 1.35 A with the task "1.35 A, 12 min - Rb." Aiming intensity for mass 87 is usually 5E-12 A (0.5 V), and is normally attained with the filament at 1.5 - 1.7 A.

(3)   The measuring routine is "Rb Static - spiked" in the "Static Multi-Coll" task directory, measuring 100 ratios. Since there is no normalizing ratio, it is best to use the unfiltered ("before rejection") grand mean in subsequent calculations.

(4)   For standard runs, use routine "Rb Static - normal," which uses mass 85 for the aiming intensity (usually 5E-12 A) instead of 87.

(5)   Results of runs of standard nRb(AAA) are shown in Table A2.4.

B. Sr

(1)   Sr is run multidynamically in cups L2 to H1 (set to "Sr Quad"), except that the 84/86 ratio (cups L2 and Ax) is static. It is therefore necessary to run a cup calibration with "L2-H1" prior to analysis.

(2)   Preheat slowly to 3 A. Attempt to analyze with the aiming intensity for mass 88 at

3E-11 A (3.0 V), which is usually attained with the filament set to 3.3 - 3.7 A.

(3)   The measuring routine is "Sr Quadruple Coll" - file "Sr Quad," which measures 150

cycles (although peak precision may be attained with fewer, say 105). You can probably

use the filtered data, although a large discrepancy between the two different grand means

is cause for concern. The percent standard error on 87/86 should be in the vicinity of

0.001 (1σ).

(4)   Offline data manipulation is by means of the Basic program "SRDATA," which

determines Rb and Sr concentrations by isotope dilution, spike-corrects all ratios by

iteration, and performs age corrections. Note that the query for "uncorrected" ratios refers

to your run results, filtered or unfiltered. Be sure that spike concentrations, spike ratios,

and normal ratios are updated to the preferred values. It is assumed that fractionation

corrections were made during data collection according to the standard ratios (e.g.,

$^{86}Sr/^{88}Sr = 0.1194$).

(5)   Results of runs of standard 987 Sr are shown in Table A2.5.

C. Sm

(1)   Sm is run statically (cups at "Sm Static ,   ⌐ in

Ax, and 152 in H3. You must therefore run a cup calibration with "L2,L1,Ax,H3" prior to

analysis.

(2)   Preheat fairly slowly to 2.5 A. Try to analyze with aiming intensity on mass 147 set

to 2.5E-12 (0.25 V), which is normally attained with the filament set to 2.7 - 3.0 V. Sm

runs are quite variable, probably owing to varying thickness of the Pt-C layer on the filament, so use care when bringing up the filament. You may need to take data at considerably lower intensities.

(3)   Measuring routine is "Sm Static" in the "Static Multi-Coll" task directory, measuring 100 cycles (you may have to settle for fewer). You can probably safely use the filtered data.

(4)   Results of runs of standard nSmβ (Wasserburg et al., 1981) are shown in Table A2.6.

D. Nd

(1)   Nd is run multidynamically on cups L2 to H2 (set up with "Nd 140-150"). It is not necessary to perform a cup calibration.

(2)   Preheat slowly to 3.0 A for 30-90 minutes and always treat gently. Aiming intensity on mass 144 is 1E-11 (1.0 V), usually achieved at filament current 3.3-3.7 A.

(3)   Measuring routine is "Nd 4cycle dynamic" - file "Nd 4 cycle," which includes mass 150. 150 cycles are measured and the percent standard error on 143/144 should be <0.001; 105 cycles may be sufficient. The filtered data are normally best, but use caution if the unfiltered results are markedly different.

(4)   Offline data manipulation is by means of the Basic program "NDDATA," which determines Sm and Nd concentrations by isotope dilution, spike-corrects all ratios by iteration, and performs age corrections. You can also adjust the Sm interference correction if (147/144) > 0.000010; this is necessary because the online correction

assumed <u>un</u>spiked Sm. Note that the query for "uncorrected" ratios refers to your run results, filtered or unfiltered. Be sure that spike concentrations, spike ratios, and normal ratios are updated to the preferred values. It is assumed that fractionation corrections were made during data collection according to the standard ratios (e.g., $^{146}Nd/^{144}Nd = 0.7219$). Note that the T_{DM} calculation is according to DePaolo (1981).

(5)   Results of runs of standard La Jolla Nd are shown in Table A2.7.

Table A2.4 - Rb standard runs (nRbAAA)

date	$^{85}Rb/^{87}Rb$
5/20/88	2.6128
5/22/88	2.6120
5/22/88	2.6197
5/24/88	2.6153
9/12/89	2.6173
9/12/89	2.6172
9/19/89	2.6194
11/21/89	2.6188
12/15/89	2.6175
3/3/90	2.6198
3/5/90	2.6159
3/9/91	2.6093
mean	2.6163 ± 0.0019 (2σ of the mean)

Table A2.5 - Sr standard runs (987 Sr)

Normalized to $^{86}Sr/^{88}Sr \equiv 0.1194$

date	$^{87}Sr/_{86}Sr$	$^{84}Sr/^{86}Sr$
1/11/88	0.710249	
1/11/88	0.710259	
1/28/88	0.710258	
3/4/88	0.710271	
5/18/88	0.710250	
7/25/88	0.710246	
10/28/88	0.710253	0.056486
12/29/88	0.710252	0.056550
2/2/89	0.710246	0.056486
4/10/89	0.710213	0.056515
5/28/89	0.710239	0.056522
8/19/89	0.710248	0.056527
9/13/89	0.710248	0.056474
9/13/89	0.710249	0.056503
10/8/89	0.710226	0.056515
11/20/89	0.710257	0.056500
1/11/90	0.710234	0.056528
3/4/90	0.710242	0.056507
3/5/90	0.710243	0.056528
3/8/90	0.710227	0.056504
4/27/90	0.710247	0.056535
8/26/90	0.710248	0.056518
11/21/90	0.710232	0.056524
5/21/91	0.710226	0.056530
mean	0.710244 ± 0.000005	0.056514 ± 0.000010

Table A2.6 - Sm standard runs (nSmβ)

Normalized to ^{149}Sm/^{152}Sm ≡ 0.51686

date	^{148}Sm/^{147}Sm	^{148}Sm/^{152}Sm
3/11/89	0.750624	0.420390
3/19/89	0.750622	0.420397
5/10/89	0.749387	0.420429
9/11/89	0.749363	0.420465
9/13/89	0.749446	0.420496
1/31/90	0.749594	0.420476
2/9/90	0.749360	0.420396
2/10/90	0.749415	0.420466
2/21/90	0.749700	0.420713
3/2/90	0.749703	0.420497
3/31/90	0.749557	0.420452
4/13/90	0.749450	0.420511
4/17/90	0.749570	0.420483
4/25/90	0.749524	0.420489
11/23/90	0.749276	0.420428
3/9/91	0.749645	0.420673
5/17/91	0.749656	0.420611
mean	0.74964 ± 0.00019	0.42049 ± 0.00005

Table A2.7 - Nd standard runs (La Jolla Nd)

Normalized to ^{143}Nd/^{144}Nd ≡ 0.7219. 2σ errors of means are in last one or two digits.

date	load type	142/144	143/144	145/144	150/144
11/24/87	triple	1.141872	0.511860	0.348433	
12/16/87	triple	1.141813	0.511855	0.348414	
12/16/87	triple	1.141852	0.511858	0.348418	
12/16/87	triple	1.141815	0.511850	0.348411	
12/17/87	triple	1.141856	0.511856	0.348405	
1/5/88	triple	1.141849	0.511858	0.348409	
1/6/88	triple	1.141908	0.511867	0.348407	
1/6/88	triple	1.141842	0.511858	0.348417	
2/3/88	triple	1.141887	0.511856	0.348405	
2/3/88	triple	1.141904	0.511861	0.348401	
2/6/88	triple	1.141851	0.511852	0.348412	
2/19/88	triple	1.141834	0.511849	0.348406	
2/23/88	triple	1.141841	0.511851	0.348409	
11/14/88	triple	1.141830	0.511850	0.348393	0.236760
1/19/89	triple	1.141688	0.511845	0.348404	0.238076
5/8/89	triple	1.141788	0.511864	0.348409	0.237068
9/11/89	Pt-C	1.141901	0.511843	0.348412	0.236526
9/12/89	Pt-C	1.141940	0.511860	0.348394	0.236625
2/9/90	Pt-C	1.141824	0.511854	0.348393	0.236547
3/2/90	triple	1.141863	0.511872	0.348421	0.236969
3/10/90	triple	1.141933	0.511853	0.348387	0.236916
3/17/90	triple	1.141833	0.511835	0.348407	0.237884
3/25/90	triple	1.141795	0.511848	0.348400	0.237422
4/27/90	triple	1.141636	0.511846	0.348414	0.236472
5/31/90	triple	1.141812	0.511850	0.348402	0.236472
6/1/90	triple	1.141683	0.511838	0.348408	0.236464
9/7/90	resin	1.141786	0.511854	0.348400	0.236446
9/7/90	resin	1.141752	0.511844	0.348408	0.236408
9/11/90	resin	1.141833	0.511852	0.348407	0.236431
12/13/90	resin	1.141840	0.511854	0.348396	0.236428
12/29/90	resin	1.141819	0.511854	0.348409	0.236463
1/27/91	resin	1.141812	0.511846	0.348404	0.236445
5/16/91	resin	1.141866	0.511856	0.348407	0.236447
mean	all	1.14183 ± 2	0.511853 ± 3	0.348407 ± 1	0.236448 ± 13*
mean	resin	1.14182 ± 3	0.511851 ± 7	0.348404 ± 2	0.236438 ± 14

* Mean for ^{150}Nd/^{144}Nd only includes last 10 runs (starting with 4/27/90). See Chapter 3 for discussion.

IV. MAKING FILAMENTS

(1)   Clean working surfaces with alcohol. Clean filament ribbons with Kimwipe and alcohol; dry with Kimwipe.

(2)   Wear gloves and safety glasses. Gently cut desired number of lengths of ribbon with "guillotine." Use the rubber pointer (found in plastic box labeled JBS) to nudge the ribbon along until it touches the opposite wall. Let cut pieces fall onto Kimwipe. When finished, replace bag over guillotine.

(3)   Using tweezers, center a piece of ribbon on the central trough of the copper welding assembly. Turn welder power on, then turn to "Set up" mode. Wait for a few seconds until you hear a click, then turn button to "45 WS". The meter should register at approximately 3.5 on the top scale, 0.7 on the lower scale. Fully turn the dial clockwise on the small welder.

(4)   Get a clean bead from the proper beaker found on the counter (do not use if rusty or misshapen). Check post alignment and adjust if necessary. Invert the bead and press onto the filament ribbon so that the posts are centered on the ribbon. The ends should bend upwards around the posts. Check alignment and make sure that the bead is vertical.

(5)   Clamp the alligator clips onto the two bead posts. Press the foot pedal gently. A beeping noise occurs and the gauge drops to zero. Release the pedal when the gauge begins to move upwards again.

(6)   Use the prong welder to weld the ends of the filament onto the posts in two different spots. To weld, squeeze gently. The assembly will click during the weld.

(7)   Inspect all welds and repeat if necessary. Put away all equipment and ribbon. Loosen the cap on the alcohol squeeze bottle and place under inverted glass cylinder. Turn dial on small control unit to zero, then turn large unit off.

(8)   Outgas the filaments according to the instructions posted in the lab. Make sure to diagram the positions of each type of filament (Re vs. Ta) on the clean piece of paper you place in front of the outgasser. The automatic program will run for 3 hours. "Filament Current Adjust" should be set on 32 - do not change. After outgassing is complete, let cool until unit is no longer warm (perhaps 1 hour). Loosen the bolts, turn off pumping unit, and open the outgasser about one minute after the turbo has completely stopped. You may need to use the bolts to help gently pry open the door by screwing them into the dead-end fittings. Store filaments in the labeled plastic box found in drawer under hood in center lab.

(9)   It is optimal to wait for three days to two weeks before using the outgassed filaments. During this period the filaments will oxidize slightly. This facilitates loading the samples as the solution tends not to spread along the oxidized filament.

V. CLEANING PROCEDURES

A. Teflon

(1)   Use liter bottle labeled "Whole Rock 1". Fill with dirty items (ex.: can fit 8 beakers, 10 vials and 2 centrifuge tubes). Avoid allowing similar items to stack together or for any openings to be blocked. It helps to place smaller vials inside beakers to keep the beakers from stacking.

(2)   Rinse several times with 1x H_2O, using strainer cap to pour out.

(3)   Using strainer, pour out H_2O and fill with 0.5% concentrated HF which is designated for cleaning of whole-rock labware. Wearing gloves, cap the wash bottle tightly and turn a few times. For this and each of the following steps, which may be followed on the printed "recipe" sheets, heat bottle overnight with cap loosened and hotplate set to 2, let cool, and pour out (not down sink!), using strainer. For the HF step, return it to its bottle. Used HNO_3 should be poured into a waste acid bottle (empty; located under acid hood) that has previously been filled approximately with tap water ("Do what you oughter - add acid to water"), using the funnel. This bottle is then taken to room 010 and the contents are carefully emptied into the sink in the corner of the acid hood. Wear glasses and heavy black gloves. The water is allowed to run for a few hours after this to assure proper rinsing and dilution.

As you add each liquid to the bottle, turn with the cap tightened to ensure that all surfaces are in contact with liquid.

(4)   Heat overnight in 1x H_2O, as a rinse.

(5)   Heat overnight in commercial concentrated HNO_3 (<u>not</u> our distilled reagent HNO_3).

(6)   Heat overnight in 1x H_2O, as a rinse.

(7)   Add 4N HNO_3. Normality is approximate only: fill bottle 3/4 full with 1x H_2O and fill with concentrated acid. Heat overnight.

(8)   Heat overnight in 2x H_2O, as a rinse.

(9)   Heat overnight in 0.1N HNO_3 made with 2x H_2O.

(10)   Heat overnight in 2x H_2O. Let cool partially, not completely, before straining.

(11)   Work on clean surface and wear gloves. Rinse each piece separately with 2x H_2O, shake out and place on crew wipe in storage box. Open beakers should be inverted, while vials should be closed with a small amount of 2x H_2O in them.

B. Glass Pipets and Holders

(1)   Use large Pyrex cylinder in center lab. Fill half-way with water. Fill each pipet with 1x H_2O and invert in cylinder. Group pipets on one side, glass tubes on the opposite side and gently wedge water-filled bottles in the empty space between in order to keep pipets vertical (optional). Add commercial HNO_3 in 1:1 proportions with the water. Heat on hot plate (setting 2) in center lab for two days.

(2)   Drain and rinse with 1X H_2O (make sure tubes drain and are rinsed). Add one part HNO_3 to three parts 1X H_2O and heat overnight.

(3)   Drain, add 1x H$_2$O, and heat all day or overnight. Drain and rinse each pipet individually with 2X H$_2$O. Shake out and store in plastic box.

C. Pipet Bulbs

(1)   Rinse in 1X then soak. Dilute one part HNO$_3$ with twenty parts 1X water, and soak bulbs at room temperature for 2-3 hours. Rinse a few times with 1X water, shake out and store in covered beaker.

D. Polyethylene Bottles (30 and 60 ml PE bottles)

(1)   These are not reused but are cleaned before using. They float, so cleaning/soaking requires wedging the bottles in the cleaning beaker. Wedge one layer of bottles and caps into large glass beaker. Fill this level with 1x H$_2$O and repeat for next layer. When beaker is less than 2/3 full, pour in concentrated HNO$_3$ (so have 2:1 H$_2$O:acid). Let soak for one week in hood in center lab.

(2)   Handle waste acid as in step A.(3). Use watch glass when pouring acid out. Rinse twice with 1x H$_2$O into funneled drain, and soak for a few days in 1x H$_2$O.

(3)   Rinse each bottle twice with 2x H$_2$O, shake out excess water and loosely cap. Store in appropriate box. These should dry out before using.

(4)   For larger PE bottles, use the same procedure as for small PE bottles, but treat only inside of bottles (i.e. do not soak in large glass beaker).

E. Glass Centrifuge Tubes

(1)   Place upright in W.R. wash bottle. Wash the same as teflon, but <u>without</u> the HF step.

F. Backwashing CAT Column Resin

       <u>Note</u>: Perform once every year. Conserving all of the resin is extremely important as the elution curve is a function of the resin volume. If much resin is lost the elution curve must be recalibrated.

(1)   Rinse labeled 60 ml PE bottle with 1.5N HCl and 2X water.

(2)   Hold the column horizontally and squirt 2X water into the bulb. Rock column back and forth to loosen resin. Pour suspended resin into PE bottle and repeat until all resin is in bottle.

(3)   Close PE bottle and let resin settle. Meanwhile, put column back in its stand, squirt 4N HCl into column to rinse down any remaining resin and let acid drip out into waste beaker.

(4)   After resin has settled, gently decant water out of PE bottle. Fill bottle with 6N HCl, close and shake. Let resin sit in acid for one hour; shake often. Let resin settle, decant, and repeat acid treatment.

(5)   Shake to suspend resin and gently pour suspension into the proper column. Resin will be treated one more time with 6N HCl prior to the next elution.

G. Cleaning Blocks and Face Plates

(1)   Cover parts in beaker with 5% HNO_3, and place in ultrasonic for 45 mins.

(2)   Heat at 2 setting for 2-3 hours.

(3)   Drain acid and rinse five times in 1x H_2O, using watch glass to drain. Leave uncovered on hot plate until totally dry (perhaps 4 hours).

VI. Quartz Still: Making 2X Water

(1)   Clean all surfaces with 1X H$_2$O and Kimwipe, including the tabletop, all parts of the still stand, and the still itself.

(2)   Open green stopcock on large water jug in corner so that you can read the word "ON". The smaller jug is for making 3X H$_2$O. If necessary, fill the large jug by turning the key near the ceiling. (Don't let it overflow.)

(3)   Raise the float assembly so that the set screw is just visible above the top of the post. Hold in place with the set screw. Let water fill the still up to the overflow stem and flow out into the large beaker. Flush in this way until 500 ml have passed through.

(4)   Lower the float assembly so that the square bracket is just below the beveled top of the post. At this point the water level in the still should be just below the overflow stem.

(5)   Turn on the cooling water so that a steady, gentle stream drains into the sink.

(6)   Plug in and turn on the Variac (setting 85).

(7)   Let the still drip for one hour into the waste beaker. This cleans the condenser rod.

(8)   Get a 2 liter "2X H$_2$O" bottle. Pour out the small amount of 2X H$_2$O remaining (this prevents any residue from drying in the bottle during storage) and put the lid in the small tupperware box. Place the bottle under the still and wrap the connection with Parafilm. It takes approximately 18 to 20 hours to fill one bottle. This can be operated overnight.

(9)   If making several bottles, repeat step (3) to flush the still after every other bottle. When finished, leave water in the still, close valve from supply tank, turn off power and cooling water, and cover still opening with parafilm.

VII. REAGENT PREPARATION

A. HCl and HNO₃ Distillation

(1)   Use gloves and glasses. Make sure acid still has been completely rinsed since previous distillation and is filled with pure 1X H_2O. Clean all surfaces with wet kimwipes, including all parts of the still apparatus, the hood tabletop, and the drain at the back of the hood. Drain H_2O from still and supply bottle into beaker, and, using funnel from cabinet to right, pour commercial acid into supply bottle to fill about 1/2.

(2)   With lowest stopcock closed, open stopcock on supply bottle to let acid into still. Fill to below top of overflow stem.

(3)   Place beaker 1/2 filled with H_2O below still, turn on cooling water, and turn on heater power supply. Let distill for 30 mins. to rinse condenser rod.

(4)   Place appropriate 1 liter acid bottle below the still and raise to slide plastic square underneath to provide a good fit between bottle mouth and still opening. Wrap the connection with parafilm.

(5)   Since the still has no float assembly, you must manually maintain the acid level in the still as distillation proceeds. Once every hour, open the supply stopcock to raise the acid to below the top of the overflow stem. Between bottles, drain the acid in the still out the lowest stopcock into the beaker (with water in it) and refill the still.

(6)   When finished, drain all acid from the still. With the tube leading to the stopcock on the right side of the hood, put water into the supply bottle, rinsing down the inner walls

as you do. Drain this water into the still, plugging the overflow stem with a piece of parafilm held by your gloved finger. When the water reaches the opening adjacent to the end of the condenser rod, hold another piece of parafilm over the bottom of this opening and gently rock the still assembly to slosh water on all inner surfaces. Drain the water from the still and supply bottle and repeat the rinsing twice. Wipe up the work area and cover still openings with parafilm.

B. Mixing HCl Reagents

(1)   For Nd-Sr whole-rock work, reagents made from quartz distilled acids and 2x H_2O do not present a blank problem. If lower-level work is planned, check the blank levels to determine your needs. (You should periodically check reagent blanks anyway.)

(2)   Calculate amounts of concentrated HCl (roughly 12N) and 2x H_2O to mix for desired normality in desired volume. There is a 1L graduated cylinder for this purpose - make sure it is clean. After mixing, check by titrating with NaOH solution (the normality of which you are confident), adjust by adding acid or water, and recheck. Tolerance is 5%.

C. Ion Exchange Column Resins and 2-methyllactic acid

For the REE columns, stores of resin (50W-X4, -400 mesh) and acid (0.21M 2-methyllactic acid or MLA) will need to be replenished. The resin for the cation columns (50W-X8, 100-200 mesh) is not replaced, but this type of resin is used in the preparation of the MLA. The PE bottles used in these steps may be reused as long as they are cleaned and rinsed. You will need large quantities of clean reagent HCl and 2X H_2O for these procedures, so keep the stills busy.

(1)   Obtain a 100 g bottle of 2-methyllactic acid powder (possible vendor: Pfalz and Bauer Inc.). Weigh a clean, dry 500 ml PE bottle. Add MLA powder to this bottle until you have 92 g; weigh by difference. Add 2X H_2O to fill the bottle, and shake well to dissolve the MLA powder.

(2)   Get a sheet of the filter paper used in the REE columns (#589 white ribbon) and fold and form in a plastic funnel over a second clean 500 ml PE bottle. Pass your 500 ml MLA solution through this filter and collect in the second 500 ml bottle (or directly in a 2 liter volumetric flask -- see step 4). The filtration is slow and is done in steps.

(3)   Meanwhile, begin cleaning the 100 ml of <u>50W-X8, 100-200 mesh</u> resin that will be used for cleaning the MLA. The 2.5 and 4.0 N HCl acids used here need not be titrated, but they should be clean.

     a. Pour resin suspension from the original jar into a clean 1 liter PE bottle so that you have 100 ml of resin (mark the PE bottle at 100 ml, check after the resin has settled, and adjust accordingly). When settled, decant the H_2O.

     b. Add 500 ml 2.5N HCl (using a 600 ml mark on bottle), close bottle, swirl well, let sit 15 minutes (or until resin is settled), decant acid. You may want to recycle these acids for nonreagent purposes.

     c. Repeat 2.5N HCl step.

     d. Do the same with 4N HCl.

     e. Repeat the 4N HCl step.

     f. Add enough 4N HCl to make a fluid slurry.

     g. Rinse the large 500 ml quartz column well with 2X H_2O and place a large ($\geq$ 500 ml) waste beaker beneath it. Pour into this column the 4N HCl slurry of resin, using extra acid, if necessary, to wash all resin out of the bottle. Let all the acid pass through.

h. Pass 300 ml 2.5N HCl through column. (Do not let the waste beaker overflow!)

i. Pass 500 ml 4N HCl through column.

j. Pass 1 liter 2X H_2O through column in two steps of 500 ml. The resin is now ready for step (7) below. If there are delays before proceeding, prevent drying by periodically adding more 2X H_2O to the column.

(4)   During step (3), the 500 ml MLA should be finished filtrating. Pour into a clean 2 liter volumetric flask and dilute with 2X H_2O to 2 liters. Pour into a 2 liter PE bottle.

(5)   Titrate the MLA in 10 ml aliquots with 0.5N NaOH; it should be >0.44M. Dilute with 2X H_2O to get to 0.42M. Don't overshoot!

(6)   Measure 1 liter of this 0.42M MLA in a clean 1 liter volumetric flask; set aside.

(7)   We now clean the 0.42M MLA with the 50W-X8 resin that we prepared in step (3). Pass the 0.42M MLA remaining in the bottle (1 liter) through the resin in the large column and collect in a clean 1 liter PE bottle. This requires two steps of 500 ml each.

(8)   Pass the 0.42M MLA from the 1 liter volumetric flask through the resin and collect in a clean 2 liter PE bottle. This requires two steps of 500 ml each. When done, clean the 1 liter volumetric flask, measure in it 1 liter of 2X H_2O, and add this to the MLA in the 2 liter bottle. It is now 0.21M.

(9)   Meanwhile, you can begin cleaning 100 ml of 50W-X4, -400 mesh resin (for REE columns) using the same procedures as in steps (3), a-f.

(10)   The 50W-X8 resin left in the large column after step (8) is no longer needed, and may be discarded; proceed to step (11). If, for some reason, the cation columns need new resin, do the following. With the resin still in the large column after step (8), pass 500 ml 2X H_2O, followed by 500 ml 4N HCl. Add a little more 4N HCl, pipet out the top 1/5 of the resin, and discard. Remove the remaining resin to a 125 ml bottle using the technique outlined in section V.F (backwashing columns). Add 15 ml of this cleaned resin to each cation column and pass 300 ml 2.5N HCl followed by 500 ml 4N HCl (in steps of 100 ml). The columns are ready for use as soon as they are calibrated and checked for blank levels.

(11)   Rinse the large column well to remove all resin traces. Now you may continue the cleaning of the 100 ml of REE resin (50W-X4, -400 mesh), begun in step (9), by following the procedures described in steps (3) g-j (except that you do not proceed to step (7) when done).

(12)   Meanwhile, adjust the pH of the two MLA solutions by adding NH_4OH (in acid cabinet). Use a pH meter that works and that you know how to use, frequently checking against a known solution. To be safe, set aside about 40 ml of the original MLA in case you overshoot while adding NH_4OH (discard this reserve when you are finished). You will be adding on the order of 30 ml of NH_4OH to reach the appropriate pH. Start by adding the NH_4OH in 10 ml steps between pH checks; when you get closer, decrease to ~ ml steps between checks, and then use a dropper bottle for fine adjustments. Be conservative and patient. Adjust the 0.42M MLA to pH=4.7, and the 0.21M MLA to pH=4.65.

(13)   The 0.21M MLA (pH 4.65) is ready for use on the REE columns. Whenever you begin using a new batch of MLA, it is necessary to recalibrate the columns and measure the column blank.

(14)   Pass the 0.42M MLA (pH 4.7) through the large column containing the REE resin after completion of step (11). This MLA serves to condition the resin; it is discarded.

(15)   Pass 1 liter 2X H_2O through the REE resin in two batches of 500 ml.

(16)   Add a little 2X H_2O to the resin, pipet out the top 1/5, and discard. Add more 2X H_2O and remove the resin to a 125 ml PE bottle using the technique described in section V.F. (backwashing columns). Store under water. The REE resin is ready for use.

VIII. COLUMN CALIBRATION

Note: Column calibration should be performed annually, or when a yield or interference problem is evident. The basic procedure is to elute a solution of known concentration in the column and to determine when all of a given element may be collected in the eluent. There are different ways of doing this; this is merely one suggestion. We first discuss the method for determining how much of each element you are retaining in the elution (the "yield"), then we describe the method for column calibration.

A. Yield Determination

(1) This can be done for any sample (spiked or not) that your are processing in the lab. Before eluting the sample, weigh bottles and vials in which each element will be collected. Weigh each element solution after elution, and spike a small weighed aliquot (enough for a decent mass spec. run; e.g., 150 ng Nd).

(2) After you have analyzed the sample itself, run this spiked aliquot on the mass spectrometer to get a rough spike/sample ratio (e.g., 84/86 for Sr). Calculate the amount of the given element in the aliquot (see isotope dilution equations in section on spike calibration - you don't need to do the corrections since this is a percent-level determination). If the sample is already spiked, you must alter your isotope dilution equations to make the "sample" ratio (e.g., 84/86) equal to the spiked ratio on the main sample. Extrapolate this amount of the element to the element solution as a whole to determine how much of that element was collected from the column. Since you know how much sample was eluted and you know the concentration of the element in the sample, you can calculate how much of the element should have been collected. The percentage actually collected is the yield. A column yield should be in the 90-100% range.

Note: When you do a yield determination on the REE columns, remember that you have already lost some sample in the CAT columns. In other words, don't underestimate the REE column yields. You may also want to check the dissolution yield by taking an aliquot before column elutions.

B. Cation Column Calibration

(1)   Start with a rock sample solution of known Rb, Sr, Sm, and Nd concentrations. Load on column as usual, but instead of collecting each element in an entire fraction, split the fraction into smaller cuts that can be analyzed for the element. For example, if Rb is normally collected in a 22 ml cut after 42 ml have passed, do the following:

2.5N HCl	36 ml	do not collect	
	2 ml	collect	
	2 ml	"	
	2 ml	"	
	2 ml	"	Previous Rb cut
	2 ml	"	↓
	2 ml	"	
	10 ml	"	
	2 ml	"	
	2 ml	"	↑
	2 ml	"	Previous Rb cut
	2 ml	"	
	2 ml	"	
	2 ml	"	

(2)   Measure the concentration of the element in each cut.   Such a scheme is recommended if you have the means for relatively quick concentration determinations, such as AA or DCP. (The detection levels of these methods may require you to dope the sample with a large amount of the element.) Work from the inner 10 ml cut outward, translating concentrations into amounts of the element. You can then determine in which cuts you have collected the entire amount of the element. You want the cuts small enough so that you can determine the locations of the tails of the elution curves (see DePaolo, 1978).

Shirey et al. (1988) describe a relatively quick method for semiquantitative measurements of Sr and the REE that involves titration with EDTA. We are equipped for these procedures, but instrumental means may prove more efficient if detection limits are low enough.

(3)   The REE are collected in 4N HCl after Sr in 2.5N.   If using instrumental measurements, you should determine elution curves for both Sm and Nd (the Shirey method does not discriminate the individual REE).

(4)   You can now construct a new elution curve. Large shifts should be met with skepticism. Check the column yields (with isotope dilution) on the first samples eluted after calibration.

IX. SPIKE CALIBRATION

The basic idea in spike calibration is to mix the spike solution with a solution of the unspiked element at a known concentration. We have a stock of only one of these "normal" solutions, nSr1, which has a concentration of 3.6133 nmol/g ^{86}Sr. Rb and Sm/Nd (mixed) normal solutions may be obtained from the Lunatic Asylum by speaking with D. Papanastassiou and/or H. Ngo. In the case of Sm and Nd, we have mixed spikes and normals, since the Sm/Nd ratio is the critical datum. After mass spectrometric determination of the sample/spike ratio, it is then simple to calculate the concentration of the spike solution. Since this concentration can change with time, most likely due to evaporation, the calibration should be carried out annually. After calibration is complete, remember to change the spike concentration values wherever they occur in the offline Basic programs SRDATA and NDDATA, as well as in Table 1 of this document.

The sample/spike ratio is calculated from the measured ratios in the opposite sense to the normal isotope dilution calculation. Thus, with the exception of Rb, iteration is necessary. (There is presently no software to do this, but it would fairly easy to write.) Your results are only as good as how well you know the concentration of the normal solution and how precise your weighings and measurements are.

In the following equations: m = measured, t = spike, s = normal sample. As with typical isotope dilution calculations, fractionation corrections during analysis should be performed with the usual ratios. The spike contribution to the normalizing ratio is corrected for in these offline calculations.

A. Rb

The isotope dilution equation is:

$$\frac{87_s}{87_t} = \frac{(85/87)_m - (85/87)_t}{(85/87)_s - (85/87)_m}$$

In the case of spike calibration, you can calculate 87_s = (wt. normal soln. mixed with spike)*(conc. normal soln. in nmol/g of ^{87}Rb), and this equation can easily be rearranged to calculate 87_t from your measured ratio $(85/87)_m$. You now can get the spike concentration (in nmol/g of ^{87}Rb) by dividing 87_t by the weight of the spike solution in the mixture.

B. Sr

The isotope dilution equation is:

$$\frac{86_s}{84_t} = \frac{(86/84)_m - (86/84)_t}{1 - (86/84)_m (84/86)_s}$$

However, your measured $(84/86)_m$ (inverted in this equation) must be corrected first because it was normalized to $(86/88)_{mixture} = 0.1194$ rather than $(86/88)_{sample} = 0.1194$. This correction is carried out with the equation (modified from Eugster et al. 1969):

$$(88/86)_s = (88/86)_m + \frac{[(88/86)_m(86/84)_t - (88/84)_t][1 - (84/86)_s/(84/86)_m]}{(84/86)_m^{-1} - (86/84)_t}$$

Normal and spike ratios are listed on the SRDATA output. In the first iteration, $(88/86)_m = (0.1194)^{-1}$, since this was how normalization was carried out during analysis. But we would like to set $(88/86)_s = (0.1194)^{-1}$, so we now treat this discrepancy as a fractionation, and correct $(84/86)_m$ and $(88/86)_m$ by the power law (Wasserburg et al., 1981):

$$p = \frac{-\ln[(0.1194)(88/86)_s]}{0.02297202}$$

$$(84/86)_m(corrected) = (84/86)_m(0.9767681)^p$$

$$(88/86)_m(corrected) = (88/86)_m(1.0232379)^p$$

In the next iteration, use these new values to calculate $(88/86)_s$. Repeat iterations until $(88/86)_s$ is within 1 ppm of $(0.1194)^{-1}$, i.e.,

$$\left|(88/86)_s(0.1194) - 1\right| < 10^{-6}$$

You can now use the final *corrected* value for $(84/86)_m$ in the above isotope dilution equation, which is rearranged to calculate 84_t given 86_s (which you calculated from your weighing of the normal as for Rb). Now calculate the concentration of the 84_t solution by dividing by the weight mixed with the normal.

C. Sm

The isotope dilution equation is:

$$\frac{147_s}{147_t} = \frac{(148/147)_m - (148/147)_t}{(148/147)_s - (148/147)_m}$$

However, your measured $(148/147)_m$ must be corrected first because it was normalized to $(149/152)_{mixture} = 0.51686$ rather than $(149/152)_{sample} = 0.51686$. This correction is carried out with the equation (modified from Eugster et al. 1969):

$$(149/152)_s = (149/152)_m + \frac{[(149/152)_m(152/147)_t - (149/147)_t][1 - (152/147)_m(147/152)_s]}{(152/147)_m - (152/147)_t}$$

where

$$(152/147)_m = \frac{(148/147)_m}{(148/152)_m}$$

Normal and spike ratios are listed on the NDDATA output. In the first iteration, $(149/152)_m = (0.51686)$, since this was how normalization was carried out during analysis. But we would like to set $(149/152)_s = (0.51686)$, so we now treat this discrepancy as a fractionation, and correct $(148/147)_m$, $(148/152)_m$, and $(149/152)_m$ by the power law (Wasserburg et al., 1981):

$$p = \frac{-\ln[(0.51686)/(149/152)_s]}{0.01996196}$$

$$(148/147)_m(corrected) = (148/147)_m(1.0068062)^p$$

$$(148/152)_m(corrected) = (148/152)_m(0.9736380)^p$$

$$(149/152)_m(corrected) = (149/152)_m(0.9802360)^p$$

In the next iteration, use these new values to calculate $(149/152)_s$. Repeat iterations until $(149/152)_s$ is within 1 ppm of (0.51686), i.e.,

$$\left| 0.51686/(149/152)_s - 1 \right| < 10^{-6}$$

You can now use the final *corrected* value for $(148/147)_m$ in the above isotope dilution equation, which is rearranged to calculate 147_t given 147_s (which you calculated from your weighing of the normal as for Rb). Now calculate the concentration of the 147_t solution by dividing by the weight mixed with the normal.

D. Nd

The isotope dilution equation is:

$$\frac{144_s}{150_t} = \frac{(150/144)_m^{-1} - (144/150)_t}{1 - [(150/144)_s/(150/144)_m]}$$

However, your measured $(150/144)_m$ must be corrected first because it was normalized to $(146/144)_{mixture} = 0.7219$ rather than $(146/144)_{sample} = 0.7219$. This correction is carried out with the equation (modified from Eugster et al. 1969):

$$(146/144)_s = (146/144)_m + \frac{[(146/144)_m(144/150)_t - (146/150)_t][1 - (150/144)_s/(150/144)_m]}{(150/144)_m^{-1} - (144/150)_t}$$

Normal and spike ratios are listed on the NDDATA output. In the first iteration, $(146/144)_m = (0.7219)$, since this was how normalization was carried out during analysis. But we would like to set $(146/144)_s = (0.7219)$, so we now treat this discrepancy as a fractionation, and correct $(146/144)_m$ and $(150/144)_m$ by the power law (Wasserburg et al., 1981):

$$p = \frac{-\ln[(0.7219)/(146/144)_s]}{0.01382265}$$

$$(146/144)_m(corrected) = (146/144)_m(1.0139186)^p$$

$$(150/144)_m(corrected) = (150/144)_m(1.0417678)^p$$

In the next iteration, use these new values to calculate $(146/144)_s$. Repeat iterations until $(146/144)_s$ is within 1 ppm of (0.7219), i.e.,

$$\left|0.7219/(146/144)_s - 1\right| < 10^{-6}$$

You can now use the final *corrected* value for $(150/144)_m$ in the above isotope dilution equation, which is rearranged to calculate 150_t given 144_s (which you calculated from your

weighing of the normal as for Rb). Now calculate the concentration of the 150_t solution by dividing by the weight mixed with the normal.

Since we use mixed Sm-Nd spikes, the ratio between $^{147}Sm_t$ and $^{150}Nd_t$ in the spike solution should not change (outside of error) from one calibration to the next. If it does, recheck all your procedures and calculations.

X. BLANKS

A blank measurement is simply isotope dilution at low levels, performed on a "sample" which can be a reagent, a column, or a procedure. A known quantity of spike is subjected to the reagent or procedure, isotope ratios are measured, and the amount of element added to the spike is calculated. Table A2.8 lists blanks measured in this laboratory.

A. Reagent Blanks

(1)   Based on previous or expected blank levels, calculate how much blank spike ("BS-1" - see Table 1) should be added to a "sample" of 1-5 ml of the given acid or water. Use the equations in section I.A.(1) in the same manner that they are used for samples. Since all four spike isotopes are mixed in BS-1, you will have to compromise. It is not so important to optimize the spike levels since the isotopic measurements are low-precision anyway; you just want to avoid having to measure (1) very high ratios if you have seriously overspiked, or (2) ratios little changed from normal if you have seriously underspiked.

(2)   Weigh out both reagent and spike and mix in a vial. Evaporate, ensuring that you know the location of the possibly invisible dried sample - this is best accomplished with a round-bottomed vial. Load on a single Re filament in ~1 µl 1.5N HCl.

(3)   Analyze all four elements during the same mass spectrometer run in the order Rb, Sr, Nd, Sm. Use the Daly multiplier and measuring routines such as "Sr rough." These routines only measure one ratio, such as $^{84}Sr/^{86}Sr$, with no fractionation correction since high precision is not needed. Precisions of around 10% are fine. It is not important, for example, whether a reagent has 60 rather than 50 pg Sr per g, but we do want to know if it is 200 rather than 50 pg/g. Scan the masses around the isotopes of interest to ensure that you are not getting interferences from other elements or oxides of elements (with your

trusty "Chart of the Nuclides" at your side). Sm has proven particularly difficult to measure - if so, it is probably safe to assume that Sm blank levels are comparable to Nd levels in a chondrite-normalized sense.

(4)   Calculations are the same as for sample isotope dilution, omitting the iterations. For example: for Sr, calculate 86_s (nmol) with the equation in section IX.B., having calculated 84_t from the weight of spike added to the reagent. Divide 86_s by the weight of the reagent to get the blank level of ^{86}Sr in nmol/g. Transform this value to nmol of Sr per gram by multiplying by the normal value for (84+86+87+88)/(86), assuming an average 87/86 (say, 0.71). Now multiply by the atomic weight of Sr to get ng/g. Change to pg/g if necessary. Note: The blank for a diluted HCl (e.g., 4N HCl) is simply a combination of the blanks for concentrated HCl and 2X H_2O.

B. Column Blanks

(1)   Weigh out ~1 g of BS-1 and evaporate to a small drop. Run it through the column (CAT or REE) as you would a sample, collecting the various fractions.

(2)   For the CAT columns, analyze separately the entire Rb, Sr, and REE fractions on the mass spectrometer, using "rough" routines as described above. Nd and Sm will have to be measured on the same filament.

(3) For the REE columns, Nd and Sm are analyzed separately and Rb and Sr are not analyzed.

(4)   Calculate blanks as described above, except that you are determining an <u>amount</u> (in pg or ng) of the element rather than a concentration. That is, omit the step wherein you divide by the weight of the reagent.

C. Procedural Blanks

This is the blank that should be reported in articles. It is the total blank added to a sample by the chemical and mass-spectrometric procedures. It should not be large enough to significantly alter the ratios determined for a sample. You can calculate such a "safe" level for, say, Sr by assuming a rather extreme but realistic 87/86 for the known amount of blank and calculating how much the addition of that blank to the Sr in a typical sample will alter the sample's 87/86. Check your reagent blanks against Lunatic Asylum values (Ngo et al., 1985) and your procedural blank against those reported by various labs in the literature.

(1)   Weigh out into each of two beakers or vials ~1 g of BS-1. Perform the blank determinations in pairs so that you will have a "sample" for each column. Take the blank spike solution through the entire chemical procedure, including dissolution, treating it as you would a sample. Take care to not lose any of the "sample" during evaporations, since doing so will leave you with less spike than you think, artificially amplifying the blank levels of subsequent procedures.

(2)   Mass spectrometric analyses can be done with "rough" measuring routines on the Daly. Calculations are as described above for column blanks, i.e. the result is an amount of the element (in ng or pg) rather than a concentration.

Table A2.8. Blank Determinations

	Rb	Sr	Nd	Sm
1X H_2O	0.12 pg/g	1.3 pg/g	0.053 pg/g	0.02 pg/g
2X H_2O	0.06 "	0.39 "	0.018 "	--
3X H_2O	0.05 "	0.32 "	0.058 " (?)	--
HCl	0.12 "	2.3 "	0.068 "	<0.07 "
HF	0.42 "	1.5 "	0.43 "	--
HNO_3	0.65 "	4.5 "	0.28 "	--
$HClO_4$	1.02 "	21.6 "	0.82 "	--
MLA	--	--	1.2 "	--
Procedural #1	12 pg	220 pg	19 pg	7.0 pg
Procedural #2	10 pg	110 pg	4.6 pg	2.4 pg

References

DePaolo, D.J., Study of magma sources, mantle structure and the differentiation of the earth from variations of ^{143}Nd/^{144}Nd in igneous rocks, Ph.D. thesis, California Institute of Technology, Pasadena, Calif., 1978.

DePaolo, D.J., Neodymium isotopes in the Colorado Front Range and crust-mantle evolution, *Nature, 291*, pp. 193-196, 1981.

Eugster, O., F. Tera, and G.J. Wasserburg, Isotopic analyses of barium in meteorites and in terrestrial samples, *J. Geophys. Res., 74*, 3897-3908, 1969.

Ngo, H.H., G.J. Wasserburg, and B.P. Glass, Nd and Sr isotopic compositions of tektite material from Barbados and their relationship to North American tektites, *Geochim. Cosmochim. Acta, 49*, 1479-1485, 1985.

Russ, G.P. III, Neutron stratigraphy in the lunar regolith, Ph.D. thesis, California Institute of Technology, Pasadena, Calif., 1974.

Shirey, S.B., J.L. Banner, and G.N. Hanson, Cation-exchange column calibration for Sr and the REE by EDTA titration, *Chem. Geol., 65*, 183-187, 1987.

Wasserburg, G.J., S.B. Jacobsen, D.J. DePaolo, M.T. McCulloch, and T. Wen, Precise determination of Sm/Nd ratios, Sm and Nd isotopic abundances in standard solutions, *Geochim. Cosmochim. Acta, 45*, 2311-2323, 1981.